Structure and Mechanical Properties of Nanophase Materials— Theory and Computer Simulation vs. Experiment

Symposium held November 28–30, 2000, Boston, Massachusetts, U.S.A.

EDITORS:

Diana Farkas
Virginia Polytechnic Institute and State University
Blacksburg, Virginia, U.S.A.

Harriet Kung
Los Alamos National Laboratory
Los Alamos, New Mexico, U.S.A.

Merrilea Mayo
Pennsylvania State University
University Park, Pennsylvania, U.S.A.

Helena Van Swygenhoven
Paul Scherrer Institute
Villigen, Switzerland

Julia Weertman
Northwestern University
Evanston, Illinois, U.S.A.

MⱤS

20010727 116

Structure and Mechanical Properties of Nanophase Materials— Theory and Computer Simulation vs. Experiment

CONTENTS

*Invited Paper

*Invited Paper

MECHANICAL PROPERTIES AND DEFORMATION BEHAVIOR III— MULTILAYERS

*Invited Paper

CLUSTERS AND OTHER NANOSTRUCTURES

*Invited Paper

PREFACE

Symposium B, "Structure and Mechanical Properties of Nanophase Materials—Theory and Computer Simulations vs. Experiment," was held November 28–30 at the 2000 MRS Fall Meeting in Boston, Massachusetts. This symposium received support from the Office of Naval Research, Los Alamos National Laboratory, JEOL USA, Inc., and the FEI Company.

This symposium focused on an examination of the mechanical properties of nanostructured materials obtained from theoretical studies, computer modeling (involving length scales from atomic to macroscopic), and from experiments. An emphasis is placed on (1) the guidance that computer modeling can give in designing experiments as well as to their interpretation, and (2) the guidance suggested by experiments and characterization of actual nanocrystalline samples in setting up the initial structure of a computer model and the development of new potentials. Nanostructured materials of interest include metals, ceramics and composites, in bulk form, thin films, and layered structures. Two half-day oral sessions were held on the topic of Mechanical Properties and Deformation Behavior of Bulk Materials. Other half-day oral sessions were devoted to the areas of Mechanical Properties and Deformation Behavior of Multilayers; Ceramic Materials; and Clusters and Other Nanostructures. In addition, a half-day joint session was held with Symposium W, "Limits of Strength in Theory and Practice." The subject of the Symposium B papers in this session concerned Softening at Very Small Grain Sizes. Finally two poster sessions were devoted to various aspects of the behavior of nanostructured materials.

Most of the papers presented at the symposium are collected in these proceedings. The editors wish to thank the authors, reviewers, Meeting Chairs, sponsors and the ever-efficient and helpful MRS staff for their help in organizing the symposium and in publishing these proceedings.

Diana Farkas
Harriet Kung
Merrilea Mayo
Helena Van Swygenhoven
Julia Weertman

March 2001

MATERIALS RESEARCH SOCIETY SYMPOSIUM PROCEEDINGS

MATERIALS RESEARCH SOCIETY SYMPOSIUM PROCEEDINGS

Prior Materials Research Society Symposium Proceedings available by contacting Materials Research Society

Mechanical Properties
and Deformation Behavior I

An Overview of Plasticity in Nanoscale Composites

J.D.Embury and C.W.Sinclair
Department of Materials Science and Engineering, McMaster University, Hamilton,
Ontario, Canada

Introduction

In the past two decades there has been great activity in the area of nanoscale composites. This has included enormous effort in the areas of epitaxial structures for microelectronics applications, organometallic systems, coatings [1], layered metallic structures and drawn in-situ composites. A great deal of progress has been made in the development of controlled fabrication methods including sputtering, electrodeposition and crystallization of amorphous structures. Also, attention has been given to the integration of ultrafine scale structures into the design of many engineering applications from high field magnets operating at cryogenic temperatures [2] to future gas turbines [3].

These developments emphasize the need to explore, at a fundamental level, the progress associated with plasticity of ultrafine scale structures.

The processes of plasticity can be explored at the macroscopic, mesoscopic, and microscopic levels in order to delineate those aspects of the mechanical response which are characteristic of ultrafine scale materials. Clearly, it is important to emphasize that there can be competition between plasticity and damage and fracture events and between competitive processes of plasticity and that these are dependent on the characteristic length scale of the structures. A classical system which reflects the competition of plasticity and fracture is the system $Fe-Fe_3C$. This was explored in the seminal work of Langford [4] illustrated in figure 1. This indicates that Fe_3C in the form of particles 1-10 μm in thickness is brittle but when the scale is reduced to 50 nm the Fe_3C is ductile and can undergo extensive plastic flow.
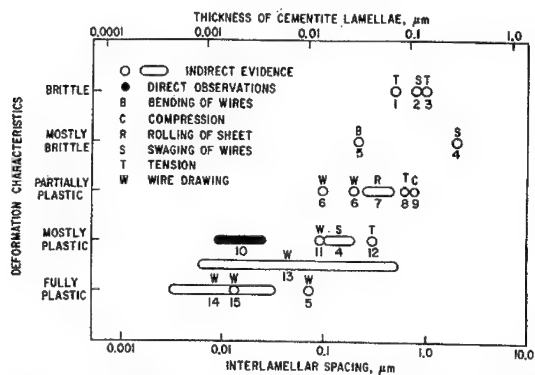
Figure 1: Langford's compilation of the data in the literature for the scale dependent ductile to brittle transition of cementite in pearlitic steels (from Ref. 4)

There are two important consequences of these observations. The first is that normally brittle phases may, when embedded in a ductile matrix, undergo plastic flow and thus exhibit a size dependent ductile-brittle transition. The second is that even complex structures which have limited numbers of slip systems may be able to co-deform with a matrix capable of general plasticity.

In addition to the competition between plasticity and fracture there is a scale dependant competition between deformation mechanisms and this can be studied via the utilization of the deformation mechanism maps described by Frost and Ashby [5]. There is a need to explore the behavior of ultrafine scale structures over a range of temperatures and strain rates in order to develop these scale dependant maps in a quantitative manner.

If we turn to a mesoscopic view of plasticity of ultrafine scale materials, the problem is essentially to examine the compatibility of flow between the constituent phases. This can be considered in terms of load transfer to an elastic embedded phase and subsequently the conditions needed for co-deformation of the constituent phases. A variety of diffraction methods can be utilized to monitor the elastic stresses in the constituent phases both under load and during load reductions or load reversals. This permits the elastic plastic transition of the embedded phase to be monitored. This can be illustrated, as in figure 2, for the system Cu-Cr [6] which after directional solidification contains 2% by volume of Cr fibres which eventually act as embedded whiskers.

The elastic stresses in the Cr can be monitored by the shift in the position of a diffraction peak with strain as shown in figure 2(a). The elastic strains in the Cr fibres vary with total imposed deformation as shown in figure 2(b). These types of observations provide valuable evidence concerning the behavior of the Cr fibres. In the elastic-plastic transition the copper matrix undergoes plastic flow and the Cr fibres
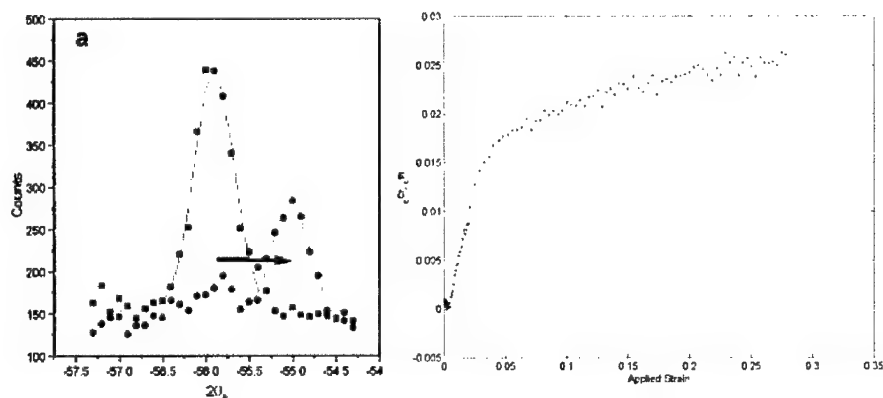
Figure 2: Residual stresses in a Cu-Cr eutectic alloy measured by unloading after various amounts of plastic strain. (a) Shift in a Bragg diffraction peak of Cr caused by high elastic residual stresses in the Cr fibers. Square and round peaks: before and after deformation. (b) The elastic strain in the Cr fibers plotted against applied strain. Strain in the fibers increases with increasing applied strain to >2%.

sustain large elastic deformations of order 2% prior to yielding of the fibres. Subsequently, the fibres deform by plasticity but continue to accumulate elastic strain but at a much slower rate. The elastic stresses in the fibres also contribute to the process of reverse flow and can be monitored by either loading-unloading experiments or by Bauschinger experiments.

At the microscopic level there has been much effort devoted to studying both dislocation structures in ultrafine scale structure and in situ electron microscopy to determine how flow occurs in terms of whether individual dislocations or groups of dislocations are involved [7]. Three salient features emerge from these studies. The first is the examination of the limits of applicability of existing models involving length scales such as Hall-Petch strengthening or the Orowan hardening process. There has been much effort on examining these processes in metallic multilayers and an example is shown in figure 3. There is evidence to indicate that at layer structures below 50nm the process of plasticity becomes one of passing individual segments of dislocation between interfaces rather than groups of dislocations [8].

This helps focus attention on the second salient feature which is the need to understand in detail the process of dislocation nucleation, transmission and accumulation at interfaces. This is a rich topic in which atomistic simulation of the events at the boundaries [9] can be compared with careful experimental work. This is at a preliminary stage but clearly variables such as the degree of misfit, differences in the elastic moduli, detailed interface crystallography and layer thickness all exert influences on these events [10] and can be used to tailor new classes of materials.

A final feature which emerges from the plasticity studies is the question of energy storage. In conventional plastic flow we consider the energy stored in terms of the accumulated dislocation density. In ultrafine scale material there is a very large ratio of internal surface to volume and the areas available for slip events are restricted. Thus other processes may occur including the creation of new surfaces [11] or compositional
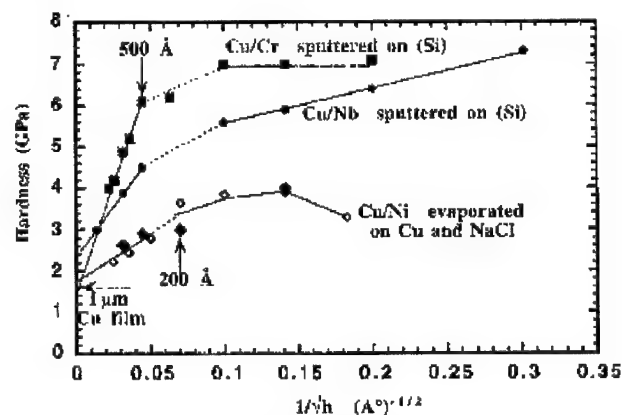
Figure 3: Hall Petch plot for various copper-based multilayers of different layer thickness (h) (from Ref. 8)

changes [12]. Also at larger strains the presence of well defined interfaces and the restriction of areal glide may introduce major changes in the development of texture.

Thus it is clear that ultrafine scale materials which possess large amounts of internal surface represent a new and exciting area of plasticity in which dislocation nucleation at interfaces becomes a dominant feature. These materials present new challenges. They can develop very large short wavelength internal stresses. They require detailed understanding of interactions at the interface. However they also present a rich area of collaboration between modeling and experiment and the possibility of producing new materials with unique functionability in terms of control of both structural and functional properties by control of the scale of the structure and their detailed architecture.

REFERENCES

1. C. R. Aita, C. M. Scanlan and M. Gajdardziska-Josifovska, *J. of M.*, 40 (1994).
2. J. T. Wood, J. D. Embury and M. F. Ashby, *Acta Mat.* **45**, 1099 (1997).
3. M. Gell, *J. of M.*, 30 (1994).
4. G. Langford, *Metall. Trans. A* **8**, 861 (1997).
5. H. J. Frost and M. F. Ashby, *Deformation Maps*, Pergamon Press (1982).
6. C. W. Sinclair, J. D. Embury and G. C. Weatherly, *Mats. Sci.&Eng.* **A272**, 90 (1999).
7. P. M. Anderson, T. Foecke and P. M. Hasseldine, *MRS Bull.* **24**, 27 (1999).
8. A. Misra, M. Verdier, Y. C. Lu, H. Kung, T. E. Mitchell, M. Nastasi and J. D. Embury, *Scripta Mat.* **39**, 555 (1998).
9. H. L. Heinisch, R. G. Hoagland, R. J. Kurtz and J. P. Hirth, *Scripta Mat.* **39**, 451 (1998).
10. S. I. Rao and P. M. Hazzeldine, *Scripta Mat.* **41**, 1085 (1998).
11. J. D. Embury, *Scripta Mat.* **27**, 981 (1992).
12. F. Danoix, D. Julien, X. Sauvage and J. Copreaux, *Mats. Sci. & Eng.* **A250**, 8 (1998).

TEM Observation of Nanocrystalline Copper During Deformation

Carl J. Youngdahl, Northwestern University, Evanston, IL 60208 USA
Richard C. Hugo, Los Alamos National Laboratory, Los Alamos, NM 87545 USA
Harriet Kung, Los Alamos National Laboratory, Los Alamos, NM 87545 USA
Julia R. Weertman, Northwestern University, Evanston, IL 60208 USA

ABSTRACT

Nanocrystalline samples of copper were prepared using inert gas condensation and an optimized sequence of powder outgassing and compaction. TEM specimens were cut, electropolished, and mounted in a straining stage. *In situ* TEM observations including real-time video were captured during straining in the microscope. Areas of presumed increased stress concentration were identified near small cracks around the perimeter of the electropolished hole. Such locations were observed in the TEM while the specimen was pulled in tension. Several microstructural changes were captured during deformation including numerous sudden shifts in contrast of grains and parts of grains, occasional dislocation motion, opening and propagation of the crack. Relationships between grain size and deformation are described.

INTRODUCTION

The empirical Hall-Petch relation describes the dependence of several mechanical properties, including yield strength and hardness, on grain size. Various theories attempt to explain the dependence in terms of dislocation activity or its suppression. At very small grain sizes (below what is commonly used in structural applications), the relationship predicts strengths beyond the ranges of those attained at conventional grain sizes. As grain size decreases even lower, the relationship predicts values of yield stress that reach the theoretical limit. Possibly the mechanisms responsible for Hall-Petch behavior at conventional grain sizes give way to another mechanism at a certain low "threshold" size.

As methods to make materials with smaller and smaller grain sizes have increased in number and effectiveness, it is clear that the measured mechanical properties fall short of the values predicted by the Hall-Petch relation. It would be interesting to discover why, as doing so would lend insight into the microstructural workings of the Hall-Petch relation and could clarify how crystalline materials deform in general. *In situ* straining experiments carried out in a TEM offer the possibility of examining those deformation mechanisms that may be active [1,2]. Dislocation motion, if present, and displacement between grains may be witnessed and captured in real time. Minute changes in grain orientation (potentially on the order of seconds) can result in changes in contrast. The present paper describes such an *in situ* straining experiment of a nanocrystalline copper foil carried out at Los Alamos National Laboratory. It must be kept in mind that the deformation behavior observed in thin foils is not necessarily the same as that in the bulk material.

SAMPLE PREPARATION

Samples in this study were compacted from powders made via inert gas condensation [3,4] using a resistive evaporator at Argonne National Laboratory [5,6]. Fresh powder was dumped into a glass beaker while still in the evaporation chamber. Under continuous pumping and at around 10^{-7} Torr, the powder was moved to a compaction unit connected to the synthesis apparatus. Powders were gradually outgassed to prevent spikes in oxygen partial pressure by slowly moving the beaker closer to heat lamps and monitoring the pressure with an ion gauge. When no more pressure increases were seen after approaching the lamp, the powder was transferred to the compaction die and then compacted. Base pressures of both devices were on the order of 10^{-7} Torr. Compaction of the powders was performed at 1.4 GPa (10 tons).

The 9 mm diameter disk-shaped samples initially ranged between 500 and 1500 μm in thickness. To minimize cutting time and to remove surface layers, the discs were ground and polished using a sequence of polishing papers. To assist in the polishing, samples were glued to a steel cylinder 10 mm in diameter using tacky crystal bond (at ~90 °C) and quickly immersed in a beaker of cool distilled water. TEM foils 3 mm in diameter were cut from the thinned 9 mm discs. The TEM samples were then electropolished in a solution of 30% phosphoric acid (HPO_4) and 70% water using Struers Tenupol double-jet electropolisher.
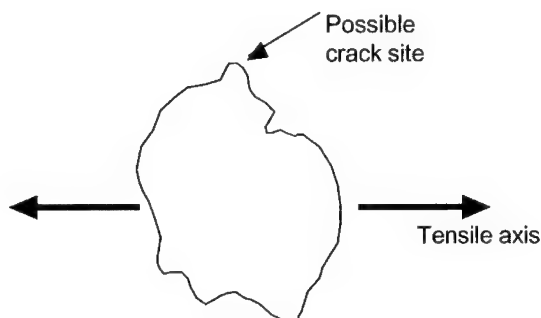
Figure 1. Orientation of TEM hole.

Before a given sample was affixed to the deformation fixture, a low-power microscope was used to find cracks or perforations around the perimeter of the hole. If a site somewhere on the perimeter was identified that appeared likely to produce a propagating crack under load, the sample was briefly examined under the TEM. If the sample looked promising (thin area near the potential crack site), a quick sketch was drawn of the hole and any notable or easily visible features. The sample was then removed from the microscope and affixed to a brass deformation fixture using very small drops of ethyl cyanoacrylate (nail glue) on each side of the hole. The sample was placed on the fixture so that the crack deemed most likely to propagate ran perpendicular to the straining axis, as shown in Fig. 1. The deformation fixture is shown in Fig. 2.

LOAD TRANSFER FIXTURE
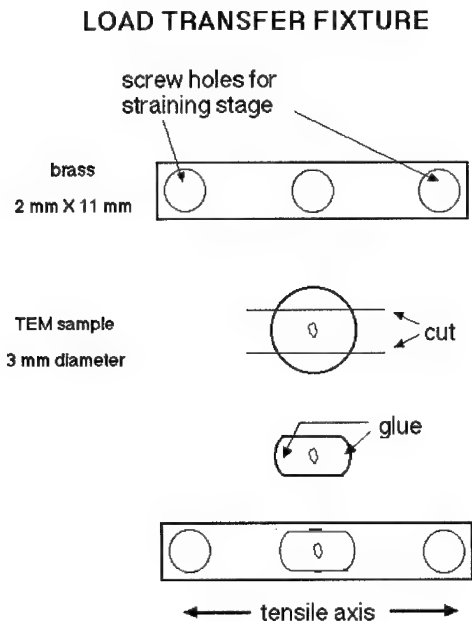
Figure 2. Fixture for supporting TEM samples during *in situ* deformation.

Straining Experiment

The *in situ* TEM tests were performed on a Philips CM30 with a LaB$_6$ filament and operating at 300 kV. Deformation was induced using a straining stage TEM specimen holder. Besides conventional micrographs, images were recorded digitally. Using a CCD camera running at 30 frames per second, real time "movies" were recorded onto half-inch digital beta videotapes. An attached Macintosh computer with a frame grabber was also used to record some digital images. When videotaping, the action was viewed on a 640 X 480 pixel monitor. The contents of the digital tapes were later transcribed onto consumer grade VHS videocassettes.

In this study, the mobile end of the straining stage was set to move at 100 nm/s. The motor can be set to push or pull the specimen. Tiny screws hold the specimen in the straining stage. The far end is fixed, and the near end moves. Since only 1-3 μm were usually in the field of view depending on the magnification, the motion from the straining stage caused the image to move steadily off the screen during the tests. To keep a particular area in view, the specimen translators were continuously adjusted during specimen extension.

When a sample was ready for straining, an appropriate location to watch was selected. Magnification was usually set to 46 kX, a compromise between obtaining sufficient detail and having a reasonable field of view. After a few pictures were taken straining was begun. The sample was too unstable to take reasonable static pictures during straining. Thus documentation of the microstructural behavior during deformation relied on the video images. The stage pulled on much more than the copper TEM sample within the field of view (brass deformation fixture, glue, and sample) so that the great majority of the displacement was accommodated outside the viewing area. While the overall displacement rate of the straining stage was known, the heterogeneity of the deformation made it impossible to determine the straining rate of the sample.

The first four samples appeared to exhibit some changes in relative positions of grains. When successive pictures were compared via computer, no grain translation was found. It is likely the perceived

changes were caused by minor contrast changes from small tilts experienced by the whole specimen during straining. A video image of a typical sample area examined during straining is shown in Fig. 3.

200 nm

Figure 3. A video image of the crack front during *in situ* tension.

RESULTS AND DISCUSSION

Activity during straining in the form of sudden contrast changes and dislocation motion was seen primarily in the intense stress fields around cracks. The contrast changes took place rapidly, were usually confined to one or a few contiguous grains, and lasted for some tens of seconds. The action then shifted to another grain or grains. The recording VCR runs at 30 frames/second. A frame-by-frame examination failed to unambiguously catch any contrast in the process of changing. Sometimes the changes were clearly confined to a single grain; in other cases it appeared that the changes took place over different regions of a large grain. However, because of grain overlap in the foil, it often was difficult to determine the positions of the grain boundaries and the "different regions" of a large grain may actually have been several small grains. Grains showing contrast changes averaged 60 nm in size as measured from video images. (However, some contrast changes were observed in regions as small as 10 nm.) The average grain size in the foil was measured to be 50 nm, though both this value and that of the average size of grains undergoing contrast changes may be overestimates for the reason just mentioned. A representative picture of the microstructure of a nanocrystalline copper sample is shown in Fig. 4.

Static dislocations were observed in grains as small as, or smaller than, 40 nm. Dislocations were seen moving in several grains, but there was no evidence of pile ups (except in very large grains of $d > 100$ nm) or transmission of dislocation arrays across grain boundaries. In one case, dislocations appeared at the edge of a hole and moved inward, where they seemed to disappear into a dislocation sink. After about 30 seconds the movement of the dislocation array abruptly stopped.

It is not clear if the sudden contrast changes observed in the present *in situ* straining experiment result from dislocation activity or from grain sliding and rotation. In one instance, contrast changes clearly seem to be from dislocation motion. A long grain was observed to be twinned into three parts, the twin boundaries running parallel to the long axis of the grain. The two sections of the "parent" grain underwent extensive contrast changes while the twin in the grain interior remained unchanged. It is unlikely that sliding would take place on a low energy twin boundary. If dislocations are indeed causing these contrast changes, it can be concluded that twin boundaries are effective barriers to dislocation motion.

All crack propagation took place in an intergranular fashion. The cracking appeared somewhat ductile. For example, formerly adjacent grains were later separated by a crack spanning 80 nm. Such positional changes happened gradually rather than via sudden brittle fracture and were not associated with an increase in cracks or porosity. Also, it was noted that throughout the test there were no sudden jolts or skips such as might be expected from an instance of brittle fracture.
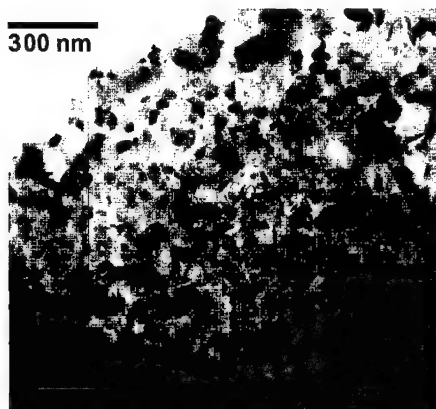
Figure 4. Microstructure of area typical for *in situ* tension tests.

CONCLUSIONS

An *in situ* straining experiment was carried out in the TEM on nanocrystalline copper with average grain size of approximately 50 nm.

• Sudden contrast changes were seen in individual grains in the stress field of cracks.

• Generally it could not be determined whether the contrast changes are caused by dislocation activity or by grain sliding and rotation. However in at least one case dislocation motion seems to be responsible.

• Dislocations are observed in grains down to at least 40 nm in size, probably lower.

• Crack propagation in the foil is intergranular.

ACKNOWLEDGEMENTS

REFERENCES

1.   W.W. Milligan, S.A. Hackney, M. Ke, and E.C. Aifantis, Nanostructured   Materials, **2**, 267-276 (1993).
2.   J.E Carsley, A. Fisher, W.W. Milligan, and E.C. Aifantis, Metallurgical and   Materials Transactions A. **29A**, 2261-2271 (1998).
3.   C.G. Granqvist and R.A. Buhrman, Journal of Applied Physics, **47**, 2200-2219   (1976).
4   R. Birringer, H. Gleiter, H.-P. Klein, and P. Marquardt, Physics Letters, **102A**,   365-369 (1984).
5   J.A. Eastman, L.J. Thompson, and D.J. Marshall, Nanostructured Materials, **2**, 377-382 (1993).
6   P.G. Sanders, G.E. Fougere, L.J. Thompson, J.A. Eastman, and J.R. Weertman, Nanostructured Materials, **8**, 243-252 (1997).

Superplasticity in Nanocrystalline Ni$_3$Al and Ti Alloys

Sam X. McFadden*, Alla V. Sergueeva*, Tomas Kruml[+], Jean-Luc Martin[+], and Amiya K. Mukherjee*
*Division of Materials Science and Engineering
University of California, One Shields Avenue, Davis, CA 95616
[+]Departement de Physique
Ecole Polytechnique Fédérale de Lausanne
1015 Lausanne, Switzerland

ABSTRACT

The advent of nanocrystalline materials has provided new opportunities to explore grain size dependent phenomenon. Superplasticity is such a grain size dependent phenomenon defined by the ability to attain tensile elongation of 200% or more. Superplasticity in microcrystalline materials has been well characterized. The constitutive equations that describe microcrystalline superplasticity predict enhanced properties for nanocrystalline materials. Enhanced properties in such nanocrystalline material include lower superplastic temperature at constant strain rate, higher superplastic strain rate at constant temperature, and lower flow stresses. Investigations with nanocrystalline Ni$_3$Al and ultra-fine grained Ti-6Al-4V alloy have shown a reduction in the superplastic temperature. However, the flow stresses in these materials are significantly higher than expected. The high flow stresses are accompanied by strong strain hardening. Transmission electron microscopy *in situ* straining of nanocrystalline Ni$_3$Al has shown that grain boundary sliding and grain rotation occurred during straining. The sliding and rotation decreased with strain. Dislocation activity was observed but was not extensive. There was no observable dislocation storage. The parameters of the generalized constitutive equation for superplasticity for nanocrystalline Ni$_3$Al and Ti-6Al-4V are in reasonable agreement with the parameters for microcrystalline material. The rate parameters suggest that nanocrystalline superplasticity shares common features with microcrystalline superplasticity. In contrast, the observed flow stresses and strong strain hardening indicate that nanocrystalline superplasticity is not a simple extension of microcrystalline behavior scaled to finer grain size.

INTRODUCTION

Nanocrystalline materials are usually characterized as having a grain size of 100nm or less. Ultra-fine grained materials have grain sizes from 1000nm to 100nm. Superplasticity is defined as tensile deformation of 200% or more. Interest in nanocrystalline superplasticity derives mainly from the grain size dependence of superplastic flow. Superplasticity is often characterized using the generalized constitutive equation

$$\dot{\varepsilon} = A \frac{DGb}{kT} \left(\frac{b}{d} \right)^p \left(\frac{\sigma}{G} \right)^n \tag{1}$$

where $\dot{\varepsilon}$ is the strain rate, D is the appropriate diffusivity (lattice or grain boundary), G is the shear modulus, b is the Burgers vector, k is the Boltzmann constant, T is the test temperature, d is the grain size, p is the grain size exponent, σ is the applied stress and n is the stress exponent [1]. A large body of data for microcrystalline superplasticity in metals, intermetallics, and ceramics, has shown the grain size exponent p to be 2 in the case of lattice diffusion control or 3 in the case of grain boundary diffusion control [2]. Consequently, a reduction in grain size can lead to a reduction in the superplastic temperature at constant strain rate, or an increase in the superplastic strain rate at constant temperature.

Early speculation regarding enhanced superplasticity in nanocrystalline materials was based primarily on the grain size dependence of superplastic flow [3]. The results with nanocrystalline materials show that a reduction in superplastic temperature has been achieved [4,5]. However, even at the lower temperatures, grain growth can be significant. The data show that the onset of nanocrystalline superplasticity coincides with the onset of microstructural instability.

The grain size dependence of Equation (1) also leads to an expectation of lower flow stresses in nanocrystalline materials compared to their microcrystalline counterparts. However, experiments have shown that the superplastic flow stresses of nanocrystalline Ni_3Al and ultra-fine grained Ti alloys are much higher than the flow stresses for microcrystalline material of the same composition, even when normalized by strain rate, grain size, and diffusivity [4]. Higher flow stresses in nanocrystalline materials have been observed in other metallic systems as well [5]. Nanocrystalline materials have also shown extensive strain hardening during superplastic deformation. In contrast, microcrystalline superplasticity is generally free of large-scale strain hardening [2].

There are two major processing routes used in the synthesis of nanocrystalline materials: (a) consolidation of nanocrystalline powders, and (b) severe plastic deformation of bulk materials by high pressure torsion straining (HPT) to large strains. Although a grain size of <100 nm can be obtained by both these methods in a variety of materials, the microstructural details vary. Grain size refinement of bulk materials by HPT eliminates problems associated with consolidation of powders as well as provides a means to study commercially important alloys that would be difficult to produce from powders. In this paper, we analyze some of the tensile superplasticity data obtained in the last few years on Ni_3Al and Ti-6Al-4V processed by HPT.

EXPERIMENTAL PROCEDURE

Samples of extruded Ni_3Al alloy IC-218, having the composition Ni-18 at.% Al-8 at. % Cr-1 at.% Zr-0.15 at. % B, and samples of Ti alloy having the composition Ti-6 wt% Al- wt% V were processed by high pressure torsion straining (HPT) to produce nanocrystalline and ultra-fine grained structures. Details of torsion straining can be found elsewhere [6,7]. Tensile specimens having a gage length and width of 1mm were electro-discharge machined from HPT processed disks approximately 12mm in diameter and 0.3mm thick. The specimens were then ground and polished to a uniform nominal thickness of 0.2mm.

Tensile testing was conducted in air at constant strain rate. Strain rate jump tests were performed to estimate the stress exponent. Between each jump, the strain rate was held constant. The relationship $n=\ln(\dot{\varepsilon}_2/\dot{\varepsilon}_1)/\ln(\sigma_2/\sigma_1)$, where the subscripts 1 and 2 refer to the lower and higher strain rates respectively, was used to calculate the stress exponent. Estimation of the grain size dependence p, was performed by analysis of data collected from tensile specimens statically annealed prior to deformation to produce different grain sizes.

Thin foils for transmission electron microscopy (TEM) investigation were prepared from annealed specimens by jet polishing. An electrolyte of 10% perchloric acid – 15% acetic acid – 75 % methanol (methyl alcohol), at –25°C and 35V was used to thin specimens of Ni_3Al. An electrolyte of 6% perchloric acid, 35% butyl alcohol, and 59% methyl methanol, at –25°C and 30V was used to thin specimens of Ti-6Al-4V alloy. TEM foils were also prepared from the deformed gage section of tensile specimens by ion milling. Grain size was determined using the mean lineal intercept method from TEM micrographs.

Transmission electron microscopy *in situ* straining of nanocrystalline Ni_3Al was performed at room temperature. The specimens were prepared by dimpling and jet polishing, using the same electrolyte and parameters as described above. Specimens were tested in both the as-processed condition, and after annealing at 650°C for 20min to produce a constant structure before the start of superplastic deformation.

RESULTS

Deformed tensile specimens of Ni_3Al and Ti-6Al-4V are shown in Fig. 1, which demonstrates the large strains characteristic of superplasticity. The as-processed microstructures of these materials are shown in Fig. 2. The structures were typical of materials processed by HPT. The indistinct grain boundaries and non-uniform contrast in the bright-field images indicated the presence of a large lattice defect density and associated internal strains. The electron diffraction patterns in Figure 2 (insets) contain rings comprised of spots that confirmed the presence of high angle grain boundaries. Streaking of the diffraction spots also confirmed the presence of a large lattice defect density.

Typical superplastic stress-strain curves for materials processed by HPT are shown in Fig. 3. The tensile data showed large flow stresses and significant strain hardening. This was contrary to the earlier predictions of low flow stresses in nanocrystalline materials. Table I shows the rate parameters of Equation (1) obtained for nanocrystalline Ni_3Al and ultra-fine grained Ti-6Al-4V.

Grain growth investigations using TEM *in situ* heating and static annealing of bulk specimens has shown that the onset of superplasticity coincided with the onset of grain growth. For Ni_3Al, grain growth was shown to be sluggish enough to maintain a grain size of 100nm or less throughout the duration of a tensile test at 650°C [4].

Figure. 1. Tensile specimens of Ni_3Al and Ti-6Al-4V.

As-machined

Ni_3Al $650°C, 10^{-3}s^{-1}, 560\%$

Ti-6Al-4V $725°C, 10^{-3}s^{-1}, 725\%$
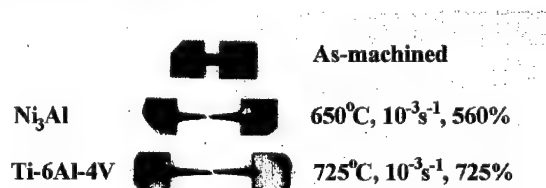
Table I: Rate parameters

	n	p	Q (kJ/mol)
	Stress exponent	Grain size dependence	Apparent activation energy
Ni_3Al	2.3	3	180
Ti-6Al-4V	2.7	-	215
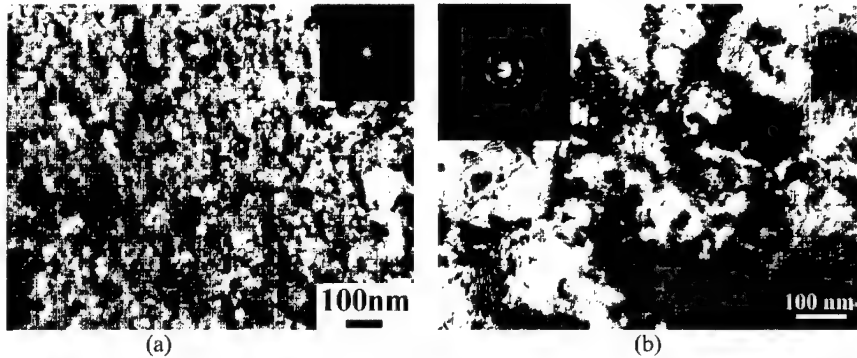
Figure 2. *Bright-field TEM of (a) Ni₃Al, and (b) Ti-6Al-4V alloy after processing by HPT.*
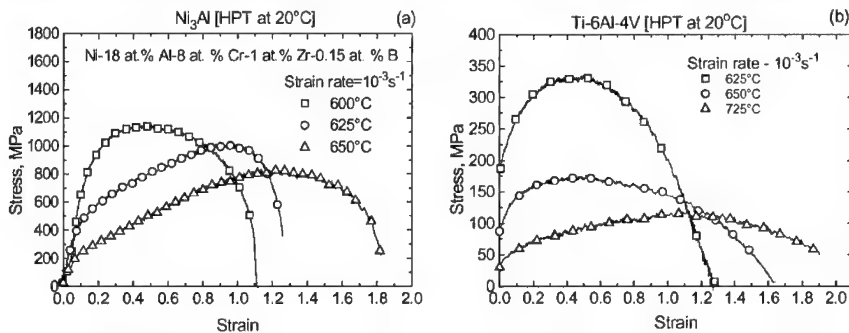
Figure 3. *Superplastic stress–strain curves for (a) Ni₃Al and (b) Ti-6Al-4V processed by HPT. Note the extensive strain hardening and high flow stresses.*

DISCUSSION

One of the assumptions of Equation (1) is that the deformation is in steady-state. Steady-state superplasticity is commonly identified by constant flow stress, which gives rise to classic flat-top flow curves in constant strain rate tensile tests. The flow curves for nanocrystalline materials do not exhibit regions of constant flow stress. However, the critical criterion for steady-state in terms of Equation (1) is that the relevant mechanistic details of deformation are in a steady-state. Consequently, the shape of the flow curve alone is not a sufficient indicator of steady-state. At this point it is not clear whether or not the relevant mechanistic details of deformation are constant during superplastic flow in nanocrystalline materials. That does not preclude the assumption of steady-state and an attempt to evaluate the parameters of Equation (1) to further understand the observed behavior.

The authors recently conducted room temperature *in situ* tensile tests in TEM on specimens of nanocrystalline Ni₃Al. Grain boundary sliding and grain rotation occurred during the *in situ* straining. Dislocation activity was observed but was not extensive. The dislocation marked "A" in Figure 4 was pinned at opposite grain boundaries and moved through the grain interior in a manner as if the dislocation pinning points were dragged along the grain boundary plane. After

some initial straining the TEM *in situ* tensile device was stopped and the deformed specimen in the specimen holder was tilted (with respect to the electron beam) to various angles up to 30° and imaged. Figure 5 shows that tilting altered the diffraction contrast of the grains as was expected but it did not reveal any discernable storage of dislocations in the microstructure. Hence, the high strain hardening and high flow stresses in nanocrystalline Ni_3Al cannot be explained by dislocation storage. Additional work is needed at elevated temperatures to fully resolve this issue.

Figure 4. *A dislocation, marked by A, with ends pinned in opposite grain boundaries, was imaged during TEM in situ straining. The dislocation was observed to glide across the grain interior.*

| Tilt angle 3° | Tilt angle 7.5° | Tilt angle 10° |
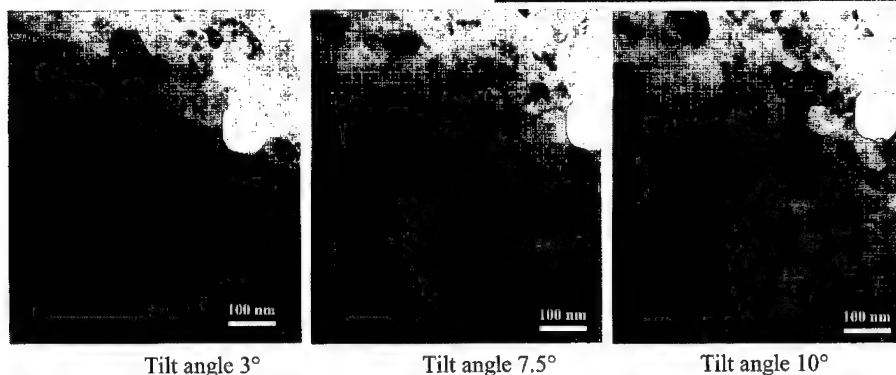
Figure 5. *Tilting during TEM in situ straining of nanocrystalline Ni_3Al showed no discernable dislocation storage.*

One way to explain the origin of higher flow stresses for superplasticity in nanocrystalline materials is to consider the influence of grain size on slip accommodation during grain boundary sliding. We suggest that lattice dislocation nucleation is difficult in nanocrystalline materials. Although the details are not clear at this stage, based on the limited data and present analysis, we propose that with increasing grain size, the mechanistic details of superplastic flow undergo a transition at a grain size where lattice dislocation generation becomes relatively easy, i.e. as in the case of microcrystalline materials.

Another issue we would like to discuss is the issue of microstructural instability. The driving force for grain growth is significantly higher in nanocrystalline materials than in microcrystalline materials. Consequently, significant grain growth can occur even at the lower superplastic temperatures for nanocrystalline materials. The strong driving force for grain growth limits the temperature range over which nanocrystalline superplasticity can be studied. If nanocrystalline

materials are tested at temperatures where microcrystalline superplasticity is observed, grain growth eliminates the nanostructure. As a result, comparison of nanocrystalline and microcrystalline superplasticity must be done on a temperature-normalized basis.

CONCLUSIONS

The experimental results show higher flow stresses for superplasticity in nanocrystalline materials compared to microcrystalline materials. The higher flow stresses result from the difficulty to nucleate and move lattice dislocations which are limited in length by the grain size. Therefore, conventional slip accommodated grain boundary sliding is likely to be difficult in nanomaterials. Based on this, a transition in the mechanistic details of superplasticity is expected at a critical grain size.

ACKNOWLEDGEMENTS

REFERENCES

[1] A.K. Mukherjee, J.E. Bird, J.E. Dorn, *Trans. ASM*, **62**, 155 (1969).
[2] A.K. Mukherjee, in: H. Mughrabi (Ed.), *Plastic Deformation and Fracture of Materials, Vol. 6 of Materials Science and Technology* (VCH, Weinheim, 1993), p. 407.
[3] H. Gleiter, *Prog. Mater. Sci.* **33**, 223 (1989).
[4] R.S. Mishra, R.Z. Valiev, S.X. McFadden, A.K. Mukherjee, *Mat. Sci. Eng.* **A252**, 174 (1998).
[5] S.X. McFadden, R.S. Mishra, R.Z. Valiev, A.P. Zhilyaev, A.K. Mukherjee, *Nature*, **398,** 684 (1999).
[6] R.Z. Valiev, R.S. Musalimov, N.K. Tsenev, *Phisica Status Solidi (a)*, **115,** 451 (1989).
[7] R.Z. Valiev, R.R. Mulyukov, A.V. Korznikov, *Phys. Metall. Metalloved*, **4,** 71 (1992).
[8] R.S. Mishra, A.K. Mukherjee, in: A.K. Gosh, T.R. Bieler (Eds.), *Superplasticity and Superplastic Forming – 1998* (TMS, Warrendale, 1998), p. 171.
[9] R.Z. Valiev, C. Song, S.X. McFadden, A.K. Mukherjee, TEM/HREM Observations of Superplastic Nanocrystalline Ni$_3$Al, accepted for publication in *Phil. Mag. A*.

The Role Played By Two Parallel Free Surfaces In The Deformation Mechanism Of Nano-crystalline Metals: A Molecular Dynamics Simulation

P. M. Derlet and H. Van Swygenhoven
Paul Scherrer Institute, CH-5253 Villigen PSI, Switzerland

Abstract

Former molecular dynamics computer simulations of polycrystalline Ni and Cu metals with mean grain sizes ranging between 3 and 12 nm demonstrated a change in deformation mechanism as a function of grain size: at the smallest grain sizes all deformation is accommodated in the grain boundaries. In this paper we report on the influence of the presence of two free surfaces on the deformation behaviour. The purpose of this simulation is to study which phenomena observed in in-situ tensile experiments performed in the electron microscope can be expected to be intrinsic properties of the deformation process and which phenomena are due to the presence of two free surfaces separated by a very small distance.

Introduction

With the reduction in grain size to the nanometre regime and a corresponding increase in the percentage of grain boundary atoms, the traditional view of dislocation driven plastic deformation has had to be reconsidered [1-5]. For nano-grain materials an alternative inelastic deformation process, driven primarily by grain boundary activity is now believed to be an important contribution. Extensive molecular dynamics has been performed by us (HVS) [6-10] on high angle randomly orientated bulk Cu and Ni nano-grain material in which the grain boundary region has a high degree of structural order. These simulations have demonstrated that the mechanism for plastic deformation changes from an intra-granular mechanism (dislocations) to an inter-granular mechanism (sliding), as the average grain size decreases.

TEM and HREM constitute important experimental techniques in the analysis of static and dynamic nanocrystalline boundary structure (see for example [11]). More recently, in situ tensile deformation experiments have been undertaken [12,13]. The requirement of thin samples for optimal contrast and resolution calls into question the assumption of a bulk structure. The current work investigates if the presence of the surface leads to additional grain boundary dynamics and thus a change or modification of the nanocrystalline plastic deformation process.

Sample Preparation and Relaxation

Nanocrystalline samples where created by constructing nanograins at random locations and crystallographic orientations until the grains overlap each other according to the Voronoi construction [14]. A more detailed description of this procedure can be found in [8]. Two samples with similar microstructure but differing mean grain sizes of 5nm and 12nm where used. The surface is introduced by removing the periodic boundary conditions in one direction of the (bulk) equilibrated sample. The samples were then relaxed under zero applied stress conditions for about 40ps, allowing the surface structure to find a more equilibrium configuration. In the present work all MD was performed at constant temperature (via velocity

re-scaling every 100 fs) and within the Parinello-Rahman approach [15]. For the interatomic potentials we employ the second moment tight-binding model of Cleri and Rosato [16]. We emphasise that the use of such atomic potentials provides insight into a so-called "model" Ni system. This potential has a stacking fault energy of 320mJ/m^2. The onset of partial dislocation activity with increasing grain size depends on this value. For example in (model) Cu, whose stacking fault energy is lower, MD simulations show dislocation activity in grain sizes slightly smaller than that of Ni.

In the case of the 12nm sample, some grain boundary growth/motion was observed at and in the vicinity of the surface and at some triple junction regions. Figure 1 demonstrates a grain boundary which before surface relaxation makes a low angle with the constructed surface, and upon relaxation the grain boundary/surface intersection achieves a lower energy state by forming a right angle intersection with the surface. In this figure the grey represents fcc coordinated atoms and the dark grey (in the grain boundary and at the surface) represent non-fcc atoms. Such a measure of the local crystalline order is obtained using the topological medium-range-order analysis developed by Honneycutt and Andersen [17]. We note that such grain boundary activity is primarily due to atomic interchange driven by the differing surface enthalpies of the grains and grain boundary region. Indeed in all computer samples, the microscopic surface stress was found to penetrate up to 15 Angstrom into the material which is about the extent of the growth region observed in figure 1. Due to the short time scales accessible by MD, long range diffusion cannot occur when using such simulation techniques.
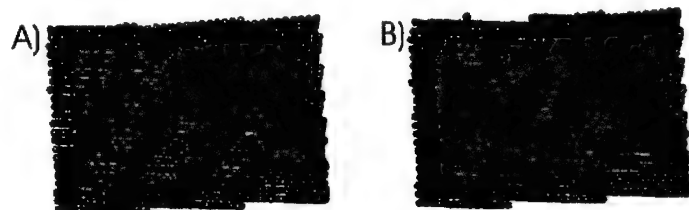
Figure 1: Grain boundary movement in the 12nm grain size sample. A) is before surface relaxation and B) is after ~40ps of surface relaxation.

General Deformation Properties

The 5nm sample was deformed with a constant applied stress of 1.5GPa for ~170ps, where as the 12nm sample was deformed with an applied stress of 2.6GPa for 52ps. The different stresses used for the two samples where chosen to achieve approximately similar strain rates [12]. Figure 2 displays the strain versus deformation time for the 5nm sample and 12nm, for both the surface and non-surface case. We see that in both cases, there is additional strain in the surface sample when compared to the non-surface sample.

Analysis of surface topography before deformation revealed a RMS roughness of approximately 0.54 Angstrom for both samples. After 52ps deformation, the 12 nm sample increased its surface roughness to 0.93 Angstrom. For the 5nm sample, the root-mean-square roughness after 170ps deformation was only 0.62 Angstrom. That there is a greater increase in surface roughness in the 12nm sample is in part be due to dislocation activity (see the following section) at the surface.
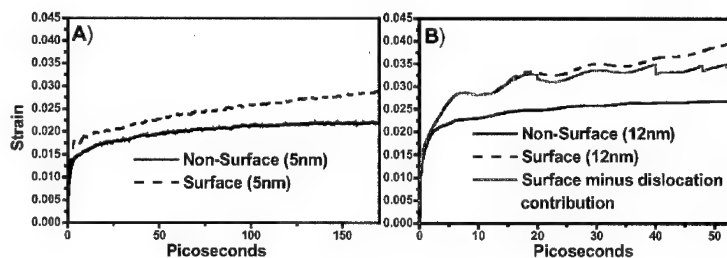
Figure 2: Strain versus deformation time curves for surface and non-surface sample for the 5nm sample at 1.5GPa, A), and the 12nm sample at 2.6GPa, B). In B), the light grey curve represents the strain remaining after the (approximate) strain due to dislocation activity has been removed from the surface case.

Figure 3a and b shows an orthogonal projection of atomic positions of the entire 12nm surface sample for the non-surface and surface case respectively. In this figure, the darker regions again represent the grain boundary structure, furthermore the top and bottom surfaces can be identified by the non-12 coordinated atoms in of the upper and lower regions of the simulation cell (3b). In addition, darker regions indicated by arrows represent HCP coordinated atoms forming double 111 HCP planes; the stacking faults due to the emission and propagation of partial dislocations through the grains. In the non-surface 12nm grain size sample, only one dislocation is observed whereas in the surface case, many dislocations are observed both in grains at the surface and within the sample. In the 5nm sample (not shown here), no such dislocations where observed in both the non-surface and surface samples.

A)   B)
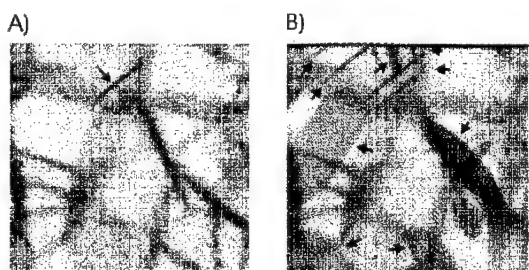
Figure 3: Projection of atomic positions of the 12nm sample for the non-surface case, A), and the surface case, B). The tensile axis is across the page. The arrows highlight darker regions within the sample and represent HCP coordinated atoms, indicating the propagation of partial dislocations through grains.

An estimation of the strain due to dislocation activity can be made by summing up the components of the Burgers vector along the tensile direction for each dislocation, weighted by the ratio of the area of the corresponding stacking fault projected onto a plane normal to the tensile direction and the gauge cross-sectional area. For this we considered the nine largest stacking faults within the surface sample and obtained a total fractional strain of approximately 0.005. The total strain due to dislocation activity is indicated in the strain versus time graph

(Figure 2b) as a subtraction from the surface strain. At 52ps approximately 40% of the additional strain in the 12nm grain size surface sample is due to the increased dislocation activity, the rest therefore being attributed to increased sliding.

Increased sliding between grains intersecting the surface was also observed in the 5nm sample. Figure 4 displays the atomic displacement of atoms between the pre-deformed configuration and the configuration after 170ps of deformation, for the non-surface A) and surface B) 5nm samples. Here the surface normal points out of the page and the tensile axis is across the page. The displacement vectors calculated come from the top atomic layers at the surface (and those equivalent layers for the non-surface case) and represent the absolute displacement of these atoms. An immediate observation is that for the surface case there is more sliding around grain G1 than there is in the non-surface case. This is particularly evident at the G1G2 grain boundary. In grain G1 for the surface case, there is also increased inhomogeneous displacement in the vicinity of triple junctions, particularly in the encircled region. A rounding of the grain boundary edges at the surface of the 5nm sample can be observed, leading to an increase in triple junction volume *at the surface*. Such an effect is also present in the 12nm sample, albeit to a lesser degree due to size effects.
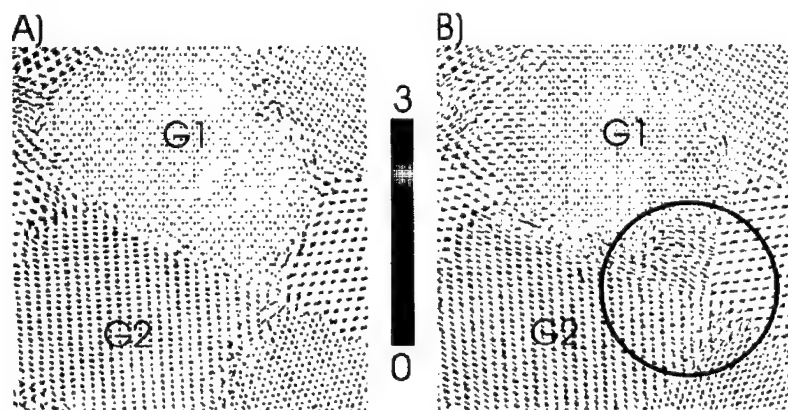
Figure 4: Difference plot between atoms positions in a selected surface region of the 5nm grain size sample for the non-surface case A), and the surface case B). The surface normal is out of the page. We see increased sliding around grain G1 in the surface case, and increased atomic activity at the indicated surface/triple junction intersection.

Analysis of Dislocation Structure

We now consider in detail one dislocation that was emitted at a grain boundary/surface intersection in the 12nm sample. The grain in question G1 (which is the same grain in the 5nm sample, as indicated in figure 4) contains a total of six dislocations in the surface case. That a single dislocation was also emitted in this grain in the non-surface case (see figure 3) makes the presence of such dislocations in the surface less surprising from the perspective of resolved critical shear stress. Analysis of the surface structure of grain G1 reveals a number of defects

that are an artefact of the method of creation of the surface. In some areas, where steps arise naturally from the artificial cleave due to the removal of the periodic boundary condition, atoms are missing (they are on the other side) leaving a defect structure. This has the effect of introducing blue atoms deeper beneath the surface at a correspondingly higher energy. The dislocation we consider here in detail was emitted from such a defect.

Figure 5 shows a selected region of the surface before and during deformation. Grain G1 is the upper grain. Here the tensile direction is across the page and the surface normal points out of the page. We consider first figure 5a in which the atoms are at their pre-deformation positions. Here a row of dark (non-12 coordinated) surface atoms are marked in grey. These atoms are infact along a 100 direction of G1. The bottom three marked atoms belong to the lower 100 plane, that is, below the 100 plane to which the upper "gray" atoms belong to. This constitutes an example of the surface defect identified in the previous paragraph. The 5b displays the atomic positions at 8ps of deformation. With 8ps of deformation, the partial dislocation has been emitted and has travelled across (up the page) to the other side of the grain. Although not easily seen in the present gray scale picture, the corresponding stacking fault in figure 5b makes an angle of approximately 45° with the surface normal.
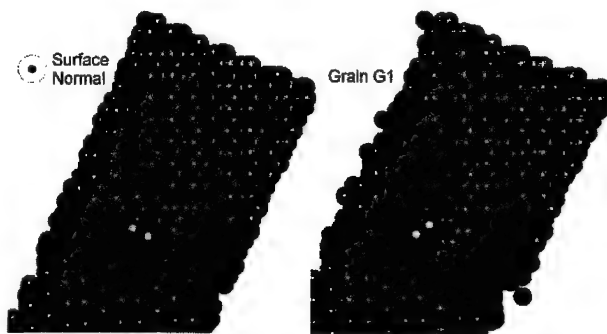
Figure 5: A) represents a selected surface region of the 12nm grain size sample before deformation and B) represents the same region after 8ps of deformation and the emission of a partial dislocation. Associated with the emission of the partial dislocation is the removal of the defect identified in more detail in the text.

The measured Burger's vector magnitude for this partial dislocation is 1.44 Angstroms and is in a direction which points down into the material (approximately 45 degrees into the page). Thus the atoms to the left of, and above, the stacking fault move collectively into the material. The two atoms marked in light grey in figure 9 indicate an example of atomic movement associated with the dislocation. The left atom of the pair has "hopped" approximately a nearest neighbour distance into the material, and the right most marked atom has moved into its position. This initial event occurs just before dislocation creation and is approximately in the direction of the future Burger's vector. We note also that those dark atoms due to the surface defect (marked with grey in figure 5) have not moved, however the line of atoms (also marked with grey) on the next 100 surface plane which form a step to the lower plane (to which the three bottom gray belong to) have shifted the appropriate Burger's vector to this lower plane. Thus through the creation and emission of the partial dislocation, the initial defect has been removed, being replaced by a surface step that extends to the other side of the grain.

Conclusions

For the 5nm and 12nm grain size samples investigated, we find that the presence of two parallel surfaces results in an increased strain for a given applied stress. Thus the free-thin-film geometry facilitates increased plastic deformation. In the case of the 5nm grain size sample, this manifested itself in an increase in grain boundary sliding, predominantly at the interface. On the other hand, for the 12nm grain size sample, the increase in plastic strain arose from a combination of increased grain boundary sliding and the creation of a large number of partial dislocations in grains. Further analysis is required to quantify the role a surface plays in both increased sliding and dislocation activity. For example, local atomic stress analysis has shown that only the top few atomic layers are affected by a surface pressure and shear component. However in the present work, dislocation activity is seen also in grains not intersecting the surface. Furthermore, the increase in surface roughness under deformation suggests that surface also plays a role in the issue of accommodation, for both grain boundary sliding and dislocation activity. We may nevertheless conclude that the presence of two free parallel surface separated by a distance comparable to the thin film geometry, does affect the plastic deformation processes in nanocrystalline material. For the current *in situ* deformation experiments, one therefore must be cautious that what is observed may indeed be a result induced by the thin-film geometry necessary to obtain maximum resolution/contrast in HRTEM, and not an intrinsic property of the nanocrystalline material studied.

Acknowledgements

References

1. W. Nieman, J. R. Weertman, and R. W. Siegel, J. Mater. Res. **6**, 1012 (1991)
2. G. Nieh and J. Wadsworth, Scr Metall. Mater. **25**, 955 (1991)
3. H. Chokshi, A. Rosen, J. Karch, and H. Gleiter, Scr. Metall. Mater. **23**, 1679 (1989).
4. Y. Gerlsman, M. Hoffmann, H. Gleiter, and R. Birringet, Acta Metall. Mater. **42**, 3539 (1994)
5. W. Siegel and G. E. Fougere, Nanostruct. Mater. **6**, 205 (1995)
6. Van Swygenhoven and A. Caro, Appl. Phys. Lett. **71**, 1652 (1997)
7. Van Swygenhoven and A. Caro, Phys. Rev. B **58**, 11246 (1998)
8. Van Swygenhoven, M. Spaczer, D. Farkas, and A. Caro, Phys. Rev. B **60**, 22 (1999)
9. Van Swygenhoven, M. Spaczer, and A. Caro, Acta Mater. **47**, 3117 (1999)
10. Van Swygenhoven, D. Farkas, and A. Caro, Phys. Rev. B **62**, 831 (2000)
11. Kizuka, N. Mitarai, and N. Tanaka, J. Mater. Sci. **29**, 5599 (1994)
12. C. Hugo, H. Kung, C. J. Youngdahl and J. Weertman, See present volume.
13. X. McFadden, A.V. Sergueeva, and A.K. Mukherjee, *ibid.*
14. Z. Voronoi, J. Reine Angew. Math **134**, 199 (1908)
15. Parrinello and A. Rahman, J. Appl. Phys. **52**, 12 (1981)
16. F. Cleri and V. Rosato, Phys. Rev. B **48**, 22 (1993)
17. D. J. Honneycutt and H. C. Andersen, J. Phys. Chem. **91**, 4950 (1987)

Mechanical Spectroscopy of Nanocrystalline Metals

E. Bonetti, L. Pasquini, L. Savini
Department of Physics, University of Bologna and INFM
v. Berti-Pichat 6/2
40127 Bologna, Italy

ABSTRACT

The mechanical behavior of nanocrystalline iron and nickel prepared by mechanical attrition and inert gas condensation was investigated using mechanical spectroscopy techniques in the quasi static-and low frequency dynamic stress-strain regimes. The measures were performed on samples previously stabilized by thermal annealing at low homologous temperatures. The results of elastic energy dissipation, creep, and creep recovery measurements performed in the low strain regime ($\varepsilon = 10^{-5}$-10^{-3}) allowed to trace a phenomenological picture of the anelastic and viscoplastic behavior of nanocrystalline Ni and Fe in the 300-450 K range with different grain sizes and interfaces disorder degree. Activation energies of the thermally activated anelastic and plastic mechanisms responsible for the mechanical behavior have been evaluated.

INTRODUCTION

In the study of the mechanical properties of metals an important role is attributed to the grain size (d), which can play a hardening or softening role [1]. As is well known since many years, in coarse grained materials, a grain size decrease down to the micrometer range is accompanied by a hardness increase, phenomenologically described according to the well known Hall-Petch relation, predicting a $d^{-1/2}$ dependence in the hardness or flow stress. Further, fine grained materials may exhibit diffusional creep or in some cases superplastic behavior at sufficiently high homologous temperatures, due to the increased volume fraction of the disordered interfaces, acting as a short circuit path for diffusion [2]. Entering the nanometer regime (10-10^2 nm) it is expected, as observed for other physical properties, that the approach of microstructural features, such as the grain size, to some physical length scale, may result in size effects on plasticity and creep behavior [2,3,4]. Recent theoretical predictions obtained by computer simulations [5,6] indicate that dislocation dynamics is strongly reduced below a critical grain size of about 10 nm. The volume fraction of intercrystalline regions increases considerably in nanocrystalline (n-) metals and therefore it is expected that the overall mechanical behavior, in particular the ductility and grain boundary sliding and migration, are modified compared to the coarse grained counterparts. Moreover also the structure of the interfaces in the n-regime may be different and thus modify the mechanical properties, as generally observed in polycrystalline metals where the grain boundary degree of order strongly affects the grain boundary anelastic relaxation. In n-metals the detailed structural configuration of the interfaces is still a matter of debate. Up to now, experimental and theoretical works have not yet provided a unified picture of the nature and degree of order of the interfaces [7,8,9].

In experimental investigations of the mechanical behavior of n-metals the sample imperfection strongly influences the results. Extrinsic structural features such as porosity and surface flaws, may lead to inaccurate results in measurements of elastic modulus and ductility in stress *vs.* strain or creep tests [10]. These difficulties are frequently encountered when studying n-metals prepared by a two-step procedure, including consolidation of the powdered products as a final processing step, as in n-powders obtained by mechanical attrition (MA) or n-particles

produced by inert gas condensation (IGC) techniques. Moreover the generally obtained small sizes of n-metal samples require the use, for tensile testing, of specially designed microtensile machines and very accurately prepared samples [11].

An alternative approach to investigate the mechanical behavior, which has been widely employed in studying polycrystalline samples, is by mechanical spectroscopy. Mechanical spectroscopy is a highly structure sensitive technique, intrinsically non destructive [12]. The mechanical properties are investigated by employing quasi-static or dynamic measurements in a low strain range (typically $\varepsilon = 10^{-5}\text{-}10^{-3}$) at the breakdown of Hooke's law. Information can be obtained on the elementary mechanisms at the basis of the deformation processes involving general interfaces, grain boundaries, and dislocations. In the present research, measurements of creep and creep recovery functions and of elastic energy dissipation coefficient, were employed to evaluate specific parameters characterizing the deformation behavior of n-nickel and iron prepared by MA and IGC.

MECHANICAL SPECTROSCOPY

Anelasticity

The physical basis of anelastic behavior is the following: after application of a stress σ (or a strain ε), the sample achieves thermodynamic equilibrium *via* a relaxation process that is characterized by a (distribution of) relaxation time(s) τ. The equilibrium relation between stress and strain is unique and the sample relaxes towards the initial state upon unloading. In a quasi-static measurement, the stress (or strain) undergoes a step-like change. Afterwards, the strain (or stress) relaxes and it approaches some equilibrium value. In creep experiments, described later, a constant stress σ_0 is applied to the sample at time $t=0$ and is maintained for $t>0$, while the variation of the strain $\varepsilon(t)$ as a function of time is monitored and recorded.

Assuming a relaxation process that depends on a single relaxation time, the creep compliance is given by:

$$J(t) \equiv \varepsilon(t)/\sigma_0 \equiv J_U + J_{an}(t) = J_U + \delta J[1 - \exp(-t/\tau)] \qquad (1)$$

where J_U and $J_{an}(t)$ represent the unrelaxed elastic and the time-dependent anelastic response, respectively. For $t \gg \tau$, $J_{an}(t)$ approaches the equilibrium value δJ. Upon unloading after a load time t_{load}, the sample undergoes a sudden strain decrease and eventually approaches zero strain as described by the creep recovery compliance:

$$J_{rec}(t) = \delta J[1 - \exp(-t_{load}/\tau)]\exp(-(t - t_{load})/\tau) \qquad (2)$$

The anelastic behavior exhibited by real materials most often involves a distribution of relaxation times $X(\ln \tau)$, with $\int_{-\infty}^{+\infty} X(\ln \tau)d(\ln \tau) = \delta J$. Equations 1-2 then transform to:

$$J(t) = J_U + \int_{-\infty}^{+\infty} X(\ln \tau)[1 - \exp(-t/\tau)]d(\ln \tau) \qquad (3)$$

$$J_{rec}(t) = \int_{-\infty}^{+\infty} X(\ln\tau)[1 - \exp(-t_{load}/\tau)]\exp(-t/\tau)d(\ln\tau) \qquad (4)$$

In creep experiments, the loading compliance generally comprises a plastic component. For this reason, it is preferable to determine $X(\ln\tau)$ from the recovery compliance. In the hypothesis of a smooth distribution of relaxation times, $X(\ln\tau)$ can be approximated by [12]:

$$X(\tau) \approx -(dJ_{rec}/d\ln t)/(1 - \exp(-t_{load}/\tau))_{t=\tau} \qquad (5)$$

The purely anelastic compliance can thus be reconstructed combining equations 3 and 5, and subtracted from the total experimental creep to obtain the plastic response.

In most cases, the relaxation process is thermally activated, i.e. $\tau = \tau_0 \exp(H/k_BT)$. If the distribution of relaxation times arises mainly from a distribution of pre-exponential factors τ_0 rather than of energy barriers, then the effective activation energy of the anelastic creep can be determined from the time shift between J_{an} curves measured at different temperatures:

$$H = k_B \left(\partial \ln t/\partial T^{-1}\right)_{J_{an}=const} \qquad (6)$$

where t is the creep time necessary to attain a fixed value of the anelastic response J_{an}.

In a dynamic measurement, the applied stress is oscillating with time, i.e., $\sigma = \sigma_0 \exp(i\omega t)$, where ω is the angular velocity. Due to the relaxation process, a phase shift between stress and strain occurs. This shift is usually represented by a complex mechanical susceptibility, or *compliance*, $J^* \equiv J_1 - iJ_2 \equiv \varepsilon/\sigma$. J_1 and J_2, known as the *storage* and *loss compliance*, give the in-phase and out-of-phase strain, respectively. The ratio J_2/J_1 represents the elastic energy dissipation of the material, and is commonly known as *internal friction, specific damping factor*, or simply Q^{-1}. For a single-time process, Q^{-1} assumes the form of a Debye peak:

$$Q^{-1} \equiv J_2/J_1 = \Delta\omega\tau/(1 + \omega^2\tau^2) \qquad (7)$$

where the *relaxation strength* Δ is equal to $\delta J/J_U$. The temperature-dependence of the internal friction is contained in the Arrhenius relation for the relaxation time.

In addition to specific relaxation peaks, the internal friction in polycrystalline metals generally exhibits a so-called *background damping*, which increases monotonically with increasing temperature and can be described by the equation:

$$Q^{-1} = (A/\omega^n)\exp(-nH_{bg}/k_BT) \qquad (8)$$

where A is a constant and $n \leq 1$ a correction factor which arises from the presence of a distribution of relaxation times [13]. The true activation energy H_{bg} must be evaluated from the temperature shift between Q^{-1} curves measured at different frequencies:

$$H_{bg} = -k_B \left(\partial \ln\omega/\partial T^{-1}\right)_{Q^{-1}} \qquad (9)$$

The correction factor n is then calculated by comparison with the slope of the background, i.e., $[\partial \ln(Q^{-1})/\partial T^{-1}]_\omega = -nH_{bg}/k_B$.

Microplasticity

The steady-state plastic creep rate is adequately expressed by the well-known phenomenological equation:

$$\dot{\varepsilon} = B\sigma^m d^{-p} \exp(-Q_C / k_B T) \tag{10}$$

where B is a material constant. The grain size dependence is given by the exponent p (with $p=2,3$ for creep controlled by volume and grain boundary diffusion, respectively). The stress exponent m and the creep activation energy Q_C can be determined performing stepped changes of stress and temperature, respectively, once the material has attained a nearly constant strain rate.

EXPERIMENTAL

Nanocrystalline Fe and Ni samples were prepared by MA, using a planetary ball milling device working in high-vacuum conditions [14]. The oxygen content of these samples was below the detection threshold (0.5 at.%) of x-ray energy dispersive analysis in the electron microscope using a windowless detector [15]. Recent studies of the magnetic properties also showed no evidence for the presence of atomic oxygen or oxides in these samples [16]. Some measurements were also performed on Ni samples prepared by IGC. The oxygen content of these samples is higher, about 5 at.%, as generally found in materials prepared by IGC [17]. No metallic impurities were detected in both MA and IGC samples. Bar-shaped samples for mechanical spectroscopy measurements were obtained by powder consolidation at room temperature under a pressure of 2 GPa. The sample density was evaluated by Archimedes' method. X-ray diffractometry was performed with a Rigaku DMAX-IIIC using Cu-Kα radiation and a graphite monochromator in the diffracted beam. The volume-weighted average grain size d and root-mean-square microstrain $\langle \varepsilon^2 \rangle^{1/2}$ were determined by Warren-Averbach analysis of the x-ray diffraction profiles. The results of x-ray analysis are in agreement with transmission electron microscopy observations. The root-mean square deviation in the grain size distribution is about 50% of the average value.

Table I. Synthesis technique, volume-weighted average grain size d, root-mean square strain $\langle \varepsilon^2 \rangle^{1/2}$ (calculated at a length $L = d/2$) and mass density ρ/ρ_{th} (referred to the theoretical bulk density) of the as-prepared n-Fe and n-Ni samples.

Sample	Synthesis	d (nm)	$\langle \varepsilon^2 \rangle^{1/2}$ (10^{-3})	ρ/ρ_{th} (%)
Fe-MA	Milling (60 h)	14 ± 2	3.0 ± 0.3	92-94
Fe-MA10	Milling (10 h)	28 ± 3	1.6 ± 0.2	92-94
Ni-MA	Milling (60 h)	15 ± 2	3.0 ± 0.3	92 – 95
Ni-MA[a]	Milling (60 h)	17 ± 2	2.1 ± 0.2	92 - 95
Ni-IGC	IGC	10 ± 2	2.0 ± 0.2	≈85

a) Annealed for 2 hours at 473 K and creep-tested at T < 450 K.
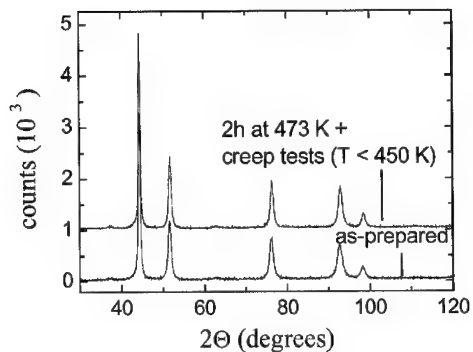
Figure 1. X-ray diffraction profiles of Ni-MA, both as-prepared and annealed.

For the measurements of the Q^{-1} vs. temperature, we made use of three apparatuses: (i) a Dynamic Mechanical Analyzer (DMA), working in forced flexural vibrations in the single-cantilever mode, in the 0.01 - 200 Hz frequency range; (ii) a torsion pendulum and (iii) a vibrating reed equipment working in resonance conditions, in the range of frequencies of 1-30 Hz and 0.1-10 kHz, respectively. The creep experiments were performed under isothermal conditions with the DMA, in the flexural mode.

RESULTS AND DISCUSSION

Dynamic tests

All the mechanical spectroscopy measurements reported in the following have been performed on samples previously submitted to *in situ* thermal annealing above the testing temperature. At sufficiently low annealing temperatures, the grain size is practically unchanged.
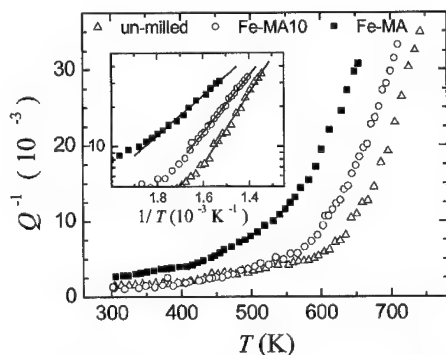
Figure 2. Internal friction Q^{-1} after a first run up to 670 K in un-milled Fe, Fe-MA10 and Fe-MA. Frequency: 3 Hz. The inset shows the same data in logarithmic vs. reciprocal scale.
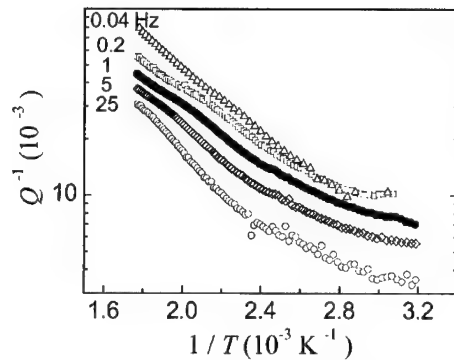
Figure 3. *Internal friction Q^{-1} in Ni-MA measured at different frequencies in the 0.04 – 25 Hz range after 1h annealing at 573 K.*

Figure 1 shows the x-ray diffraction profiles of Ni-MA, both as-prepared and creep-tested at $T<450$ K after 2 h annealing at 473 K. From the Warren-Averbach analysis (table I), no appreciable grain growth is detected, while the microstrain decreases significantly. The pre-annealing procedure is necessary to measure mechanical properties in a relatively stable state, avoiding spurious effects due to healing of the internal stresses accompanied by structural relaxation [18].

The elastic energy dissipation measurements performed in the dynamic regime (0.04-1000 Hz), are strongly sensitive to the microstructure. In particular, for both Fe [19] and Ni [14] the background damping is higher for n-samples than for coarse-grained samples. This is exemplified for Fe in figure 2 over an extended temperature range. The underlying relaxation processes can be investigated by measuring the elastic energy dissipation at different frequencies, as exemplified for Ni-MA in figure 3. In the case of n-Ni, a relaxation peak already discussed elsewhere [14] is superposed to the background damping. From the shift between the background curves, an activation energy H_{bg} spanning the ranges reported in table II is determined according to equation 9. These values are within those reported for grain boundary diffusion (table II). The value of the factor n, close to 0.2, is similar to those reported for the high temperature behavior of pure metals and reflects a background damping of anelastic character [20].

Such values of n much less than 1 are typical of a wide distribution of relaxation times arising from a distributed configuration of crystalline defects. In the case of coarse-grained polycrystalline metals, a distribution of dislocation link lengths within the grains is present, and the activation energies H_{bg} correspond to those for dislocation cross-slip or climb. Such values, close to those for lattice self-diffusion, are significantly higher than the ones reported in the present study (table II). In n-metals, the experimental available evidence suggests that dislocations are rarely present and scarcely mobile [21]. This fact and the low values of H_{bg} suggest that interface sliding mechanisms are responsible for the enhanced damping in n-metals where a high volume fraction is occupied by disordered interfaces. It is difficult to assess if the distribution in grain sizes affects the nature and structure of the interfaces and therefore contributes to the spectrum of relaxation times.

Table II. Activation energy H_{bg} and correction factor n of background damping, and activation energy of plastic creep Q_C in different nanocrystalline samples. Literature values of the activation energies for lattice (Q_L^D) and grain boundary (Q_{GB}^D) diffusion in coarse-grained Fe and Ni are also reported.

Sample	H_{bg} (eV)	n	Q_C (eV)	Q_L^D (eV)	Q_{GB}^D (eV)
Fe-MA	1.4 – 1.8	≈ 0.2		2.5 [22]	1.4-1.9 [23]
Ni-MA	1.1 – 1.4	≈ 0.2	1.3-1.5	3.0 [24]	1.15-1.35 [25]
Ni-IGC			≈ 1.3		

Quasi-static tests

In polycrystalline metals, different mechanisms contribute to the creep behavior, strongly depending on structure, stress and temperature: non-conservative dislocation motion, volume diffusion (Nabarro-Herring creep) and grain boundary diffusion (Coble creep). The grain size is an important structural parameter, a d^{-2} or d^{-3} dependence of the creep rate being predicted for Nabarro-Herring and Coble creep, respectively. In n-metals, several phenomenological models have been proposed to explain plastic deformation without dislocation activity: grain boundary sliding [26], Coble creep [27], and grain boundary shearing [28]. A typical creep test including the creep recovery stage is reported in figure 4.

In all present experiments, the strain developed on loading is not completely recovered. This result indicates that an irreversible (plastic) strain develops during creep, in the entire stress range (10-150 MPa) investigated. This permanent strain can be evaluated according to the procedure illustrated in figure 4 using equations 3 and 5, i.e., subtracting from the experimental creep curve the anelastic component calculated from the recovery curve. With increasing time, the plastic strain rate overwhelms the anelastic one (figure 4).

The anelastic creep strain is strongly dependent on temperature (figure 5) in agreement with the results of dynamic measurements. From equation 6, activation energy values similar to those of H_{bg} are determined. This fact indicates that the same processes are effective in static and dynamic anelastic behavior, as expected. Figure 6 also shows that, in the stress range explored, the anelastic creep strain depends linearly on stress.
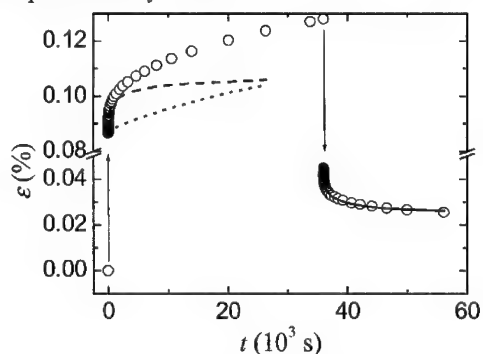
Figure 4. *Creep and creep recovery (initial part) in Ni-MA. T=433K, σ=78 MPa. Continuous line: modeling of the recovery based on equations 4-5. Dashed line: anelastic strain reconstructed from creep recovery (equations 3, 5). Dotted line: plastic strain (difference between total and anelastic strain).*
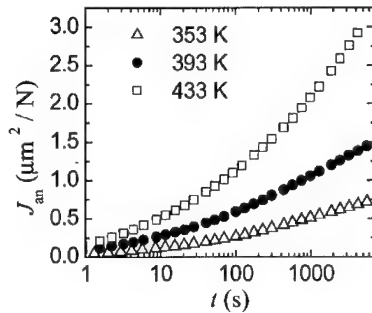
Figure 5. *Temperature dependence of the anelastic creep compliance in Ni-MA. $\sigma = 112$ MPa*
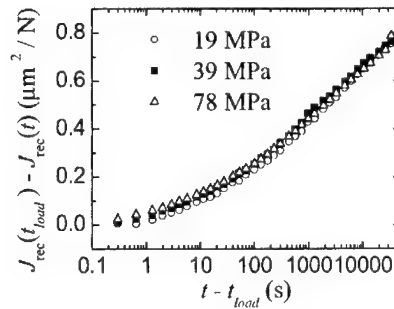
Figure 6. *Stress dependence of the recovery compliance in Ni-MA. T=353 K.*

Turning to the plastic strain, it is observed that its strain rate decreases continuously with time. In agreement with results on n-Cu and n-Pd [29], a true stationary creep state is not attained in the time-temperature domain investigated ($t \leq 8 \times 10^4$ s, $T \leq 450$ K). This may indicate that small structural modifications induced by the plastic deformation and/or by the measuring temperature are continuing. Moreover, mainly due to the low testing temperatures which were selected to avoid grain growth ($T \leq 0.25$ T_m), the strain rates are very low ($\approx 10^{-8}$ s^{-1}). In agreement with ref. 29, the enhanced creep rate predicted by extrapolating the Coble creep equation to the n-regime is not observed. As an attempt to determine the effective activation energy Q_C and stress exponent m, we have performed stepped changes of temperature and stress after a prolonged loading time, so that the anelastic strain rate becomes negligible (figures 7-9). The quasi-stationary strain rates corresponding to different temperature/stress conditions are extrapolated to the time instant when the abrupt change in temperature/stress is imposed to the sample. This procedure is needed in order to eliminate the effects of structural variations on the evaluation of Q_C and m.
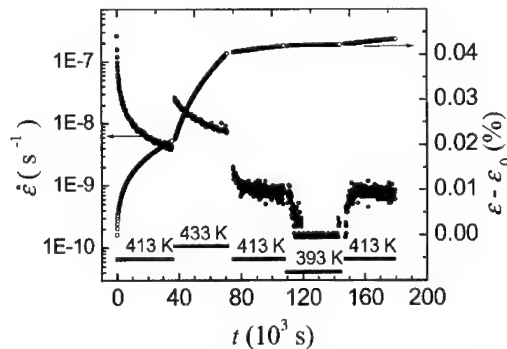
Figure 7. *Determination of the effective activation energy of creep in Ni-MA by stepped temperature changes. The temperature history is schematized in the bottom. $\sigma = 84$ MPa.*
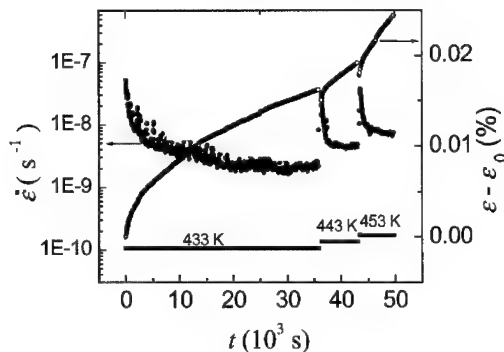
Figure 8. *Determination of the effective activation energy of creep in Ni-IGC by stepped temperature changes. The temperature history is schematized in the bottom.* $\sigma = 55$ *MPa.*

The evaluation of Q_C from upwards and downwards temperature jumps yield consistent results. The Q_C values, reported in table II, are similar to those for grain boundary diffusion for both Ni-MA and Ni-IGC. Preliminary measurements to determine m (figure 9) in Ni-MA samples yield quite high values in the m=5-7 range.

The similarity of the activation energies for plastic creep, anelastic creep and exponential background damping, all close to the values for grain boundary diffusion, strongly suggests that the elementary mechanisms at the basis of these deformation processes are similar and involve atomic jumps in the interfacial regions. The measurements on different samples are highly reproducible and do not exhibit any dependence on the actual sample density in the range investigated (see table I). On these grounds it seems that the presence of some internal porosity resulting from incomplete densification, which strongly affects high-stress mechanical tests as reported by several authors [30], does not significantly influence the present results obtained in low strain regime.
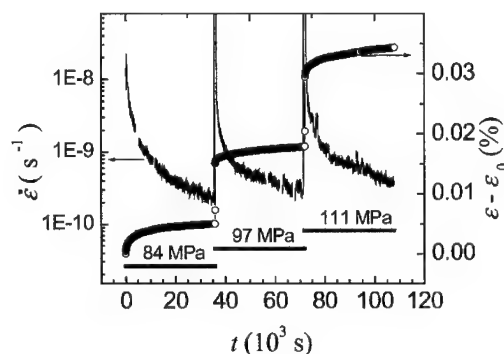
Figure 9. *Determination of the stress exponent m in-Ni-MA by stepped stress changes. The stress history is schematized in the bottom. T=353 K.*

CONCLUSIONS

We have measured the anelastic and (micro)plastic behavior of n-Ni and n-Fe samples prepared by MA and IGC and submitted to appropriate annealing treatments which stabilize the nanostructure without extensive grain growth. The microstructure stabilization is accompanied by a significant reduction of the internal strains.

Dynamic measures show an exponential background damping which increases by decreasing the grain size. From its frequency dependence an average activation energy corresponding to the one for grain boundary diffusion both in Ni and Fe was obtained. This enhanced damping is attributed to interface sliding mechanisms.

The creep measurements reveal an important anelastic strain component, linearly dependent on stress and thermally activated, with an activation energy similar to the one deduced from dynamic measurements. A plastic component is also detected, whose magnitude encompasses the anelastic one with increasing time. Its strain rate decreases with time without reaching a stationary state, and is lower than predicted by extrapolation of the Coble creep equation to n-materials. No significant differences were observed in creep measurements performed on Ni samples prepared by MA and IGC. The plastic creep is characterized by an activation energy similar to those reported for grain boundary diffusion. This value, coupled to the quite high stress exponent, $m= 5$-7 in Ni-MA samples, makes it difficult to explain the plastic creep on the basis of simple mechanisms. As a matter of fact, our results point to an important role played by the interfaces in determining the inelastic behavior of n-metals. Further measurements in a wider temperature and grain size range are presently underway.

Mechanical spectroscopy is a very effective tool to investigate n-metals in order to gain insight into the mechanisms at the basis of inelastic behavior and to complement the information provided by other experimental techniques and computer simulations.

ACKNOWLEDGEMENTS

REFERENCES

1. A. Lasalmonie and J.L. Strudel, *J. Mater. Sci.*, **21**, 1837 (1986).
2. E. Harzt, Acta Mater., **46**, 5611 (1998).
3. R.W. Siegel and G.E. Fougere, Nanostruct. Mater., **6**, 205 (1995).
4. J.R. Weertman et al., in *Mechanical Behaviour of Bulk Nanocrystalline Materials*, MRS Bulletin, **24** (n.2), 44 (1999).
5. H.Van Swygenhoven, A.Caro, *Appl. Phys. Lett.*, **71**, 652 (1997).
6. J. Schiøtz, F. Di Tolla, and K.W. Jacobsen, *Nature*, **391**, 561 (1998).
7. H. Van Swygenhoven, D. Farkas, A. Caro, *Phys. Rev. B*, **62**, 831 (1999).
8. P. Keblinski, D. Wolf, S.R. Phillpot, and H. Gleiter, *Scripta Mater.*, **41**, 631 (1999).
9. H.-E. Schaefer, K. Reimann, W. Straub, F. Phillipp, H. Tanimoto, U. Brossmann, and R. Würschum, *Mater. Sci. Eng.* A, **286**, 24 (2000).
10. C.C. Koch, D.G. Morris, and A. Inoue, in *Mechanical Behaviour of Bulk Nanocrystalline Materials*, MRS Bulletin, **24** (n.2), 54 (1999).

11. M. Legros, B.R. Elliott, M.N. Rittner, J.R. Weertman, and K.J. Hemker, Philos. Mag. A, **80**, 1017 (2000).
12. A.S. Nowick and B.S. Berry, *Anelastic Relaxation in Crystalline Solids* (Academic Press, 1972).
13. G. Schoeck, E. Bisogni and J. Shyne, *Acta Metall.*, **12**, 1466 (1964).
14. E. Bonetti, E.G. Campari, L. Pasquini and E. Sampaolesi, *J. Appl. Phys.*, **84**, 4219 (1998).
15 L. Del Bianco, A. Hernando, E. Bonetti, and C. Ballesteros, Phys. Rev. B **59**, 14778 (1999).
16 E. Bonetti, L. Del Bianco, D. Fiorani, D. Rinaldi, R. Caciuffo, and A. Hernando, Phys. Rev. Lett. **83**, 2829 (1999).
17 J.F. Löffler, J.P. Meyer, B. Doudin, J.P. Ansermet, and W. Wagner, Phys. Rev. B **57**, 2915 (1998).
18. E.Bonetti, E.G. Campari, L. Del Bianco, L.Pasquini, E. Sampaolesi, Nanostruct. Mater., **11**, 709 (1999).
19 E.Bonetti, L.Del Bianco, L.Pasquini, E. Sampaolesi, Nanostruct. Mater., **10**, 741, (1998).
20. I.Z. Harangozó, F.J. Kedves, in *Internal Friction in Solids,* eds. S. Gorczyca, L.B. Magalas (Wydawnictwo AGH, Krakow 1984) p. 209.
21. R.W. Siegel and G.E. Fougere, in *Nanophase Materials*, edited by G.C. Hadjipanayis and R.W. Siegel, (Kluwer Academic Publishers, 1994) p. 233.
22. J. Kučera, B. Million, J. Ružickova, V. Foldyna and A. Jakobova, *Acta Metall.*, **22**, 135 (1974).
23. H. Gleiter and B. Chalmers, *High Angle Grain Boundaries*, (Pergamon Press, 1972).
24. M.B. Bronfin, G.S. Bulatov and I.A. Drugova, *Fiz. Met. i Metalloved.*, **40**, 363 (1975).
25. N.W. De Reca and C.A. Pampillo, *Scri. Metall.*, **9**, 1355 (1975).
26. H. Chang, H. Höfler, C. Alstetter, and R. Averbach, *Scripta Metall. Mater.*, **25**, 1161 (1991).
27. A. Chookshi, A. Rosen, J. Karch, and H. Gleiter, *Scripta Metall.*, **23**, 1679 (1989).
28. H. Conrad and J. Narayan, *Scripta Mater.*, **42**, 1025 (2000).
29 P.G. Sanders, M. Rittner, E. Kiedaisch, J.R. Weertman, H. Kung, and Y.C. Lu, *Nanostruct. Mater.*, **9**, 433 (1997).
30 G.E. Fougere, J.R. Weertman, and R.W. Siegel, Nanostruct. Mater. **5**, 127 (1995).

Dislocations in Submicron Grain Size and Nanocrystalline Copper

T. Ungár[1], G. Tichy[2], P. G. Sanders[3] and J. R. Weertman[4]
[1]Dept. of General Phys. and [2]Dept. of Solid State Phys.,
Eötvös University Budapest, H-1518, P.O.B. 32, Budapest, Hungary,
[3]Harvard University, 402 Gordon McKay, 9 Oxford St, Cambridge, MA, 02138 U.S.A.
[4]Dept. of Mater. Sci. and Eng., Northwestern University Evanston, IL, 60208 U.S.A.

ABSTRACT

Using the dislocation model of strain anisotropy in X-ray diffraction peak profile analysis it is shown that in nanocrystalline copper produced by inert gas condensation dislocations are present, at least, down to average grain sizes of the order of 20 nm. Based on the analysis of the dislocation contrast factors it is suggested that with decreasing grain size the proportion of Lomer-Cottrell type dislocations increases.

INTRODUCTION

The existence and type of dislocations in bulk nanocrystalline metals is still under debate [1-3]. High resolution electron microscopy indicates the presence of dislocations in the grain boundary regions, while the grain interior regions become clear of dislocations with decreasing grain size [4]. Using the method of X-ray diffracion peak profile analysis it was shown earlier that nanocrystalline copper produced by inert gas condensation does contain dislocations [5]. The previously used interpretation of X-ray data has been further developed and refined [6,7]. In the present work a series of copper specimens produced by inert gas condensation and deformed in some cases either by tension or compression will be analysed for the grain size, the grain size-distribution, the dislocation densities and the type of dislocations. Instead of the earlier suggested screw type it is found that as the grain size decreases the proportion of Lomer-Cottrell dislocations increases.

The evaluation of broadened X-ray diffraction peak profiles is based on the dislocation model of strain anisotropy [5]. This means that neither the FWHM (full width at half maximum) nor the integral breadth nor the Fourier coefficients of diffraction profiles are monotonous functions of the diffraction vector. A procedure has been developed to determine the crystallite size-distribution function and the dislocation structure in terms of the median and variance of a log-normal size-distribution and the density, the arrangement and the character (edge or screw type) of dislocations [6-8]. The FWHM, the integral breadths and the Fourier coefficients are analysed in terms of the *modified* Williamson-Hall and Warren-Averbach procedures.

EVALUATION OF X-RAY DIFFRACTION EXPERIMENTS

The Fourier transform of diffraction peak profiles can be written in the form of the Warren-Averbach equation [9]:

$$ln\, A(L) \cong ln\, A_L^{S} - 2\pi^2 L^2 g^2 <\varepsilon_{g,L}^2> , \tag{1}$$

where $A(L)$ are the absolute values of the Fourier coefficients of the physical profiles, A_L^S are the size Fourier coefficients, g is the absolute value of the diffraction vector and $<\varepsilon_{g,L}^2>$ is the mean square strain in the g direction. L is the Fourier length, $L=na_3$ [6], where $a_3=\lambda/2(sin\theta_2-sin\theta_1)$, n are integers starting from zero, λ is the wavelength of X-rays and $(\theta_2-\theta_1)$ is the angular range of the measured diffraction profile. In a dislocated crystal, for small L values, $<\varepsilon_{g,L}^2>$ can be given as [10,11]:

$$<\varepsilon_{g,L}^2> \cong (\rho \overline{C} b^2/4\pi)ln(R_e/L) , \qquad (2)$$

where ρ, b and R_e are the density, the modulus of Burgers vector and the effective outer cut-off radius of dislocations, respectively. Peak broadening caused by dislocations depends on the relative orientations between the Burgers and line vectors of dislocations and the diffraction vector, b, l and g, respectively. This effect is taken into account by the dislocation contrast factors C [6,7,10-13]. In a texture free polycrystal or if the Burgers vector population on the different slip systems is random the C factors can be averaged over the permutations of the hkl indices [6]:

$$\overline{C} = \overline{C}_{h00} (1-qH^2) , \qquad (3)$$

where $\overline{C}_{h00}$ are the average dislocation contrast factors for the $h00$ reflections, $H^2=(h^2k^2+ h^2l^2+ k^2l^2)/(h^2+k^2+l^2)^2$ and q is a parameters depending on the elastic constants of the crystal and on the edge or screw character of the dislocations [7].

$$\Delta K = 0.9/D + \alpha' (K\overline{C}^{1/2})^2 + O(K\overline{C}^{1/2})^4 , \qquad (4)$$

where $K=2sin(\theta)/\lambda$, $\Delta K=2cos(\theta)(\Delta\theta)/\lambda$, D is the apparent size parameter corresponding to the FWHM. It is obtained by extrapolation to $K=0$ in the usual manner. O stands for higher order terms not interpreted here [14]. A similar equation can be given for the integral breadths and the corresponding apparent size parameter is denoted by d [8]. The *modified* Warren-Averbach equation is [5]:

$$lnA(L) \cong lnA^S(L) - \rho BL^2ln(R_e/L) (K^2\overline{C}) + O(K^4\overline{C}^2) , \qquad (5)$$

where $B=\pi b^2/2$ and O stands for higher order terms, cf [14]. The size parameter corresponding to the Fourier coefficients, denoted by L_0, is obtained from the size Fourier coefficients A^S as described by Warren [9]. d and L_0 give the volume- and area-weighted mean column length, respectively [15,16]. A simple and pragmatic method has recently been developed to obtain the median and the variance, m and σ, of a log-normal size distribution of crystallites from the three apparent size parameters, D, d and L_0 [8]. For spherical crystallites with log-normal size distribution the area-, volume- and arithmetically-weighted mean crystallite sizes $<x>$ are [15]: $<x>_{area}=mexp(2.5\sigma^2)$, $<x>_{vol}=mexp(3.5\sigma^2)$ and $<x>_{arithm}=mexp(0.5\sigma^2)$, respectively.

EXPERIMENTAL

Six different specimens are investigated: five specimens are bulk nanocrystalline copper prepared by inert gas condensation and hot compaction at Argonne National Laboratory [17]: O_2, P_2 and N_2 in the as-prepared state and P_2 and N_2 after tensile and compression tests. The sixth specimen, denoted as V, has been prepared by equal channel angular compression (ECA) [18]. O_2 was measured twice: once after mechanical polishing and a second time after additional chemical etching. P_2 and N_2 were measured in the as-prepared state soon after synthesis and again after natural ageing at room temperature (RT) for about 9 months. P_2 and N_2 were measured also after tensile and compression tests, respectively. The mechanically tested P_2 and N_2 specimens were also measured in a second run after natural ageing RT. After ageing at RT, grain growth and/or recovery has been observed, especially in the undeformed P_2 and N_2 specimens. All different states of the specimens are listed in Table 1. The X-ray diffraction experiments were carried out by a special double crystal diffractometer with negligible instrumental peak broadening using a Nonius FR 591 Cu or Co rotating anode. More details are found in [9].

RESULTS AND DISCUSSION

The FWHM of a bulk nanocrystalline (O_2) and the ECA pressed (V) specimens (1a,b and 6 in Table 1.) are shown in the conventional Williamson-Hall plot [19] in Fig.1. The non-monotonous increase of the FWHM with K indicates strain anisotropy. The same data are shown in the *modified* Williamson-Hall plot according to eq. (4) in Fig. 2. The best fitting q values according to eq. (3) are indicated in the figure. In the case of the bulk nanocrystalline specimen (open circles and squares) stacking faults were also taken into account, as in [5]. The very different q values are in accordance with the very different strain anisotropy visualized qualitatively by the horizontal solid and slanted dashed lines in Fig. 1. passing through the FWHM of the 200, 220 and 222 reflections, respectively. From the three apparent size parameters, D, d and L_0, obtained by using eqs. (4) and (5) for the FWHM, the integral breadths and the Fourier coefficients of profiles, the median and the variance, m and σ, of the log-normal crystallite size-distribution have been determined. The values of q, σ, m and $<x>_{vol}$ for the investigated specimens are given in Table 1. Typical errors of the data are indicated in a few cases. The m and $<x>_{vol}$ values show that RT exposure of some of the samples for a period of about 9 months led to increase in the mean grain size. The increase of the variance in the same cases indicate the widening of size distribution and a heterogeneous grain growth. TEM grain size measurements of the same specimens are in good correlation with the present results [20].

The q parameter [see eq. (3)] is plotted *vs.* the arithmetic average crystallite size $<x>_{arithm}$ in Fig. 3. The TEM grain size measurements of the same specimens [20] have shown that the X-ray and TEM results are in closer agreement for finer grain size. In the following the finer grain size region will be discussed therefore the term grain will be used instead of crystallite. In the figure it can be seen that as the grain size decreases the value of q increases. The line through the measured data is to guide the eye and the vertical line at 200 nm is a typical error bar. The values of q were calculated numerically as a function of the elastic anisotropy $A_z = 2c_{44}/(c_{11}-c_{12})$, where c_{ij} are the elastic constants of the crystal, for Burgers vectors: $b=a/2<110>$, $b=a/2<111>$ and $b=a/2<100>$ in cubic crystals. For $b=a/2<110>$ edge or screw dislocations, the q values are plotted *vs.* A_z in Fig. 4. In the case of edge dislocations they depend slightly on the ratio c_{12}/c_{44}.

For copper A_z=3.21. The vertical line in the figure shows that for dislocations with these Burgers vectors the q parameter values in copper vary between 1.68 and 2.37. For dislocations with Burgers vectors $b=a/2<111>$ this range is between 1.60 and 2.68 [7].

Next the q values of $<100>$ type dipoles will be evaluated. The displacement field between the two dislocations of a dipole is homogeneous. For homogeneous strain q_{hom} is:

$$q_{hom} = 3 - [(\varepsilon_{xx} + \varepsilon_{yy} + \varepsilon_{zz})^2 + 4(\varepsilon_{xy}^2 + \varepsilon_{yz}^2 + \varepsilon_{zx}^2)]/(\varepsilon_{xx}^2 + \varepsilon_{yy}^2 + \varepsilon_{zz}^2), \qquad (6)$$

where ε_{ij} is the strain tensor. Assuming that the dislocation lines are in the z direction in a cartesian coordinate system the strain tensors for the two possible dipole configurations perpendicular to each other are: (i) $\varepsilon_{xx} = -\varepsilon_{yy} = (1+\nu)b/\delta$; $\varepsilon_{zz} = 0$ or (ii) $\varepsilon_{xx} = \nu b/\delta$, $\varepsilon_{yy} = -b/\delta$; $\varepsilon_{zz} = \nu b/\delta$, where ν is Poisson's ratio and δ is the separation of the dipoles. Poisson's ratio for the $<100>$ direction in copper is: $\nu = 0.42$ [21]. Using eq. (6) it can be shown that for the two dipole configurations: (i) $q_{hom} = 3$ and (ii) $q_{hom} = 2.981$. In both cases, the q values for the $<100>$ type dipoles are practically 3.

On the basis of the above considerations the following mechanism is suggested for the increase of the q parameter with decreasing grain size. The $<100>$ type dipoles consist of Lomer-Cottrell sessile locks which are well known to be present in the dislocation structure in copper. As long as the average grain size is above a certain limit the overwhelming fraction of the dislocation density is of the usual dislocations with Burgers vectors $b=a/2<110>$. In this case the value of q is in the range corresponding to these dislocations, since the few Lomer-Cottrell locks do not contribute much to this average value. As, however, the grain size decreases, the $<110>$ type mobile dislocations move to the grain boundaries where they annihilate by the usual mechanisms. The sessile Lomer-Cottrell locks can more successfully survive this annihilation mechanism. As a result the fraction of the Lomer-Cottrell locks in the total dislocation density increases with decreasing grain size. The increase of the q value with decreasing grain size indicates the increase of the volume fraction of Lomer-Cottrell locks in the entire dislocation structure. The model still has to be verified by TEM investigations.

Table 1. The values of q, σ, m and $<x>_{vol}$ for the different specimens ($<x>_{vol}$ is the volume averaged particle size)

Specimen	q	σ	m [nm]	$<x>_{vol}$ [nm]
1a. O$_2$, mechanical polish	2.69$\pm$0.1	0.7$\pm$0.02	6.6$\pm$0.2	29
1b. O$_2$, +chemical etching	2.61	0.7	6.6	29
2a. P$_2$, as-received	2.13	0.62	22	68
2b. P$_2$, undeformed +9 m at RT	2.0	1.15	5.2$\pm$0.5	207
3a. N$_2$, as-received	2.1	0.64	22	77
3b. N$_2$, undeformed +9 m at RT	2.1	0.84	9.5$\pm$0.5	87
4a. P$_2$, tensile deformed	2.47	0.58	17	45
4b. P$_2$, tensile deformed +9 m at RT	2.34	0.73	9.8	49
5a. N$_2$, compression deformed	2.3	0.69	13.5	59
5b. N$_2$, compression deformed + 9 m at RT	1.9	0.79	13.5	87
6. V, deformed by ECA	1.96	1.06	11.8	307

CONCLUSIONS

Based on X-ray diffraction peak profile analysis of nanocrystalline and submicron grain size copper specimens it is suggested that with decresing grain size the surviving type of dislocations are most probably the <100> type Lomer-Cottrell locks.

ACKNOWLEDGEMENTS

REFERENCES

1. A. H. Chokshi, H. Gleiter and A. R. Rosen, *Scripta Metall.* **23**, 1679 (1989).
2. H. Van Swygenhofen and A. Caro, *Nanostr. Mater.* **9**, 669 (1997).
3. J. R. Weertman, D. Farkas, K. Hemker, H. Kung, M. Mayo, R. Mitra and H. Van Swygenhofgen, *MRS Bull.* **24**, 44 (1999).
4. T. Braisaz, P. Ruterana, G. Nouet, Ph. Komninou, Th. Kehagias, Th. Karakostas, P. Poulopoulos, M. Aggelakeris, N. Flevaris and A. Serra, *This Solid Films*, **319**, 140 (1998).
5. T. Ungár, S. Ott, P. G. Sanders, A. Borbély and J. R. Weertman, *Acta mater.* **46**, 3693 (1998).
6. T. Ungár and G. Tichy, *phys. stat. sol. (a)*, **147**, 425 (1999).
7. T. Ungár, I. Dragomir, Á. Révész and A. Borbély, *J. Appl. Cryst.* **32**, 992 (1999).
8. T. Ungár, J. Gubicza and G. Ribárik, *J. Appl. Cryst.* submitted for publication.
9. B. E. Warren, *Progr. Metal Phys.* **8**, 147 (1959).
10. M. A. Krivoglaz, in Theory of X-ray and Thermal Neutron Scattering by Real Crystals, Plenum Press, N. Y. 1969; and in X-ray and Neutron Diffraction in Nonideal Crystals, Springer-Verlag, Berlin Heidelberg New York, 1996.
11. M. Wilkens, *phys. stat. sol. (a)* **2**, 359 (1970).
12. M. Wilkens, *phys. stat. sol. (a)*, 1987, **104**, K1.
13. R. Kuzel Jr. and P. Klimanek, *J. Appl. Cryst.* 1989, **22**, 299.
14. I. Groma, *Phys. Rev. B*, **57**, 7535 (1998).
15. W. C. Hinds, *Aerosol Technology: Properties, Behavior and Measurement of Airbone Particles*, Wiley, New York. (1982).
16. J. I. Langford, D. Louer and P. Scardi, *J. Appl. Cryst.* **33**, 964 (2000).
17. P. G. Sanders, G. E. Fougere, L. J. Thompson, J. A. Eastman, and J. R. Weertman, *Nanostruct. Mater.*, **8**, 243 (1997).
18. R. Z. Valiev, E. V. Kozlov, Yu. F. Ivanov, J. Lian, A. A. Nazarov and B. Baudelet, *Acta metall. mater.* **42**, 2467 (1994).
19. G. K. Williamson and W. H. Hall, *Acta metall.* **1**, 22 (1953).
20. R. Mitra, T. Ungár, T. Morita, P. G. Sanders and J. R. Weertman, *in Advanced Materials for the 21st Century*, Eds. Y. W. Chung, D. C. Durand, P. K. Liaw, G. B. Olson, TMS, Warrendale, PA, 1999, p. 553.
21. R. F. S. Hearmon, in *Landolt-Börnstein*, **1**, pp. 1-39 (1966).
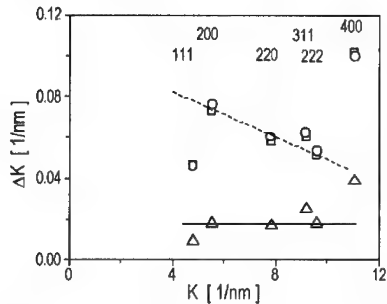
Figure 1. Conventional Williamson-Hall plot of the FWHM of a bulk nanocrystalline (O_2, open circles after polishing, open squares after additional chemical etching) and the ECA pressed (V, open triangles) specimens. The horizontal solid- and slanted dashed lines go through the FWHM of the 200, 220 and 222 reflections, respectively.
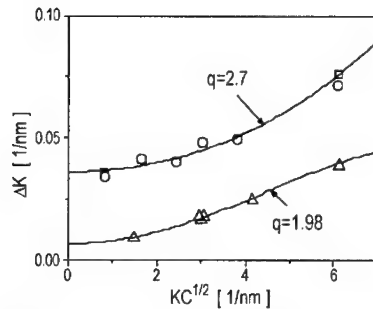
Figure 2. The same data as in Fig. 1. plotted in the modified Williamson-Hall plot. The best fitted q values in eq. (3) are indicated in the figure. The solid lines are the best fitted curves according to eq. (4).
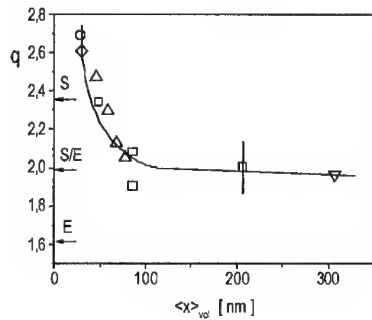
Figure 3. The experimentally determined q values vs. the volume averaged crystallite size. The symbols according to Table 1. are: open circle and diamond: 1a, 1b; open up-triangle: 2a, 3a, 4a, 5a; open square: 2b, 3b, 4b, 5b; open down-triangle: 6. S, S/E and E stand for screw, screw/edge and edge dislocations, respectively.
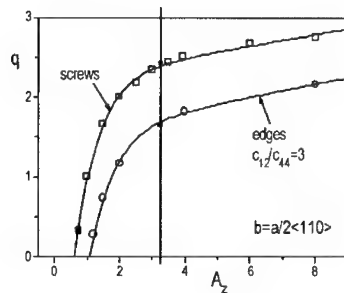
Figure 4. The variation of the q parameter [see eq. (3)] as a function of the elastic anisotropy (or the Zener constant) A_z in an fcc crystal for dislocations with $b=a/2<110>$ Burgers vectors [7].

Microstructural Evolution in cryomilled Inconel 625

Jianhong He and Enrique J. Lavernia

Department of Chemical and Biochemical Engineering and Materials Science,

University of California Irvine, Irvine, CA 92697-2575

ABSTRACT

Nanocrystalline Inconel 625 alloy, with a uniform distribution of grains, was synthesized using cryogenic mechanical milling. Microstructures of the powder, cryomilled for different times, were investigated using transmission electron microscopy (TEM), scanning electron microscopy (SEM) and X-ray diffraction (XRD). The results indicated that both the average powder particle size and average grain size approached constant values as cryomilling time increased to 8 hours. The TEM observations indicated that grains in the cryomilled powder were deformed into elongated grains with a high density of deformation faults, and then fractured *via* cyclic impact loading in random directions. The fractured fragments from the elongated coarse grains formed nanoscale grains. The occurrence of the elongated grains, from development to disappearance during intermediate stages of milling, suggested that repeated strain fatigue and fracture caused by the cyclic impact loading in random directions, and cold welding were responsible for the formation of a nanocrystalline structure.

1. INTRODUCTION

J. Benjamin and his colleagues stated that the mechanical milling/alloying involves repeated welding, fracturing and re-welding of powder particles under a highly energetic ball charge [1-3]. In terms of milling mechanisms, however, Benjamin and his co-workers primarily studied inter-particle behavior, whereas the issue of grain size evolution was not addressed [1-3]. The formation of a nanocrystalline structure is thought to evolve from the development of dislocation cell structures within shear bands [4]. Plastic deformation leads to the formation of dislocation cell within shear bands, then dislocation cells transform into low-angle grain boundaries, and finally form nanocrystalline grains surrounded by high-angle grain boundaries via grain rotation [4-6]. In such a dislocation cell mechanism, the contribution of the fracture and welding processes in the powder particles to the formation of a nanocrystalline structure has heretofore never been studied. It is anticipated that the welded fragments of the original coarse grains should form new grains, although Benjamin and his co-workers did not explicitly demonstrate the relationship between the repeated fracturing-welding process and the refinement of grains.

In view of the above findings, the primary objective of the present investigation is to perform structural evaluation of cryomilled materials. Particular attention is paid to enhancing our understanding of the mechanisms that govern the evolution of microstructure in the cryomilled powder during distinct milling stages.

2.   EXPERIMENTAL PROCEDURE

Commercially available gas atomized Inconel 625 (Diamalloy 1005 AMDRY 625) powder were mechanically cryomilled in a attritor at a rate of 180 rpm up to 20 hours. The ball to powder mass ratio used was 20:1, and a liquid nitrogen medium was continuously introduced into the tank during the milling. XRD measurements were performed using Mo Kα (λ=0.07093 nm) radiation in a Siemens D5000 diffractometer. A low scanning rate of 0.12 degrees/min. was used to guarantee the accuracy of the measurements. SEM observations were performed on a Philips XL 30 microscope. TEM studies were conducted on a Philips CM microscope operated at 200 keV.

3.   RESULTS AND DISCUSSION

Fig. 1(a) shows the morphology of the as-received powders. The powder particles showed a spherical morphology and the particle size varied significantly from a few micrometers to approximately 60 micrometers. Fig. 1(b) through (d) shows the changes in the powder morphology after cryomilling for 8, 16 and 20 hours, respectively. With an increase of cryomilling time, the majority of powder particles changed from spheres to disk-shaped particles. The average particle size increases with milling time from the original 42 μm and approaching a maximum value of 84 μm. XRD spectra of the powders for different milling times are shown in Fig. 2. The as-received Inconel 625 powder is a single-phase Ni-base solution with a fcc crystal structure. To illustrate change in the sharpness/width of XRD reflections visually, $K\alpha_2$ peaks are included in the spectra shown in Fig. 2 although the effects of $K\alpha_2$ were corrected in the calculation of grain size. With increasing milling time, XRD peaks broaden and decrease drastically. Peaks originated from $K\alpha_2$ are clearly visible in the spectrum of the as-received powder, but not in the cryomilled powders because the broadening of the reflections caused by cryomilling. The grain sizes of the milled powders following different milling times were determined on the basis of the Scherrer equation [7]. With an increase in cryomilling time, grain size decreased and approached a constant value of 14 nm after 16 hours.

Fig. 3 reveals a cross-section SEM image of the as-received powder. The equiaxed grains possess an average grain size of 2.71 μm. Fig. 4 shows a typical TEM image of the Inconel 625 powder cryomilled for 4 hours. Grains are not clearly visible in the powder; however, the presence of significant difference in contrast is observable. The dimension of the Moire fringes indicates grains size of approximately 30 nm although the grain boundaries are not visible. Fig. 5 (a) and (b) show a region with the darkest contrast, which usually reveals an elongated morphology with an average dimension of 0. 15 (width) x 0.7 (length) μm, in which a high density of deformed faults is present. The corresponding dark field image indicates that one the darkest regions is one elongated grain, in the case of Fig. 5(b), with a size of 0.13 x 0. 58 μm. Therefore, the powder cryomilled for 4 hours exhibits a mixed configuration of elongated coarse grains and nanoscale grains. These elongated grains containing a high density of deformation faults. The density of faults is too dense, as well as their small dimensions, to identify the nature of the faults. As cryomilling time increased, the dimension of the elongated grains decreased. Fig. 6 shows the elongated grains in the powder cryomilled for 6 hours. The average size of the elongated grains decreased to approximately 30 nm (width) x 120 nm

(length). In addition, fractured fragments, with regular morphology, were widely observed in the powder following cryomilling for 6 hours. Fig. 7 shows the elongated grains that fractured into a few segments. As the cryomilling time was increased further, the elongated grains disappeared. Fig. 8 shows TEM bright field images of the powder cryomilled for 8 hours. Inserted selected area diffraction pattern (SAD) indicates {111}, {200}, {220}, {113} and {222} diffraction rings of a single phase fcc structure from inside to outside; hence no new phases formed during cryomilling, consistent with the results of the XRD.

During mechanical cryomilling, powder particles are repeatedly stressed by impact loading in a direction that changes randomly with increasing cryomilling time. Plastic deformation significantly occurred in powder particles as evident by the powder morphology shown in Fig. 1. Therefore, the random cycling loading and resultant strain, with an amplitude in the plastic deformation regime, is thought to promote random strain fatigue (or a random low-cycle fatigue) of the powder particles. In related studies, Plumtree and Pawlus [8] carefully examined the changes in microstructures in Al during strain fatigue. In this work the development of dislocation cells was stated as the primary characteristic of the deformed microstructure during strain fatigue. Dislocation cells formed at the onset of steady-state (corresponding 30 cycles) with thick and uncondensed walls. There was a high density of dislocations in the interior of the cells. As the number of cycles increased, the cells became more distinct, dislocations in the interior of the cells drastically decreased. At failure (11,300 cycles), a well-defined cell structure was observed, the cell walls were narrow and the interior of the cells contained very few dislocations. However, quantitative analysis of the dislocation cells, shown in Fig. 9, indicated that the cell size and misorientation between neighboring cells remained unchanged from the onset of steady-state to failure. The increase in strain amplitude from 1.0% to 2.0% does not influence the misorientation value. These results imply that the development of dislocation cells during strain fatigue do not promote grain size refinement. It is possible that there is a significant difference in strain amplitude and number of cycles between conventional strain fatigue and mechanical milling, however, Koch [9] stated that the total strain, rather than milling energy or ball-powder-ball collision frequency, is responsible for determining the nanocrystalline grain size. Presumably, it is therefore that the strain amplitude and number of cycles are not crucial factors for the achievement of nanocrystalline structure under usual mechanical milling conditions.

It is well that the strain fatigue leads to fracture of materials. Benjamin and his colleagues indicated that the repeatedly fracturing and cold welding of powder particles occur during mechanical milling [1-3]. As long as the fracturing occurs transgranularly (strain fatigue at room/low temperature always leads to transgranular fracture), the fracturing and cold welding are likely to refine grains because the welded fragments of original coarse grains should be new grains. The refinement model of fracturing and cold welding is consistent with the co-existence of the elongated coarse grains and nanoscale grains in the present Inconel 625 powder cryomilled for 4 hours. The larger fragments appear as elongated coarse grains and finer ones present as nanoscale grains. However, it is difficult to explain the occurrence of the elongated coarse grains on the basis of the dislocation cell model [4-6].

Under the present cryomilling conditions, the powder particles first transform into disks from an initially spherical geometry. The radius of the ball is significantly larger than that of the powder particle (5 mm to 84 μm), therefore, the loads applied to powder particle are simplified as impact loads normal to the large faces of the disk powder particle. A compressive stress is normal to the large faces of the disk, and the tensile stress is parallel to the directions of disk radius, so the grains would be elongated along the direction of disk radius.

4. CONCLUSIONS

Nanocrystalline Inconel 625 alloy with a uniform distribution of grains was synthesized using cryogenic mechanical milling. The primary results indicated that as cryomilling time increased, both the average powder particle size and average grain size approached constant values. During intermediate stages of cryomilling, grains in the powder were deformed into elongated grains with a high density of deformation faults, and then fractured by cycling impacting loading in random direction. The fractured fragments from the elongated coarse grains formed nanoscale grains. The evolution of the elongated grains from development to disappearance suggested that repeatedly strain fatigue fracturing caused by cycling impacting loading in random directions, and cold welding were responsible for the formation of a nanocrystalline structure.

REFERENCE
1.   J. S. Benjamin, *Metall. Trans.*, 1970, **1**, pp. 2943-2951.
2.   P. S. Gilman and J. S. Benjamin, *Ann. Rev. Mater. Sci.*, 1983, **13**, pp. 279-300.
3.   J. S. Benjamin, *Mater. Sci. Forum*, 1992, **88-90**, pp. 1-18.
4.   E. Hellstern, H. J. Fecht, C. Garland, and W. L. Johnson, *J. Appl. Phys.*, 1989, **65**, pp. 305-310.
5.   H. J. Fecht, *NanoStruct. Mater.*, 1995, **6**, pp. 33-42.
6.   J. Eckert, J. C. Holzer, C. E. Kill III, and W. L. Johnson, *J. Mater. Res.*, 1992, **7**, pp. 1751-1761.
7.   H. P. Klug and I. E. Alexander, in *X-ray diffraction procedure*, John Wiley & Sons, New York, 1974, p. 643.
8.   A. Plumtree and L. D. Pawlus: in *Basic Questions in Fatigue*, Vol. 1, ASTM STP 924, Fong and Fields, eds., ASTM, Philadelphia. 1988, pp. 81-97.
9.   C. C. Koch, *NanoStruct. Mater.*, 1997, **9**, pp. 13-22.

(a) As-received powder;

(b) Powder cryomilled for 8 hours;

(c) Powder cryomilled for 16 hours;

(d) Powder cryomilled for 20 hours.
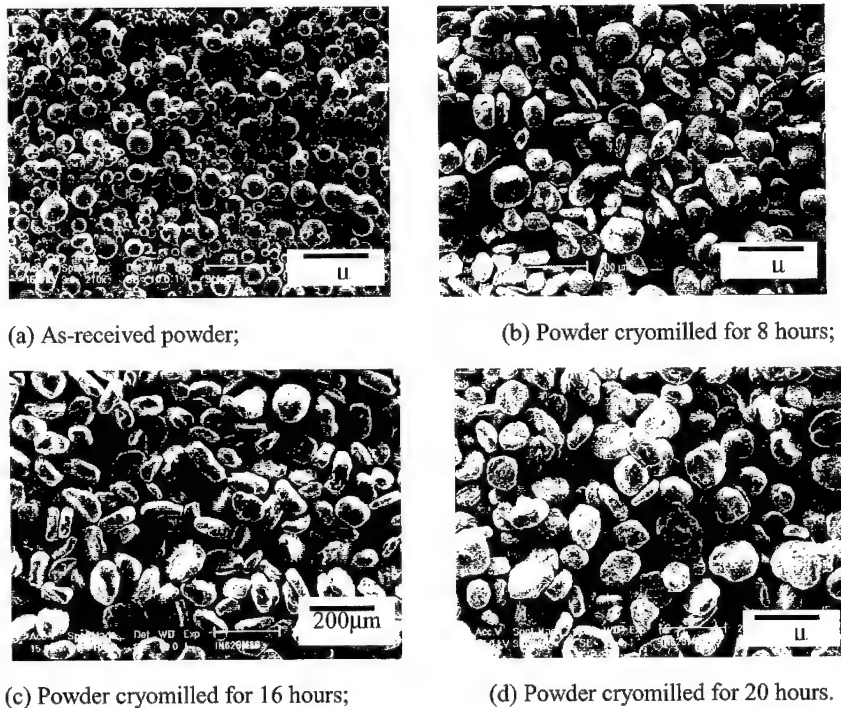
Fig. 1   Morphology of Inconel 625 powders.
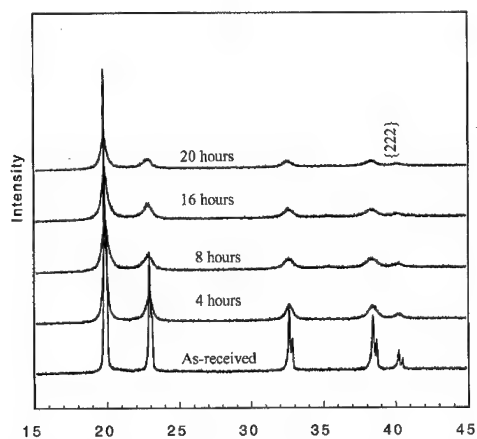
Fig. 2   X-ray diffraction spectra of Inconel 625 powders following different cryomilling time.
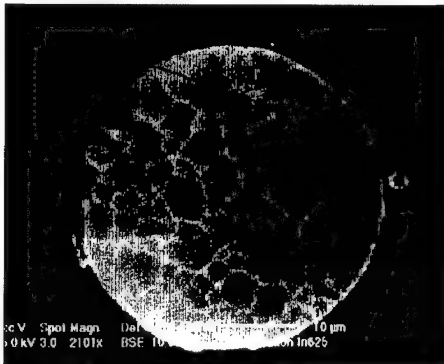
Fig. 3 SEM micrograph indicating grains.

20 nm
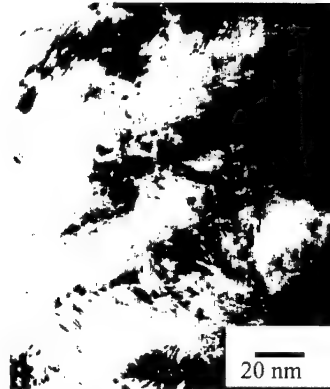
Fig. 4 A typical TEM image of Inconel 625 powder cryomilled for 4 hours.

100 nm

(a) Bright field image;

100 nm

(b) Dark field image;

Fig. 5 Elongated grains in Inconel 625 powder cryomilled for 4 hours.

Fig. 6 Elongated grains, with smaller dimension, in Inconel 625 powder following cryomilling of 6 hours.
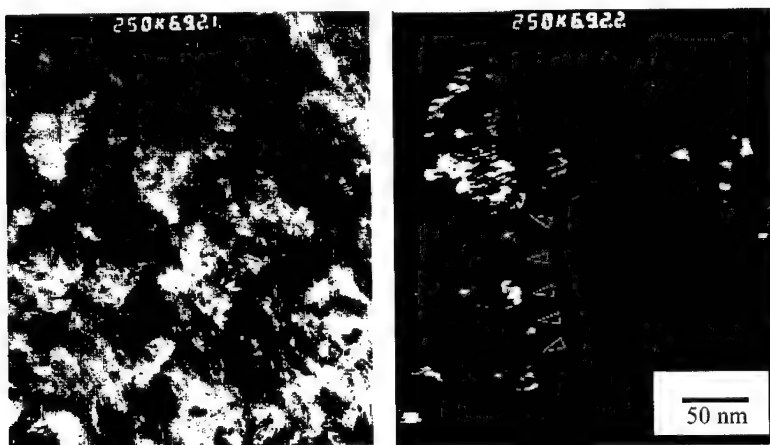
(a) Bright field image;

(b) Dark field image of (b), arrows indicate a fractured grain.

Fig. 7 Elongated grains fracture into a few segments during cryomilling.

(a) Bright field image;   (b) Magnification of (a).
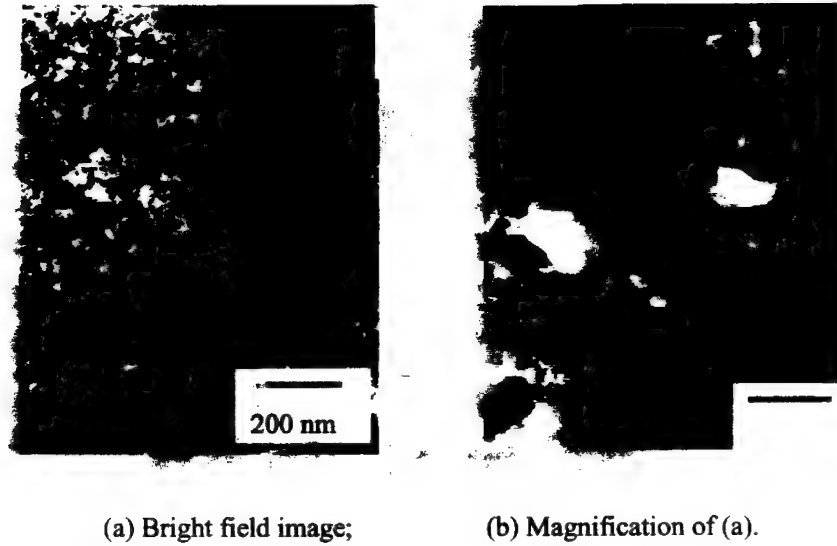
Fig. 8   Nanocrystalline Inconel 625 structure with uniform distribution of grain size.

(a) Variation of cell size with cycles for $\Delta\varepsilon_T$=1.0%;   (b) Misorientation between cells for $\Delta\varepsilon_T$=1.0%, and 2.0%.
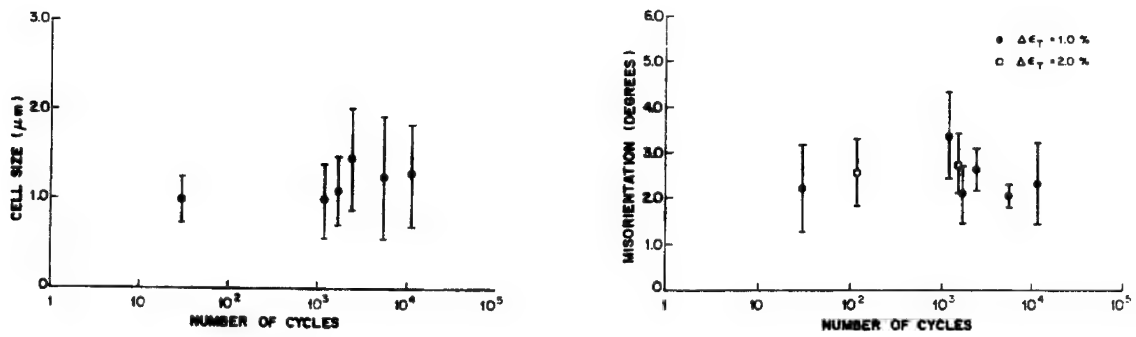
Fig. 9 Size of dislocation cells and misorientation between neighboring during strain fatigue of Al [8].

MOLECULAR DYNAMICS SIMULATION OF NANO-SIZED CRYSTALLIZATION DURING PLASTIC DEFORMATION IN AN AMORPHOUS METAL

R. TARUMI, A. OGURA, M. SHIMOJO, K. TAKASHIMA and Y. HIGO
Precision and Intelligence Laboratory, Tokyo Institute of Technology,
4259 Nagatsuta-cho, Midori-ku, Yokohama, 226-8503, Japan

ABSTRACT

An NTP ensemble molecular dynamics simulation was carried out to investigate the mechanism of nano-sized crystallization during plastic deformation in an amorphous metal. The atomic system used in this study was Ni single component. The total number of Ni atoms was 1372. The Morse type inter-atomic potential was employed. An amorphous model was prepared by a quenching process from the liquid state. Pure shear stresses were applied to the amorphous model at a temperature of 50 K. At applied stresses of less than 2.4GPa, a linear relation between shear stress and shear strain was observed. However, at an applied shear stress of 2.8 GPa, the amorphous model started to deform significantly until shear strain reached to 0.78. During this deformation process, phase transformation from amorphous into crystalline structure (fcc) was observed. Furthermore, an orientation relationship between shear directions and crystalline phase was obtained, that is, two shear directions are parallel to a (111) of the fcc structure. This crystallographic orientation relationship agreed well with our experimental result of Ni-P amorphous alloy. Mechanisms of phase transformation from amorphous into crystalline structure were discussed.

INTRODUCTION

When a liquid metal is quenched below its melting temperature, it enters a super cooled state. If the cooling rate is so high as to suppress the nucleation and growth of crystalline phases, a solid-state metal which has a random atomic structure is obtained. This is called an amorphous metal. Amorphous metals are thermally non-equilibrium state, so that solid-state phase transformation from amorphous into nano-sized crystalline phase (crystallization) may occur not only by heat treatment but also by plastic deformation [1]. Many plastic deformation models of amorphous metal have been proposed [2-3], however these models cannot explain the mechanism of crystallization during plastic deformation.

Molecular dynamics (MD) simulation is one of the most valuable tools to investigate the phenomena that are difficult to investigate experimentally. In the field of amorphous metal, several researchers have simulated the crystallization by thermal diffusion [4-5]. However, no MD simulation has been performed focused on crystallization by plastic deformation. The purpose of this study is to investigate the crystallization process during plastic deformation using a molecular dynamics simulation. Furthermore, the result of simulation was compared with our experimental result of Ni-P amorphous alloy to confirm its validity.

CALCULATION METHOD

Algorithm

The atomic system used in this study was constructed from 1372 Ni atoms. This

model was employed to compare with our experimental result of a Ni-P amorphous alloy. Inter atomic potentials for Ni atoms have been proposed by many researchers [6-8]. However, these potentials did not directly support the amorphous structure because these are developed for crystalline structure. In this study the simplest Morse type pair potential [6] was employed. The Morse type pair-wise potential is given by the following equation,

$$\phi(r) = \frac{D}{m-1} \{ \exp[-m\alpha(r-r_0)] - m\exp[-\alpha(r-r_0)] \}, \tag{1}$$

where r represents the distance between two atoms in the model. The parameters of the potential, listed in Table 1, are adjusted to reproduce the lattice parameter and elastic constants of fcc Ni [6].

The ensemble used in this study was an NTP ensemble (this indicates that the total number of atoms, temperature and pressure in the model kept constant) based on Parrinello-Rahman's [9] and Nose's [10] methods. According to these methods, the Hamiltonian (H) of the total system can be expressed as follows,

$$H = \sum_{i=1}^{N} \frac{\pi_i^T G^{-1} \pi_i}{2mf^2} + \phi(q) + \frac{1}{2Wf^2} \mathrm{Tr}(\Pi^T \Pi) + P\Omega + \frac{1}{2}\mathrm{Tr}(\Gamma G) + \frac{P_f^2}{2Q} + gk_B \ln f, \tag{2}$$

where the first and second terms represent the kinetic and potential energies of the atomic system, the third and fourth terms represent the kinetic and potential energies of the MD cell, the fifth term represents the external anisotropic pressure (stress), the sixth and seventh terms represent the kinetic and potential energies of the thermostat, respectively. g and k_B represent the degree of freedom and Boltzman's constant, respectively. Definitions of the other variables are listed in the appendix and the values of parameters are listed in Table 1. The initial value is shown for the parameter Q, which changes linearly with a change in temperature. The equation of motion for each variable is obtained from the Hamiltonian (see (A4)-(A6)). These equations can be solved numerically using a Gear's fifth order predictor-corrector algorithm with a time step of 0.5 fs. Three dimensional periodic boundary condition was employed throughout the simulation. The model is therefore under plane strain condition under external stresses.

Table 1. *The parameters of the simulation*

m	r_0 ($\times 10^{-10}$ m)	a ($\times 10^{10}$ m^{-1})	D ($\times 10^{-20}$ J)	W (g/mol)	Q (kJ/mol)(ps)^2
2.0	2.527516	2.487655	3.5059	50.0	0.003644

Procedure

An fcc structure of Ni was constructed and heated from 50 K to 2100 K at a constant heating rate of 20 K/ps and maintained for 10,000 steps (=5.0 ps) to obtain an equilibrium liquid state. It was then quenched down to 50 K from the liquid state at a constant cooling rate of 100 K/ps and maintained at this temperature for 10,000 steps

(=5.0 ps) to obtain a stable amorphous structure. Pure shear stresses of τ_{yz} were applied to the amorphous model at a temperature of 50 K. The applied shear stresses were increased stepwise by 400 MPa every 10,000 steps (=5.0 ps) at stresses of less than 2.8 GPa. The strain of the model was calculated from the following equation [11],

$$\varepsilon_{ij} = \frac{1}{2}\left(\frac{\partial u_i}{\partial h_j} + \frac{\partial u_j}{\partial h_i} + \sum_k \frac{\partial u_k}{\partial h_i}\frac{\partial u_k}{\partial h_j} \right), \tag{3}$$

where h and u represent the position and the displacement vector of the MD cell, respectively.

RESULTS AND DISCUSSION

Figure 1 shows the radial distribution functions (RDFs) of (a) the liquid state at a temperature of 2100 K, (b) after quenched down to 50 K from the liquid state and (c) the perfect fcc crystalline state (in this case, vertical axis indicates the relative intensity). In Fig.1 (b), each peak is slightly higher than that of the liquid state and the splitting of the second peak was clearly observed. This is a typical RDF of amorphous metals. Figure 2 shows the three dimensional locations of atoms observed from the x-axis direction. The size of MD cell was $2.5 \times 2.5 \times 2.5$ nm³. In this figure, no long range ordering was observed. From these results, it is considered that a Ni single component amorphous metal was obtained by the quenching process, and this amorphous model was employed for the following analysis.
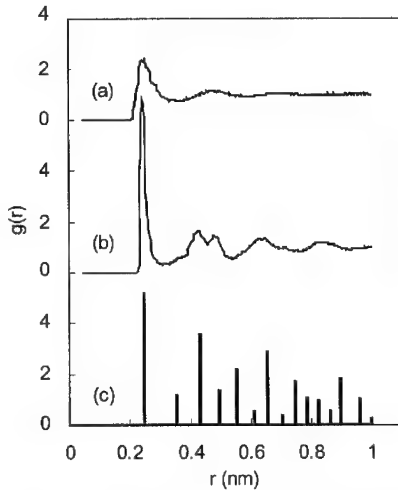
Fig. 1. Radial distribution functions of (a) liquid state, (b) quenched from the liquid and (c) fcc crystal.
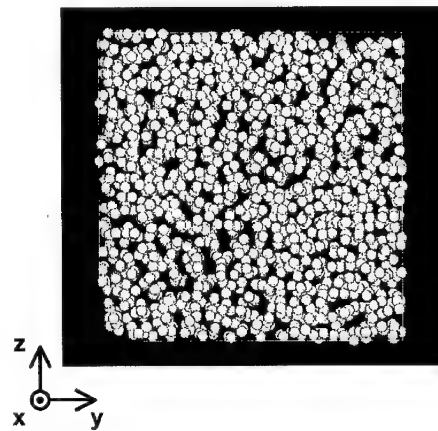
Fig. 2. Three dimensional locations of atoms observed from the x-axis direction.
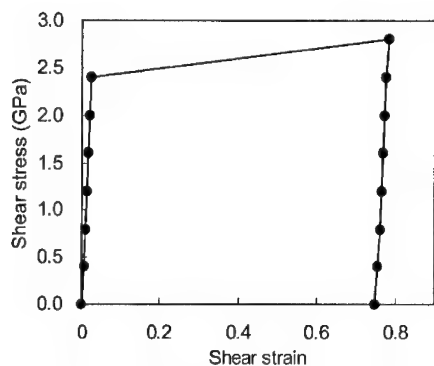
Fig. 3. *Calculated shear stress - shear strain curve at 50 K.*

Figure 3 shows a calculated shear stress - shear strain curve of the amorphous model at a temperature of 50 K.   At applied shear stresses of less than 2.4 GPa, a linear relationship between shear stress and shear strain was observed.   However, at an applied shear stress of 2.8 GPa, the amorphous model started to deform significantly until shear strain reached to 0.78.   During this shear deformation process, a drastic decrease in potential energy was observed.   Furthermore, the RDF of the deformed model was consistent well with that of fcc structure [10].   This result indicates that phase transformation from amorphous into crystalline structure (fcc) occurred during shear deformation.

Figures 4 (a) and (b) show three dimensional locations of the atoms observed from the x-axis direction of the MD cell at a shear strain of 0.74 and 0.78, respectively.   In these figures, only central parts of the model are shown.   In fig. 4 (a), the existence of crystalline phase is confirmed in the circled regions.   With increasing shear strain, the size of crystalline phase increased.   Finally, at a shear strain of 0.78, the amorphous model fully transformed into a crystalline structure.   Furthermore, from the crystallographic orientational analysis, an orientation relationship between shear directions and crystalline phase was obtained, that is, two shear directions are parallel to a (111) of the fcc structure.   This crystallographic orientation relationship is confirmed in another amorphous model, furthermore, it agreed well with our experimental result of a Ni-P amorphous alloy [11].   We therefore discuss the reason of this crystallographic orientation.
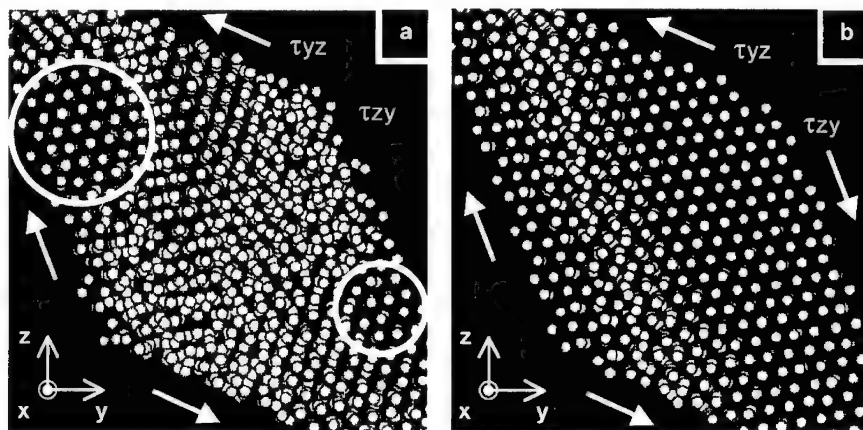
Fig. 4. *Three dimensional locations of atoms observed from the x-axis direction at (a)* γ = 0.74 *and (b)* γ = 0.78, *respectively.*

As noted above, the amorphous model is in a plane strain condition under external stresses because of the three dimensional periodic boundary condition. It is therefore considered that the motion of atoms toward the x-axis direction is suppressed under the shear stress of τ_{yz}. The potential energy can be minimized when atoms are close-packed, namely, (111) of fcc structure are formed. This may be the reason for the orientation relationship between the crystalline orientation and the direction of applied stress. However, the reason of orientation dependence of fcc structure on shear stresses is now under investigation.

Using this phenomenon, it may be possible to control not only the size of crystalline phase but also the orientation of crystalline phase. Finally it should be noted that the size of crystalline phase is uncertain because of the limitation of model size. However we confirmed that the size of crystalline phase was nano-meter order in Ni-P amorphous alloy [12].

CONCLUSIONS

Solid-state phase transformation from amorphous into crystalline structure during plastic deformation in a Ni amorphous metal has been investigated using an NTP ensemble molecular dynamics simulation. The conclusions of present study are summarized as follows.
1. Phase transformation from amorphous into crystal structure (fcc) occurred during shear deformation, and this transformation underwent by nucleation and growth process.
2. An orientation relationship between shear directions and crystalline phase was obtained, i.e., two shear directions and a (111) of the fcc structure are parallel.
3. These results agreed well with our experimental study on a Ni-P amorphous alloy.
4. Using these phenomena, it may be possible to control the orientation of crystalline phase.

REFERENCES

1. H. S. Chen, Y. He, G. J. Shiflet and S.J.Poon: Nature **367** (1994) 541.
2. J. J. Gilman: J. Appl. Phys. **46** (1975) 1625.
3. C. A. Pampillo: J. Mater. Sci. **10** (1975) 1194.
4. V.A.Likhachev, A.I.Mikhailin and L.V.Zhigilei: Phil. Mag. A, **69** (1994) 421
5. J. K. Bording and J. Tafto: Phys. Rev. B **62** (2000) 8098
6. F. Milstein: J. Appl. Phys. **44** (1973) 3825.
7. V. Rosato, M. Guillope and B. Legrand: Phil. Mag. A, **59** (1989) 321.
8. H. R. Taber and A. P. Sutton: Phil. Mag. Let., **63** (1991) 217.
9. M. Parrinello and A. Rahman: J. Appl. Phys. **52** (1981) 7182.
10. S. Nose: J. Chem. Phys. **81** (1984) 511.
11. L. D. Landau and E. M. Lifshitz: *Theory of Elasticity*, (Pergamon press, (1985)) Vol. 7 of Course of Theoretical Physics.
12. A. Ogura, M. Sato, R. Tarumi, M. Shimojo, K. Takashima and Y. Higo: MRS 2000 fall meeting, B1.10, Abstract, 40
13. R. Tarumi, A. Ogura, M. Shimojo, K. Takashima and Y. Higo: Jpn. J. Appl. Phys. **39** (2000) L611

APPENDIX

Variables used in equation (2) are defined as follows.

q_i :   position of the i th atom
p_i :   momentum of the i th atom
h :   matrix of the MD cell
II :   momentum of the MD cell
f :   time scaling factor
P_f :   momentum of the f

Pressure of the system was controlled by Parrinello-Rahman's method [7].   In this method, the position and momentum of atoms are scaled using a matrix of MD cell h, namely,

$$s_i = h^{-1} q_i, \quad \pi_i = h^T p_i, \tag{A1}$$

$$G = h^T h, \tag{A2}$$

where superindex 'T ' indicates the transverse matrix. G is called metric matrix.   The temperature of the system was controlled by Nose's method [8].   In this method, each variable is scaled using a time scaling factor of f, that is,

$$s_i = s_i, \quad \pi_i = \frac{1}{f} \pi_i, \quad h = h, \quad \mathit{II} = \frac{1}{f} \mathit{II}, \quad P_i = \frac{1}{f} P_f. \tag{A3}$$

The Hamiltonian of the system (Eq. (2)) was obtained from these equations.

Equations of motion for each variable were obtained from the Hamiltonian of the system (Eq. (2)).   In Lagrangian form, these are

$$\frac{d}{dt}\left(m \frac{ds}{dt} \right) = -h^{-1} \frac{d\phi(q)}{dq} - mG^{-1} \frac{dG}{dt} \frac{ds}{dt} - \frac{m}{f} \frac{df}{dt} \frac{ds}{dt}, \tag{A4}$$

$$\frac{d}{dt}\left(W \frac{dh}{dt} \right) = \sum_{i=1}^{N} mh \frac{ds_i}{dt} \left(\frac{ds_i}{dt} \right)^T - \sum_{i=1}^{N} \frac{\partial\phi(q)}{\partial q_i} s_i^{\ T} - P\varLambda - h\varGamma - \frac{W}{f} \frac{df}{dt} \frac{dh}{dt}, \tag{A5}$$

$$\frac{d}{dt}\left(Q \frac{df}{dt} \right) = f\left(\sum_{i=1}^{N} \frac{\pi_i\, G^{-1}\, \pi_i}{m} + \frac{1}{W} Tr\left(\mathit{II}^T \mathit{II} \right) - gk_B T \right) + \frac{Q}{f}\left(\frac{df}{dt} \right)^2. \tag{A6}$$

These equations can be solved numerically by Gear's algorithm.

Formation of Nano-Sized Crystals During Plastic Deformation in Amorphous Alloys

A. Ogura, M. Sato, R. Tarumi, M. Shimojo, K. Takashima and Y. Higo
Precision and Intelligence Laboratory, Tokyo Institute of Technology
4259 Nagatsuta-cho, Midori-ku, Yokohama 226-8503, Japan
aogura@pi.titech.ac.jp

ABSTRACT

Microstructural change in deformation bands was observed in a Ni-P amorphous alloy using transmission electron microscopy (TEM).   Bending strain was applied to a micro-sized cantilever beam specimen.   A TEM specimen was prepared from the micro-sized specimen with keeping the information on the relationship between the deformed direction and the specimen orientation.   TEM observation in deformation bands revealed that plastic deformation induces the precipitation of nanocrystalline Ni particles.   An orientation relationship between deformation direction and crystal orientation was obtained, that is, a (111) plane of all crystalline particles are parallel to the side surface of the specimen.

KEYWORDS: nano structure, amorphous alloy, plastic deformation, crystallization, TEM observation

INTRODUCTION

Micromachines and micro electro mechanical system (MEMS) devices are expected to be applied more widely in many fields in the near future.   The devices are used not limited in biomedical fields, but in automobiles, home appliances, computers and telecommunication fields. Application examples include accelerometers, pressure sensors, flow detectors, disc drives, and so on.   The size of some components used in these devices is considered to be in the order of microns.   The mechanical properties of such materials may be different from those of bulk materials due to the size effects such as the effects of crystal grain size.   Amorphous alloys are potential candidate materials for future micromachines and MEMS because of their isotropic mechanical properties, high strength and uniform structure [1].   In addition, amorphous alloys can be formed on substrates by sputtering and depositing techniques.   Then, surface integrated micromachines can be constructed on the substrate material.   However, the elongation of amorphous alloys is low accompanied with localized deformation at room temperature [2].   Strengthening methods for such micro-sized components are considered to be indispensable using nano-structural control techniques.   The materials which contain nano-sized crystals in amorphous matrix may have improved deformation behavior.   Such nanocrystalline amorphous alloys can be produced by two different methods.   One method is a heat treatment on amorphous alloys (thermal crystallization).   A partially crystalline material with crystal sizes ranging from 2 to 15nm was obtained by annealing a Ni based amorphous alloy for 2 months at a temperature well below the crystallization temperature [3].   The other is a plastic deformation process (mechanical crystallization).   It has been reported that Fe and

Al based amorphous alloys, which have been deformed by high-energy ball milling, have nano-sized crystals in amorphous matrices [4-6]. In thermal crystallization, nanocrystals are only obtained at relatively low temperatures and it consequently takes a long time. Thus, mechanical crystallization is considered to be a quicker process for material strengthening compared to the thermal crystallization. However, the mechanism of mechanical crystallization has not yet been clarified. Relationships between deformation directions and the orientation of crystals are still unclear. It is considered that these relationships would give us important information to elucidate the crystallization mechanisms. The aim of this study is to determine the relationships between deformation directions and the orientation of nano-sized crystals induced by plastic deformation in an amorphous alloy.

EXPERIMENTAL DETAILS

Specimen preparation

Amorphous alloys have many different mechanical characteristics compare to crystalline alloys; for example, inhomogeneous plastic deformation occurs in localized shear bands [7] without work hardening. As plastic deformation in amorphous alloys is limited to thin shear bands, it is difficult to prepare a transmission electron microscopy (TEM) specimen including a shear band from a deformed large specimen with keeping the information on the relationship between the deformed direction and the specimen orientation. Thus, micro-sized specimen was used in this study. The material used in this study was a Ni-11.5wt%P amorphous thin film that was electroless deposited on an Al-Mg alloy. The amorphous layer was separated from the Al-Mg alloy substrate by dissolving the substrate with a NaOH aqueous solution. The amorphous layer, the thickness of which was 12μm, was cut into a half circle disk of 3mm in diameter. A cantilever beam specimen was produced near the straight-line part of a half circle disk by focused ion beam (FIB) machining. A micro-cantilever beam specimen is shown in figure 1. The height, length, thickness and the distance from the loading point to the fixed end of the specimen were 8.5μm, 55μm, 12μm and 45μm, respectively. The cantilever
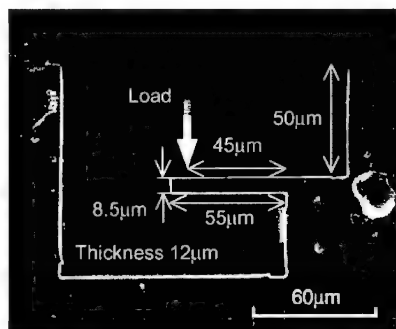
Figure 1. A SEM image of the micro-sized cantilever specimen before bending test.
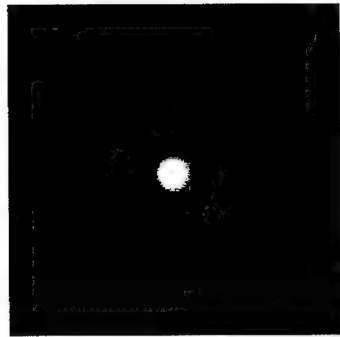
Figure 2. An electron diffraction pattern from a part of the specimen, away from the straight edge, indicating the existence of only an amorphous structure. This shows that the influence of the cutting and FIB machining is negligible.
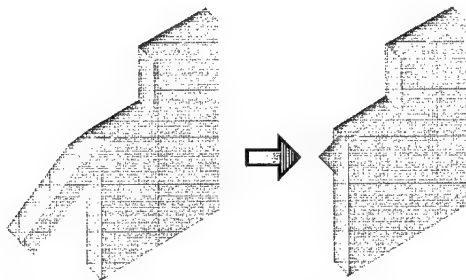
Figure 3. Schematic images of TEM specimen preparation. The deformation bands were thinned to less than 0.1μm remaining near the center in the thickness direction of the micro-cantilever beam by FIB machining.

beam was produced away from the straight edge of the half circle disk for a distance of 50μm in order to avoid any influence of the cutting. The influence of the cutting procedure to make the half circle disk was investigated in a preceding experiment. Another half-circle disk specimen was thinned by FIB machining to observe microstructure using TEM. Figure 2 shows the electron diffraction pattern from a part of the specimen, which was 15μm away from the straight edge, indicating only a halo pattern, which is a characteristic of amorphous phases. This suggests that the influence of the cutting procedure on the microstructure is limited within 15μm, and the influence of FIB machining is negligible.

Bending test

A bending test was performed on the micro-cantilever beam specimen using a micro-mechanical testing machine. The details of the testing machine are described in a

previous paper [8]. The specimen can be positioned with an accuracy of 0.1μm using a precise X-Y stage. The load resolution was 10μN, and the displacement resolution was 5nm. The testing machine has a pushrod with a tip radius of 5μm, and the pushrod is connected to a load cell. Bending deflection was applied to the specimen by pushing through the pushrod. The specimen was observed in-situ using a CCD camera at a magnification of 3000 times during the bending test. The bending test was performed in air at room temperature.

Electron Microscopy

The surface morphology of the specimen before and after bending test was observed using a field emission gun scanning electron microscope (FE-SEM). The structural change caused by bending was observed using TEM operated at an accelerating voltage of 200kV. TEM specimen including deformation bands was prepared by FIB machining following the bending tests. The deformation bands were thinned to less than 0.1μm remaining near the center in the thickness direction of the micro-cantilever beam. Schematic images of TEM specimen preparation are shown in Fig.3. This procedure enable one to prepare a TEM specimen including deformation bands from a deformed specimen with keeping the information of the deformed direction. The electron beam axis was perpendicular to the side surface of the specimen.

RESULTS AND DISCUSSION

FE-SEM images of the micro-cantilever beam specimens after bending tests are shown in fig. 4. The specimens were successfully bent down at the fixed end of the beam without any torsion. Steps and shear bands are found near the fixed end, caused consequently by bending. Figure 5(a) shows an electron diffraction pattern taken in deformation bands with a selected area aperture with a diameter of 0.2μm. Not only a halo pattern, but also some spots are observed, which indicates the existence of a crystalline phase. The diffraction spots show a pattern of an f.c.c. Ni phase, and a (111) plane is perpendicular to the electron beam direction. Sizes of the crystals are approximately 20nm. It is also interesting to note that a (111) plane of
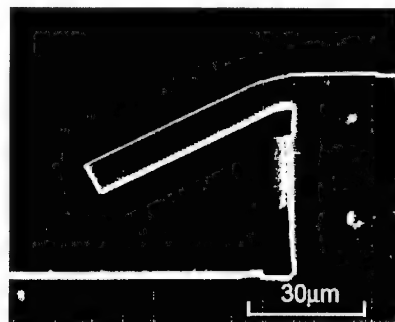
Figure 4. A SEM image after a bending test. The specimen was bent down at the fixed end of the specimen without any torsion.

all the Ni crystals is parallel to the side surface of the specimen. This crystallographic orientation relationship agrees well with our molecular dynamics study of a Ni amorphous metal [9]. This morphology is clearly different from those induced by annealing. Amorphous alloys are in a non-equilibrium state, so that structural change occurs into crystalline with increasing temperature above the crystallization temperature. Sui [10] reported that the crystals induced by heating of a Ni-11.3wt%P amorphous alloy consisted of two phases; Ni (f.c.c.) and Ni_3P (b.c.t.) and that crystal grains had random orientation relationship one another. Therefore, it is concluded that crystallization induced by deformation is not due to a temperature effect. It is also revealed that a local temperature increase in shear bands is rather limited and the maximum temperature is considered to be below the crystallization temperature T_c in this bending test. Another important aspect in order to understand the mechanism of deformation-induced crystallization is a deformation mode in the micro-sized cantilever beam specimen. A previous study [11] showed the fracture behavior of micro-cantilever specimens with a notch and fatigue pre-crack. On the fracture surface, both plane stress and plane strain areas exist even for micro-sized specimens. It is, therefore, considered that the area observed in this paper using TEM is in a plane strain state as well. This means that the atoms have no or little mobility towards the thickness direction in this state. As Ni atoms prefer closed packing and have little mobility in the thickness direction, the closely packed plane, that is (111) plane, is considered to be formed and orientated perpendicular to the thickness direction. The results obtained in this investigation strongly suggest that the control of nanocrystalline orientation in amorphous alloys would be possible by application of stress field.
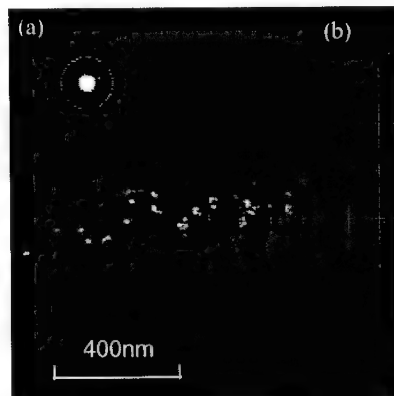
Figure 5. TEM images after a bending test.
(a) an electron diffraction pattern taken in deformation bands, showing patterns of an amorphous structure and a f.c.c. Ni phase. The f.c.c. pattern shows that [111] direction is parallel to the electron beam direction.
(b) a dark field image of the deformation band. Nano-sized Ni particles having the same orientation are found.

CONCLUSIONS

Crystallization induced by plastic deformation was studied in a Ni-P amorphous alloy. Nano-sized crystals are observed in deformation bands, and a (111) plane of the crystalline phase is parallel to the side surface of the micro-sized cantilever beam specimen.   As Ni atoms prefer close packing and have little mobility to the thickness direction, the closely packed (111) plane is considered to form parallel to the side surface of the specimen.   This indicates that mechanisms of the crystallization induced by deformation are different from those caused by annealing.   These results agreed well with our molecular dynamics study on a Ni amorphous metal.

REFFENCES

1.   A. Masumoto and R. Madding, *Acta metall.,* **19**, 725 (1971)
2.   C. A. Pampillo and H. S. Chen, *Mater. Sci. Eng.,* **13,** 181, (1974)
3.   S. J. Thorpe, B. Ramaswami and K. T. Aust, *Acta Metall.* **36**, 795, (1988)
4.   M. L. Trudeau, D. Dussault, A. Van Neste and R. Schulz, *Phys. Rev. Lett.* **64**, 99 (1990)
5.   Y. He, G. J. Shiflet and S. J. Poon, *Acta metall.,* **43**, 83. 1995
6.   H. Chen, Y. He, G. J. Shiflet and S. J. Poon, *Nature,* **367**, 541, (1994)
7.   F. Spaepen, *Acta metall.,* **25**, 407, (1977)
8.   K. Takashima, T. Kimura, M. Shimojo, Y. Higo, S. Sugiura and M. V. Swain, *Proc. 7th Int. Fatigue Cong.* (Higher Education Press, Cradley Health. UK.) 1871 (1999)
9.   R. Tarumi, A. Ogura, M. Shimojo, K, Takashima and Y. Higo. *Jpn. J. Appl. Phys.,* **39**, L611, (2000)
10. M. L. Sui, K. Lu and Y. Z. He, *Phil. Mag B.,* **63**, 993, (1991)
11. A. Ogura, Y. Ichikawa, M. Shimojo, K. Takashima, Y. Higo and M. V. Swain, Proc. 3rd Int. Conf. Poster Exhibition on MicroMaterials (MicroMat 2000), 574, (2000)

Mechanical Properties and Deformation Behavior II— Bulk Materials

Cyclic Deformation and Fatigue Properties of Ultrafine Grain Size Materials: Current Status and Some Criteria for Improvement of the Fatigue Resistance

Haël Mughrabi and Heinz Werner Höppel
Institut für Werkstoffwissenschaften, Universität Erlangen-Nürnberg
D-91058 Erlangen, Germany

ABSTRACT

In this review, some general conclusions based on studies performed to date on fatigued materials of ultrafine grain (UFG) size produced by equal channel angular pressing (ECAP) are drawn, and open issues of current interest are defined. Important aspects addressed include the apparent discrepancy between improved fatigue strengths in Wöhler (S-N) plots as opposed to inferior fatigue strengths in Manson-Coffin plots, the clarification of the microstructural mechanisms of severe cyclic softening in conjunction with dynamic (local) grain/subgrain coarsening and damaging large-scale catastrophic shear banding. The important roles of the cyclic slip mode, the friction stress, the crystal structure and the temperature of cyclic deformation with respect to stable cyclic deformation behaviour are emphasized. Based on such considerations, criteria are formulated that must be observed, when designing ECAP-processed UFG-materials of superior fatigue strength.

INTRODUCTION

The mechanical properties of materials of nanocrystalline structure and of ultrafine grain (UFG) size (some 100 nm) have received considerable attention in recent years. Most related studies have been motivated by the advent of new (bulk) materials of extraordinary strength and by the desire to obtain a fundamental understanding of the factors that govern the strength of these new materials under different loading conditions. While bulk truly nanocrystalline materials have not yet become a reality, a variety of UFG-materials obtained by severe plastic deformation, most notably by the equal channel angular pressing (ECAP) technique, have been produced and investigated in considerable detail. The proceedings of a recent NATO Advanced Study Institute, dedicated to „Investigations and Applications of Severe Plastic Deformation" [1], and a recent review by Valiev et al. [2] document the results of most of the research performed to date.

Until quite recently, more detailed studies of the cyclic deformation and fatigue properties of different UFG-materials were rather scarce, most of the more detailed work being performed on UFG-copper, as reviewed by one of the authors [3] in ref. [1]. Nonetheless, based on earlier work on grain-size effects in the fatigue of metals of conventional grain size and on the available data on fatigued UFG-materials, a number of conclusions could be drawn. Thus, some problems on which future research should focus more strongly could be defined. In the context of the present review, the following aspects are considered particularly relevant:

- Predictions on grain-size effects in fatigue cannot generally be made solely on the basis of grain-size effects in monotonic deformation [3,4], as described primarily by the Hall-Petch relation which applies to macro- and not to microyielding as in the case of fatigue.
- Rather, it has been recognized that the cyclic slip mode and the crystal structure must also be considered as important factors [3,4]. In addition, the cyclic stability of UFG-materials is limited to much lower homologous temperatures than for conventional grain size materials.

- While the fatigue strength of UFG-materials, when considered in a Wöhler (S-N) plot, is superior to that of materials of conventional grain size, the opposite is usually true, when viewing the data in a Coffin-Manson plot.
- Early and severe cyclic softening, frequently accompanied by dynamic (local) grain/subgrain coarsening and by large-scale catastrophic shear banding, have been identified as the main causes of early fatigue failure (in strain-controlled tests).
- The microscopic processes of grain/subgrain coarsening, cyclic softening and of large-scale shear banding in fatigued UFG-materials are poorly understood and demand a more thorough investigation in order to develop suitable measures to reduce or avoid cyclic softening and shear banding.
- Quite generally, single-phase planar-slip materials that have so far not been investigated should be less susceptible to cyclic softening and should hence exhibit a more stable cyclic deformation behaviour. On the other hand, precipitation-hardened alloys with shearable precipitates that can also exhibit a planar slip mode would be expected to undergo severe cyclic softening.
- Until quite recently, there was a general lack of cyclic stress-strain data (cyclic saturation stress versus plastic strain amplitude). Such data are needed for fatigue life predictions.
- In the search for UFG-materials of potentially high fatigue strength, it should first be clarified which of these materials are at all suitable for unproblematic ECAP-processing. Next, the criteria mentioned above should be taken into account appropriately in the "design" of fatigue-resistant UFG-materials.

In the following, the above issues will be addressed, taking into account some of the more recent fatigue studies on UFG-materials. A number of questions will be raised, and only a few will be answered conclusively.

RECENT STUDIES ON FATIGUED UFG-MATERIALS

First, it is expedient to recall that the most detailed knowledge on the fatigue of UFG-materials still pertains to the studies on UFG-copper, most notably by Vinogradov et al. [5], Hashimoto et al. [6], Agnew and Weertman [7] and by Agnew et al. [8], as reviewed earlier [3]. More recently, some new results have been obtained by Brunnbauer [9] and Höppel et al. [10] on fatigued UFG-copper of 99.99% purity with a mean grain/subgrain size $d \approx 300$ nm, prepared by R. Valiev's laboratory. This work comprised both stress- and strain-controlled cyclic deformation tests at room temperature until failure. The tests were performed both on UFG-copper in the as-ECAP-processed state and after an annealing treatment. In order to obtain an idea how stress and plastic strain are related in the regime of interest to fatigue studies, a series of tensile straining tests with intermittent unloadings/reloadings in the microstrain regime were carried out, as shown in figure 1. One can conclude from such figures that fatigue studies should cover a range of stress amplitudes $\Delta\sigma/2$ ($\Delta\sigma$: stress range) up to about 300 MPa and plastic strain amplitudes $\Delta\varepsilon_{pl}/2$ ($\Delta\varepsilon_{pl}$: plastic strain range) from about 10^{-4} to some 10^{-3}. Turning first to strain-controlled tests at constant $\Delta\varepsilon_{pl}$, severe cyclic softening, with catastrophic shear banding, as first reported by Agnew and Weertman [7], dependent on the initial UFG-structure [5-8], was observed in the range $10^{-4} < \Delta\varepsilon_{pl}/2 < 10^{-3}$ [9,10]. The fatigue life N_f (number of cycles to failure) was shorter than for copper of conventional grain size. Based on the "saturation" stress level at $N = N_f/2$, a "pseudo" cyclic stress-strain (CSS) curve could be constructed, as shown in figure 2.
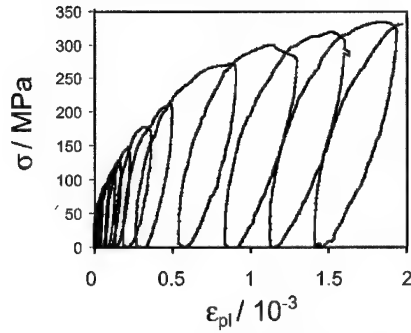
Figure 1. Stress-strain behaviour (stress σ versus plastic strain ε_{pl}) of UFG-copper at 293 K in microstrain regime, with repeated unloadings and reloadings. From [9,10].

Since the reason for early failure was seen in the instability of the severely predeformed material, when subjected to cyclic deformation, attempts were made to apply a suitable heat treatment in order to obtain a more stable microstructure at the expense of loosing some of the initial strength. For this purpose, an annealing treatment at the temperature of 170°C, as suggested by DSC-measurements, was applied in some preliminary tests to a number of specimens for different times up to 240 min. The specimens were subsequently fatigued at an amplitude of $\Delta\varepsilon_{pl}/2 = 10^{-3}$, and the cyclic deformation curves [9,10] and the fatigue lives (figure 3a) were recorded as a function of the annealing time. Based on these results, an annealing treatment of 120 min. at 170°C was considered as optimal. As shown in figure 3b, a specimen subjected to this heat treatment and fatigued subsequently at $\Delta\varepsilon_{pl}/2 = 10^{-3}$ exhibits a similar fatigue life as a copper specimen of conventional grain size (ca. 40 μm [11]), albeit at a significantly higher stress amplitude. The beneficial effect of the heat treatment on the fatigue life is also demonstrated in figure 4 which shows in a Coffin-Manson plot that, in the range of plastic strain amplitudes of about $2 \cdot 10^{-4}$ to about 10^{-3}, significant enhancements of the fatigue life by typically a factor of 7 were observed in all cases [9,10]. Moreover, when compared with data on commercial purity copper of conventional grain size [12,13], the fatigue lives were longer.
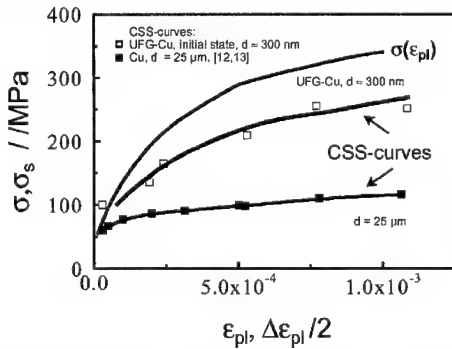
Figure 2. "Pseudo" cyclic stress-strain (CSS) curve of UFG-copper ("saturation" stress amplitude at $N = N_f/2$ versus plastic strain amplitude $\Delta\varepsilon_{pl}/2$), at 293 K, comparison with monotonic stress-strain curve $\sigma = \sigma(\varepsilon_{pl})$ and with CSS-curve of copper of conventional grain size [12,13]. d: grain/subgrain size. From [9,10].
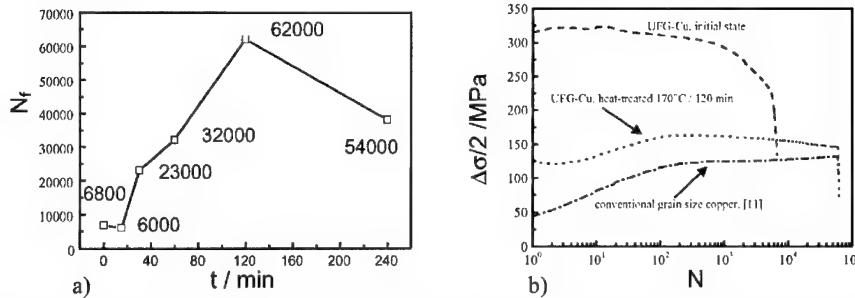
Figure 3. *Effect of annealing treatment on fatigue lives of UFG-copper. a) Fatigue lives N_f of annealed UFG-copper at $\Delta\varepsilon_{pl}/2 = 10^{-3}$, 293 K, after different annealing times at 170°C. b) Cyclic deformation curves at $\Delta\varepsilon_{pl}/2 = 10^{-3}$, 293 K, of UFG-copper in the as-ECAP-processed state and after annealing at 170°C for 120 min. Comparison with cyclic deformation curve of copper of conventional grain size (ca. 40 µm [11]. From [9,10].*

Turning now to stress-controlled tests displayed in Wöhler (S-N) plots, UFG-materials in general and also UFG-copper exhibit superior fatigue resistance compared to material of conventional grain size [3,8,14]. The enhanced fatigue strength of as-ECAP-processed UFG-materials in the Wöhler (S-N) plot, compared to the reduced fatigue resistance in the Coffin-Manson diagram, is best explained in a total strain ($\Delta\varepsilon_t$: total strain range) fatigue life diagram [3], as shown schematically in figure 5. Here, the limiting curves in the low cycle fatigue (LCF) and the high cycle fatigue (HCF) regimes correspond to the Coffin-Manson law and the Wöhler/Basquin (S-N) plot, respectively. Thus, it is easily seen that the enhanced fatigue strength of UFG-materials in the HCF regime results from the increased fatigue strength coefficient σ_f', whereas the reduced fatigue resistance in the LCF-regime is a consequence of the lowering of the fatigue ductility coefficient ε_f' [3].

It is not clear from earlier published work, how the stress amplitudes were built up in stress-controlled tests. In the work of Höppel et al. [10], the stress amplitudes were built up slowly over several hundred cycles for two reasons, namely to reduce the danger of buckling during the compressive half cycle at the higher stress amplitude and, secondly, to avoid too large (and presumably damaging) plastic strains during the first few cycles. Examples of the cyclic
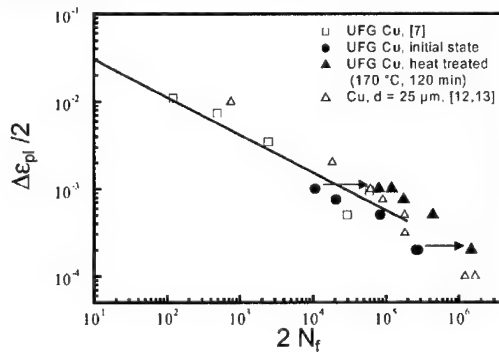
Figure 4. *Comparison of fatigue lives of annealed UFG-copper at 293 K in Coffin-Manson plot with fatigue lives of as-ECAP-processed UFG-copper and of copper of conventional grain size d = 25 µm [12,13]. From [9,10].*

$$\Delta\varepsilon_t/2 = \frac{\sigma_f'}{E}(2\,N_f)^b + \varepsilon_f'(2\,N_f)^c$$
$$\text{(HCF)} \qquad \text{(LCF)}$$
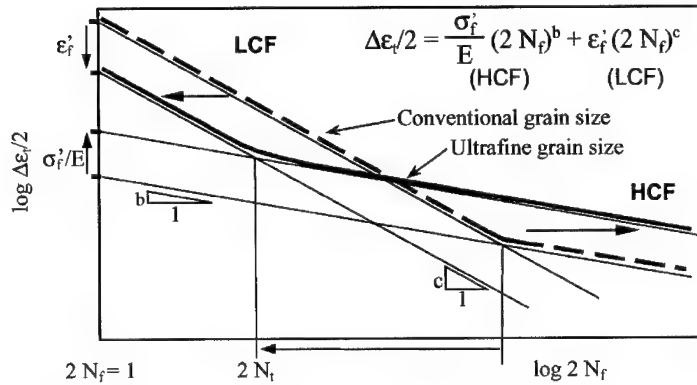
Figure 5. *Schematic illustration of enhanced high-cycle fatigue (HCF) life and reduced low-cycle fatigue (LCF) life of UFG-materials due to increased fatigue strength coefficient σ_f' and reduced fatigue ductility coefficient ε_f', respectively. Note also the reduced transition fatigue life N_t. E: Young's modulus.*

deformation curves in the form of $\Delta\varepsilon_{pl}/2$ versus the number of cycles, N, are shown in figure 6. It is important to note that these curves display a rather well-defined cyclic saturation regime without cyclic softening (!) and that, even at the rather high stress amplitude of $\Delta\sigma/2 = 200$ MPa, the plastic strain amplitude barely reached 10^{-4}. Hence, it is not surprising that the fatigue lives were generally found to be rather large, compared to both fatigue lives of copper of conventional grain size and to UFG-copper investigated by Agnew et al. [8], as shown in figure 7. In this figure, also the results of stress-controlled tests by Thompson and Backofen [4] and strain-controlled tests by Lukáš and Kunz [15] on copper of conventional grain size are included. Additional data on UFG-copper in the as-ECAP-processed state and in the heat-treated state (170°C, 120 min.), fatigued in strain-controlled tests, can be found in Höppel et al. [10]. It is
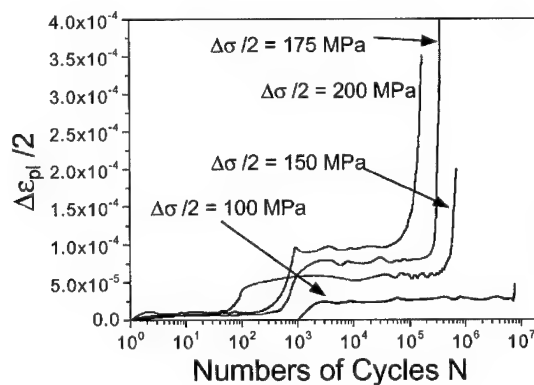
Figure 6: *Cyclic deformation curves ($\Delta\varepsilon_{pl}/2$ versus N) of UFG-copper fatigued after slow stress build-up at constant stress amplitude $\Delta\sigma/2$ at 293 K. From [10].*
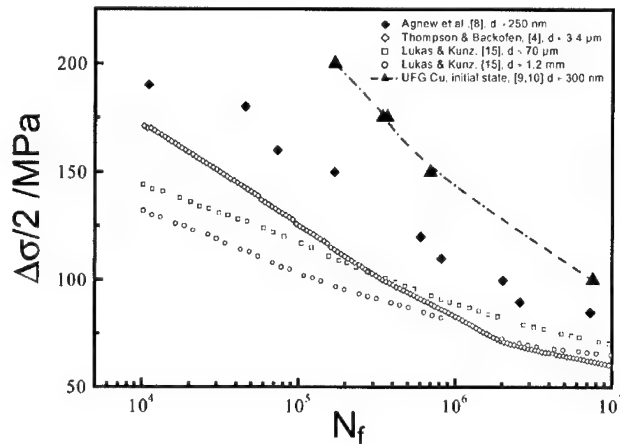
Figure 7. Wöhler (S-N) plots of UFG-copper fatigued under stress control at 293 K. Comparison with data from literature on UFG-copper and copper of conventional grain size. From [10].

quite evident that, in a Wöhler (S-N) plot, UFG-copper is found to be distinctly more fatigue-resistant than copper of conventional grain size. Moreover, the fatigue lives of UFG-copper reported by Höppel et al. [10] are significantly larger than those of Agnew et al. [8]. One explanation could be that the microstructure of the UFG-copper used by Höppel et al. [10] was more stable than that in the work of Agnew et al. [8]. Another reason could lie in the slow building-up of the stress amplitude which, by avoiding large initial plastic strain amplitudes, has a beneficial "coaxing" effect.

While the available data on fatigued UFG-nickel (grain size: ca. 300 nm) by Thiele et al. [16] are perhaps a little less detailed than those on UFG-copper, they are indeed very interesting, since the experiments by Thiele et al. [16] were performed not only at room temperature but also at 425 K. A result of particular interest is that, at room temperature (homologous temperature of 0.17), UFG-nickel was cyclically stable inspite of dynamic grain coarsening in strain-controlled tests. On the other hand, at the moderately high temperature of 425 K (homologous temperature of 0.25), dynamic recrystallization was observed. The stable cyclic behaviour at room temperature is borne out in the comparison of the cyclic stress-strain curve and the monotonic stress-strain curve, as shown in figure 8. Both curves are found to be almost identical, confirming the stability of the UFG microstructure against cyclic softening at the homologous temperature of 0.17.

To round up this brief survey of observations on fatigued UFG-material, some recent works on room-temperature fatigue of UFG 5056 Al-Mg alloy [14,17], UFG titanium [18] and UFG dispersion-hardened Cu-Cr-Zr bronze [19] are considered. Thus, Vinogradov et al. [14] and Patlan et al. [17], studying UFG-5056 Al-Mg alloy, noticed that while the cyclic deformation behaviour was rather stable, the fatigue crack growth rate was rather high. Although a considerable enhancement of fatigue life in a Coffin-Manson plot could be achieved by an annealing treatment, the fatigue lives were still shorter than in material of conventional grain size [17]. In the case of (hexagonal close-packed) UFG titanium, Vinogradov et al. [18] noted a quite stable cyclic deformation behaviour at room temperature and an enhanced fatigue strength in a Wöhler (S-N) plot, compared to material of conventional grain size, and no degradation in fatigue strength in strain-controlled tests, displayed in a Coffin-Manson diagram. Finally, it is interesting
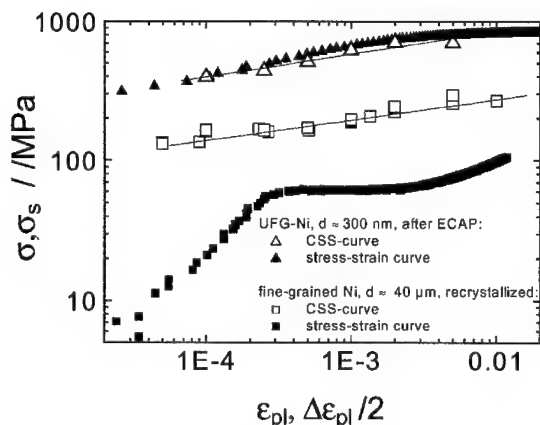
Figure 8. *Cyclic and monotonic stress-strain curves of UFG-nickel (ca. 300 nm) at 293 K, comparison with data of recrystallized nickel of conventional grain size (40 μm). Courtesy of E. Thiele.*

to note that the cyclic deformation of dispersion-hardened Cu-Cr-Zr bronze is unstable and characterized by pronounced cyclic softening as in the case of UFG copper but that the fatigue lives are not enhanced but reduced by an annealing treatment [19].

Patlan et al. [17] and Vinogradov et al. [18] have made first attempts to model both the shape of the hysteresis loop and the cyclic stress-strain curve by an approach based on a consideration of multiplication and annihilation of dislocations [20]. It will be interesting to see how far this modelling can be carried and how general the results obtained are.

CYCLIC SOFTENING AND DAMAGING LARGE-SCALE SHEAR BANDING

Fatigue damage in UFG-materials is frequently related to cyclic strain localization extending over much longer distances than the original grain size. This kind of strain localization can occur locally in "patches" or in extended shear bands, as shown in SEM-micrographs of the surface in figures 9a and 9b. It is tempting to believe that this kind of strain localization is closely related to regions of markedly coarsened grain size, as observed in the bulk by TEM (figure 9c). Grain coarsening of this type has also been observed in patches and in bands [10].

Since the pioneering work of Feltner and Laird [21], cyclic softening of predeformed material, accompanied and caused by cell/subgrain coarsening, is a well-known phenomenon. However, this kind of cyclic softening merged into a state of stable cyclic saturation and was thus not related to cyclic strain localization and fatigue damage. In the case of UFG-materials that have been produced by severe plastic deformation, local coarsening of the original UFG microstructure (denoted in this review as grain/subgrain structure) and damaging (large-scale) cyclic strain localization must be viewed as different aspects of one and the same damaging mechanism. However, the sequence of events remains to be clarified. Thus, the question is whether the process is initiated by local grain/subgrain coarsening which then leads to bands of cyclic strain localization, as illustrated schematically in figure 10a, or whether at first a catastrophic shear localization, which destroys the original UFG structure, occurs, followed subsequently by the formation of a new coarsened microstructure in the bands of localized shear deformation,
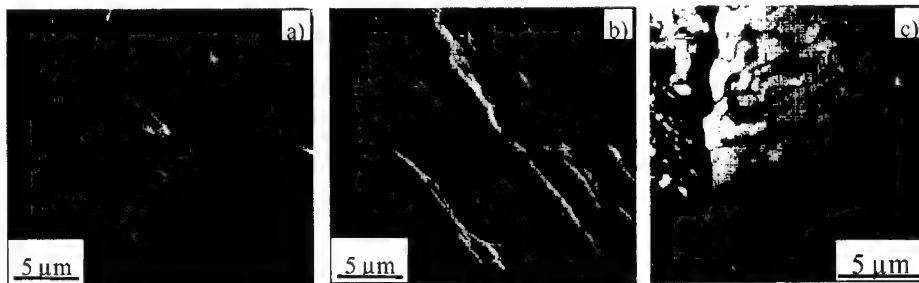
Figure 9. *Cyclic strain localization and shear banding in UFG-copper fatigued at 293 K. Surface observations of shear bands with extrusions (stress axis horizontal): a) in "patches". b) in extended shear bands. c) TEM observation of locally coarsened grain/subgrain microstructure. From [10].*

compare figure 10b. As remarked in [3], the bands of localized shear are reminiscent of microstructural instabilities leading to microbands in severely deformed materials and are also typical of shear strain localization of the kind frequently observed during deformation of strongly predeformed material after a "strain-path change". The large variety of processes that can contribute to cyclic softening of UFG-material have been summarized in ref. [3]. In any case, an interesting point concerning cyclic softening of ECAP-processed UFG-material is that, in addition to dislocation annihilation and rearrangement, it must obviously also involve dynamic grain/subgrain coarsening, as first noted by Witney et al. [22], requiring grain boundary mobility at rather low homologous temperatures down to about 0.2. An interesting observation regarding grain/subgrain coarsening is the following. In the work of Höppel et al. [10], a coarsened microstructure was observed on UFG-copper fatigued till failure at $\Delta\varepsilon_{pl}/2 = 2.0\cdot10^{-4}$ but not after fatigue till failure at $\Delta\varepsilon_{pl}/2 = 1.0\cdot10^{-3}$. A similar observation had been reported earlier by Agnew and Weertman [7]. The findings of Höppel et al. find their explanation in the fact that, with a constant mean plastic strain rate of $10^{-3}s^{-1}$, the time till failure was four times larger at the lower plastic strain amplitude of $2.0\cdot10^{-4}$. This suggests strongly that dynamic grain/subgrain coarsening is a thermally activated process which requires time, in particular at low homologous temperatures. In the following, the nature of processes of "dynamic" grain boundary mobility during cyclic deformation at rather low temperatures and the factors that facilitate or impede the processes of dislocation annihilation during cyclic softening will be discussed with the aim to define the requirements for the design of fatigue-resistant UFG-materials.
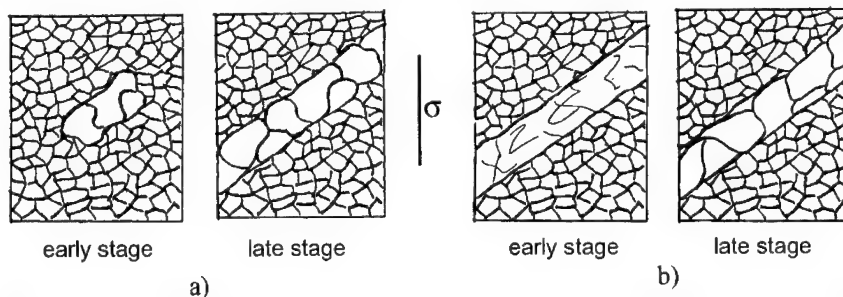
Figure 10. *Alternative scenarios of formation of large-scale fatigue shear bands with coarsened microstructure. Stress axis vertical. a) Local grain/subgrain coarsening spreading out, forming a shear band. b) Catastrophic extended shear band, caused by "strain-path change", with subsequent formation of coarsened microstructure in the shear band.*

MICROSTRUCTURAL PROCESSES AND GOVERNING FACTORS OF CYCLIC SOFTENING AND GRAIN/SUBGRAIN COARSENING

First, it must be noted that, while it is not always clear whether the initial UFG microstructure is predominantly a very fine-scaled grain or a subgrain structure [1,2], the grain/subgrain boundaries in the as-ECAP-processed state must be viewed as non-equilibrium boundaries [2] of relatively high energy. Moreover, the extraordinary strength of UFG-materials stems not only from a reduced grain size but, more generally, from a very high defect (dislocation) content. Thus, there is a strong driving force to reduce the overall energy by reducing the dislocation content by processes of dislocation annihilation, by converting the non-equilibrium boundaries into structures that are closer to equilibrium and by reducing their total area. The latter is only possible by dynamic grain/subgrain coarsening (or even dynamic recrystallization), involving the motion of grain/subgrain boundaries. At the same time, processes of dislocation annihilation will occur. The combined effect of the processes mentioned will result in cyclic softening.

Cyclic Softening by Annihilation of Dislocations

Following Essmann and Mughrabi [20], the differential change of dislocation density $d\rho$ occurring in a particular glide system in an interval of shear strain $d\gamma$ can be written as:

$$d\rho/d\gamma = 2/b \cdot L - 2y \cdot \rho/b, \qquad (1)$$

where b is the modulus of the Burgers vector, L the dislocation glide path which is usually a function of the shear strain γ, and y is the so-called annihilation distance within which two dislocations of opposite sign on neighbouring glide planes can just annihilate. The first term describes the rate of production of dislocations and the second term the rate of annihilation. The annihilation distance y depends on the dislocation character. In the case of screw dislocations, easy cross slip, especially in materials of low friction stress [20], facilitates annihilation. The annihilation distance becomes larger with increasing temperature, implying that, in general, cyclic softening will be more pronounced at higher temperatures. Conversely, there will be less softening at lower temperatures.

In single-phase materials, the susceptibility to cyclic softening is generally related to the ease of cross slip. Hence, cyclic softening is more pronounced in wavy-slip than in planar-slip materials. However, in precipitation-hardened materials with shearable precipitates, another type of localized damaging planar-slip mode is induced through cyclic strain localization in persistent slip bands in which the precipitates are destroyed more or less completely. This kind of localized planar slip leads to severe cyclic softening and should not be confused with the planar slip in single-phase materials in which cyclic softening can occur only to a limited extent.

When one considers cyclic softening of ECAP-processed UFG-material, it is important to note that, since subsequent cyclic deformation corresponds to a strain-path change, the active slip systems will usually differ from those that were operating during ECAP. However, dislocations produced on a certain glide system during ECAP can only be eliminated, i.e. annihilated, efficiently during subsequent cyclic deformation, if that particular slip system operates actively. Therefore, UFG-materials having crystal structures with many slip systems sharing the production and annihilation of dislocations should be less prone to cyclic softening. On the other hand, UFG titanium with its hexagonal close-packed crystal structure and only a limited number

of slip systems has been shown to be cyclically stable at room temperature [18], whereas face-centred UFG copper with its many more slip systems is not. The reason probably is that room temperature is a much lower homologous temperature (0.15) for titanium than for copper (0.2).

To summarize this section, it is concluded that factors which stabilize cyclic deformation by impeding cyclic softening caused by annihilation of dislocations are difficult cross slip, a high friction stress, crystal structures with many slip systems and low homologous temperatures.

Cyclic Softening by Dynamic Grain/Subgrain Growth and Coarsening

As a general introductory remark, it is noted that, since foreign atoms retard both dislocation motion and grain growth, less pure materials or solid solution alloys with a high friction stress can be expected to be more resistant against grain/subgrain coarsening. Next, it is of interest to discuss in the context of dynamic grain/subgrain coarsening the factors governing the mobility of grain/subgrain boundaries at rather low homologous temperatures ($\lesssim 0.2$). In a number of papers by Langdon and co-workers [23,24] and by Gottstein and co-workers [25,26], it was shown that, during high-temperature fatigue, grain boundary displacements of several microns per cycle, leading to coarsening of the grain structure, occurred in a number of different metals investigated. While these studies were all performed at homologous temperatures of 0.5 or higher, it is nevertheless inferred that, at lower temperatures, grain boundary migration with correspondingly smaller displacements must be considered as a possible process, especially in metastable microstructures. It is well known that, during cyclic deformation, vacancies are produced [27,28]. In this context, a model put forward by Estrin et al. [29] is of particular interest. In the model, the vacancies act as an inhibiting factor, leading to a decrease in the grain growth rate. On the other hand, the authors conclude that there exists a (temperature-dependent) "limiting stable grain size" above which grain growth uninhibited by vacancies is possible. In conjunction with the observation that dynamic grain/subgrain coarsening occurs during the cyclic deformation of UFG-materials at homologous temperatures as low as 0.2, the results discussed here suggest that a) grain/subgrain boundary migration is possible down to rather low homologous temperatures and that b) the grain/subgrain size of ECAP –processed UFG-material exceeds the limiting stable grain size defined by Estrin et al. [29]. Thus, an enhancement of the cyclic stability of UFG structures would be expected for less pure materials or for alloys with very small grain/subgrain sizes below the stable limiting size and at low homologous temperatures ($\lesssim 0.2$).

SOME CONCLUSIONS AND SOME CRITERIA FOR THE DESIGN OF FATIGUE-RESISTANT UFG-MATERIALS

In the first review of the cyclic deformation and fatigue behaviour of UFG-materials [3], some areas of future research which are still relevant today were formulated in the concluding section. Since then, some progress has been made. While, at first sight, the fatigue performance of UFG-materials was not always as impressive as expected or desired, deeper insight has been achieved, as more data on different UFG-materials became available. Thus, it is now possible to define better the microstructural requirements for the design of fatigue-resistant ECAP-processed UFG-materials. In particular, the following points are noted:

1) The number of different UFG-materials whose fatigue properties have been studied is increasing steadily.
2) Cyclic stress-strain data of some UFG-materials are now becoming available. There is, however, still a lack of systematic studies at different temperatures.
3) It is commonly observed (and understood) that UFG-materials exhibit enhanced fatigue strengths in a Wöhler (S-N) plot but not in a Coffin-Manson diagram. However, recent work shows that, by the application of a suitable annealing treatment, improved fatigue properties, displayed in a Coffin-Manson plot, can be achieved in some cases.
4) The stability of the heavily predeformed UFG microstructure under conditions of cyclic deformation depends on several factors. Desirable features with respect to the design of fatigue-resistant UFG-materials are considered to be
   - less pure materials or alloys (with a high friction stress),
   - a planar slip mode,
   - crystal structures with a larger number of slip systems,
   - a small UFG grain/subgrain size below the "stable limiting size" and
   - a rather high melting point in order to ensure that, when UFG-materials are subjected to fatigue, the ambient temperature corresponds to a low homologous temperature ($\lesssim 0.2$).

Similar considerations should apply also to microstructural stability under other conditions of loading than cyclic deformation.

ACKNOWLEDGMENTS

REFERENCES

1. T.C. Lowe and R.Z. Valiev, eds., *Investigations and Applications of Severe Plastic Deformation*, (Kluwer Academic Publishers, 2000).
2. R.Z. Valiev, R.K. Islamgaliev and I.V. Alexandrov, *Progr. in Mater. Sci.*, **45**, 103 (2000).
3. H. Mughrabi, in *Investigations and Applications of Severe Plastic Deformation*, eds. T.C. Lowe and R.Z. Valiev (Kluwer Academic Publishers, 2000) p. 241.
4. A.W. Thompson and W.A. Backofen, *Acta metall.*, **19**, 597 (1971).
5. A. Vinogradov, Y. Kaneko, K. Kitagawa, S. Hashimoto and R. Valiev, *Mater. Sci. Forum*, **269-272**, 987 (1998).
6. S. Hashimoto, Y. Kaneko, K. Kitagawa, A. Vinogradov and R.Z. Valiev, *Mater. Sci. Forum*, **312-314**, 593 (1999).
7. S.R. Agnew and J.R. Weertman, *Mater. Sci. Eng. A*, **244**, 145 (1998).

8. S.R. Agnew, A. Yu. Vinogradov, S. Hashimoto and J.R. Weertman, *J. Electron. Mater.*, **28**, 1038 (1999).
9. M. Brunnbauer, Diplomarbeit, *Dauerschwingverhalten und Schädigung von ultrafeinkörnigen (UFG) Kupfervielkristallen*, Universität Erlangen-Nürnberg (1999).
10. H.W. Höppel, M. Brunnbauer, H. Mughrabi, R.Z. Valiev and A. Zhilyaev, in *Proc. of Materialsweek 2000*, Munich, WILEY-VCH, in press, and unpublished work.
11. M. Falkner, Diplomarbeit, *Zyklische Verfestigung und Ermüdungslebensdauer unterschiedlicher metallischer Werkstoffe bei Temperaturen zwischen –100°C und +150°C*, Universität Erlangen-Nürnberg (1997).
12. R. Wang, Doctorate Thesis, *Untersuchungen der mikroskopischen Vorgänge bei der Wechselverformung von Kupferein- und -vielkristallen,* Universität Stuttgart (1982).
13. H. Mughrabi and R. Wang, in *Basic Mechanisms in Fatigue,* eds. P. Lukáš and J. Polák (Academia, Prague, and Elsevier Science Publ. Co., 1988) p. 1.
14. A. Vinogradov, S. Nagasaki, V. Patlan, K. Kitagawa and M. Kawazoe, *Nanostruc. Mater.*, **11**, 925 (1999).
15. P. Lukáš and L. Kunz, *Mater. Sci. Eng.*, **85**, 67 (1987).
16. E. Thiele, J. Bretschneider, L. Hollang, N. Schell and C. Holste, in *Investigations and Applications of Severe Plastic Deformation*, eds. T.C. Lowe and R.Z. Valiev (Kluwer Academic Publishers, 2000) p. 173, and unpublished results.
17. V. Patlan, A. Vinogradov, K. Higashi and K. Kitagawa, *Mater. Sci. Eng. A*, in press.
18. A. Yu. Vinogradov, V.V. Stolyarov, S. Hashimoto and R.Z. Valiev, submitted to *Acta mater.*
19. A. Yu. Vinogradov, personal communication (2000).
20. U. Essmann and H. Mughrabi, *Phil. Mag. A*, **40**, 731 (1979).
21. C.E. Feltner and C. Laird, *Acta metall.*, **15**, 1631 (1967) and **15**, 1633 (1967).
22. A.B. Witney, P.G. Sanders, J.R. Weertman and J.A. Eastman, *Scripta metall.*, **33**, 2025 (1995).
23. T.G. Langdon and R.C. Gifkins, *Scripta metall.*, **13**, 1191 (1979).
24. V. Raman and T.G. Langdon, *J. Mater. Sci. Letters*, **2**, 180 (1983).
25. S. Weiss, D. Ponge and G. Gottstein, *Can. Metall. Quart.*, **34**, 237 (1995).
26. S. Weiss and G. Gottstein, *Mater.Sci. Tech.*, **14**, 1169 (1998).
27. J. Polák, *Czech J. Phys. B*, **19**, 315 (1969).
28. U. Essmann, U. Goesele and H. Mughrabi, *Phil. Mag. A,* **44**, 405 (1981).
29. Y. Estrin, G. Gottstein, E. Rabkin and L.S. Shvindlerman, *Scripta mater.*, in press.

Effect of Grain Size Distribution on Tensile Properties of Electrodeposited Nanocrystalline Nickel

Fereshteh Ebrahimi, Zunayed Ahmed and Kristin L. Morgan
Materials Science and Engineering Department, University of Florida, Gainesville, FL 32611

ABSTRACT

We have produced dense and ductile nanocrystalline nickel with various grain size distributions using electrodeposition techniques. The strength of the nickel deposits fell within the scatter band of the general Hall-Petch curve for nickel. However, large variations in yield strength, strain hardening rate and tensile elongation were associated with a relatively small change in the average grain size. The scatter in the elongation data has been attributed to the formation of nodules and the presence of voids. The variations in strength and strain hardening rate have been shown to be associated with the changes in the grain size distribution. A model based on confined dislocation motion and composite behavior has been developed for predicting the stress-strain behavior of the nanocrystalline nickel.

INTRODUCTION

Figure 1 shows the flow stress of nickel as a function of $d^{-1/2}$, where d is the average grain size. A linear relationship indicative of the Hall-Petch relationship may be recognized in this plot (slope $\cong$ 7,000 MPa nm$^{1/2}$). However, there is a large scatter in the data. Many sources contribute to this scatter. The flow stress values shown in Figure 1 represent hardness (flow stress = hardness/3), strength at 1% plastic strain and ultimate tensile strength (UTS) for specimens with a low ductility [1]. Since ultra-fine grained metals (d<1μm) show a high strain hardening rate the inconsistency in defining the flow stress contributes considerably to the scatter. Another important contributing factor is the synthesis method. The main techniques for fabrication of metals with ultra-fine grains are inert gas condensation (ICG), sever plastic deformation and electrodeposition. The defect type (e.g., impurities, second-phase particles, voids, twins) and content and the presence of crystallographic texture are dependent on the fabrication method. For example, in the case of electrodeposited nanocrystalline nickel, the UTS values measured by Erb and his co-workers [2] are much smaller than the strength values predicted from their hardness data. They [3] add considerable amounts of saccharin as a grain refiner in order to decrease the grain size of nanocrystalline nickel below 40nm. The decrease in the UTS observed with grain refinement [2], is possibly associated with the increase in the sulfur content of their deposits. The uncertainty in the grain size measured can

Figure 1. *Hall-Petch plot for nickel [1].*

also contribute significantly to the scatter in the Hall-Petch curve. For example, Sanders et al. [4] have shown that the analysis method and the choice of the x-ray diffraction (XRD) peak influence the evaluated grain size of metallic nanocrystals considerably.

As shown in Figure 1, there are limited data for nanocrystalline nickel with a grain size less than 40nm. Furthermore, the existing data are predominantly measured by hardness testing and those measured in tension are from samples with a low ductility. In order to validate the results of modeling of stress-strain curves in nanocrystalline metals ductile samples with relatively pure boundaries are needed. The purpose of this research was to fabricate ductile nanocrystalline nickel by electrodeposition techniques without using grain refining additives. In this investigation the grain size of deposits is characterized with both XRD and transmission electron microscopy (TEM) methods. The strength is evaluated by tensile testing and the stress-strain curves are compared with theoretical modeling.

EXPERIMENTAL PROCEDURES

A conventional rotating disc set-up was employed for the deposition of nickel specimens. The substrate was an annealed copper disc with a 35mm diameter. The counter electrode was a 10×10 cm^2 platinum foil. A sulfamate-based electrolyte was used at 30°C. Nickel was deposited galvanostatically using a PAR273 potentiostat/galvanostat, which was interfaced with a computer for control and data acquisition purposes. The potential was measured against a saturated calomel electrode (SCE). The grain size was varied by changing the current density, deposition technique (direct versus pulse plating) and hydrodynamic conditions. The thickness of the deposits was approximately 25 μm. Tensile testing, XRD, TEM and scanning electron microscopy (SEM) were employed for characterizing the free-standing deposits. The tensile tests were conducted using dog-bone specimens with a gage length of 10mm. Details of these procedures are given elsewhere [1].

RESULTS

Figure 2 presents tensile stress-strain curves for four deposits whose properties are given in Table I. The grain size was measured from x-ray results using both Single Line (SL) and

Table I. A summary of the average grain size measured by various techniques and the strength of nanocrystalline nickel samples produced by electrodeposition methods.

Sample			1	2	3	4
d (nm), XRD	sub	WA	34.9	-	28.2	15.6
		SL	85.1	-	87.5	15.2
	sol	WA	17.1	-	16.3	11.8
		SL	29.5	-	26.6	13.4
d (nm), TEM			30.8	29.9	27.4	25.9
$\sigma_{0.2\%}$ (MPa)			667	895	913	1162
$\sigma_{1\%}$ (MPa)			1062	1274	1293	1525
σ_{UTS} (MPa)			1300	1332	1328	1696
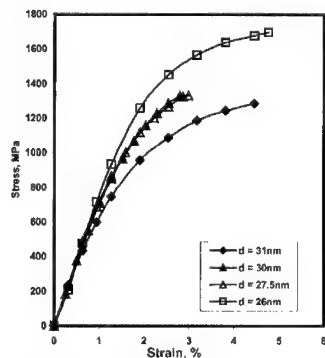
Figure 2. *Tensile stress-strain curves of electrodeposited nanocrystalline nickel samples.*

Warren-Averbach (WA) methods. The SL analysis was performed on the (200) peak and the (200) and (400) peaks were used for the WA analysis. The grain size measurement was conducted on both the solution and the substrate sides of each deposit. In electrodeposits, the grain size varies through the thickness of samples. For deposits with a grain size in the nano-range the crystallite size is larger on the substrate side [5]. The change of the grain size usually occurs within the first few micrometers from the substrate side and therefore, the grain size measured on the solution side is a better representation of the average grain size of thick deposits. Here (see Table I) also we see that both analysis methods measure a larger grain size on the substrate side. In general, the SL method results in larger grain size measurements. The difference between the results obtained by the WA and SL methods seems to increase with the grain size. The average grain sizes measured from the dark field images produced using the TEM technique are comparable with the SL results obtained from the solution side of samples 1 and 3, but significantly larger for sample 4. The smaller grain size measured by the XRD methods is partially due to the fact that both the high angle and low angle boundaries are counted. However in our TEM analysis we considered only the high angle boundaries. Another source of discrepancy is the variation of grain size through the thickness of deposits, which is not included in the results obtained from the planar TEM specimens analyzed in this study.

The flow stress ($\sigma_{1\%}$) varied in the 1100 to 1500 MPa range for a change in the $d^{-1/2}$ from 0.18 to 0.2 $nm^{-1/2}$. This result is within the scatter band of the general Hall-Petch curve presented in Figure 1. However, as shown in Figure 3, the results of this study can be fitted to a curve with a much larger slope ($\cong$ 30,000 MPa $nm^{-1/2}$). It has been recognized that the grain size distribution plays an important role in strengthening of nanocrystalline materials [6]. The significant increase in the strength with a small decrease in the average grain size observed in this study is attributed to the associated change in the grain size distribution. The grain size distributions obtained by TEM are presented in Figure 4. Note that sample 1 with a large average grain size has a wider grain size distribution than sample 4, which has a smaller average grain size. Also a comparison of the crystallite size on the substrate side with that on the solution side (see Table I) reveals that sample 4 has a more uniform grain size through its thickness.

All tensile specimens fractured in a ductile manner as represented by the knife- edge fracture
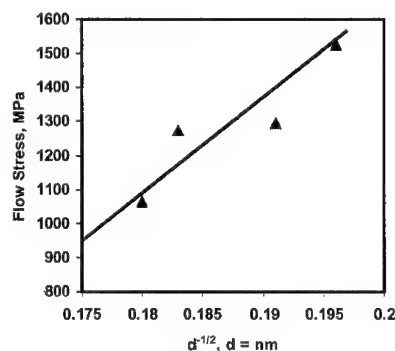
Figure 3. *Hall-Petch curve for the samples produced in this study.*
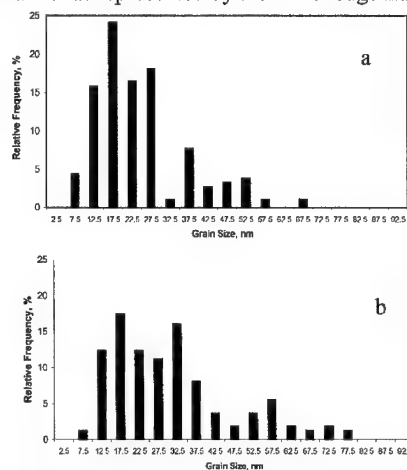
Figure 4. *Grain size distribution in sample (a) 4 and (b) 1.*

behavior shown in Figure 5a. Fracture by the microvoid coalescence mechanism, as shown in Figure 5b, is believed to be associated with the presence of nano-size pores in the deposits that act as the void initiation sites [7]. The low tensile elongation of samples 2 and 3 was found to be due to the formation of isolated areas with nodules as shown in Figure 6. Nodules appear as surface roughness and the columnar growth associated with them is responsible for the observed brittleness. As can be seen in Figure 6b, the crack follows an inter-columnar path.

(a)   (b)
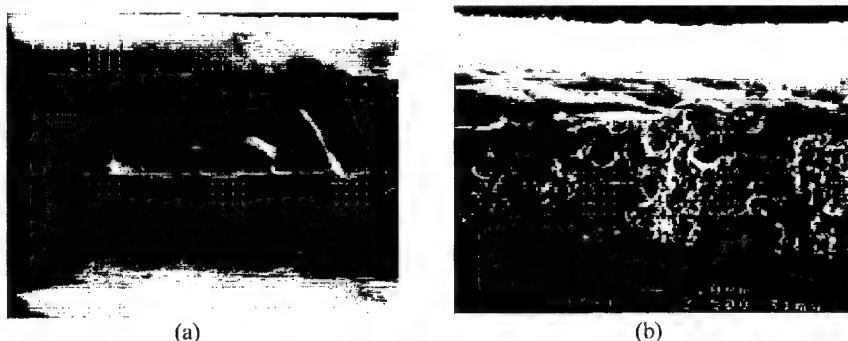
Figure 5. *SEM fractographs showing (a) the knife-edge fracture behavior in sample 1 and (b) the microvoid coalescence fracture mechanism in sample 4.*

(a)   (b)

Figure 6. *SEM micrographs showing (a) the nodular growth in an isolated area and (b) the brittle fracture associated with nodular growth in sample 3.*

Figure 7 presents the strain-hardening rate as a function of strain for samples 1 (d=31nm) and 4 (d=26nm). These samples showed extremely high initial strain hardening rates typical of composite materials. Furthermore the strain-hardening rate increased with a decrease in grain size. These observations are contradictory to the predictions made by the deformation models based on creep mechanisms [8], however they are consistent with the micro-mechanical modeling based on a composite behavior [6]. Mitra et al. [6] have calculated the stress-strain curve of nanocrystalline copper based on a deformation model for two-phase materials. The critical stress for plastic deformation was taken as the stress required for a dislocation to move through the forest of dislocations located at grain boundaries ($\tau_C = \alpha Gb/(d)^{1/2}$, where G is the
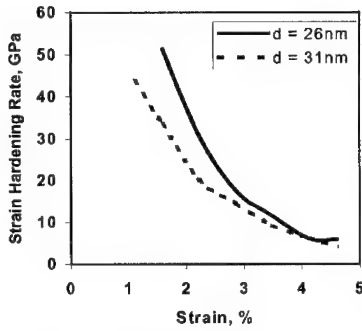
Figure 7. *Strain hardening rate as a function of strain.*

shear modulus, b is the burgers vector and α is a constant). Their theoretical calculations for copper indicate that for a given average grain size, a tighter grain size distribution results in a higher strain-hardening rate. However, their theoretical predictions could not be validated due to a lack of experimental results for ductile nanocrystalline copper.

We have assumed that the plastic deformation of nanocrystalline nickel is controlled by the confined motion of dislocations that are pinned by the grain boundaries. The tensile stress required for moving a dislocation in a grain is given as [9]:

$$\sigma_i = M\tau_i = M\{(Gb/\pi d_i)\ln(d_i/b)\}\cos\theta \qquad (1)$$

Here M is the Taylor factor (for FCC metals $M \simeq 3.1$). The pinning angle, θ, depends on the nature of the boundaries as well as the nature of the dislocation. We have assumed that the pinning angle is $55°$ ($\cos\theta = 0.568$) for all grain sizes. Since the stresses achieved in our samples are well below the stress required for balancing the stacking fault energy (γ_{SFE}) in nickel ($\gamma_{SFE}/b = 320 / 0.14385 = 2224$ MPa), we have considered the motion of perfect dislocations rather than partial dislocations. At a given stress level, the plastic strain, ε_p, was calculated as:

$$\varepsilon_p = \gamma/M = (1/M)(bNA/V) = (b/M)\{[\textstyle\sum_{(PD)} N_i(\pi d_i^2/4)]/[\sum_{(all)} N_i(\pi d_i^3/6)]\} \qquad (2)$$

where γ is the shear strain, N is the total number of dislocations, A is the total area swept by dislocations, V is the total volume and PD stands for "Plastically Deformed". Here it is assumed that grains are spherical and the area swept is a circle with a diameter equal to the grain size. The number of dislocations activated in grains with diameter d_i, N_i, was estimated as:

$$N_i = (n_i)(m_i)(m_i/2) \qquad (3)$$
$$m_i = [\pi(\sigma/M) d_i]/(Gb) \qquad (4)$$

Here n_i is the number of grains with diameter d_i and m_i is the number of dislocations that can be accommodated on a given slip plane in the absence of a pile-up. However, in a given grain many parallel slip planes can be activated. The number of these activated slip planes is controlled by the interaction of dislocations on adjacent planes. The spacing between the parallel slip planes was approximated as the distance between dislocations in a given slip plane. Therefore, the m_i value was also taken as an estimate of the number of parallel slip planes activated. The factor $m_i/2$ represents the swept area multiplier. For example, when there are four dislocations on a slip plane ($m_i = 4$), they will be separated by a distance equivalent to d/3, which corresponds to one dislocation traversing the whole grain area, A_i, the second dislocation $(2/3)A_i$, the third dislocation $(1/3)A_i$ and the fourth dislocation just coming out of a grain. Therefore, the total area swept is $2A_i$ when $m_i = 4$. The nanocrystalline microstructure was considered to consist of plastically and elastically deforming grains, which follow the rule of mixture as follows:

$$\sigma = \sigma_{PD}V_{PD} + \sigma_{ED}(1-V_{PD}) \qquad (5)$$

Here σ_{PD} is the stress carried by the plastically deforming grains, V_{PD} is the volume fraction of plastically deforming grains and σ_{ED} is the stress carried by the elastically deforming grains. The criterion for plastic deformation is given by Equation 1. We have considered two scenarios for the composite effect. In one scenario the fraction of the undeformed grains is calculated such that
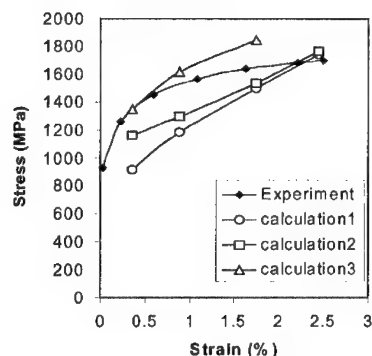
Figure 8. *Experimental and theoretical predictions of stress-strain curve for sample 4.*

no grain is loaded beyond its critical stress for yielding (calculation 2). In the other scenario the fraction is calculated such that elastic grains deform as much as the average strain resulting from the plastically deforming grains (calculation 3). The results of our modeling are compared with experimental results in Figure 8. The calculation 1, in which the contribution of elastically deforming grains to the total stress has been ignored, predicted a low yield strength. The best match was obtained with the equal strain model (calculation 3). The predicted strain-hardening rate is high in all three calculations suggesting that either more dislocations, i.e. larger than the number estimated based on Equation 3, become activated or other deformation mechanisms should be considered. It is acknowledged that a true deformation mechanism must include the dislocation velocity and thermally activated processes.

SUMMARY

We have produced ductile nanocrystalline nickel with average grain sizes between 31 to 26nm using electrodeposition techniques. In the absence of defects such as nano-pores and nodules, the samples fractured by the knife-edge mechanism. These samples showed a very high strain-hardening rate that increased with the tightness of the grain size distribution as well as a decrease in the average grain size. An attempt in modeling the strain hardening behavior of the nanocrystalline nickel revealed that recovery mechanisms in addition to increases in the number of slip systems activated and the fraction of plastically deforming grains should be considered.

ACKNOWLEDGMENT

REFERENCES

1. Z. Ahmed, "Synthesis and Deformation of Nanocrystalline Nickel," Master thesis, University of Florida, (2000).
2. N. Wang, Z. Wang, K. T. Aust and U. Erb, *Mater. Sci. Eng.*, **253**, 150 (1997).
3. A. M. El-Sherik and U. Erb, *J. Mater. Sci.*, **30**, 5743 (1995).
4. P. G. Sanders, A. B. Witney, J. R. Weertman, R. Z. Valiev and R. W. Siegel, *Mater. Sci. Eng.*, **204**, 7 (1995).
5. F. Ebrahimi, G. R. Bourne, M. S. Kelly and T. E. Matthews, *Nanostructured Materials*, **11**, 343 (1999).
6. R. Mitra, T. Ungar, T. Morita, P. G. Sanders, and J. R. Weertman, The 1999 J. R. Weertman Symposium, ed. P. K. Liaw et al., TMS Publication, Warrendale, PA, 553 (1999).
7. F. Ebrahimi, Q. Zhai and D. Kong, *Scripta Materialia*, **39**, 315 (1998).
8. H. S. Kim, Y. Estrin and M. B. Bush, *Acta mater.*, **48**, 493 (2000).
9. J. D. Embury and J. P. Hirth, *Acta metall. mater.*, **42**, 2051 (1994).

Mechanical Properties of Nanocrystalline Ni in Relation to its Microstructure

F. Dalla Torre[1], H. Van Swygenhoven[1], M. Victoria[2], R. Schaeublin[2], W. Wagner[1]
[1]Paul Scherrer Institut, SWITZERLAND;
[2]EPFL Lausanne, Dept. of Fusion Technology CRPP, SWITZERLAND.

ABSTRACT

Mechanical properties of nanocrystalline Ni made by Inert Gas Condensation and Electrodeposition are presented in relation to their microstructure. Significant plasticity is only observed at elevated temperatures for both types of nanocrystalline Ni. However, a higher temperature is needed in the Inert gas condensated material. Careful analysis of the microstructure by means of X-ray diffraction and conventional electron microscopy reveal initial differences in as-prepared samples. The change in microstructure during deformation at elevated temperatures and during heat treatment without external load is investigated and information about the deformation mechanisms is reported.

INTRODUCTION

Because nanocrystalline samples are usually very small, research on mechanical properties has concentrated mainly on measurements of hardness as function of grain size. Results at the smallest grain sizes remain controversial: some results even indicate a yield stress independent of the grain size, or a reverse Hall-Petch relation and others confirm an increasing yield stress with decreasing grain size [1, 2]. It has however been shown that sample imperfections and microstructure play a key factor in these controversial results [3]. Mechanical properties for larger amounts of submicrocrystalline (produced by Severe Plastic Deformation (SPD) [4]) and nanocrystalline (produced by Electrodeposition (ED) [5]) materials have been studied by means of stress-strain curves at room temperature and higher temperatures, where diffusion controlled mechanism become dominant. Superplasticity has been observed in ED Ni, having an initial mean grain size of 35nm, at temperatures above 280°C. The plasticity is accompanied by rapid grain growth [6].
Recently a tensile machine has been developed allowing tensile testing of tiny dog-bone shaped samples with a gauge length of only 300 microns [7]. This allows samples synthesised with techniques producing only very small amount of material, such as Inert Gas Condensation (IGC), to be used for tensile testing. In the present work we use a similar miniaturised tensile machine to deform nanocrystalline Ni synthesised by IGC and ED. The initial microstructure and influence of deformation and/or temperature on the microstructure are reported and compared for both materials.

EXPERIMENTAL PROCEDURE

Nanocrystalline Ni samples prepared by ED (supplied by Goodfellow Ltd.) and by IGC are investigated. For preparing the IGC samples, a high vacuum chamber of 2×10^{-7} mbar was filled with 3 mbar of high-purity (99.999%) helium. High-purity nickel (99.99+%) wire was evaporated from resistively heated tungsten boats, with the resulting metal clusters collected on a

liquid nitrogen-cooled finger. The clusters were removed from the cold finger with a copper scraper and then compacted under uniaxial pressure at 2 GPa and 500°C for 6 hours to produce disk-shaped samples of 8 mm diameter and 0.2 -0.3 mm thickness.

A new tensile machine was designed for testing small 3 mm long specimens. The specimens, having a gauge length of 1.72 mm and a thickness of 0.2 to 0.25 mm were machined by a wire Electro- Discharging- Machine. Due to local grain growth at the machined surfaces, specimens were afterwards electropolished for 45 sec in 3% Perchloric acid, 30 % Ethylenglycol and 67% Methanol at 15 V and −10°C. Each specimen was then checked by scanning electron microscopy to rule out possible machining artefacts on the samples. Typically, large surface grains were no longer observed.
In order to have free access to the gauge length of the specimen and to provide fast heating rates, a resistive heating device was chosen. Heat was measured via a Pyrometer, where the minimal measuring spot size was in the order of the cross section of the gage length. A high temperature gradient of up to 50°C leading to local deformation on the gauge length has always to be taken into account in the interpretation of any results. The force controlled actuator (a magnetic coil) provides a force resolution of 8 mN, which is within the resolution range of the load cell. Type 304 stainless steel of normal grain size was used to show good agreement with conventional tensile testing.

Densities of the samples were measured via Archimedes principle with a Mettler microgram balance. Diethylphthalate with a density of 1.1175 g/cm^3 was used as a reference liquid. X-ray measurements were made with a Siemens D500 X-ray detector and mean grain size was determined using the Scherrer formula after Krill et al [8]. Conventional TEM investigations were made with a Jeol 2010 operated at 200kV. Specimens were mechanically prethinned and then electropolished with the above mentioned solution. Tested tensile specimens were prethinned with a tripod to wedgeshape like samples and afterwards bombarded by argon ions in a Gatan Duo Mill - Series 600.

RESULTS

Density measurements of the samples showed almost full density (99.3%) for the ED samples and an impurity content of about 0.5% composed of sulfur and carbon [9]. For the IGC samples densities of 96% - 98% were measured and wet chemical analysis showed up to 6% impurities (H, O, N) [10]. X-ray measurements of IGC samples showed mean grain sizes of 23 nm over four samples with a standard deviation of 4 nm and with strains of 0.12 ± 0.02 % for the <111>/<222> family of planes. The ED Nickel exhibited a mean grain size of about 18 nm and a high internal strain of the order of 0.4% for <111>/<222> planes. TEM results of ED samples showed a slightly higher grain size. Some bigger grains, up to 40-60 nm were observed, some of them showing twinning (~ 5%). Because of high strain fields in some grain aggregates (Fig.1(a)) visualised by the bowed Moiré fringes observed in TEM, single grains were difficult to distinguish. Selected area diffraction (SAD) patterns (Fig.1(a)) confirm the high strain in the sample by the presence of ellipsoidal spots. The SAD pattern reveals also the presence of texture along the <111> planes. The preferential orientation can also be observed in the bright field image by the little contrast between grains (Fig.1(a)). Texture was only observed at higher magnification in SAD patterns of areas of 0.05 to 0.5 microns diameter. In summary, the initial

microstructure of the ED samples shows local regions of mainly small angle grain boundaries, that are confined by high angle grain boundaries. The textured regions are small in size so that no texture can be detected by X-ray diffraction.

TEM analysis of IGC samples showed grain sizes between 20 to 100 nm with a typical size of 30 nm. The grains are randomly oriented and no texture can be observed even at high magnification (Fig.1(b)). Clear distinct spots in the SAD pattern indicate less strained grains. About 10 % of the grains could be counted as twinned by tilting the specimen.
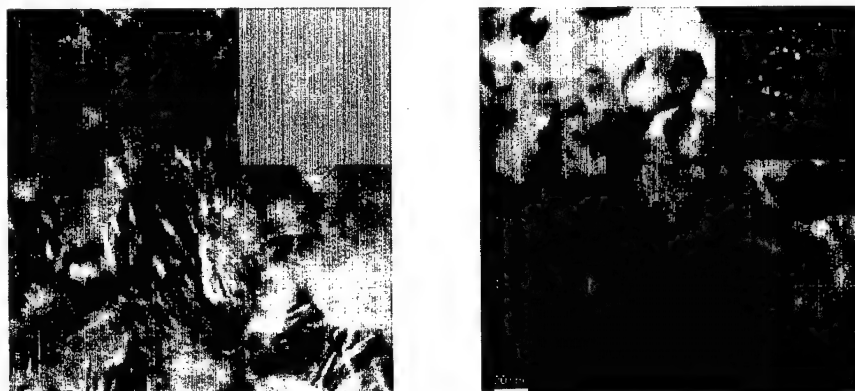
Figure 1.(a) and (b). Bright field images with its SAD patterns of the as received samples for ED Nickel (a) and IGC Nickel (b). The sizes of the SAD patterns are approximately 150 to 200 nm. In ED high strain is visible by the bowed Moiré fringes. IGC Ni shows much less strain with mostly distinct high angle grain boundaries.

TENSILE TESTS

Figure 2 (a) and (b) show the stress-strain curves for respectively the ED and the IGC samples at different temperatures and a strain rate of 10^{-4} s^{-1}. At room temperature little plasticity with ductile fracture surfaces is observed in the ED samples, whereas the IGC broke in a brittle manner in the elastic region, probably due to the propagation of microcracks along the pore volume. In both types of material, a transition temperature from little plasticity and high flow stress to significant plasticity at low flow stress can be observed. In the ED samples the transition temperature is between 250 and 280°C. The transition temperature for the mechanical behaviour agrees with the onset temperature for instantaneous grain growth, as described in Wang et al. [11] and will be discussed in the next paragraph. The curve at 250°C shows irregular deformation behaviour. Temperature fluctuations, which are of the order of ±20°C with this type of heating system, might be the reason of the irregular behaviour, since 250°C is about the transition temperature. Maximal strain of about 50% is reached at 320 and 400°C.

The tensile curves for the IGC samples in figure 2(b) show a similar change in plastic behaviour, although at a much higher onset temperature. No plasticity was observed below 400°C . The onset temperature for significant plasticity starts at about 500°C. Compared to the ED samples, maximal strain to failure is lower with 14% strain at 600°C.

Further tensile experiments showed that the yield stress is dependent on the strain rate and is increasing as strain rate increases.

a)

b)
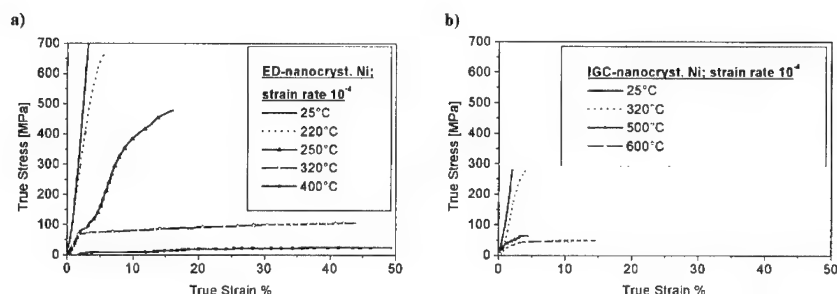
Figure 2(a) and (b). Stress strain curves at a strain rate of $10^{-4} s^{-1}$ for various temperatures for ED Ni and IGC Ni.

ANNEALING EXPERIMENTS

In order to better understand the above tensile curves, annealing experiments on 3 mm TEM discs were performed, to study the influence of temperature without deformation on the microstructure. We compared the microstructure at annealing times of 30 sec., the elapsed time in the tensile machine prior to load, as well as the total time of the deformation experiment, i.e. the time until failure.

After annealing an ED sample during only 30 sec. at ~300°C , just above the transition temperature to high plasticity, the ED sample showed huge almost instantaneous grain growth (Fig.3(a)). Grain growth can be described as abnormal in the sense of preferential growth of few grains to a grain of 0.5 microns size, while the surrounding small nanosized grains still show the original features.
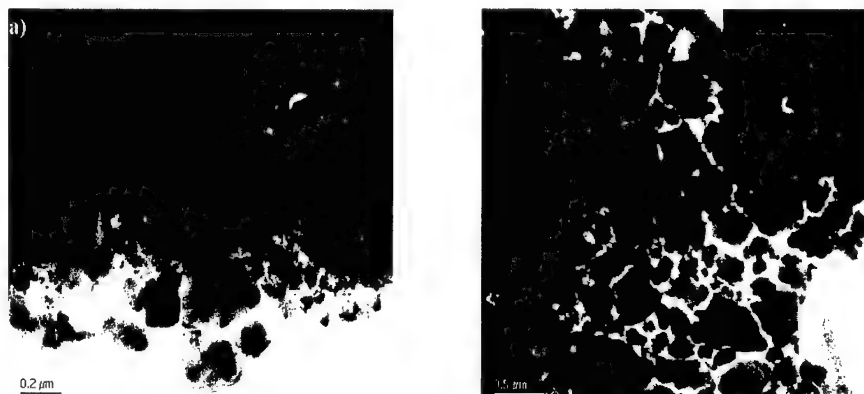
Figure 3 (a) and (b). Bright field images with its SAD patterns having approximately the same size as that in the micrograph of ED Ni after annealing at ~300°C during 30 sec.(a) and during 15 min. showing abnormal grain growth. 3(a) shows big grains surrounded by nanosized grains, while after 15 min. (3(b)) all the nanosized grains are consumed by the big grains.

Further annealing for ~15 minutes at ~300°C shows a continuous evolution of the matrix of the small grains, finally ending in a microstructure with grain sizes ranging between 0.2 and 2

microns (Fig.3(b)). Wang et al. [11] explained the abnormal growth by preferential enhanced grain growth in regions with small misorientation angles between adjacent grains. In our ED samples, similar regions of grains with preferred crystal orientations, which have small misorientation angles, have been observed.

Annealing of IGC specimens for 30 sec. at ~300°C showed a similar broad grain size distribution as before annealing with a mean grain size of about 60 nm. A homogenous increase in grain size of about 30 nm reveals a normal grain growth. Although, heating for 15 minutes at the same temperature shows huge grain growth with grains of up to 3 microns together with groups of nanosized grains. That less grain growth at 300°C for 30 sec. is observed for IGC samples compared to ED ones could be possibly due to the presence of impurities in the grain boundaries, which can pin the boundaries. Annealing during 1 min. at 600°C, the temperature needed for significant plasticity, showed instantaneous grain growth. The microstructure consists of micron sized (0.5-2 microns) and nanosized grains, which is similar to the 300°C ED sample. The big grains are however in contact with each other and nanosized grains are mainly grouped locally together (Fig.4(a)).

Figure 4.(a) and (b). Bright field images of IGC Ni after annealing at 600°C during 1min. (a) and during 15 min. Both time and temperature correspond to the beginning and end point, where significant plasticity was measured. 4(a) shows big grains in contact with each other and nanosized grains locally distributed; 4(b) shows micron sized grains after 15 minutes annnealing, at the grain boundaries voids indicated by the arrow are eventually filled with gas.

After annealing at 600°C during 15 minutes , grains have grown to sizes between 0.5 and 3 microns and no nanosized grains could be detected (Fig.4(b)). Voids located at the grain boundaries which eventually fills with gas [12], indicate a migration of free volume and/or trapped inert gas to the grain boundaries during heat treatment. Inert gas might be incorporated during compaction. These are probably the reasons for reduced plasticity in IGC prepared nc Ni.

DISCUSSION AND CONCLUSION

The above mentioned tensile tests show that temperature is necessary for obtaining significant plasticity in nanocrystalline Ni and that in this regime plasticity goes along with low flow stress. Annealing without applying load, shows instantaneous grain growth at the temperatures where significant plasticity is observed. We therefore expect a strong relation between the dynamic change in microstructure and the deformation mechanism. The above mentioned results suggest

that plasticity is driven by grain growth. However, additional tensile testing revealed that grain growth alone is not a necessary condition for plasticity, since prior annealing of samples at 320°C for 15 minutes before pulling at 320°C showed similar flow stress and 10% less plasticity as deforming without first annealing.

To check if a coarser grained microstructure, obtained by the instantaneous grain growth during the first 30 sec. annealing prior to load, might be the reason for the low yield strength and significant plasticity, ED samples where first annealed for 3 min. 40 sec. and 15 min. at 320°C and then pulled at 250°C. Stress -strain curves for these tests showed no significant plasticity nor low flow stress. This indicates, that the microstructure alone is not sufficient for large plasticity, but that the deformation temperature plays also a role.

As suggested by Wang et al.[11] the temperature and the activation energy needed for grain growth is similar to the activation energy for grain boundary diffusion. Therefore it is likely that a diffusion controlled deformation mechanism can explain the large amount of plasticity.

In summary, the difference in the initial microstructure at room temperature and the difference in grain growth results in higher strain values at lower temperatures for the ED Ni as compared to IGC one. The increase in strain rate is linked to an increase in flow stress for both materials. The incorporation of impurities and the creation of pore volume in the IGC during compaction leads to embrittlement of the grain boundaries and therefore less plasticity compared to ED Nickel.

ACKNOWLEDGMENTS

REFERENCES

1. S.R. Agnew, B. R. Elliot, C. J. Young'sdahl, K. J. Hemker, and J. R. Weertman, in *Modelling of Structure and Mechanics from Microscale to Product*, edited by J. V. Carstensen, T. Leffers, T. Lorentzen, O. B Pedersen, B. F. Sorensen, and G. Winther (Risø National laboratory, Roskilde, Denmark, p. 1, (1998)
2. A. M. El-Sherik, U. Erb, G. Palumbo, K. T. Aust. Scripta Metall. Mater. 27, 1185 (1992)
3. J.R. Weertman, D.Farkas, K. Hemker, H. Kung, M. Mayo, R. Mitra, and H. Van Swygenhoven, MRS Bull., Vol. 24, No. 2. pp. 44 (1999)
4. R.Z. Valiev, R.K. Islamgaliev, I.V. Alexandrov, Prog. in Mat. Sci. 45, 103-189, (2000)
5. S.X. McFadden, R.S. Mishra, R.Z. Valiev, A.P. Zhilyaev, A.K. Mukherjee, Nature 398 (1999) 684-686.
6. S.X. McFadden, A.P. Zhilyaev, R.S.Mishra, A.K. Mukherjee, Materials Letters 45 345, (2000).
7. M. Zupan, K.J. Hemker, Met. and Mat. Trans. A, Vol. 29A, pp. 65, (1998)
8. C.E. Krill and R. Birringer, Philosophical- Magazine- A-77 (3) 621-640. (1998)
9. A.M. El-Sherik, U. Erb, J. Mater. Sci. 30 5743, (1995).
10. J.F. Löffler, PhD Dissertation, ETHZ, Zürich, Switzerland, (1998)
11. N. Wang, Z. Wang, K.T. Aust, U. Erb, Acta Mater. 45, 1655 (1997).
12. P.G. Sanders, J.A. Eastman, J.R. Weertman, Acta Mater. Vol.46, No.12, pp. 4195, (1998)

Computer Simulation of Misfit Dislocation Mobility in Cu/Ni and Cu/Ag Interfaces

Richard J Kurtz[1], Richard G. Hoagland[2] and Howard L. Heinisch, Jr.[1]
[1]Pacific Northwest National Laboratory
 Richland, WA 99352
[2]Los Alamos National Laboratory
 Los Alamos, NM 87545

ABSTRACT

The mobility of misfit dislocations in semicoherent Cu/Ni and Cu/Ag interfaces is determined by molecular dynamics and elastic band simulation methods. Cube-on-cube oriented Cu/Ni and Cu/Ag systems were studied with the interfaces parallel to (010). Core structures of misfit dislocations in semicoherent interfaces are found to be quite different in these systems. In Cu/Ni the misfits have very narrow cores in the plane of the interface. Consequently, the shear stress to move these dislocations is large, ~1.1 GPa. The core width and hence the misfit mobility can be changed by placing the misfit away from the chemical interface. Placement of the misfit one-atom layer into the Cu increased the core width a factor of 1.6 and lowered the threshold shear stress to 0.4 GPa. The misfit dislocations in Cu/Ag interfaces, on the other hand, are wide and therefore are much more mobile. The threshold shear stress for misfit movement in Cu/Ag is very low, ~0.03 GPa.

INTRODUCTION

Nanolayered bimetallic composites of semicoherent Cu/Ni and Cu/Ag prepared by co-deformation or physical vapor deposition techniques display near theoretical tensile strengths and substantial ductility [1]. Arrays of misfit dislocations exist in semicoherent interfaces to accommodate lattice parameter mismatch between the layers. The strength of the interface is controlled, in part, by the mobility of the misfits and interactions with glide dislocations. In this paper we apply elastic band techniques and molecular dynamics simulation methods to study the properties and attendant mobility of misfit dislocations in Cu/Ni and Cu/Ag interfaces.

COMPUTATIONAL DETAILS

The methodology we have used to calculate the atomic arrangements of interfaces have been described in detail previously [2] in connection with calculations of the structures of grain boundaries. For brevity, only an outline of the methodology is provided here. The model consists of a two-part rectangular computational cell. One part, Region 1, contains movable atoms embedded in a semi-rigid part, Region 2. The interface approximately bisects the model as shown in Figure 1. Equilibrium structures at T ~ 0K are obtained via relaxation using molecular dynamics with an energy quench. The two crystals on either side of the interface are free to move and undergo homogenous strain in all three directions. This movement occurs during the relaxation via a viscous drag algorithm, i.e., the velocities and strain rates associated

with such motions are proportional to the net forces acting on each of the two crystals within Region 1. In addition, we employed a mapping scheme whereby average displacements within Region 1 were used to adjust the positions of individual atoms near the interface but within the surrounding Region 2. Periodic boundary conditions were employed parallel to the z-axis. Embedded atom method potentials of the Voter-Chen type [3,4] were used to describe the energetics of atomic interactions in the Cu/Ni and Cu/Ag systems.
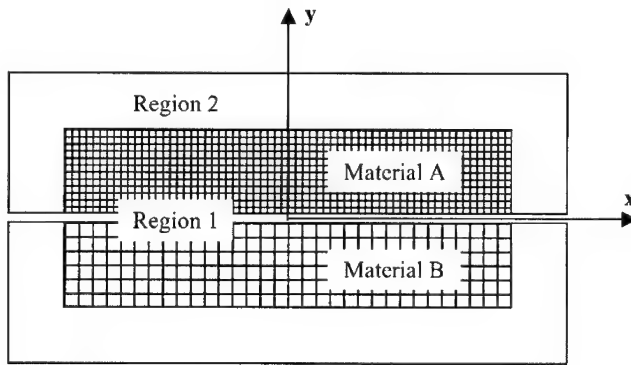
Figure 1. Schematic of the model. The interface is parallel to the x-z plane.

Two techniques were used to introduce dislocations into the model. In one method the dislocations are directly introduced by application of the anisotropic linear elastic displacement field of a dislocation on an interface separating two elastically dissimilar materials [5] followed by relaxation of the model in the same manner as described above. The dislocation lines are parallel to the z-axis in all cases and the dislocation fields are applied to atoms in both the movable and fixed regions of the model. Alternatively, misfit dislocations are spontaneously created when two semi-infinite, perfect crystals with different lattice parameters are joined together and relaxed. In this case, the long-range elastic portion of the dislocation is not present in Region 2, and consequently Region 1 contains an image field. However, the stress and displacement fields of a periodic array of such dislocations with spacing, **d**, have relatively short range, dying out with distance away from the interface. Thus, in composites where the spacing is less than the height of the model, it is not necessary to adjust the positions of the atoms in the adjacent Region 2 material.

Dislocation positions and core sizes were determined from the disregistry, Φ, a vector composed of the components of the relative displacements on each side of the slip plane, i.e.,

$$\Phi = \mathbf{u}^{+} - \mathbf{u}^{-} \qquad (1)$$

where the displacement vectors, **u**, are computed with respect to a reference crystal. Given a pair of atoms on either side of the slip plane, $\mathbf{u}^{+}$ is the displacement vector of an atom on the positive side of the slip plane and $\mathbf{u}^{-}$ is the displacement vector of an atom on the negative side of the slip plane.

DISCUSSION

The misfit dislocations that make a {100} interface between two FCC crystals semicoherent, in both Cu/Ni and Cu/Ag bilayer systems, have the shortest possible perfect Burgers vectors, a/2<110>. They are arranged as a nominally square grid with line directions parallel to <110> directions. The equilibrium misfit spacing, d_c, depends on layer thickness, but, in the limit of semi-infinite layers, is about 96 Å in Cu/Ni and 23 Å in Cu/Ag. Such misfits remove the coherency stresses at distances from the interface greater than about $d_e/2$.

It is instructive to compare the structure and properties of misfit dislocations artificially placed in single crystals of Cu, Ni and Ag to the same misfits that form at bilayer interfaces. Simulations were performed in which an a/2<110> dislocation was placed on a {100} plane in a Cu single crystal. The "misfit" dislocation is unstable and spontaneously dissociates into a Lomer-Cottrell (LC) lock composed of two Shockley partials, one each on the two-{111} slip planes that intersect the {100} plane. The Shockley partials are joined by stacking faults to an a/6<110> stair-rod that resides at the position of the original "misfit". This configuration has been called a Type I LC lock by Jossang et al. [6]. The lock is immobile under applied shear stresses parallel to the {100} plane. Misfits on {100} planes in bilayer systems display nascent dissociation, but complete formation of the lock is suppressed by large compressive coherency stresses present in the material with the larger lattice parameter. Application of a large tensile stress will overcome the compressive coherency stress and permit the LC lock to form.

The mobility of misfits in Cu/Ni interfaces was explored by introducing a single misfit dislocation at the center of the model. The 96 Å misfit spacing in Cu/Ni allows us to consider only one misfit dislocation since the elastic interaction with its neighboring misfit dislocations will be small for small movements. Two methods were employed to study misfit movement. One method involves the nudged elastic band technique, in which the energy differences to transition between two, fixed end-state atom configurations are determined. The method finds a minimum energy path connecting local minima on a multidimensional potential energy surface. Such methods are described in detail elsewhere [7]. Typical output from an elastic band calculation is shown in Figure 2. The stress to move a misfit was determined by

$$\tau = \frac{1}{bL}\frac{\partial E}{\partial x} \tag{2}$$

where **b** is the magnitude of the Burgers vector, **L** is the repeat distance along the **z**-axis and $\partial E/\partial x$ is the maximum slope of the relative energy change versus distance moved curve. The results in Figure 2 demonstrate that misfits located at the Cu/Ni interface are difficult to move requiring about 1.1 GPa.

The effect of distance of the misfit from the chemical interface on the stress to move it was also studied. A misfit was inserted so that one atom layer of Cu separated the misfit from the interface. Elastic band calculations showed that the stress to move the misfit decreased

dramatically to about 0.4 GPa, Figure 3. Placing the misfit five layers into the Cu resulted in little additional decrease in slip resistance. Examination of the misfit core width provides a possible explanation for the increase in misfit mobility. When the misfit is located at the Cu/Ni interface the core width is about 1.17Å, whereas when the misfit is separated from the interface by one atom layer of Cu the core width increased to 1.88Å. Placement of a misfit one atom layer into the Ni increased the resistance to slip by almost a factor of four compared to inserting the misfit at the interface. This large increase in slip resistance is due to dissociation of the misfit into the LC lock. Large tensile coherency stresses in the Ni promote dissociation such that the Shockley partials actually penetrate the interface and enter the Cu.
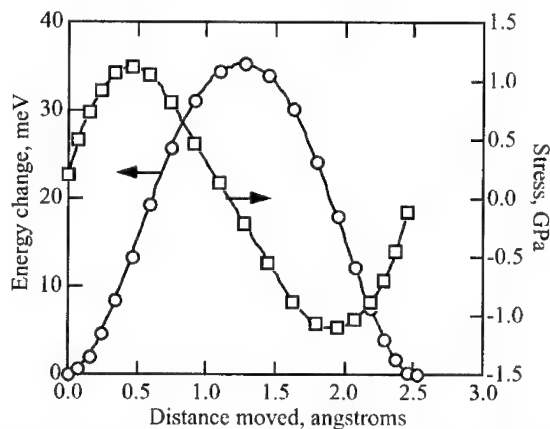
Figure 2. Relative energy change and stress to move misfit dislocation at the Cu/Ni interface.
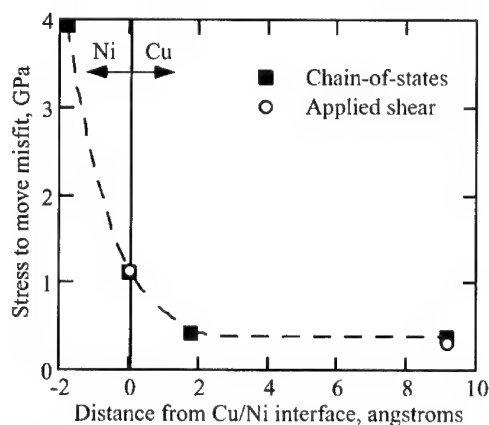
Figure 3. Dependence of stress to move the misfit dislocation on distance from the Cu/Ni interface.

As a compliment to the elastic band calculations, the threshold shear stress for misfit movement was also computed by direct application of shear strain to the model. For these cases, the relaxation procedure was modified slightly. The energy quench was turned off for the first 800 time steps (5.6 ps) to give the misfit an opportunity to move in response to the applied strain. Assuming linear-elastic behavior the critical shear stress for misfit movement is given by

$$\tau_{crit.} = 2C_{44}\varepsilon_{crit.} \qquad (3)$$

where $\varepsilon_{crit.}$ is the critical strain to produce misfit motion and C_{44} is the average of the elastic stiffness coefficients for the two materials comprising the interface. Figure 3 shows that this procedure yields estimates of the threshold shear stress for misfit movement that is nearly equivalent to the elastic band results.

The lattice parameter mismatch for Cu/Ag composites is much larger than for Cu/Ni multilayers so the misfit dislocation spacing is correspondingly much smaller. The properties of misfits in Cu/Ag are significantly different than in Cu/Ni. Misfit spacing is not uniform but varies periodically along the interface. The misfit core widths are also variable with some misfits so widely spread that core-core overlap occurs. For this situation, it is neither appropriate nor feasible to study the motion of a single isolated misfit since elastic interactions between misfits cannot be neglected. Consequently, misfit mobility was studied by applying shear strains to a relatively large model containing one complete period of misfits. The results are presented in Figure 4. In this figure, the stress dependence of the distance moved in 5.6 ps by each misfit as a function of its initial position is depicted. It is apparent that Cu/Ag misfits are mobile at very low applied stress levels (~0.03 GPa), and some misfits are more mobile than others. The most mobile misfits are those with the widest cores. Because of image forces present at the Region 1/Region 2 border the movement of misfits in these areas is constrained.

CONCLUSIONS

1. The core structures of misfit dislocations in bimaterial interfaces significantly affect their mobility. Misfits with wide cores were more mobile than compared to misfits with narrower cores in agreement with the Peierls model.
2. Misfit dislocations in Cu/Ni exhibit tight cores (~1.2 Å) and are uniformly spaced at 96 Å intervals. The stress to move misfits in Cu/Ni is high (~1.1 GPa) when the misfit is at the interface. The resistance to misfit motion in Cu/Ni decreases by about 2.5 and the core width increased by a factor of 1.6 when the misfit is placed so that one atom layer of Cu separates the misfit from the interface. Conversely, the stress to move misfits in Cu/Ni increased by almost a factor of four when the misfit is placed so that one atom layer of Ni separates the misfit from the interface. Such placement of misfits promoted LC lock formation, which significantly decreases misfit mobility.
3. Misfit dislocations in Cu/Ag exhibit variable core widths and spacing. The stress to move misfits in Cu/Ag is low (<0.03 GPa) and those misfits with spread cores displayed the highest mobility.
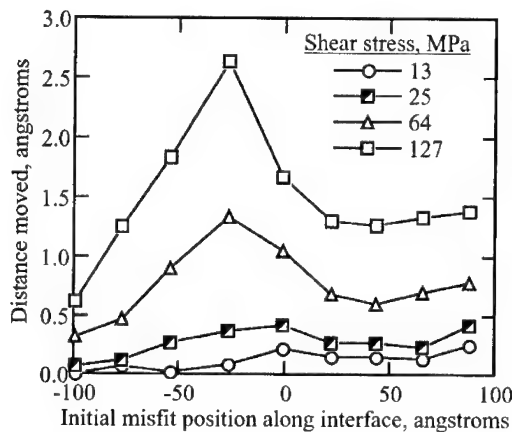
Figure 4. Stress dependence of the distance moved in 5.6 ps plotted against the initial misfit position for the Cu/Ag interface.

REFERENCES

[1] A. Misra, M. Verdier, Y. Lu, H. Kung, T. Mitchell, M. Nastasi, and J. Embury, "Structure and mechanical properties of Cu-X (X-Nb, Cr, Ni) nanolayered composites," *Scripta Materialia*, vol. 39, pp. 555, 1998.

[2] R. J. Kurtz, R. G. Hoagland, and J. P. Hirth, "Effect of Extrinsic Grain-Boundary Defects on Grain-Boundary Sliding Resistance," *Phil. Mag. A*, vol. 79, pp. 665, 1999.

[3] A. F. Voter and S. P. Chen, "Accurate Interatomic Potentials for Nickel, Aluminum and Ni sub 3 Al," presented at Characterization of Defects in Materials, Boston, Massachusetts, 1987.

[4] A. F. Voter, *Intermetallic Compounds, Principles and Practice*, vol. 77: J. Wiley, 1993.

[5] D. M. Barnett and J. Lothe, "Image Force Theorem for Dislocations in Anisotropic Bicrystals," *J. Phys. F: Metal Phys*, vol. 4, pp. 1618, 1974.

[6] T. Jossang and J. Hirth, "Anisotropic Elasticity Solutions for Dislocation Barriers in Face-Centered Cubic Crystals," *J Appl Phys*, vol. 36, pp. 2400, 1965.

[7] G. Mills, H. Jonsson, and G. K. Schenter, "Reversible work transition state theory: application to dissociative adsorption of hydrogen," *Surf. Sci.*, vol. 324, pp. 305, 1995.

Poster Session

Femtosecond Ultrasonics for the Characterization of Layered Micro- and Nano Structures

Jacqueline Vollmann, Dieter Profunser, Jürg Dual
Center of Mechanics
ETH Zürich, (Swiss Federal Institute of Technology)
CH 8092 Zürich, SWITZERLAND

ABSTRACT

The precise measurement of thicknesses, mechanical properties, and film-substrate bonding qualities of sub-micron metallic films, multi-layers, and microstructures in a nondestructive way is of growing importance for the semiconductor industry as well as for MEMS manufacturers.

Short laser pulses having durations of less than 100 fs are an ideal – not to say the only – way in order to provide sub-surface visualization in nanometer scale perpendicular to the film surface.

In this investigation, an enhanced pump-probe set up is presented. A dual frequency modulation technique is implemented in order to eliminate optical and electrical cross talk between the excitational pump pulse and the measuring probe pulse.

Up to the 5th acoustic echo in an aluminum film having a thickness of 50 nm on a sapphire substrate has been measured. From the time of flight and from the amplitude decay between the echoes the material properties of the film and of the substrate have been derived.

Further directions of the on going research project are presented.

INTRODUCTION

Short laser pulses have been used for more than two decades in order to investigate structural properties in the field of solid-state physics. In 1986 researchers at Brown University [1] proposed the use of laser-generated ultrasound (i.e. phonons) for film thickness measurement in integrated circuit manufacturing. Since that time non-destructive pulse laser based ultrasonics is receiving growing attention because of its crucial advantage to provide mechanical and geometrical information about thin metallic films and layered microstructures in a fast and non-contact manner [2]. Therefore the technology can easily be integrated in a line production process. On the other hand the variety of applications was promoted by the availability of "easy to use" solid-state laser units.

Nevertheless the authors believe that there is still much scope for further research and development of metrology- and subsurface visualisation techniques in that field.

Compared with "classical" ultrasonics, used to inspect machine parts or airplane structures, in which the mechanical wavelength amounts 0.5 to 2 mm, wavelength of about 10 - 20 nanometers can be achieved with laser pulses of 70 femtoseconds duration. The corresponding frequencies amount to 5 - 10 MHz and 0.3 - 0.6 THz, respectively. According to the authors experience metallic films can still be considered as a linear-elastic continuum for this particular wavelength range.
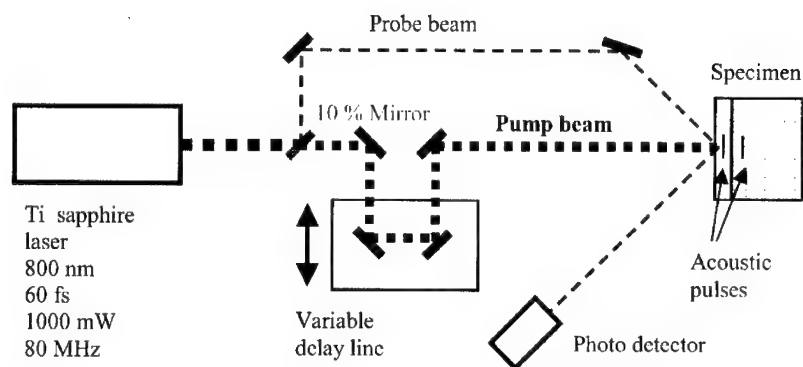
Figure 1. *Simplified experimental set-up.*

However, the thinner the film or the structure to be investigated is compared with the wavelength, the more important is a profound quantitative analysis of the light-matter interaction shaping the form of the mechanical pulse.

MEASUREMENT PRINCIPLE

Laser pulses of 810 nm wavelength having durations of less than 70 femtoseconds are created by a Titan sapphire laser at a repetition rate of 80 MHz.

Following the laser pulses from the left to the right hand side (see figure 1), the beam is split into a pump beam carrying 90 % of the energy and a weaker probe beam by a partly transmitting mirror. The pump pulses are used to excite the mechanical waves thermo-elastically whereas the probe pulses are used to detect optical effects at the thin film surface, which are caused by the echoes of the initial mechanical pulse. The optical reflectivity at the film surface is scanned versus a variable relative time shift between a pump pulse and a corresponding probe pulse. This time shift is controlled with a variable optical path length. Provided that the difference of the acoustic impedances of the film and of the substrate is sufficient in order to create an acoustic echo heading back to the surface, the time of flight of the acoustic pulse propagating twice through the film can be measured. If the elastic properties i.e. the Young's modulus, the Poisson's ratio, and the density are known, the film thickness can be determined. Or, if the film thickness is known the speed of sound propagating perpendicular to the film surface can be measured. A crucial point of the method presented above is that the quantity to be measured i.e. the optical reflectivity change caused by the acoustic echoes ΔR, is very small. Therefore some further improvements had to be added to the set-up shown in figure 1:

In order to avoid optical cross talk between the excitation and the detection, the pump and the probe beam propagate in different polarization planes. Furthermore the pump and the probe beam are modulated at different frequencies and a dual lock-in amplification scheme is applied to extract the signals of interest. This set up has an estimated sensitivity $\Delta R/R$ of about 10^{-5} and has shown to be sufficient to measure up to the 5th echo in a 50 nm aluminum film on sapphire.
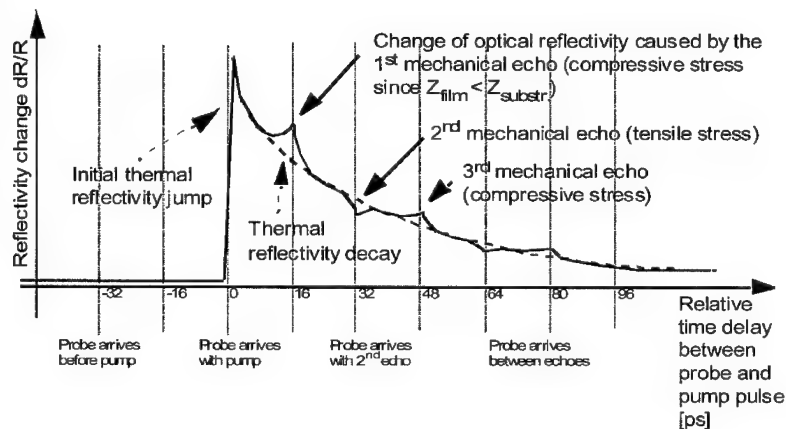
Figure 2. Idealized intensity curve of the measured probe beam vs. relative time delay between the pump- and the probe pulse for a 50 nm aluminium film on a sapphire substrate.

Figure 2 shows an idealized intensity curve of the optical reflectivity at the surface versus a relative time scale having its origin at the pump pulse arrival. The optical reflectivity properties are mainly governed by thermal effects (dashed line). Superimposed the effects of mechanical strain caused by the acoustic echoes are visible (solid line). Reading the diagram, shown in figure 2, from the left to the right, one can see that the reflectivity remains constant as long as the probe pulse arrives prior to the pump pulse. If the pump and the probe pulse arrive at the same time, a strong thermal reflectivity change can be identified. Since the heating pump pulse is much shorter than the thermal relaxation time of the surface region, the thermal reflectivity is assumed to decay exponentially. On the right hand side the reflectivity changes caused by the mechanical strain reaching the surface are visible.

Time of flight of the acoustic pulses is not the only information that can be extracted from a measured reflectivity curve: Considering the shape of two consecutive echoes one can see that its shape is inverted. The reason for this shape inversion is the fact that in the case of an aluminium film on a sapphire substrate, the acoustic impedance of the substrate is higher than the one of the film. The reflected part of a compressive stress pulse, which is generated at the film substrate interface, is a compressive stress pulse as well. When this compressive stress pulse reaches the free surface it is converted to a tensile stress pulse, which is reflected back into the film. Taking off the effects of the thermal reflectivity, one can quantify the acoustic impedance of the substrate by measuring the amplitude decay of the mechanical echoes. Thus a non-destructive, sub-surface material characterisation in nanometer scale is possible.

RESULTS
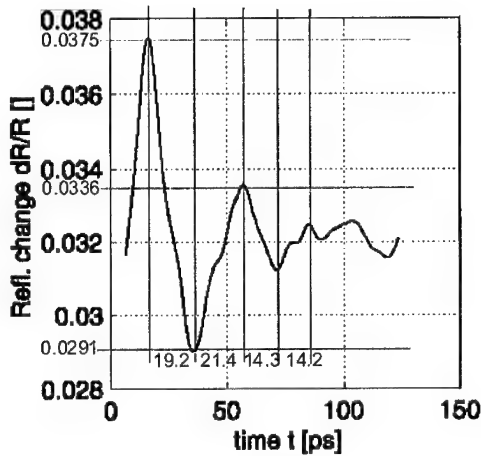
Figure 3. *Measured reflectivity change caused by the mechanical strain of the echoes only for a 50 nm aluminium film on sapphire (thermal reflectivity change is eliminated).*

The diagram in figure 3 shows the first five acoustic echoes after the effects of the thermal reflectivity change have been eliminated. The average time of flight for an acoustic pulse travelling to the film/substrate interface and back to the surface amounts to 17.3 ps. Assuming the film thickness to be exactly 50 nm this would lead to a speed of sound of 5780 m/s in the aluminium film. Compared with common handbook values this result is within a 10% error limit. On the other hand, if the speed of sound is assumed to be 6100 m/s the measurement presented above would lead to a film thickness of 52.8 nm. Since a detailed calibration has not been performed yet, the question which of the assumptions above is closer to the reality is open.

Analysing the amplitude decay between the first three echoes leads to the following results:

The acoustic impedance is defined as the product of the density and the speed of sound: $Z := \rho \, c_p$. For two neighbouring materials the force reflection coefficient (see equation 1) describes the fraction of stress that is reflected.

$$R_{force} = \frac{Z_2 - Z_1}{Z_1 + Z_2} \quad (1)$$

With $Z_{aluminium} = 1.647 * 10^7$ Pa s/m and $Z_{sapphire} = 4.086 * 10^7$ Pa s/m a force reflection coefficient of 0.43 is expected.

Provided that the optical reflectivity change is linearly depending on the mechanical strain the force reflection coefficient can be determined from the amplitude decay seen in figure 3. The measured force reflection coefficient amounts to 0.54. This is astonishing since neither material damping nor the effects of an imperfect bonding which would reduce the expected value, are taken into account. So the most possible reason for the difference between the predicted and the measured value is that the material parameters on which the predicted value is based are not correct.

DISCUSSION AND FURTHER DIRECTIONS

The measurements shown above represent preliminary results of an ongoing research project. The time of fight and the amplitude decay measurements have shown to provide reasonable results in a rapid and non-contact manner. Further improvements can be achieved by optimising various parameters of the experimental set-up. Pulse shape analysis is performed by implementing a two temperature model according to Qiu et. al. [3] in order to extract material parameters with higher accuracy. Results will be published elsewhere.

To make the method applicable to three-dimensional microstructures like MEMS devices several techniques are developed in order to obtain higher lateral resolution.

ACKNOWLEDGMENTS

REFERENCES

1. C. Thomsen, H.J. Maris, J. Tauc, "Picosecond Acoustics as a Non-Destructive Tool for the Characterization of very thin films", Thin Solid films, Vol. 154, 1987, pp. 217-223.
2. J.A. Rogers et.al. "Optical Generation and Characterization of Acoustic Waves in Thin Films", Annual Review Material Science 2000, Vol. 30, pp. 117-157.
3. T.Q. Qiu and C.L. Tien, "Short-Pulse Laser Heating on Metals", International Journal of Heat Mass Transfer, Vol. 35, No.3, 1992, pp. 719-726.

Simulation of Positron Characteristics in Nanocrystalline Materials

Jan Kuriplach[1], Steven Van Petegem[2], Danny Segers[2], Charles Dauwe[2],
Marc Hou[3], Eugenij E. Zhurkin[4], Helena Van Swygenhoven[5],
and Alvaro L. Morales[6]

[1]Department of Low Temperature Physics, Charles University, V Holešovičkách 2,
CZ-180 00 Prague 8, Czech Republic
[2]Department of Subatomic and Radiation Physics, Ghent University, Proeftuinstraat 86,
B-9000 Ghent, Belgium
[3]Physics of Irradiated Solids, Free University of Brussels, Bd du Triomphe, B-1050
Brussels, Belgium
[4]Department of Experimental Nuclear Physics, St. Petersburg State Technical University,
Polytekhnicheskaya 29, 195251, St. Petersburg, Russia
[5]Paul Scherrer Institute, CH-5232 Villigen-PSI, Switzerland
[6]Department of Physics, University of Antioquia, A.A. 1226, Medellín, Colombia

ABSTRACT

The theoretical calculations of the positron response to different types of defects can be very helpful in order to interpret properly positron measurements. In this contribution a new computational technique to determine positron properties in nanocrystalline materials is presented. In such calculations we employ the realistic models of n-materials obtained using molecular dynamics. The new technique is based on the so-called atomic superposition method where atomic densities are superimposed in a selected region of the model (virtual) sample to approximate the electron density of the system. We study the virtual samples of n-Cu, n-Ni, n-NiAl, and n-Ni$_3$Al, for which we calculate positron lifetimes and positron binding energies corresponding to defects located in selected regions of the samples. The regions of interest for positron calculations comprise grain boundaries including triple points, nano-voids, and bulk-like regions.

INTRODUCTION

Nanocrystalline materials attract attention of scientists due to their interesting properties, underlying physics of which is not yet well known in many cases. The detailed knowledge of the structure of n-materials is of primary importance. In such materials an important fraction of their volume is constituted by inter-grain interfaces.

Positron annihilation spectroscopy (PAS) [1] is an efficient tool to study open volume defects which are hardly accessible by other techniques, e.g., by widespread transmission electron microscopy (TEM). For instance, PAS techniques are able to detect single vacancies in concentrations as low as 0.1 ppm. On the other hand, one cannot observe single defects in contrast to TEM, but annihilation events from the whole sample are summed in a spectrum and one has to make an appropriate evaluation of the spectrum and subsequent interpretation because not only one type of defect can be present in the sample.

There have been many positron lifetime experiments on nanocrystalline materials (see, e.g., [2]). Usually, four components are observed in measured spectra. The longest
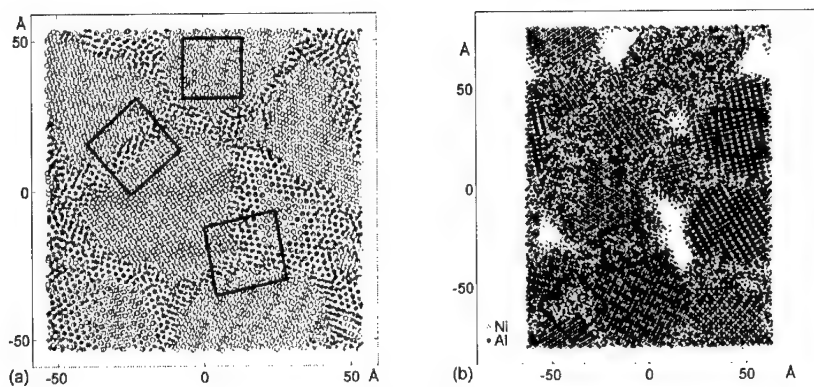
Figure 1: *Layers with thickness 6 Å taken from (a) Cu sample SF1 and (b) Ni₃Al sample CA2. Atoms in the perfect lattice are marked by circles; other symbols denote atoms at grain boundaries and close to voids. The examples of cuts chosen for positron calculations are also shown.*

component (with a small intensity) in the nanosecond range is attributed to the annihilation of ortho-positronium (o-Ps). Two shorter components are associated with positron annihilation in small free volumes: nano-voids and grain boundaries (GBs). The shortest component corresponds to delocalized positrons annihilating inside grains. In the present paper we try to give an explanation of the measured lifetime components (not considering the o-Ps one) using the microscopic models of the studied n-materials.

METHOD

The simulations of the structure of selected n-materials were performed using molecular dynamics (MD) simulations. In the case of binary alloys, the Metropolis Monte Carlo (MC) technique was combined with MD in order to study segregation effects (see [3] for details). Two types of virtual samples were examined (see figure 1). Starting atomic configurations for the 'cluster assembled' (CA) samples were created using several nano-grains placed randomly in space. As for the 'space filling' (SF) samples, centers of grains are randomly placed into a box and grains are 'growing' so that they fill up completely the box. Then, these starting configurations were pressed to 2 GPa at 300 K using the MD technique. In the case of binary systems, MC simulations are performed at 300 K after the release of pressure. For NiAl and Ni₃Al both types of samples contain about 100 thousand atoms. The Cu and Ni samples with about 100 and 300 thousand atoms were studied. The grains in virtual samples have sizes up to 80 Å.

To calculate the positron properties of interest, the atomic superposition (ATSUP) technique [4] was used. It is a non-selfconsistent technique which makes use of the atomic densities and electron Coulomb potentials of all atomic species in the system considered in order to approximate the electron density and Coulomb potential of the system. More specifically, the electron densities and Coulomb potentials are superimposed numerically on a three dimensional (3D) mesh according to the atomic structure of the system supposing its periodicity. The total positron potential is constructed as a sum of two parts

$V_+ = -V_{Coul} + V_{corr}$; V_{Coul} being the electron Coulomb potential originating from the superposition of atomic potentials (the '$-$' sign is due to the opposite charge of positrons) and V_{corr} is the correlation potential which is supposed to depend on the electron density n_- obtained in the same way as V_{Coul}. Then, the Schrödinger equation for positrons

$$(T + V_+)\psi_+ = E_+\psi_+ \tag{1}$$

is solved using a conjugate gradient method [6] on the 3D mesh and the positron ground state ψ_+ and energy E_+ are obtained. In the above equation, T stands for the kinetic energy operator. The positron lifetime τ is calculated using the following formula [5]

$$1/\tau = \pi r_e^2 c \int n_-(\mathbf{r}) n_+(\mathbf{r}) \gamma[n_-(\mathbf{r})] \, d\mathbf{r}, \tag{2}$$

where r_e is the classical electron radius, c is the speed of light, the positron density $n_+ = |\psi_+|^2$, and γ is the so called enhancement factor describing the pile up of electrons around the positron. The positron binding energy to a defect is determined as the positron energy difference between the delocalized positron state and the positron state corresponding to the defect. In our calculations the parametrization of $\gamma[n_-]$ and $V_{corr}[n_-]$ according to Ref. [7] was employed.

However, we had to modify the ATSUP technique to allow the treatment of n-materials. First, virtual samples are too big to be taken as one cell for positron calculations and smaller regions ('cuts') have to be considered. In general, a box (parallelepiped) containing a region of interest is 'cut' from a virtual sample. But such a cut is not periodic. Nevertheless, the electron densities and electron Coulomb potentials are first superimposed for all atoms in the cut assuming its periodicity, but for further considerations a smaller (inner) part of the cut is taken into account to avoid an influence of the 'false' (imposed) periodicity.[1] The positron potential is then determined using the Coulomb potential and correlation potential as described above. Furthermore, we adjust appropriately the positron potential at the sides of the smaller cut to omit artificial shallow positron traps at these sides.[2] To be precise, the value of the positron potential V_+ at the side is set to a certain value V_0. However, if $V_- > V_0$, V_+ remains unchanged. V_0 is chosen to be equal to (or slightly lower than) the positron energy in the defect free material. In this way the positron is 'forced' to stay in the cut and a physically reasonable behavior of the positron wave function is ensured. The results presented in the next section are nearly insensitive to the choice of V_0 (if the above rules for V_0 are respected).

After these adjustments the cut can be considered to be quasiperiodic, as V_+ is set to V_0 nearly everywhere at the cut sides, and the periodic boundary condition for the positron wave function can be applied when solving the Schrödinger equation. As the selected box can contain more positron traps, we extended the ATSUP method so that it is possible to look for more positron states [6]. In our calculations we use typically cuts with dimensions $20 \times 20 \times 20$ Å^3 (see figure 1) employing the 3D-mesh spacing about 4 points/Å.

---

[1] When superposing the atomic potentials (densities) at a given mesh point, all atoms in a sphere with a certain radius are considered. If such a point is close to the cut side, the sphere 'folds' to the other cut side and in this way two atoms from the opposite sides of the cut may become too close or too far (as the cut is non-periodic) giving thus unrealistic contributions to the potential (density) at the considered point.

[2] Due to the non-periodicity of the cut, regions with a lowered positron potential can be present at the cut sides. These regions attract positrons.

Table I: The results of calculations of the positron lifetime (τ) and binding energy to defects (E_b) for n-Cu and n-Ni.

sample	bulk-like regions τ (ps)	grain boundaries τ (ps)	E_b (eV)
Cu - SF1	112 113	124 126	0.5
Cu - SF2	112–113	126-132; 174	0.5–0.7; 1.5
Ni - SF1	99–100	122–137	1.4–1.8
Ni - SF2	100	120 137	1.4 1.8

RESULTS

Cu and Ni

Two SF samples with the grain sizes 50 and 80 Å (labeled further as SF1 and SF2, respectively) were studied in the case of Cu and Ni. A layer with a thickness of 6 Å taken from the Cu SF1 sample is shown in figure 1a to demonstrate the structure of n-Cu. In this figure examples of cuts (their projections onto the layer) are also plotted. An analogous plot for Ni would look very similar to figure 1a. The results of positron lifetime calculations are summarized in table I. The positron binding energies to defects are also specified in this table. Each specified range is deduced from the results obtained for several cuts.

It is important to note that the positron lifetimes calculated for bulk-like regions (centers of grains) agree well with the lifetime obtained for defect free (periodic) material for which we are getting 109 and 97 ps for Cu and Ni, respectively (cf. table I). Because one can expect that bulk-like regions will have similar positron properties as the perfect material, this is a simple test of adequacy of our computational method.

As for grain boundaries, we can see that the corresponding positron lifetimes exceed the bulk ones only by 10 - 20 ps in the case of Cu and 20 40 ps for Ni. This indicates that the free volumes connected with GBs are rather small; smaller than the free volume associated with single vacancies. However, in one cut in the Cu SF2 sample we observed at the grain boundary a defect having a lifetime of 174 ps, which corresponds to a single vacancy. In table I we did not specify results for triple points, which are common points of three or more GBs. The corresponding lifetimes and binding energies are similar to those obtained for GBs (see table I).

Finally, we could see that the positron lifetime corresponding to positrons trapped at GBs exceeds the bulk lifetime more in n-Ni than in n-Cu. This is also reflected in the binding energies. Namely, we determined the average binding energy of positrons in Ni to be about 1.6 eV, whereas in Cu it is 0.6 eV only (see table I). This means that the positron traps at GBs in n-Ni are somewhat deeper than those in n-Cu. This effect should be reflected by a difference in the grain boundary structure of n-Cu and n-Ni, which will be the subject of another study.

In Cu and Ni virtual samples, there are no nano-voids (see figure 1a) and we cannot present any results concerning positron trapping in them.

NiAl and Ni$_3$Al

We will continue with results regarding binary systems. We studied the CA samples (see figure 1b for an example) and in the case of Ni$_3$Al we examined also the SF samples.

Table II: The results of calculations of the positron lifetime (τ) and binding energy to defects (E_b) for n-NiAl and n-Ni$_3$Al. $\Delta\mu$ is the difference between the chemical potentials of Ni and Al.

sample	$\Delta\mu$ (eV)	bulk-like regions τ (ps)	grain boundaries τ (ps)	E_b (eV)
Ni$_3$Al - SF1	0.0	104	180–213	4.5–5.9
Ni$_3$Al - SF2	0.6	106	183–225	4.2–5.4
Ni$_3$Al - CA1	0.0	107	118–124; 175	0.9; 2.7
Ni$_3$Al - CA2	0.6	108	124–126	0.6
NiAl - CA1	1.0	123–124	134–194	0.6–2.2
NiAl - CA2	1.6	123–129	148–192	0.6–2.1

The effect of segregation of Al was taken into account by fixing the difference between the chemical potentials of Ni and Al in MC simulations. The corresponding differences are specified in table II. The case with the lower (higher) difference corresponds to the situation with no (maximum) segregation at GBs (see Ref. [3] for details). The results of positron calculations are also shown in table II.

Concerning positron annihilation in grains, we are getting lifetimes which are very close to the value 105 ps for the perfect Ni$_3$Al material. In the case of NiAl, we obtained 115 ps, which slightly differs from the values of about 125 ps calculated for bulk-like regions in NiAl virtual samples. This deviation originates from the slightly different atomic volumes in perfect NiAl and the bulk-like regions in the n-NiAl samples.

Table II shows a large difference between the lifetimes of positrons annihilating at grain boundaries in the SF and CA samples of Ni$_3$Al. In particular, the GBs in SF samples exhibit much larger free volumes (one to three vacancies) compared to the CA samples, where the situation is similar to the n-Cu and n-Ni SF samples discussed above. This is also reflected in the positron binding energies to defects shown also in the table. In the case of NiAl, the range of lifetimes corresponding to GBs is quite wide. The maximum size of free volumes corresponds approximately to single vacancies. As for segregation, it seems that there is no apparent effect on the studied positron characteristics.

Concerning nano-voids, again there are no such voids in SF samples. On the other hand, in the CA samples there are large voids which create networks (see figure 1b). We cannot perform any calculations for such voids because we would have to take the whole samples as 'cuts' for positron calculations, which is not managable. Anyhow, the corresponding lifetimes would be very large (close to 500 ps) and this is not observed experimentally. Hence, nano-voids are not properly represented in the studied samples.

The results for both Ni-Al systems presented above are compared in detail with available experimental data in Refs. [8] and [9]. Here we give only the essential point. The shortest lifetime components observed in NiAl and Ni$_3$Al are 224 and 185 ps, respectively. The lifetime value for Ni$_3$Al fits to the lower end of the calculated ranges for the SF samples (see table II) and, therefore, the corresponding model seems to describe reasonably the GBs in n-Ni$_3$Al. Concerning NiAl, the measured value lies slightly above the calculated ones. However, one may expect that the SF model would result in values comparable with experiment. On the basis of our lifetime calculations, we can state that the above mentioned experimental lifetime components can be attributed to positrons annihilating in

small open volume defects located at the grain boundaries of nanocrystalline samples.

CONCLUSIONS

We presented the results of positron calculations in several nanocrystalline materials. These materials were modeled using molecular dynamics and Monte Carlo techniques. We concentrated on the positron lifetime – as a measure of free volume in materials – and calculated this quantity for selected regions of the studied n-materials. The presented simulations of positron lifetimes allowed for the verification of the interpretations of earlier experimental lifetime data for n-materials. In particular, we proved that one of the lifetime components observed in measured lifetime spectra corresponds to positrons annihilating at defects associated with grain boundaries. Such defects have sizes from one to several vacancies.

ACKNOWLEDGMENTS

REFERENCES

1. *Positron Spectroscopy of Solids*, edited by A. Dupasquier and A.P. Mills. Jr. (IOS Press, Amsterdam, 1995).

2. H.E. Schaefer and R. Würschum, Phys. Lett. A **119**, 370 (1987).

3. E.E. Zhurkin, M. Hou, H. Van Swygenhoven, B. Pauwels, M. Yandouzi, D. Schryvers, G. Van Tendeloo, P. Lievens, G. Verschoren, J. Kuriplach, S. Van Petegem, D. Segers, and C. Dauwe, this proceedings.

4. M.J. Puska and R.M. Nieminen, J. Phys. F: Metal Phys. **13**, 333 (1983); A.P. Seitsonen, M.J. Puska and R.M. Nieminen, Phys. Rev. B **51**, 14057 (1995).

5. M.J. Puska and R.M. Nieminen, Rev. Mod. Phys. **66**, 841 (1994).

6. M.P. Teter, M.C. Payne, and D.C. Allan, Phys. Rev. B **40**, 12255 (1989).

7. E. Boroński and R.M. Nieminen, Phys. Rev. B **34**, 3820 (1986).

8. J. Kuriplach, S. Van Petegem, M. Hou, E.E. Zhurkin, H. Van Swygenhoven, F. Dalla Torre, G.Van Tendeloo, M. Yandouzi, D. Schryvers, D. Segers, A.L. Morales, S. Ettaoussi, and C. Dauwe, accepted for publication in Mater. Sci. Forum (2001).

9. S. Van Petegem, D. Segers, C. Dauwe, F. Dalla Torre, H. Van Swygenhoven, M. Yandouzi, D. Schryvers , G. Van Tendeloo, J. Kuriplach, M. Hou, and E.E. Zhurkin, this proceedings.

Positron Lifetime Measurements in Nanostructured Ni-Al Samples

S. Van Petegem[1], D. Segers[1], C. Dauwe[1], F. Dalla Torre[2,] H. Van Swygenhoven[2], M. Yandouzi[3], D. Schryvers[3] , G. Van Tendeloo[3], J. Kuriplach[4], M. Hou[5] and E.E. Zhurkin[6]

[1]NUMAT, Subatomic and Radiation Physics Dept., Ghent University, Proeftuinstraat 86, B-9000 Ghent, Belgium
[2]Paul Scherrer Institute, CH-5232 Villigen-PSI, Switzerland
[3]EMAT, Centre for Electron Microscopy and Materials Science, University of Antwerp, Groenenborgerlaan 171, B-2020 Antwerp, Belgium
[4]Dept. of Low Temperature Physics, Charles University, V Holesovickach 2, CZ-18000 Prague 8, Czech Republic
[5]Physique des Solides Irradiés CP234, Université Libre de Bruxelles, Bd du Triomphe, B-1050 Brussels, Belgium
[6]Dept. of Experimental Nuclear Physics, St. Petersburg State Technical University, Polytekhnicheskaya 29, 195251, St. Petersburg, Russia

ABSTRACT

Positron lifetime spectroscopy is an effective tool to study various types of defects in materials including nanostructured ones. The size of free volumes associated with defects can be estimated using the lifetime components found in the measured spectra. Positron lifetime experiments are performed on nanocrystalline Ni-Al samples synthesized by the inert-gas condensation technique. The samples are further characterized by means of X-ray diffraction, electron diffraction and microscopy techniques as well as density measurements. In the lifetime spectra we observe three lifetime components corresponding to different annihilation sites in the samples. These lifetimes are compared with the results of simulations of positron lifetimes in modeled Ni-Al samples obtained using molecular dynamics and Monte Carlo calculations. Finally, we present positron lifetime results for nanocrystalline Ni_3Al samples which were produced or annealed at different temperatures.

INTRODUCTION

Positron lifetime spectroscopy is a well-established technique to study open volume defects in solids [1]. The positron lifetime is primarily determined by the average electron density seen by the positron [2]. In a defect-free solid, the positron lifetime is a characteristic of the material. Positrons can get trapped into defects due to the formation of an attractive potential at open volume defects such as vacancies, vacancy clusters, dislocations, etc. When the positron is trapped into such a defect, its lifetime increases as a function of the defect size due to the locally reduced electron density. In large open volumes, positronium can be formed which is a bound state of a positron and an electron, analogous to a hydrogen atom.

Nanocrystalline materials are a big challenge for positron lifetime spectroscopy due to the complexity of their structure. In this work, positron lifetime experiments in nanocrystalline Ni-Al samples with different composition are described. In these binary alloys, effects like segregation

at the grain boundary interfaces and chemical ordering play an important role in the microstructure.

EXPERIMENTAL DETAILS

Ni-Al nanocrystalline powder was produced by the inert-gas condensation technique [3] and compacted into pellets at 2GPa at room temperature (RT). The original coarse-grained Ni-Al samples had two different compositions: 73 at% and 62 at% Ni. The corresponding nanocrystalline samples will be referred to as sample A and B respectively. The samples were characterized by X-ray diffraction (XRD), transmission electron microscopy (TEM), energy dispersive X-ray analysis (EDX) and selected area electron diffraction (SAED). The density was determined by the Archimedes immersion method.

A coarse grained Ni_3Al sample was prepared to be used as a reference sample. It was annealed at 1200 K for 100h to obtain a homogeneous pellet. Its composition was determined to be $Ni_{76}Al_{24}$. To create vacancies, this sample was irradiated at RT with 2 MeV electrons at the LINAC facility [4] at the University of Ghent up to a dose of 1×10^{18} e$^-$/cm^2.

Positron lifetime spectra were measured using a conventional fast-fast lifetime spectrometer with a resolution (FWHM) of about 220 ps using the sandwich arrangement. The positron source (about 0.4 MBq) was made by evaporating ^{22}NaCl onto a standard kapton foil (7 μm thickness), which was then sealed with another one. In order to avoid electronic drifts during the measurements, the complete set-up was temperature controlled. In that way, the peak position was stable within half a channel (using a channel width of 20 ps). The number of counts in each spectrum (after background subtraction) exceeded 15×10^6. The spectra were analyzed using the multi-component fitting program LT by Kansy [5].

RESULTS

Characterization

The results of the electron microscopy experiments and density measurements are shown in Table 1. EDX measurements, obtained from different regions but with fixed experimental conditions yielding an estimated precision of 2%, show that the composition of sample A is somewhat more uniform in comparison to sample B where local variations between 59 at% and 65 at% Ni were found. SAED measurements show the presence of the $L1_2$ phase in sample A. In sample B the metastable $L1_0$ martensitic phase was found beside the stable B2 and $L1_2$ phase, which is in agreement with the phase diagram of Ni-Al. The grain size distribution is for both samples about the same but for sample B also some bigger grains with sizes up to 30 nm were

Table 1: Overview of the sample characteristics

	$Ni_{73}Al_{27}$ (sample A)	$Ni_{62}Al_{38}$ (sample B)
Composition	72 at% - 76 at% Ni	59at % - 65 at% Ni
Phases	$L1_2$	B2, $L1_2$, $L1_0$
Grain size	8nm – 14 nm	5 nm – 15 nm
Density	89%	75%

found (for more details see [6]). The density of sample A is about 89% of the theoretical density for this composition. Sample B has a much lower density.

The lifetime of (free) delocalized positrons in the reference sample was 115 ps. For the irradiated sample a lifetime component of 182 ± 1 ps was found. Both values are in good agreement with literature (see e.g. [7,8]).

The positron lifetime spectra for both samples could be analyzed using three discrete components. The results are summarized in Table 2. There is no signal from delocalized positrons. This is due to the fact that the positron diffusion length in metallic systems is of the order of 100 nm [9], which is much longer than the grain sizes in the samples studied here. Because the distance between defects in n-materials is of the order of the average grain size, all positrons can get trapped into defects. In this context it is useful to note that in the case of n-materials, one can expect positron diffusion along grain boundaries in contrast to coarse-grained materials where positrons diffuse inside grains.

The shortest lifetime of sample A is comparable with the vacancy lifetime of the irradiated coarse-grained Ni_3Al sample. According to a simple model proposed by Schaefer [10], this signal originates from vacancy-like defects situated in the grain boundaries. In sample B, this lifetime is somewhat larger. In both samples a second lifetime of more than 400 ps was found. This is an indication for the existence of nano-voids. In order to estimate the size of these voids, lifetime calculations in well-known defects were performed in Ni_3Al [11], (see also Figure 1). From these calculations, it was concluded that the nano-voids have a size of about 10Å. Concerning the intensities, one can see a clear difference between both samples; in sample B, relatively more positrons are found to annihilate in the vacancy-like defects.

The third lifetime is due to the formation of ortho-positronium. In this case, there is no significant difference between both samples concerning the lifetimes and intensities.

Simulations

In order to check the lifetime results given above, positron lifetime calculations were performed in modeled nano-structured samples. These 'virtual' samples were created using molecular dynamics and Monte Carlo simulations (see [12] for more details). Two different compositions were used: n-NiAl (having a B2 structure) and n-Ni_3Al ($L1_2$ structure). For the latter composition, two different configurations were considered: space-filling (SF) and cluster-assembled (CA) samples, whereas only CA configurations are available for the B2 case (see [12] for further explanations). For the positron calculations, specific parts of the modeled samples were taken such as bulk-like regions, grain boundaries, triple points and nano-voids (see [13] for more details about these calculations and the results). Here only a short overview of the results is given: for the bulk-like regions in the Ni_3Al samples, lifetimes of about 104 up to 108 ps were found for both the CA and SF samples which agree quite well with the value of 105 ps calculated in perfect Ni_3Al (see also Table 3). In the NiAl samples, lifetimes of about 123 -129 ps were found which is somewhat higher than 115 ps calculated in perfect NiAl. As mentioned before, no signal from these regions could be found in the experiment due to the small grain sizes.

Table 2: Positron lifetime results in sample A and B

	τ_1 (ps)	τ_2 (ps)	τ_3 (ns)	I_1 (%)	I_2 (%)	I_3 (%)
Sample A	181 ± 1	427 ± 1	2.8 ± 0.05	43 ± 1	55 ± 1	2.0 ± 0.5
Sample B	224 ± 1	443 ± 2	2.8 ± 0.05	61 ± 1	37.5 ± 1	1.5 ± 0.5
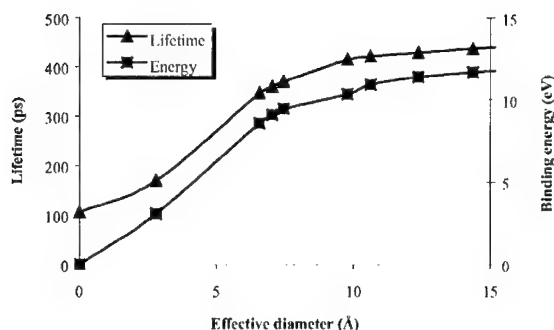
Figure 1: *Positron lifetime and binding energy as function of defect size.*

The results for the grain boundaries are summarized in Table 4. For Ni₃Al, big differences between the SF and CA samples were found: in the SF samples, defects with size from 1 to 3 vacancies were found which agree quite well with the experimental values. In the CA samples, the lifetimes are only about 20 ps higher than the bulk values. Vacancy-like defects were found only in a few grain boundaries. In the NiAl samples, a variety of defect sizes was found ranging from almost perfect NiAl up to vacancy-like defects. As for triple points, i.e. intersections of three or more grain boundaries, about the same values as in the grain boundaries were found for both compositions.

Concerning the nano-voids, the situation is completely different: in the SF samples, there are no nano-voids, which is inherent to the technique used for the construction of these samples. There are lots of voids in the CA samples but they are mostly interconnected and form a 'network' that is too big for the calculations. Anyhow, such big voids would result in lifetimes which would be apparently larger than those observed in the experiment.

The third lifetime could not be calculated as this lifetime originates from positronium. Within the current limits of our technique, we are not able to calculate positronium lifetimes in nano-voids.

Table 3: Results of the positron lifetime calculations in bulk-like regions

	Ni₃Al (L1₂)	NiAl (B2)
SF	104 ps – 106 ps	/
CA	106 ps– 108 ps	123 ps -129 ps

Table 4: Results of the positron lifetime calculations in grain boundaries

	Ni₃Al (L1₂)	NiAl (B2)
SF	180 ps – 225 ps	/
CA	118 ps- 124 ps and 175 ps	134 - 194 ps

Temperature effects

In order to change the defect sizes, the temperature was varied during and after the compaction of nanocrystalline Ni_3Al. The temperature during compaction varied between RT and 500°C. The positron lifetime results are shown in Table 5. The temperature treatment had almost no influence on the shortest lifetime and its intensity, whereas the positron lifetime of the nano-voids decreased from 424 to 343 ps, corresponding to a decrease of the size of the nano-voids from 10 Å to 6.5 Å (see Figure 2). No significant changes were found in the ortho-positronium contribution. Furthermore, two samples compacted at room temperature were annealed at 200 °C and 300 °C. They both revealed a lifetime of about 340 ps but with a small difference for the relative intensity (see Table 6). This lifetime is comparable with the lifetime observed for the sample compacted at 500 °C. However, the amount of positrons annihilating in nano-voids is larger compared to the non-annealed samples. This indicates a larger concentration of nano-voids in the annealed samples.

Table 5: Overview of the positron lifetime calculations in Ni_3Al as function of the compaction temperature. The errors are comparable to the ones given in Table 2.

Temperature (°C)	τ_1 (ps)	τ_2 (ps)	τ_3 (ns)	I_1 (%)	I_2 (%)	I_3 (%)
25	181	427	2.8	43	55	2
100	185	417	1.4	49	49.5	1.5
300	183	410	1.3	47	52	1
400	178	396	1.6	51	48	1
500	186	343	1.3	44	54.5	1.5

Table 6: Overview of the positron lifetime calculations in annealed Ni_3Al.

Annealing temp (°C)	τ_1 (ps)	τ_2 (ps)	τ_3 (ns)	I_1 (%)	I_2 (%)	I_3 (%)
200	189	342	1.9	35	63.5	1.5
300	183	339	1.6	29	70	1
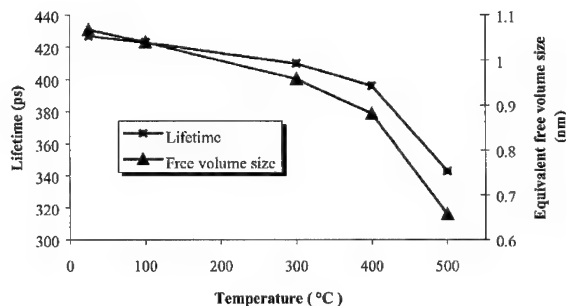
Figure 2: *Positron lifetime and corresponding free volume size as a function of temperature during compaction in nanocrystalline Ni_3Al.*

CONCLUSIONS

Coarse-grained and nanocrystalline Ni-Al samples were investigated by positron annihilation lifetime spectroscopy. In the nanocrystalline samples vacancy-like defects and nano-voids with sizes of about 10 Å were found. These results were compared with positron lifetime calculations in modeled nanocrystalline samples. In one of the considered models, defects of about 1-3 vacancies could be found in the grain boundaries and at triple points, which agrees well with the experimental values. Nano-voids were not described correctly in any model considered. Temperature treatments of nanocrystalline Ni_3Al resulted in a significant decrease of the size of the nano-voids. The vacancy-like defects at grain boundaries were not influenced by this treatment.

ACKNOWLEDGMENTS

REFERENCES

1. P.Hautojärvi and C. Corbel, in *Positron Spectroscopy of Solids*, edited by A.Dupasquier and A.P.Mills, Jr. , (IOS Press, Amsterdam, 1995) p. 491
2. R. M. Nieminen, in *Positron Spectroscopy of Solids*, edited by A.Dupasquier and A.P.Mills, Jr. , (IOS Press, Amsterdam, 1995) p. 443
3. P. G. Sanders, G. E. Fougere, L.J. Thompson, J. A. Eastman and J. R. Weertman, *Nanostructured Materials* **8**, 243 (1997)
4. W.Mondelaers, K.Van Laere, A.Goedefroot and K.Van den Bossche, *Nucl.Inst.Met.A* **368**, 278 (1996)
5. J.Kansy, *Nucl. Instr. Meth.* A **374**, 235 (1996).
6. B.Pauwels, M.Yandouzi, D.Schryvers, G.Van Tendeloo, G.Verschoren, P.Lievens, M.Hou and H.Van Swygenhoven, this proceedings
7. T.Wang, M.Shimotomai and M.Doyama, *J.Phys. F* **14**, 37 (1984)
8. A.DasGupta, L.C.Smedskjaer, D.G.Legnini and R.W.Siegel, *Mat.Sci.For*, **15-18**, 1213 (1997)
9. A.P.Mills and R.J.Wilson, *Phys.Rev. A* **26**, 490 (1982)
10. H.E.Schaefer and R.Würschum, *Phys.Lett. A* **119**, 370 (1987)
11. S.Van Petegem, J.Kuriplach, M.Hou, E.E.Zurkin, D.Segers, A.L.Morales, S.Ettaoussi, C.Dauwe and W.Mondelaers, accepted for publication in *Mat.Sci.Forum* (2001)
12. E.Zhurkin, M.Hou, H.Van Swygenhoven, B.Pauwels, M.Yandouzi, D.Schryvers, G.Van Tendeloo, P.Lievens, G.Verschoren, J.Kuriplach, S.Van Petegem, D.Segers and C.Dauwe, these proceedings
13. J.Kuriplach, S.Van Petegem, M.Hou, E.E.Zhurkin, H.Van Swygenhoven, F.Dalla Torre, D.Segers, A.L.Morales and C.Dauwe, these proceedings

Logarithmic Relaxation of Resistance in Time of Annealed and Plastically Deformed Au$_{80}$Fe$_{20}$

P.Allia[1], M.Baricco[2], E. Bosco[2], M.Coisson[1], D. Falletti[2], V. Selvaggini[1], P.Tiberto[3], F.Vinai[3]

[1]DIFIS-DISPEA, Politecnico di Torino and INFM, Corso Duca degli Abruzzi 24, I-10129 Torino, Italy
[2]IFM, Università di Torino and INFM, Via Pietro Giuria 7, I-10125 Torino, Italy
[3]IEN Galileo Ferraris and INFM, Corso M. d'Azeglio 42, I-10125 Torino, Italy

ABSTRACT

Rapidly solidified Au$_{80}$Fe$_{20}$ ribbons were prepared either by melt spinning or by solid-state quenching of a homogenised master alloy. The as-quenched sample displays a paramagnetic behavior indicating a perfect solid solution of Fe in the Au matrix. Subsequent anneals have been performed to induce the precipitation of Fe particles. X-ray diffraction technique have been exploited to determine the alloy microstructure. The structural stability have been studied by measuring electrical properties in isothermal and tempering condition. The variation of magnetisation and electrical resistance have been measured after submitting the samples to plastic deformation. A logarithmic relaxation of the electrical resistance is observed in all studied samples after deformation. Magnetic hysteresis loops have been measured in as-quenched and annealed samples at different temperatures. X-ray diffraction and magnetic measurements indicate that thermal treatments have been successful in inducing the precipitation of both bcc and fcc Fe clusters.

INTRODUCTION

The Au$_{100-x}$Fe$_x$ magnetic system has been thoroughly studied since many decades owing to its notable magnetic properties at low and high temperature, including magnetic cluster formation, mictomagnetism, superparamagnetism, Kondo effect in various ranges of Fe concentration [1]. The AuFe alloy, usually consisting of very small Fe clusters (composed of a few adjacent Fe atoms) often associated with larger, superparamagnetic Fe particles, is known to be a spin glass [2]. These features make this alloy eligible as a system displaying giant magnetoresistance [3]. Metastable metallic alloys rapidly quenched from the melt are usually characterised by attractive physical properties [4]. Thermal treatments, acting to modify the structure and properties of Au-Fe metastable systems may lead to Fe precipitation and to a stabler configuration. The study of relaxation processes of magnetic and electrical properties, strictly connected to the intrinsic metastability of the alloy, becomes of particular relevance to gain a better knowledge of application-oriented properties. In particular, the electrical resistance in AuFe alloys has been shown to change with time after being submitted to mechanical deformation [5,6]. This peculiar behavior has been explained by off-equilibrium displacement of defects/vacancies induced by plastic deformation, whose relaxation is connected to the time variation of the electrical resistance [5,6].
In this work, the microstructural and compositional stability of rapidly quenched Au$_{80}$Fe$_{20}$ have been studied and related to the relaxation of magnetic and electrical properties.

EXPERIMENTAL

$Au_{80}Fe_{20}$ alloys were produced either by rapid solidification from the melt (using a standard melt-spinning apparatus in vacuum), or by solid-state quenching. In the first case, continuous ribbons were formed (width 2 mm, average thickness 120 μm), while in the latter one, platelets were obtained and subsequently laminated to a thickness of 150 μm. The samples for magnetic and electrical measurements were produced either by cutting ribbon pieces or by platelet punching. The composition (routinely verified by SEM and lattice-constant measurements through X-ray diffraction) was chosen in order to deal with a system paramagnetic at room temperature and above (the Curie temperature of homogeneous $Au_{80}Fe_{20}$ occurs at 290 K) [7]. Low-temperature furnace anneals for long times (up to 200 hrs at $T_a = 593$ K), i.e., well below the *solvus* temperature, were chosen in order to enhance the tendency towards heterogeneity of quenched samples, which are supposedly fully homogeneous. In this system, homogenisation anneals usually involve much higher temperatures ($T_a = 1173$ K) [7].

Magnetic measurements were performed at a maximum applied field $H_{max} = \pm 20$ kOe in the temperature range 300 K $\leq$ T $\leq$ 620 K by means of a vibrating-sample magnetometer (VSM). The measuring temperature was monitored by a compensated thermocouple placed in close proximity of the sample. Electrical resistance measurements were performed as a function of time and temperature by means of a standard four-probe technique with soldered contacts using a digital bridge.

Selected samples were plastically deformed by applying a pressure of the order of 10 MPa for a fixed time (10 s). Magnetic and electrical properties were studied as a function of deformation. The time evolution of electrical resistance and magnetization were studied on stressed annealed and as-quenched samples.

RESULTS

X-ray diffraction patterns of selected $Au_{80}Fe_{20}$ annealed and as-cast ribbons are reported in Fig. 1. The anneals resulted substantially ineffective in inducing massive Fe precipitation from the solid solution, because only the peaks of the solution Au-fcc are visible in the spectra. The fcc lattice constant a_0 can be calculated by properly analysing the XRD patterns. As shown Table I the resulting a_0 values stay almost constant for all heating treatments at $T_a = 673$ K. A slight increase in a_0 is seen both in samples annealed for a much longer time at $T_a = 593$ K and in those annealed at temperatures higher than 673 K, indicating a slight reduction of the Fe content in the solid solution, related to a precipitation reaction. The maximum change in Fe content, estimated by X-ray diffraction data, is limited to 8.2 ‰ after annealing at 773 K for 16 hours.
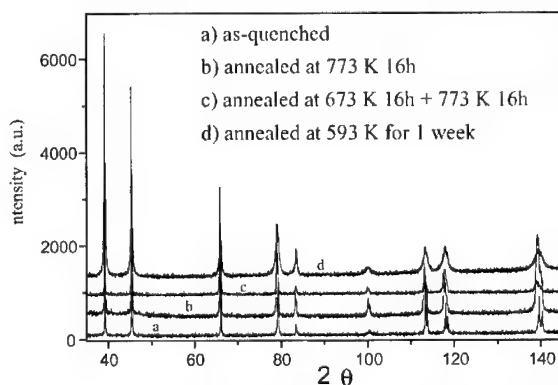
Fig.1 - X-ray diffraction patterns of selected $Au_{80}Fe_{20}$ ribbons.

a) as-quenched
b) annealed at 773 K 16h
c) annealed at 673 K 16h + 773 K 16h
d) annealed at 593 K for 1 week

Sample	a_0 (Å)	% at. Fe
as quenched	4.0239 ± 6.1E-4	19.59 ± 0.2
673 K, 2h	4.0239 ± 3.4E-4	19.70 ± 0.11
673 K, 4h	4.0238 ± 1.0E-4	19.62 ± 0.30
673 K, 16h	4.0235 ± 4.0E-4	19.83 ± 0.12
593 K, 168h	4.0265 ± 2.0E-3	18.88 ± 0.65
773 K,16h	4.0285 ± 3.8E-4	18.24 ± 0.12
16h at 673 K + 16h at 773 K	4.0288 ± 4.5E-4	18.14 ± 0.15

Table I - Lattice constant of the $Au_{80}Fe_{20}$ solid solution and Fe concentration as a function of annealing.

The variation of electrical properties have been measured in isothermal and tempering conditions. The electrical resistance is reported in Fig. 2 as a function of temperature for $Au_{80}Fe_{20}$ as-cast platelet (curve (a)), annealed at $T_a = 698$ K for 16h (curve (b)) and annealed at $T_a = 773$ K for 16h (curve (c)). Sharp compositional or phase transitions are not observed in the as-quenched material (no abrupt resistance variation during heating and cooling). The room-temperature resistance value is seen to be lower in both annealed samples with respect to the as-cast material. As expected, for all studied samples R is seen to increase with increasing temperature up to a broad minimum occurring at T = 823 K. For T > 823 K, R increases again, eventually reaching the solid solution value. Further measurements were performed by submitting an as-received sample to the thermal history plotted in Fig. 3 (bottom).

The time dependence of the electrical resistance, measured in isothermal conditions at the reported temperatures, is shown in Fig. 3 (top). These temperature values were selected in order to follow the nucleation/growth process. The electrical resistance is observed to decrease as a function of time for T = 703 K. The same behavior is observed at a higher temperature (T = 798 K) which is close to the *solvus* line (approximately at T= 823 K). Room temperature mechanical
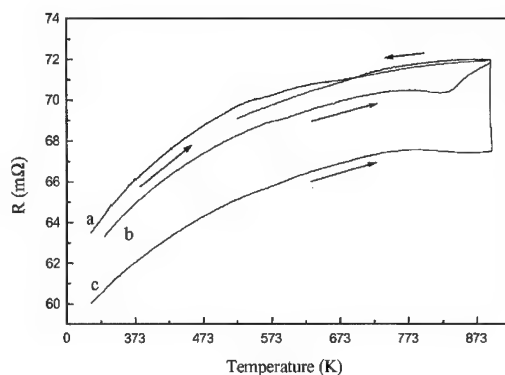
Fig. 2 - Isochronal resistance variation in as-quenched and annealed $Au_{80}Fe_{20}$. See details in text.
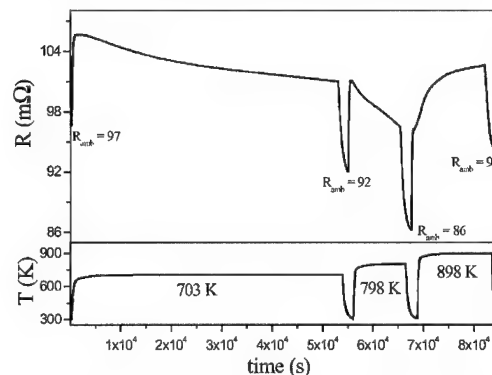
Fig. 3 - Time variation of electrical resistivity of an as-quenched sample of $Au_{80}Fe_{20}$ submitted to the thermal history shown below.

treatments inducing a plastic deformation were applied to as-cast and annealed ribbons in order to study their effect on structure-sensitive properties such as electrical resistivity and magnetic susceptibility. The electrical resistivity measured immediately after deformation appears to be higher than the value observed in the undeformed sample. The time evolution of the room-temperature resistivity, reported as the relative variation $\Delta R/R_i$ % (defined as [R(t)-R(t=0)]/R(t=0) x 100]), is shown in Fig. 4 (top) for as-quenched and annealed $Au_{80}Fe_{20}$ ribbons. All curves display a non-saturating logarithmic behavior. The normalised $\Delta R/R_i$ curves measured in the $Au_{80}Fe_{20}$ as-quenched ribbon and in a sample of pure Au are reported in Fig. 4 (bottom).

Selected magnetization curves measured in an as-quenched sample after subsequent plastic deformations are shown in Fig. 5. It should be noted that in this case the magnetization is always linear with the applied field over the entire magnetic field-range, with no detectable hysteresis.

Fig. 4 - Isothermal relaxation of electrical resistivity of $Au_{80}Fe_{20}$ after plastic deformation.

The initial magnetic susceptibility χ is reported in Fig. 6 as a function of the number of subsequent deformations. Susceptibility measurements were also performed as functions of time after a single plastic deformation. Immediately after deformation, the magnetization at H = 10 kOe (proportional to the magnetic susceptibility) is lower than the value measured before; M is seen to subsequently relax towards a higher value, corresponding to that of the unstressed sample. The time behavior of $\Delta M/M_i$ (defined as [M(t)-M(t=0)]/M(t=0) x 100]) is reported in Fig. 7. Although such a relaxation is again of logarithmic type, its kinetics appears to be slightly different from the one of the electrical resistance.

DISCUSSION

Electrical resistivity measurements in isothermal and tempering conditions (Figs 2-3) were performed in order to evaluate the alloy stability and to study the precipitation process kinetics. Transport properties have been usually exploited owing to their dependence on the transformations occurring in metastable systems.

As shown in Fig. 2, the room-temperature resistance value of annealed samples is lower than the one of the as-cast material indicating a decrease of Fe content in the solid solution in the starting material. Moreover, the resistance increase observed with increasing temperature is presumably related to an enhanced formation of additional Fe clusters. The increase in R following the occurrence of the minimum indicates re-dissolution of Fe clusters and full homogenization of the solid solution. On the other hand, the decrease of the electrical resistance observed in isothermal conditions (see Fig. 3) at $T_a = 703$ K and $T_a = 798$ K can be ascribed to the decrease of Fe concentration in the metallic matrix. By performing an isothermal treatment at higher temperature (898 K, for four hours), R is seen to approximately reach the initial value indicating a tendency to re-dissolution of Fe clusters in the matrix. The processes of particle formation from the solid solution and of particle re-dissolution in the solid solution are therefore almost completely reversible. The electrical resistance relaxation reported in Fig. 4 may be ascribed to the annihilation of an excess
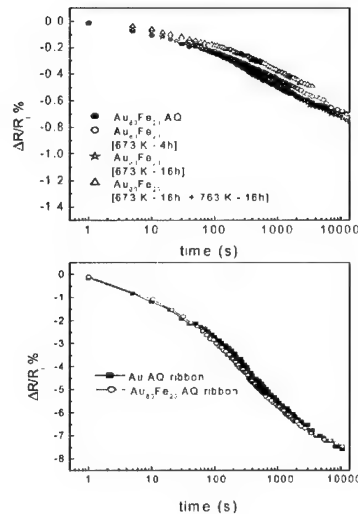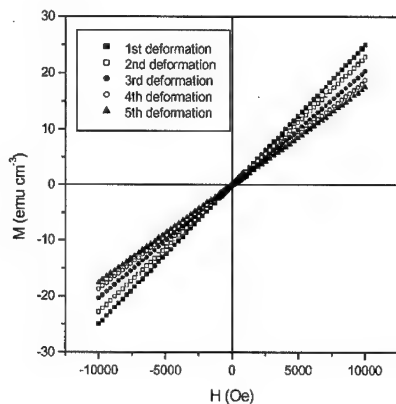
Fig. 5 - Room-temperature paramagnetic magnetization of the same $Au_{80}Fe_{20}$ sample after subsequent deformations.
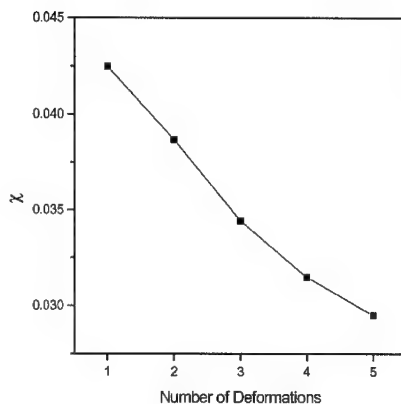
Fig. 6 - Room-temperature magnetic susceptibility of $Au_{80}Fe_{20}$ with number of subsequent deformations.

number of scattering centres (vacancies or dislocations) introduced by deformation. On the other hand, these Au-Fe systems have been shown to display a tendency towards segregation of Fe nanoclusters by effect of thermal treatments and/or plastic deformation [5,6]. Such a mechanism should give rise to a different effect, i.e., a sudden decrease of R immediately after deformation, followed by an upward relaxation to the equilibrium value. In our opinion, in the present case the electrical resistivity variation is dominated by effects of defect annihilation, overwhelming those of Fe cluster segregation. The latter phenomenon affects instead the magnetic properties of the samples, as discussed below. This conclusion is supported by the close analogy existing between the $\Delta R/R_i$ curves observed in the $Au_{80}Fe_{20}$ as-quenched ribbon and in a sample of pure Au, (see Fig. 4, bottom), where the relaxation kinetics of the two samples is virtually the same. Annealed samples of $Au_{80}Fe_{20}$ are characterised by curves displaying the presence of processes with higher time-constant values with respect to the as-quenched material. This may be ascribed to the existing differences among the microstructures (as-quenched ribbons: nearly homogeneous solid solution, annealed ribbons: presence of Fe nanoclusters in the AuFe matrix, as discussed previously). The magnetic susceptibility is instead sensitive to possible changes in the number and size of Fe clusters. Magnetic measurements were therefore performed at room temperature on samples submitted to the same mechanical treatments giving rise to the resistivity relaxation described above. The pure paramagnetic behavior observed by measuring the magnetisation curves is well described at room temperature and above by a Curie-Weiss law of the form $\chi = N \mu^2_{eff}/3k(T-T_c)$, where N is the number of magnetic particles, k is the Boltzmann constant, μ_{eff} is the effective magnetic moment value. This circumstance implies that the as quenched ribbon is still a nearly-homogeneous solid solution of the two elements. However, the values of μ_{eff} and T_c obtained for the unstressed sample are respectively higher and lower than those found in a homogenized, bulk $Au_{80}Fe_{20}$ [7] (see Table II). Usually, both circumstances are associated to a tendency towards the formation of additional atomic-scale Fe clusters (involving a few Fe atoms each) out of the AuFe matrix. Therefore, our results indicate that in the present case atomic-scale Fe clusters are already present.

Subsequent mechanical deformations of the same sample induce a progressive decrease of the slope of the M(H) curve. This peculiar feature is evidenced in Fig. 6 reporting the initial magnetic susceptibility χ as a function of the number of subsequent deformations.

Since a single process of plastic deformation at room temperature does not give rise to detectable nucleation of either nanometric bcc-Fe particles (which should bring about a magnetic hysteresis) or of nanometric fcc-Fe particles, the observed variations of χ must be ascribed to variations in T_c and/or μ_{eff}. These two parameters, obtained as usual by plotting $1/\chi$ vs. T, are shown in Table II for the same sample in the as-received state and immediately after deformation. The deformed sample appears to be characterized by a higher μ_{eff} and a lower T_c with respect to the unstressed one. This result can be again interpreted in terms of an increased concentration of very small subnanometric Fe clusters. Such a clusterizing effect over very short distances

Fig. 7 - Isothermal relaxation of magnetic susceptibility of $Au_{80}Fe_{20}$ after plastic deformation.

may be related to the presence of the excess number of defects introduced by deformation and evidenced by the behavior of the electrical resistivity. In any case, the nearly-logarithmic increase in χ towards the value characterizing the unstressed sample (see Fig. 7) should be related to an effect of re-dissolution of these new Fe clusters, possibly associated with the annihilation of the stress-induced defects. These atomic ordering processes, involving displacements over distances of the order of the lattice constant, are likely to occur even at room temperature.

In conclusion, combined measurements of the relaxation of electrical resistivity and magnetic susceptibility give an adequate picture of the microscopic processes introduced by plastic deformation in these rapidly solidified materials, and of their interplay.

$Au_{80}Fe_{20}$	$\mu_{eff} (\mu_B)$	$T_c (K)$
Homogenized Platelet, after [7]	4.5	290
Ribbon, Relaxed	6.5	230
Ribbon, After Stress	6.71	224

Table II - Effective magnetic moment and Curie Temperature of selected samples.

ACKNOWLEDGMENTS

REFERENCES

[1] G. Zibold, *Landolt-Bornstein: Magnetic Properties of Metals*, Vol. 19b, ed. H.J. Wijn, (Springer-Verlag, 1987) pp. 111-123
[20] J.A. Mydosh, *Spin Glasses, An Experimental Introduction*, (Taylor & Francis, London, 1993), Sec. 3.2.1 and 3.2.3
[3] J. Xu, B.J. Hickey, M.A. Howson, D. Greig, R. Cochrane, S. Mahon, C. Achilleos and N. Wiser, *Phys. Rev. B* **56**, 14602 (1997)
[4] F.E. Luborski, *Amorphous Metallic Alloys*, ed. F. E. Luborski (Butterworths, London, 1983) p. 1
[5] P. Meisterle and W. Pfeiler, *Phys. Status Solidi A*, **80**, K87 (1983)
[6] M. Migschitz, F. Langmayr and W. Pfeiler, *Mat. Sci. Eng. A*, **177** (1994)
[7] E. Scheil, H. Specht, and E. Wachtel, *Z. Metallkde* **49**, 590 (1958)

The Effect of Deposition Parameters on Tensile Properties of Pulse-Plated Nanocrystalline Nickel

K. L. Morgan, Z. Ahmed, and F. Ebrahimi
Department of Materials Science and Engineering, University of Florida,
Gainesville, FL 32611, U.S.A.

ABSTRACT

The microstructure and tensile properties were investigated for pulse-plated nanocrystalline nickel electrodeposits prepared from an additive-free sulfamate-based solution. Square-wave cathodic current densities were varied from 25 to 75 mA/cm^2. The samples deposited at 25 mA/cm^2 showed the smallest grain size (d ~ 12 nm), and the grain size was found to increase with increasing current densities. The grain size of the electrodeposits ranged from approximately 27 to 12 nm. Tensile results indicated that the yield strength of the specimens increased with decreasing grain size. Scanning electron microscopy revealed that all electrodeposits fractured through a ductile mechanism.

INTRODUCTION

Electrodeposition has successfully been used to fabricate metallic nanostructures [1]. The commercial plating industry has recently adopted the pulse-plating deposition technique due to its ability to produce finely grained coatings with less surface roughness. Pulse-plating differs from conventional plating in that it utilizes interrupted DC current to deposit metal ions onto a substrate. A series of equal-amplitude DC pulses are delivered for a short time (t_{on}), and separated by longer times (t_{off}) of zero current. Generally, as the current density delivered to the working electrode increases, the overpotential at the electrode increases, which increases the driving force for nucleation. Therefore, by using the pulsed electrodeposition technique and increasing the current density, deposits with increasingly finer grain sizes are expected to be produced. The objective of this study has been to investigate the effect of pulsed-current density on the microstructure and tensile properties of electrodeposited nanocrystalline nickel fabricated without the use of grain-refining organic additives.

EXPERIMENTAL PROCEDURES

A conventional three-electrode cell with a copper rotating disk working electrode, a parallel Pt foil anode, and a saturated calomel reference electrode (SCE) was used in this study. The copper substrate (diameter = 35 mm) was annealed at 150°C and electropolished before deposition. The working electrode was rotated at a speed of 400rpm. Pulsed current densities of 25, 50, and 75 mA/cm^2 were used in the investigation. The pulse cycles were composed of t_{on} = 1ms and t_{off} = 9ms. The deposition ran for 54 to 72 hours to achieve a deposit thickness of ~ 25 µm. The electrolyte used in the study was a sulfamate solution containing 90 g/L Ni, 15 g/L boric acid, and .075 g/L sulfamate-nickel-anti-pit (SNAP). The pH of the solution was adjusted to 4.7 through additions of nickel carbonate. After adding nickel carbonate, the solution was

vacuum-filtered. Prior to deposition, the electrolyte was deaerated with nitrogen for one hour. During all depositions, the solution temperature was maintained at 30°C.

The deposits were cut into four rectangular strips (area ~ 25 mm x 5 mm). The copper substrate was chemically dissolved from the nickel strips using a commercial copper stripper. X-ray diffraction (XRD) was performed on both the solution side and substrate side of the strips in order to evaluate the crystallographic texture and grain size of the nickel deposits (*substrate side*: Ni adjacent to substrate; *solution side*: Ni at solution interface). The Warren-Averbach (WA) and Single-line (SL) methods were both used to approximate the average crystallite size of the samples. The (200) and (400) peaks were used for the WA analysis. The SL analysis used only the (200) peak.

The strips were then individually filed into dog-bone tensile specimens (width = 3 mm, gage length = 10mm). Tensile testing was performed at room temperature using a strain rate of 0.002 s^{-1}. Fracture surfaces of the tensile specimens were investigated using scanning electron microscopy (SEM).

Thin foils for transmission electron microscopy (TEM) were prepared by jet polishing. The grain size was measured from dark-field images obtained at various tilt angles. Grain size measurements were taken from over 150 grains. In order to evaluate the grain size, the lengths of the longest grain direction and the perpendicular to this direction were measured. The grain size distribution and the average grain size were evaluated from these data.

RESULTS AND DISCUSSION

The XRD data for the Ni deposits is shown in Table 1. The texture of the samples was determined from the ratio of the (200) peak intensity to the (111) peak intensity ($I_{(200)}/I_{(111)}$). The deposits showed a change in texture through their thickness. The substrate side grains favored a <200> crystallographic texture, reflecting the crystallographic rolling plane of the copper substrate. However, the $I_{(200)}/I_{(111)}$ ratio decreased from a strong <100> orientation on the substrate side toward randomness ($I_{(200)}/I_{(111)} \sim 0.5$) on the solution side. This decrease in the <100> texture usually reflects grain refinement through the deposit thickness [3]. Consistently the deposits showed smaller grain sizes on the deposit solution side than on the substrate side. It should be noted that this change in grain size occurs within the first 1-2 μm from the substrate size. Therefore, the solution side grain size more accurately represents the average grain size of the deposit.

The correlation between texture and grain size can also be noticed by comparing the two deposits that were both made at 25 mA/cm^2. Note that although the samples 1-4 were all deposited at the same current density, the $I_{(200)}/I_{(111)}$ ratio and the substrate side grain size of samples 3,4 are considerably greater than those of samples 1,2. The difference in the strength of <100> texture, and corresponding grain sizes, results from the influence of the copper substrate. Substrate effects are difficult to control and can markedly vary the microstructure of the deposit. However, the substrate surface condition had negligible influence on the average grain size of the deposits, since the samples had comparable solution side grain sizes.

The average sample grain sizes and their associated variations as measured by the WA and SL methods are given in Table 1. The variation in each sample grain size primarily reflects its grain size distribution and also includes the measurement error. The SL method consistently

Table I. XRD and TEM results

Sample	Current Density (mA/cm^2)	Average Thickness (μm)	$I_{(200)}/I_{(111)}$		Crystallite Size (nm)				TEM
					WA		SL		
			sub	sol	sub	sol	sub	sol	
1,2	25	21.0	2.1	1.7	10.1 ± 3.0	9.0 ± 2.7	15.7 ± 11.1	12.1 ± 7.3	-
3,4	25	21.6	36	1.6	44.8 ± 21.3	NA	74.9 ± 12.5	12.0 ± 5.8	-
5,6	50	27.8	330	3.9	121 ± 80.1	16.9 ± 5.1	165 ± 71.2	22.3 ± 2.1	-
7,8	75	26.0	72	7.0	28.2 ± 8.5	16.3 ± 4.9	87.5 ± 21.9	26.6 ± 1.6	27.4

estimated larger grain sizes than the WA method for each sample. The grain size measured from TEM images was similar to the SL estimate, but was greater than the WA estimate for the solution side of the sample deposited at 75 mA/cm². XRD methods usually measure a smaller grain size because of the inclusion of small-angle boundaries (such as twin boundaries) in the analysis. The TEM grain size measurements were taken only between high-angle boundaries, thus yielding a larger average grain size.

Generally as the current density increases, the overpotential at the electrode increases, which enhances the driving force for nucleation [4]. However the samples deposited at 25 mA/cm² showed the smallest average grain sizes, and the grain size of the deposits increased by increasing the current density. The trend of decreasing grain size with decreasing current has also been recognized in direct-current (DC) electrodepositions of Ni [5]. Bakonyi *et al.* [6], suggested that the increase in nucleation rate for Ni depends not only on the current density amplitude, but also on the concentration of Ni^{2+} at the electrode/solution interface. In DC plating, if the concentration of Ni^{2+} at the interface is less than the concentration of Ni^{2+} in the bulk electrolyte, then the rate of nucleation of Ni at the electrode will decrease and a large-grained deposit is produced. Similarly in pulse-plating, as the current density amplitude of the pulse increases, more Ni^{2+} is depleted from the electrode/solution interface [7]. If the t_{off} is insufficient to replenish the Ni^{2+} concentration at the interface, then the nucleation rate of Ni will decrease and a larger-grained deposit will result. Since the t_{on}/t_{off} pulse cycle was held constant for all current densities in these experiments, the trend of increasing grain size with increasing current density could result from a greater Ni^{2+} depletion at the electrode/solution interface. It is suggested that at increased current densities, t_{off} should be extended or the rotation speed should be increased in order to eliminate the concentration gradient of Ni^{2+} at the electrode/solution interface and perhaps produce finer-grained deposits.

The stress-strain curves for the samples are shown in Figure 1. The following tensile properties were measured for each sample: 0.2% offset yield strength ($\sigma_{0.2\%}$), 0.1% offset yield strength ($\sigma_{1.0\%}$), ultimate tensile strength (σ_{UTS}), total plastic strain ($\%e_f^p$), and total strain ($\%e_{total}$). The tensile data are summarized in Table 2. The tensile data are consistent among the specimens from the same deposits. The samples deposited at 25 mA/cm² and 75 mA/cm² showed high σ_{UTS} values, which correspond to their fine grain sizes. The samples deposited at 50 mA/cm² displayed the lowest strength and largest grain sizes. The samples from the deposit made at 75 mA/cm² had an average grain size of 27.4 nm (measured from TEM) and an average σ_{UTS} of 1320 MPa. This value is lower than 1450 MPa which has been reported for a nanocrystalline Ni sample produced by the inert gas condensation method with an average grain

size of 28 nm [8]. Though comparable, the difference in measured σ_{UTS} data may be attributed to different processing procedures. The samples deposited at 25 and 75 mA/cm^2 both showed high strain-hardening rates and low ductility. The samples deposited at 50 mA/cm^2 displayed the lowest strain-hardening rate and the greatest ductility.
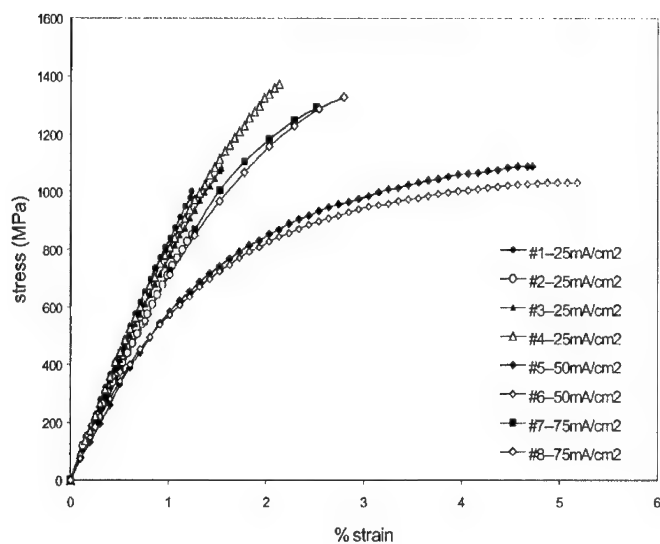
Figure 1. *Stress-strain curves for the electrodeposits.*

Table II. Tensile data for the electrodeposits.

Sample	Current Density (mA/cm^2)	Thickness (μm)	$\sigma_{0.2\%}$ (MPa)	$\sigma_{1.0\%}$ (MPa)	σ_{UTS} (MPa)	%e$_f^p$	%e$_{total}$
1,2	25	20.0	NA[*]	NA[**]	1001	~ 0	1.24
		21.9	NA[*]	NA[**]	852	~ 0	1.24
3,4	25	21.4	NA[*]	NA[**]	1081	~ 0	1.54
		21.7	NA[*]	NA[**]	1372	~ 0	2.13
5,6	50	27.4	489	710	866	3.18	4.72
		28.1	462	702	842	3.84	5.18
7,8	75	27.0	961	NA[**]	1291	0.8	2.5
		25.0	913	1328	1340	1.1	2.9

NA[*] -- The samples broke in the linear range. $\sigma_{0.2\%}$ could not be measured.
NA[**] -- The total plastic strain was less than 1%, and $\sigma_{1.0\%}$ could not be measured.
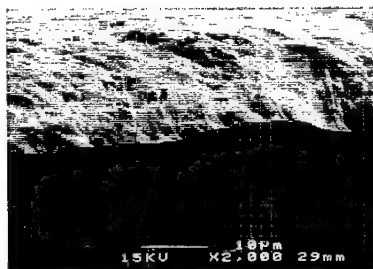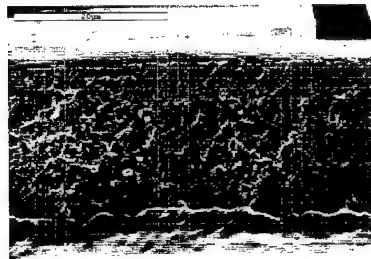
(a)   (b)

Figure 3. *(a) SEM fractograph depicting typical knife-edge fracture surface of the samples deposited at 50 and 75 mA/cm². (b) SEM fractograph showing necking and microvoid coalescence of sample deposited at 25 mA/cm².*
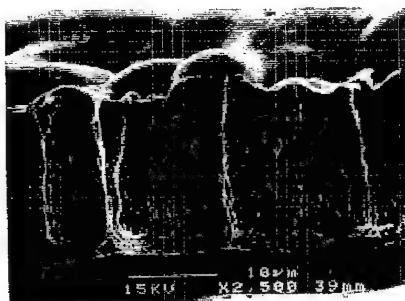
Figure 4. SEM image of nodules found in localized areas on the fracture surface of the sample deposited at 75 mA/cm².

A study of all fracture surfaces revealed that plastic instability (necking) preceded fracture in the nanocrystalline Ni samples. Figure 3 presents SEM fractographs of the tensile specimens. The samples deposited at 50 and 75 mA/cm² primarily showed knife-edge fracture behavior characteristic of pure FCC metals, as shown in Fig.3a. The pre-mature fracture and low ductility of the tensile specimens from the 75 mA/cm² deposit were found to be associated with nodule formation. Figure 4 shows an SEM image revealing nodule formation in the sample deposited at 75 mA/cm². These nodules were found only on a few spots on the solution side of the samples. Note the presence of columnar features along the deposition direction. It is suggested that defective columnar grain growth under the nodules causes inter-columnar brittle fracture [9].

These nodules usually develop randomly, and often their development is associated with the formation of large hydrogen bubbles at the deposit interface.

The samples deposited at 25 mA/cm^2 fractured by the microvoid coalescence mechanism, and as shown in Figure 3b., necking was more prevalent to one side of the specimen. The microvoid coalescence mechanism requires void initiation. In pure nanocrystalline metals fabricated by electrodeposition, the ultra-fine pores produced by hydrogen incorporation in the deposit are the source of void initiation [5]. These pores promote pre-mature plastic instability of the specimens deposited at 25 mA/cm^2 and led to fracture by microvoid coalescence. Note that if these samples had not necked pre-maturely, their yield strengths would be considerably higher than the strengths seen in Table 2.

CONCLUSIONS

Very small grain sizes as low as 12 nm can be achieved in electrodeposited nickel without additions of organic grain refiners. The results of this study indicate that increasing the pulse current density did not result in grain refinement and the grain size actually increased. Defects, such as nodules and ultra-fine voids, lead to pre-mature plastic instability and decrease the ductility and apparent yield strength of the deposits.

ACKNOWLEDGEMENT

REFERENCES

1. F. Ebrahimi, D. Kong, T. E. Matthews, and Q. Zhai, in *Processing and Fabrication of Advanced Materials VII*, edited by T .S. Srivastan and K. A. Khor (TMS Publication, Warrendale, PA, 1998), p. 509.
2. A. M. El-Sherik and U. Erb, J. Mater. Sci. **30**, 5743 (1995).
3. F. Ebrahimi, G. R. Bourne, M. S. Kelly, and T. E. Matthews, NanoStructured Mater. **11** (3), 343 (1999).
4. W. Schmickler, *Interfacial Electrochemistry* (Oxford University Press, New York, 1996) p.129.
5. Z. Ahmed, *Synthesis and Deformation of Nanocrystalline Nickel*, M. S. Thesis (2000).
6. I. Bakonyi, E. Tóth-Kádár, L. Pogány, A. Cziráki, I. Gerocs, K. Varga-Josepovits, B. Arnold, K. Wetzig, Surface and Coatings Tech.**78**,124 (1996).
7. E. Tóth-Kádár, I. Bakonyi, L. Pogány, and A. Cziráki, Surface and Coatings Tech. **88**, 57 (1996).
8. J. R. Weertman, D. Farkas, K. Hemker, H. Kung, M. Mayo, R. Mitra, and H. Van Swygenhoven , MRS Bulletin. **24** (2), 48 (1999).
9. F. Ebrahimi, Q. Zhai, D. Kong, Mater. Sci. Eng. **A255**, 20 (1998).

EXTENSION OF HIGH CYCLE FATIGUE LIFE BY THE FORMATION OF NANO-SIZED MARTENSITE PARTICLES AT INTERSECTIONS OF DISLOCATIONS IN AN AUSTENITIC STAINLESS STEEL

T. Inamura, M. Shimojo, K. Takashima and Y. Higo
Precision and Intelligence Laboratory, Tokyo Institute of Technology, Nagatsuta-cho, Midori-ku, Yokohama, 226-8503, Japan

ABSTRACT

A new fatigue strengthening method which is applicable for both the micro-sized materials and ordinary-sized materials have been proposed. Dislocations are pinned at their intersections by the formation of nano-crystals after cold work in this strengthening method. Nano-sized α'-martensite particles, the diameter of which was approximately 5 nm, were formed by a cryogenic treatment at a certain temperature above $M_{s\alpha}^{b}$ (martensite burst starting temperature) in a commercially available 316-type austenitic stainless steel. These nano-particles are considered to be formed at intersections of dislocations. Fatigue life tests using ordinary-sized specimens revealed that high cycle fatigue life of the 316-type austenitic stainless steel was extended by the cryogenic treatment and this is considered to be due to the pinning of dislocations by the formation of nano-sized α'-martensite particles.

Keywords : fatigue life extension, pinning dislocations, nano-sized α'-martensite

INTRODUCTION

MEMS devices and/or micromachines have been intensively developed for the use in information technology, bio-medical technology and so on. The size of the components of these machines will be in the order of microns or sub-microns. Fatigue strength is one of the most important properties in micro-sized materials because the maintenance or the exchange of the damaged elements is practically impossible in such tiny machines. Thus, the development of a fatigue strengthening method for micro-sized materials is extremely beneficial. For micro-sized materials, the microstructure which is beneficial for the improvement of fatigue properties must be smaller than sub-micron, i.e. in the order of nanometer, to minimize the microstructural heterogeneity which is increased by the miniaturization of materials. Dispersion hardening using nano-crystals and work-hardening are adequate methods for the strengthening of micro-sized materials from the point of view that the size of the strengthening microstructure (nano-sized crystals, dislocation) is in the nanometer order. However, neither of them are designed for fatigue strengthening, but for an increase in tensile strength. In many cases, dislocations cut dispersed nano-crystals and then re-solution of the precipitates occurs under cyclic stresses. Fatigue softening is caused by cyclic loading in work-hardened materials due to the re-arrangement of dislocations. Therefore, neither of the methods is so effective on fatigue strengthening.

We propose a new fatigue strengthening method which is a combination of nano-crystal-dispersion and cold-work. Fatigue of metallic materials is mainly due to the accumulation of irreversible motion of dislocations. Pinning dislocations at their intersections by nano-crystals after cold-work is considered to be an effective method for the suppression of

Figure 1: *Schematic of the concept of the new fatigue strengthening method. Intersections of dislocations are pinned using nano-crystals after cold work.*
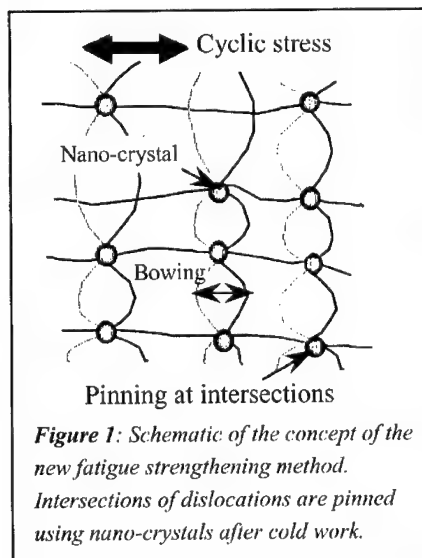
the accumulation of microscopic damage. Figure 1 shows a schematic illustration of the concept of the pinning by nano-crystals. The motion of pinned dislocations is expected to become bowing motion under cyclic stress and not to cause re-arrangement of dislocations under cyclic stress. The cyclic plastic deformation in this case should be homogeneously distributed, and localized slips or the formation of stress concentrated fields should be suppressed. Consequently, fatigue lives of materials are expected to be extended using this strengthening method. It should be noted that this strengthening method is not supposed to suppress plastic deformation, but to suppress the accumulation of the plastic deformation under cyclic stress. This strengthening method is considered to be effective on both the micro-sized materials and the ordinary-sized materials.

According to the model proposed by Bogers and Burgers [2], some of the intersections of partial dislocations in f.c.c. metals are expected to have b.c.c.-like stacking. It is well known that α'-martensitic transformation is caused by simple cooling and/or deformation in metastable austenitic stainless steels [3-5]. In austenitic stainless steels, the b.c.c.-like stacking regions are considered to be preferential nucleation sites of α'-martensite. The b.c.c.-like stacking regions may transform into very fine α'-martensite particle by means of careful temperature control above $M_{s\alpha}^{b}$ temperature during cooling. ($M_{s\alpha}^{b}$ temperature is defined as the temperature at which spontaneous burst-like α'-martensitic transformation occurs during cooling in this study.) These very fine martensites are considered to be able to pin dislocations because b.c.c. stacking (nano-sized.martensite) is incoherent to f.c.c. stacking (austenite).

In our previous study [1], the formation of nano-sized α'-martensite particles (diameter of approximately 5nm) was confirmed in 304-type and 316-type austenitic stainless steels which had been cryogenically treated above their $M_{s\alpha}^{b}$ temperatures and these particles are considered to be formed at intersections of dislocations. High cycle fatigue lives of a 304-type austenitic stainless steel were extended without any decrease in ductility by the formation of nano-sized α'-martensite particles [6] or micro-sized α'-martensites [7]. Therefore, high cycle fatigue lives of 316-type austenitic stainless steel is also expected to be extended by the formation of nano-sized α'-martensites.

The purpose of the present study is to investigate the effects of nano-sized α'-martensites on high cycle fatigue life of a 316-type austenitic stainless steel.

EXPERIMENTAL PROCEDURE

The material used in this study was a hot-rolled 316-type (Fe-18Cr-10Ni-2Mn-2Mo-0.06C) austenitic stainless steel which is commercially available. The grain size was approximately

50μm.   The chemical composition of the received rods were the same as used in our previous study [1].   Normal-sized rotary bending fatigue specimens were machined from the received rods.   The sub-surface layer of the fatigue specimens was considered to be cold-worked during machining.   Half the specimens were cryogenically treated at 195 K ($M_{s\alpha}^{b}$ temperature of this material is lower than 77 K) to form nano-sized α'-martensite particles [1].   These specimens are termed "cooled-specimens" , hereafter.   The other specimens which were not cryogenically treated are termed "non-treated specimens".

Fatigue life tests were carried out using a four-point rotary bending fatigue testing machine at room temperature, at an R-ratio of -1.   The temperature of the specimen surface was measured using an infrared thermometer.   Test frequency was chosen to be set at 2~10Hz so that the temperature of specimen surface did not exceed 313K during the test.   The stress amplitude below which specimen did not fail after 10^7 cycles was defined as fatigue limit in this study.

Scanning laser microscopy (SLM) observation and transmission electron microscopy (TEM) observation were carried out to observe the microstructure of the specimens.   The resolution of the SLM used in this study was less than 1 μm.   The specimens for the SLM observation was cut using a wheel cutter and the work hardened layer introduced during cutting was removed by an electro-polishing technique.   Electro-etching was performed on the observation area using an oxalic acid solution.   Thin films for TEM observation were prepared by twin-jet polishing using an acetic-perchloric acid solution at 273 K.   TEM observations were performed at an accelerating voltage of 200 kV.

RESULTS and DISCUSSION

The as-received rods were fully austenite and no martensites were observed. In our previous study [1], nano-sized α'-martensite particles were confirmed in the specimens which had been cryogenically treated at 195 K and these particles are considered to be formed at intersections of dislocations in the cooled specimens.   Thus, fatigue specimens were cooled down to 195 K also in this study.   Figures 2 represent the typical microstructure of sub-surface region of a specimen (a) before and (b) after the cryogenic treatment at 195 K (the same place of (a), etched again after the cryogenic treatment).   The sub-surface layer of the fatigue specimens is cold-worked during machining and thus includes some amount of "coarse martensites" (optically visible ϵ-martensites (h.c.p.)) which were induced by plastic deformation.   However, no additional
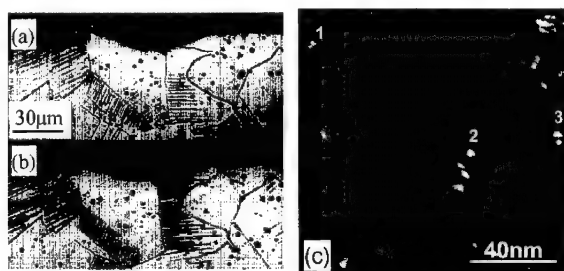
Figure 2 : *(a)SLM image of the surface layer of the specimen before the cryogenic treatment and some deformation induced ϵ-martensites were observed. (b) The same place of (a) after the cryogenic treatment. No additional formation or growth of martensites were observed using the SLM after the cryogenic treatment.*

(c) TEM dark field image of sub-surface layer (depth ~ 50 μm from the surface) shows that nano-sized α'-martensite particles were formed by the cryogenic treatment at 195 K [1].

formation or growth of martensites was observed in the sub-surface layer after the cryogenic treatment at 195 K in SLM observation (the contrast of deformation induced martensites in (b) is higher than that in (a) because etching was performed on the same place again.) Then, TEM observation was carried out. Figure 2(c) shows a dark field image of sub-surface layer using reflection from $(101)_\alpha$ and nano-sized α'-martensite particles, the diameter of which was approximately 5 nm, were observed [1]. These nano-sized α'-martensites were considered to be formed at the intersections of dislocations as mentioned above. It is expected that the formation of nano-sized α'-martensites in sub-surface region can affect fatigue strength of the specimen because the fatigue life tests were performed by rotary bending (stress becomes maximum at the surface in bending).

Figure 3 shows the S-N curves of non-treated specimens and cooled specimens. The arrow indicates that the specimen did not fail after 10^7 cycles of loading. No significant increase in fatigue life was observed in the low cycle regime (Nf < 10^5 cycles) i. e., above the stress amplitude of about 350 MPa in this experiment. However, the fatigue lives of the cooled specimen were longer than that of the non-treated specimens especially in the high cycle regime (Nf > 10^5 cycles). The initiation site of fatal cracks was the surface of the gage area in both the cooled and non-treated specimens. Crack propagation behavior was in a ductile manner in both the specimens, judging from the fracture surface of the failed specimens. The results of fatigue life tests obtained in this study correspond well to that obtained in our previous study using a 304-type austenitic stainless steel [6-7].

In general, the formation of "coarse martensites" has large influence on the fatigue life of metastable austenitic stainless steels [4, 8-10]. The formation of "coarse martensite" is considered to degrade fatigue properties of austenitic stainless steels because the interface between austenite and martensite is a preferential nucleation site of microcracks [8].
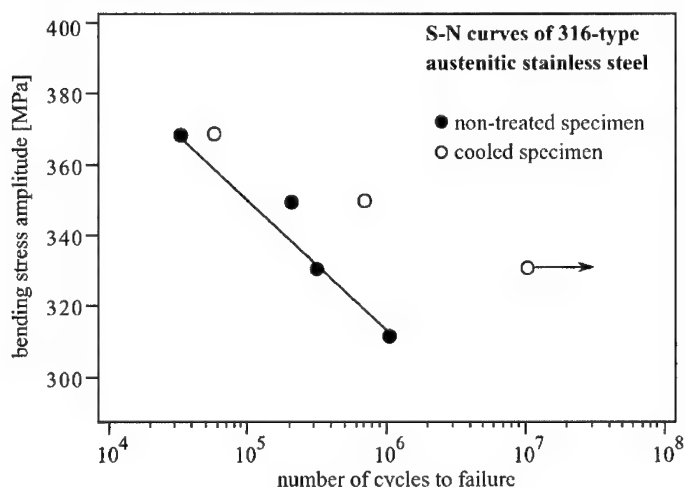
Figure 3 : *S-N curves of non-treated specimens and cooled specimens. Fatigue lives of a 316-type austenitic stainless steel were extended especially in a high cycle regime only by the cryogenic treatment.*

Franke et al. reported that a small amount of "coarse" α'-martensite is beneficial for fatigue strength, but a large amount of it is not beneficial [9]. However, it should be reminded that no "coarse martensites" were formed by the cryogenic treatment in this study. The high cycle fatigue life was extended only by the simple cryogenic treatment at 195 K in this material without any additional formation of "coarse martensites". The only difference in microstructure between cooled specimen and non-treated specimen is the formation of nano-sized α'-martensite. Thus, the extension of high cycle fatigue life is considered to be due to the formation of nano-sized α'-martensite particles. Nano-sized α'-martensite particles are so small (~5nm, [1]) that pinning mechanism cannot operate under a greater stress. This is the reason for the absence of fatigue life extension in the low cycle regime in this study.

A non-treated specimen and a cooled specimen were fatigue damaged under the same condition of fatigue loading to observe the difference in dislocation structures after cyclic loading. Figures 4(a) and 4(b) show typical dislocation structures of a non-treated specimen and a cooled specimen after fatigue loading at a stress amplitude of 331MPa for 5×10^4 cycles, respectively. None of the specimens failed during this fatigue loading as shown in Fig. 3. TEM foils were prepared from the gage areas of both the specimens. Thin foils were taken from subsurface regions, which existed at approximately 100 μm in depth from the surface of the gage area. The formation of dislocation bundles was observed in the non-treated specimen (Fig.4(a)). However, no bundles were observed and the configuration of dislocations seemed to be planar in the cooled specimen. These results indicate that the progression of the rearrangement of dislocations is suppressed in the cooled specimen, compared to that in the non-treated specimen. Thus, the suppression of the rearrangement of dislocations is considered to be the reason for the fatigue life extension and is suggested to be due to dislocation pinning by nano-sized martensites. Thus, the formation of nano-sized α'-martensite particles is confirmed to be effective for fatigue strengthening in normal-sized 316-type austenitic stainless steel, as well as in 304-type austenitic stainless steel.

A goal of this investigation is to improve the fatigue strength of micro-sized austenitic stainless steel specimen. Effects of nano-sized α'-martensite particles on fatigue life of micro-sized austenitic stainless steel specimens will be investigated using the micro-fatigue-testing machine (MFT 2000, [11]) in the near future.

CONCLUSIONS

Extension of high cycle fatigue life of a commercially available 316-type austenitic stainless steel was accompanied by the formation of nano-sized α'-martensite particles. Fatigue life extension in a high cycle regime was considered to be achieved by the retardation of the rearrangement of dislocations under cyclic stress. The rearrangement of dislocations was supposed to be suppressed by the pinning at their intersections by nano-sized α'-martensite particles.
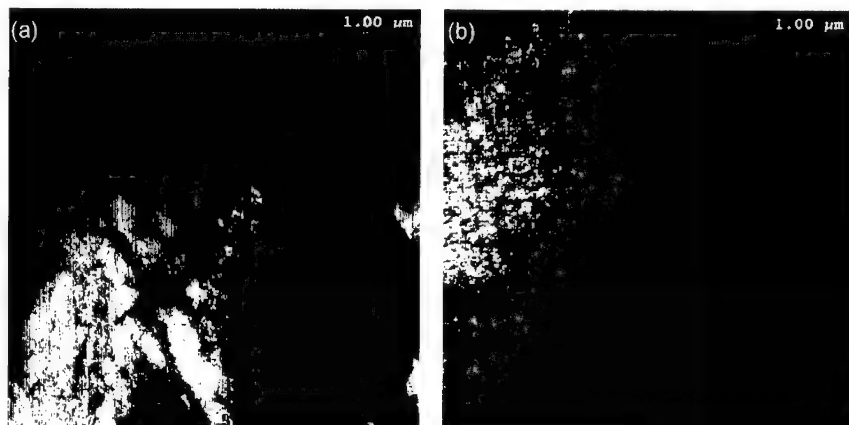
Figure 4 : *Dislocation structures of a non-treated specimen (a) and a cooled specimen (b) after fatigue loading of 5×10^4 cycles at a stress amplitude of 331 MPa. Dislocation bundles were frequently observed in the non-treated specimen (see left upside corner of image (a)). However, no such bundles were observed and planar configuration of dislocations was observed in the cooled specimen (b). These result indicates that the re-arrangement of dislocations were suppressed in the cooled specimens compared to the non-treated specimens in a high cycle regime.*

REFERENCES

[1] M. Shimojo, T. Inamura, T. H. Myeong, K. Takashima and Y. Higo, *Metall. Trans. A, accepted for publication*

[2] A. J. Bogers and W. G. Burgers, *Acta Metall.* **12**, (1964) 255.

[3] J. A. Venables, *Phil. Mag.* **7**, (1962) 35.

[4] J. -B. Vogt, J. Foct, C. Regnard, G. Robert and J. Dhers, *Metall. Trans A* **22A**, (1991) 2385.

[5] V. Shrinivas, S. K. Varma and L. E. Murr, *Metall. Trans. A* **26A**, (1995) 661.

[6] T. Inamura, R. Abe, T. H. Myeong, M. Shimojo and Y. Higo, in Proceedings of the seventh International Fatigue Congress. 1, June 1999, edited by X. R. Wu and Z. G. Wang (Higher Education Press, Beijing, 1999) p. 633

[7] T. H. Myeong, Y. Yamabayashi, M. Shimojo and Y. Higo, *Int. J. Fatigue* **19**, (1997) S69.

[8] S. Horibe, Y. Seki, T. Fujita, T. Araki, *Transactions ISIJ* **20**, (1980) 398.

[9] G. Franke and C. Altstetter, *Metall. Trans. A* **7A**, (1976) 1719.

[10] V. S. Srinivasan, R. Sandhya, K. Bhauu Sankara Rao, S. L. Mannan and K. S. Raghavan, *Int. J. Fatigue* **13**, (1991) 471.

[11] S. Maekawa, K. Takashima, M. Shimojo, Y. Higo, S. Sugiura, B. Pfister and M. V. Swain, *Jpn. J. Appl. Phys.* **38** (1999) 7194

Monte Carlo Simulations of Grain Boundary Sliding and Migration: Effect of Temperature and Vacancy

P.Ballo[1], N.Kioussis[2] and Gang Lu[2]
[1]Department of Physics, Faculty of Electrical Engineering and Information Technology
Slovak University of Technology, Ilkovičova 3,812 19 Bratislava, Slovak Republic
[2]Department of Physics and Astronomy, California State University, Northridge,
CA 91330-8268, U.S.A.

ABSTRACT

We have carried out Monte Carlo (MC) simulations using the embedded atom potential to study the sliding and migration of the $\Sigma5$ [001] (210) tilt grain boundary (GB) in aluminum and the effect of vacancies on the sliding properties. We find that the simulated annealing allows the system to gradually anneal to a global-minimum configuration, thus increasing the number of migrations and reducing the GB sliding energy barriers to about a factor of three compared to the corresponding "static" values. The distribution of atomic energies as a function of GB displacement, provide insight into which atoms are responsible for the GB migration. The vacancy formation energy is found to be lower when the vacancy is placed on the first layer to the boundary, in excellent agreement with *ab initio* electronic structure calculations. The sliding and migration properties depend very sensitively on the position of the vacancy in the GB core.

INTRODUCTION

Grain boundary sliding (GBS), i.e., the rigid translation of one grain over another parallel to the boundary interface, is one of the principal mechanisms of plastic flow of polycrystalline materials at intermediate-to-high temperatures (above $0.4T_M$, where T_M is the melting point) [1]. Another process that may occur during the GBS is grain boundary migration, which is the motion of the interface in the direction *perpendicular* to the boundary plane [2]. Finally, the interaction between a grain boundary and other defects in the crystal, such as substitutional impurities, vacancies and dislocations will affect the grain boundary motion [3]. Despite the important role of GB in materials properties, our knowledge at the microscopic level is limited. The direct observation is limited due to lack of resolution of experimental techniques such as high resolution transmission electron microscopy (HRTEM) and by the fact that only a full relaxed structure can be observed. With the advent of highly powerful computers, simulations at atomic level can play an increasingly prominent role as an effective alternative to experimental observation. Computer simulation offers the ability to examine the details at microscopic scale that cannot be obtained from experiment. For example, some simulations have been done by Bishop et al. [4] using pair-like potential. Recently Chandra et al.[5] using an Embedding atom method potential and Molteni et al. [6] using an *ab initio* simulation of GBS received evidence of interface migration. However, the vast majority of computer simulation studies of GB have been concerned with the equilibrium structure at zero temperature. The results obtained with these simulations may often be incorrect compared with those obtained by HRTEM. Simulation at elevated temperatures using

simulated annealing (SA) technique in combination with effective interatomic potential should be the right key for all atomistic simulations.

The main goal of the present work is to apply a SA technique combined with an Embedding atom method (EAM) potential to investigate the microscopical origin of characteristic GB properties. In order to achieve this, we have studied the structure and sliding energy of a Σ5 tilt perfect GB in aluminium (without a vacancy) as well as for a vacancy in the crystal lattice at elevated temperature. The remainder of this paper is organized as follows. Computational details as the quality of relaxation process and EAM potential used in atomic simulations are discussed in the next section. In the subsequent section, we discuss the equilibrium structure and energy of a perfect interface as well as a vacancy-containing interface. Using equilibrium GB we examine sliding and interface migration under lateral force conditions.

METHODS

The GB energy was determined from the difference of the energy of a supercell containing the GB and the energy of a supercell containing an equal number of atoms in the bulk environment divided by the total GB area. It is well known that the GB energy minimization (geometry optimization) represents a very difficult problem even for simple systems. Perhaps the most celebrated minimalization technique has been introduced by Kirkpatric, Gellar and Vechi [7] by simulating the annealing process. The SA technique is a numerical simulation method based on the dynamics of crystalization. It means that a system should be gradually annealed to a minimum energy configuration by lowering the system temperature in successive steps. Geman and Geman [8] provided that if the temperature is reduced slowly enough SA algorithm guarantees to find the global minimum. In our experiment, we used initial temperature of 465K and the system was then cooled at the final temperature of 28K. The cooling process was implemented using a stepwise-exponential decrease of temperature and this process took 155×10^3 steps. For a fixed temperature T, the atomic coordinates were changed using the standard Metropolis technique [9]. The maximum atomic displacement was adjusted in order to get an acceptance ratio of 0.5. It was not systematically determined that this acceptance ratio was an optimum, but we obtained well converged statistical averages, with a typical number of MC moves of about 10^3 trials for each temperature step.

The potentials based on EAM [10] give probably the most realistic description of metallic materials, in which an important contribution to the interatomic interaction comes from the interactions of the atomic cores with the conduction electrons. The accuracy of computed results mainly depends on approximation of embedding function and its ability to treat electron density deviations in local coordination [11]. The EAM potential used in this work was constructed on a large set of experimental and *ab-initio* data [12]. In contrast to other potentials it gives excellent results on Σ5 GB in aluminium.

RESULTS AND DISCUSSION

The tilt Σ5 [001] (210) GB is constructed by means of the coincidence site lattice (CSL) model, in which the lattices of the two grains share 1 out of 5 lattice sites. We show in Fig. 1 the relaxed supercell for the Σ5 tilt GB employed in the EAM calculations

viewed along the [001] direction. The 160-atom cell is simulated by forty-one [210] layers corresponding to grain-boundary separation of 18.46Å and two layers of atoms along the [001] direction. The closed and open circles represent atoms distributed on the first and second [001] planes, respectively. With twenty layers in between, the GB interaction introduced artificially in the supercell calculation is small. The aluminium lattice constant is set to the value of 4.05 Å [13].
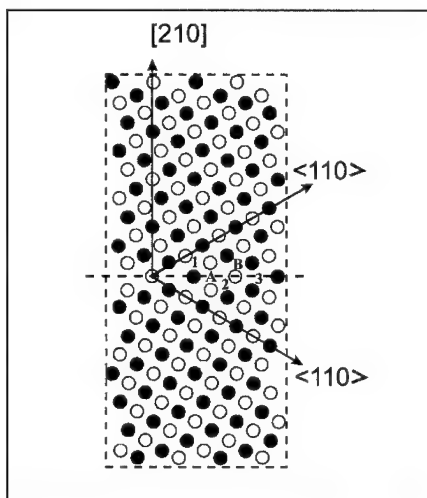
Figure 1: *Relaxed geometry of 160 atoms supercell for the Σ5 tilt GB in aluminium. Atoms located in different [001] planes are shown with filed and open circles. It can be seen that during the relaxation process, most of the atomic movement occurs near the GB plane.*

In Fig. 2 we plot the GB energy as a function of the MC annealing temperature. The starting atomic configuration for each anneal was taken from the previous one. Tests have indicated that, overall, equilibration of the GB requires about thousand MC steps. Note, that the use of MC simulations to anneal the boundary structure produces new lower energy structures which are different from those obtained using conjugate gradient techniques. The extrapolated zero-temperature GB energy is 0.482 Jm^{-2}, which is smaller compared to the EAM and *ab initio* values of 0.495Jm^{-2} [12] and 0.502 Jm^{-2} [14], both obtained by conjugate gradient techniques. As will be discussed below, the annealing process has a larger effect on the activation energy barriers associated with GB sliding and migration.

In Fig. 3 we show vacancy formation energy E_v^f versus perpendicular distance from the GB. The oscillation of the E_v^f with change of the distance is observed. For a vacancy formatted a large distance from GB, E_v^f is the same as vacancy formation energy in bulk ($E_{v,bulk}^f$=0.68eV [15]).
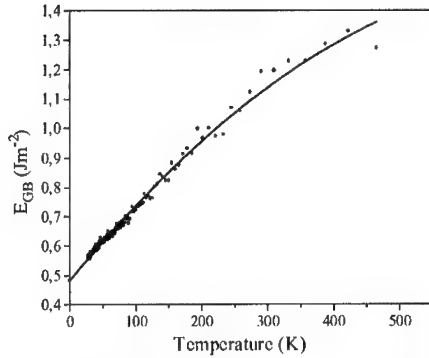
Figure 2: Grain boundary energy as a function of the MC anneal temperature. Solid line indicates the least square approximation. Extrapolation at zero temperature gives $E_{GB} = 0.482 \, Jm^{-2}$.
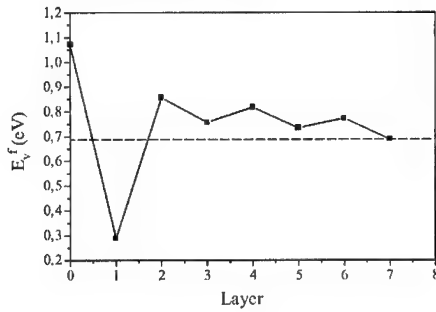
Figure 3: Vacancy formation energy E_v^f versus number of layers from the GB. Dashed line indicates $E_v^f = 0.68eV$ bulk value.

As seen from this figure, the formation energy for a vacancy created at the first layer is significantly lower than other layers. With the loss of coordination caused by the creation of the vacancy in the first plane, there is a clear tendency for the remains twin atom to fill the empty site. The atom moves essentially perpendicularly toward the interface, a distance of 0.56 Å. This strong structural relaxation reduces the vacancy formation energy by 58 %.

The GBS is simulated quasi-statically, by rigidly shifting the top grain with respect to the bottom by a small specified amount along the [1$\bar{2}$0] direction. At each displacement the system is then relaxed using a MC simulations. In order to investigate the effect of annealing on the GBS properties, namely, the energy barriers and the shear displacement at which the GB migration occurs, we have carried out two sets of MC simulations. However, in the first, which we will refer to as "static", the probability acceptance of any higher-energy configuration is set equal to zero, driving the system to the local-minimum configuration. In the second set of simulations, the probability acceptance follows standard MC rules by lowering the temperature from 465K to 28K. In Fig. 4 we show the relative variation of the GB energy (with respect to its value for zero displacement) as a function of the grain displacement relative to the coincidence lattice cell a_{CLS}, for both the "static" (circles) and SA (triangles) calculations. In both cases the energy profile is

smooth, exhibiting several peaks and energy valleys between them, the latter being associated with GB migration. Note that the effect of simulated annealing is to reduce the energy barrier about a factor of three compared to the corresponding "static" values. It also increases the number of migrations trough a Displacement Complete Lattice Shift (CLS) unit cell. Thus, the migrations in the SA simulations occur earlier, for example, the first migration occurs when the shear displacement is about 22 CLS cell % compared to the corresponding value of 40 CLS cell % in the "static" calculation.

Atoms that control the energetics of GB are in Fig.1. labeled 1,2 and 3 in one plain and A and B in other plain. The sliding process destroys the arrangement of the initial equilibrium GB structure. In the new configuration atoms across the interface change relative distance and the twin atoms are not at positions directly facing each other. Atoms 1 and B lying in the top grain are pushed toward atoms A and 3 in bottom grain, hence, have very high energy. Note, the twin atom to atom 3 decreases in energy, because it increases its distance across the GB in such way to maintain optimal bulk coordination. The distance increase between atom 2 and its twin across
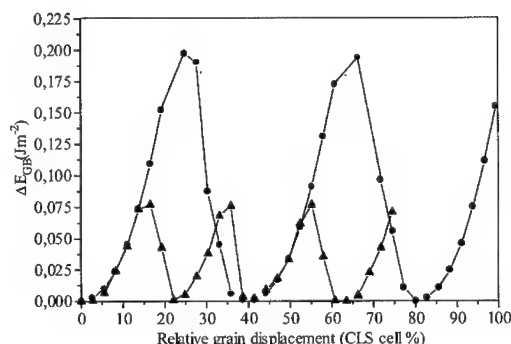
Figure 4: The variation of relative GB energy during the GB sliding. Circles: forward sliding using "static" relaxation; triangeles: the same sliding as previous using simulated annealing relaxation.

the interface caused by the upper grain sliding forms empty site in the first plane. Atom 2 as a candidate to fill the empty site is separated from the new position by the energy barrier. Using the "static" relaxation frozen atom 2 could not relase local position, however GB energy increases. Elevated temperature during the relaxation process (SA technique) enables relase atom 2 from its freezing position. Relaxation drives the atom a distance 0.45 Å toward the empty site, which compensates for the loss of coordination. The ability to relax atom 2 has been shown to be crucial in the process of GB migration. A surprising small relaxation causes atom 3 to find a new position in the upper GB side. The atomic displacement is accompanied by GB migration. However, because only a small number of atoms in near neighbour GB distance is employed in atomic relaxation, the interface migration is very fast. The GB interface never passes through a perturbed configuration, because of the simple structural rearrangement.

In Fig.5 we plot the variation of the GB energy as function of the grain displacement relative to the coincidence lattice cell for a vacancy placed at the GB plane (circles), the

first plane (triangles). As a reference, we also plot the variation of the GB energy for the vacancy free GB (crosses). Variation in GB energy for the vacancy placed at the first plane is very similar to the energy variation of the perfect GB and is accompanied by GB migration. Lost of short distance repulsion between the near neighbour twin atoms invokes a small change in the
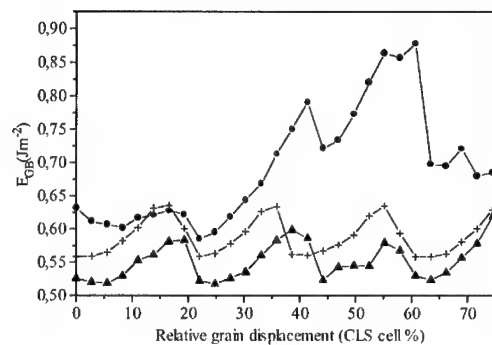
Figure 5: *The variation of GB energy during the GB sliding containing a vacancy at various positions. Circles: vacancy placed at the grain boundary plane; triangles: vacancy placed in the first plane; crosses: reference for vacancy free grain boundary.*

mechanism of GB migration. This occurs because the missing atom in first plane does not affect relaxation of atom 2 and the GB never forms perturbed configuration. As might be expected, the sliding and migration is considerably more complex if a vacancy is placed in GB plane. The missing atom in the GB plane strongly affects the energy of near neighbour atoms. As shown above, a very high energy barrier separates this configuration from a position of low E_v^f in the first plane. Weak structure relaxation and the high formation energy that accompanies vacancy creation in the GB plane destroy coupling between sliding and migration. However, from geometry, if sliding is not accompanied by migration, structure passes through a perturbed configuration. This in fact pushes up the GB energy during the sliding.

CONCLUSION

We have presented a study of energy variation as well as atoms rearrangement during the GBS at the Σ5 tilt GB in aluminium. We received a surprising result for the GB containing a vacancy at the core. The simulation shows that the vacancy is not free to leave the boundary core due to the very high energy barrier that separates the GB core and the first layer. It has been shown that the computed GB energetics may be dramatically altered if the atomic relaxation is provided at elevated temperature. The influence of annealing temperature on GB migration was evaluated by computing the energy associated with incremental equilibrium configurations during the GBS process. The magnitude of the energy barriers as well as mobility of the GB was found to be sensitive to the annealing temperature. For computed GB energetics good

correspondence with experimental data was obtained. Thus, the study clearly shows that well tuned EAM potential gives reasonable results for the Σ5 GB in aluminium. Atomic relaxation based on the SA technique is very useful for effective atomic rearrangement as well as for more realistic atomic simulation of the GB migration.

REFERENCES

1. R. Z. Valiev, V. G. Khairullin and A. D. Sheikh-Ali, *Structure and property relationships for interfaces*, eds J. L. Walter, A. H. King and K. Tangri p.309 (ASM International, Metals Park, Ohio).
2. D. A. Smith, *Materials Interfaces, Atomic-level structure and properties,* eds D. Wolf and S. Yip p. 212. (Cambridge UP, Cambridge 1992).
3. C. H. Wörner and A. Cabo, Acta Metall., **35**, 2801 (1987).
4. G. H. Bishop, R. J. Harrison, T. Kwok and S. Yip, J. Appl. Phys. **53**, 5609 (1982).
5. N. Chandra, and P. Dang, J. Mater. Sci. **34**, 655 (1999).
6. C. Molteni, N. Marzari, M. C. Payne and V. Heine, Phys. Rev. Lett. **79**, 869 (1997).
7. S. Kirkpatrick, D. C. Cellar and M. P. Vechi, Science **220**, 671 (1983).
8. S. Geman and D. Geman, IEEE Trans. Pattern. Anal. Mach. Intell. PAMI-6, 721 (1984).
9. M. P. Allen and D. J. Tildesley, *Computer Simulation of Liquids* (Oxford UP, Oxford 1996). 10. M. S. Daw and M. I. Baskes Phys. Rev. B **29**, 6443 (1984).
11. S. M. Foiles, M. I. Bashes and M. S. Daw, Phys. Rev. B **33**, 7983 (1986).
12. Y.Mishin,D. Farkas, M.J.Mehl and D.A.Papaconstantopoulos, Phys. Rev. B **59**, 3393 (1999).
13. C. Kittel, *Introduction to Solid State Physics*, Wiley -Interscience, New York (1986).
14. Gang Lu and N. Kioussis, unpublished.
15. H.-E.Schaefer, R.Gugelmaier, M.Schmoltz and A.Seeger, Mater.Sci.Forum,**15-18**,111(1987).

Biased Deposition of Nanocrystalline Be$_{1-x}$Cu$_x$ Coatings

A. Jankowski
Chemistry and Materials Science, Lawrence Livermore National Laboratory
Livermore, CA 94551-9900

ABSTRACT

Coatings of Be$_{1-x}$Cu$_x$ are prepared by magnetron sputter deposition onto spherical polymer mandrels. The application of an applied bias during deposition refines the columnar morphology of the coating and surface finish to the nanoscale. A mechanical testing technique is developed to load the thin-walled spherical capsules under uniaxial tension at constant strain to fracture. The bias-deposited material exhibits an increase in strength by a factor of three or more following a Hall-Petch type relationship with surface roughness.

INTRODUCTION

The properties of sputter deposited coatings are sensitive to growth morphology and microstructure. The variation of deposition conditions will often affect the formation of the deposited coating. The application of a bias potential applied to the substrate can promote a dense crystalline microstructure through ion bombardment that minimizes porosity and can increase the mechanical strength of the coating.

A promising, inertial confinement fusion target design is a uniformly thick, Be-based fuel capsule.[1] A specific alloy system of interest is Be$_{1-x}$Cu$_x$ as it offers the potential for improved performance as an ablating material since it has lower opacity, a larger ablation rate, more initial mass, and higher bulk strength than many polymeric counterparts. The performance advantages for Be capsules are accompanied by demanding material requirements. The design criteria include a surface finish of less than 2 nm rms roughness, hence the microscopic control of both structure and concentration. A coarsening of textured crystalline growth produces roughness in the capsule surface that sequentially leads to Rayleigh-Taylor instability during the ablation, degradation in compression, and cooling of the fuel. Therefore, it's advantageous if the deposition process can accommodate an in-situ smoothing of the surface. In addition, the need to fill and store (at room temperature) a high pressure gas is facilitated by mechanical strength.

The refinement of grain size to the nanoscale is potentially optimal to smooth the coating surface and increase the material strength. It is widely known from prior studies of evaporation and sputter deposition that the grain size of nominally pure beryllium can be dramatically refined through the incorporation of impurities such as transition or refractory metals.[2-5] A complimentary evaluation is provided in this report of the changes in growth morphology and strength found for the biased deposition of Be-rich coatings.

EXPERIMENTALS

The samples are prepared by combining sputter deposition with vibration levitation as described in detail elsewhere.[6] The deposition chamber for this study contains a circular array of three 3.3 cm diameter planar magnetrons. Two of the magnetron sources are used to sputter nominally pure Be and the third a Be$_{0.94}$Cu$_{0.06}$ target blend. The center of each magnetron source is located along the circumference of a 7 cm diameter circle at a 120° separation. The deposition chamber is cryogenically pumped to a 5×10^{-6} Pa base pressure. A 0.4 Pa sputter gas pressure is maintained using a 30 cm^3 min^{-1} flow of Ar. The nominal deposition rate from each
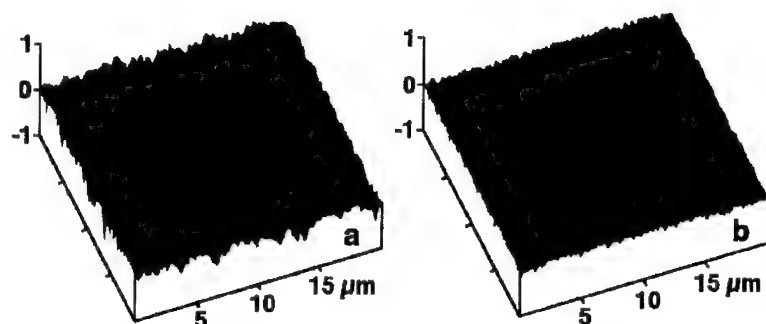
Figure 1. Atomic force microscope images of 10 μm thick, $Be_{1-x}Cu_x$ coatings as sputter deposited (a) without an applied bias and (b) with a -120 V applied bias.

sputter target is 0.2 nm $W^{-1}min^{-1}$. The substrates are spherical capsules of a (CH) polymer with a wall thickness of 12-15 μm and an outside diameter of 1 mm. The substrates are levitated 6 cm beneath the center of the magnetron source array. A bowl-shaped substrate pan is driven with an ultrasonic pulse that causes the spheres to randomly bounce and produce a uniformly thick coating. A negative bias potential applied to the substrate pan provides the condition for the ionized Ar sputter gas to collide with the coating surface during the deposition process.

The composition of the alloy is determined from calibrated deposition rates and confirmed through measurements of coating thickness (t) using a contact profilometer and as measured using an electron microprobe. The roughness of the capsule coating is determined through the use of a sphere mapper, i.e. an atomic-force microscope (AFM).[7-8] The root-mean-square (rms) measure of roughness is directly computed from the topological surface profile.

The capsule strength is measured by uniaxially loading a 1 mm diameter hollow sphere in tension. To accomplish this objective the capsule is bonded, through the use of a high strength epoxy, between the ends of two concentrically aligned stainless steel tubes of an appropriate 0.76 mm (i.e. 30 mil) inner diameter. The free ends of the steel tubes are first fed through uniaxially aligned sleeves that are pin-mounted into the universal C-clamps of the tensile tester. A 5 N (i.e. 1.1 lb) load cell applies the tensile load (P) at a constant strain rate of 0.5 mm min^{-1}. The tensile load is monitored as a function of crosshead displacement. The stress normal to the shell cross-section is equal to $P \cdot A^{-1}$ where the area (A) equals $\pi (r_o^2 - r_i^2)$ and r_o, r_i represent the outer and inner radii, respectively. An equivalent rupture pressure (p) equaling $2\sigma_r \cdot t \cdot r_c^{-1}$ can be computed at the fracture stress (σ_r).

RESULTS

The physical properties of $Be_{1-x}Cu_x$ coatings are sensitive to the growth morphology and microstructure of the sputter deposit. The application of an applied bias to the substrate can increase the density of the columnar microstructure of a crystalline coating through ion bombardment and smooth the surface by milling. The effect of bias on the $Be_{1-x}Cu_x$ coating is a minimization of porosity, increased mechanical strength, and a reduction of surface roughness. Detailed results and the limitations to each improvement will be quantified for the specific case of 7-11 μm thick $Be_{0.98}Cu_{0.02}$ coatings.

The use of AFM to characterize $Be_{1-x}Cu_x$ coatings provides a useful measurement of the surface finish. Two typical examples are seen in the AFM patch scans (of Fig. 1) for 10 μm thick, sputter deposited $Be_{0.98}Cu_{0.02}$ coatings.[7] The application of bias refines the columnar
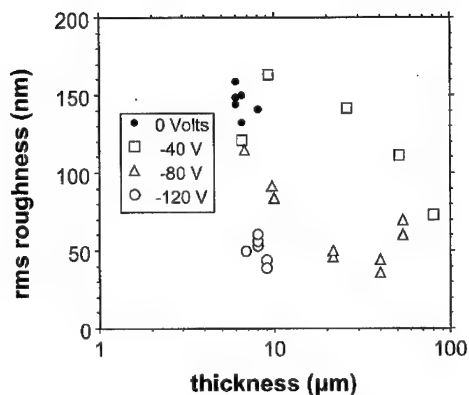
Figure 2. The variation of rms surface roughness with the thickness of $Be_{1-x}Cu_x$ coatings sputter deposited on capsules as a function of applied bias voltage.

size and concurrently reduces the rms surface roughness from 0.15 μm for the condition of no bias (Fig. 1a) to only 40 nm for a -120 V bias (Fig. 1b) in these samples. The variation of surface finish with the $Be_{1-x}Cu_x$ coating thickness (for x less than 0.03) is plotted (Fig. 2) with the applied bias voltage. In general, a progressive decrease in surface roughness occurs with an increase in coating thickness and applied bias. The apparent lower plateau in rms roughness seen at 40 nm for the -80 V bias condition (Fig. 2) makes it uncertain whether further improvement in surface finish can be obtained for $Be_{0.98}Cu_{0.02}$ coatings greater than 0.1 mm in thickness.

The $Be_{1-x}Cu_x$ coated, spherical capsules are loaded under uniaxial tension to failure at a constant strain rate. The halves to a fractured capsule (Fig. 3a) and a higher magnification image in cross-section (Fig. 3b) are seen in the optical microscope images of a 25 μm thick coating on a 15 μm thick, 1 mm diameter mandrel. The following criterion is adopted to enable a comparative analysis of the bias effect on load data. The fracture of the capsule must occur near its equator. Otherwise, the cross-section can't be assumed to have failed in tension. For

Figure 3. The optical microscope images of the (a) 1 mm dia. $Be_{1-x}Cu_x$ coated capsule tested to failure and (b) fracture cross-section at higher magnification.
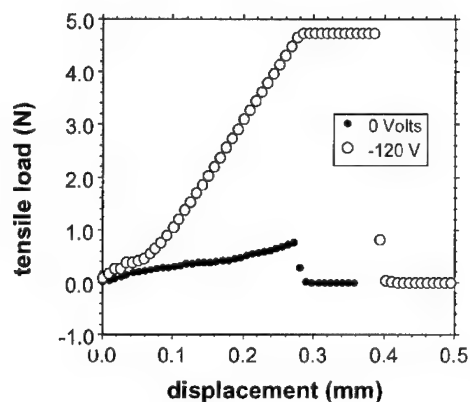
Figure 4. The load versus displacement variation of coated capsules tested to failure under tension as deposited with (a -120 V) and without (a 0 V) substrate bias.

example, the high magnification view (Fig. 3b) shows a continuous topology to the 25 μm thick, coating cross-section indicating that initial fracture likely propagates from the capsule coating through the mandrel.

The effect of a -120 V substrate bias on increasing the material strength is seen in the load versus displacement curves (of Fig. 4). The applied bias voltage increases the tensile load of a 10 μm thick coating to a value of 6.9 N (extrapolated) at failure in comparison to the 0.8 N load measured for a 7 μm thick coated capsule deposited without a substrate bias. (The test cell loads to failure but stops displaying data at 5 N.) For reference in computing the $Be_{1-x}Cu_x$ coating strength, the uncoated (CH) polymer mandrel fails at 0.2 N. The mandrel strength equivalence is only 6 MPa.

ANALYSIS

The surface roughness measurements for the 7-10 μm thick coatings are listed in Table 1 as a function of applied bias voltage. Only a few of the 7-10 μm thick, $Be_{0.98}Cu_{0.02}$ coated capsules are available for tensile testing. The average strength for those coatings that failed at or near the capsule equator are computed and listed in Table 1. The results for the applied bias conditions of 0 V and -40 V are combined in order to analyze the relationship between surface finish and strength. This rationale is applied for a meaningful quantitative analysis since (a) only one -40 V bias deposited sample, tensile test result is available, and (b) the values for roughness are statistically indistinguishable for the 7-10 μm thick coatings deposited at 0 V and -40 V bias. A plot (Fig. 5) of the fracture stress, i.e. strength, versus the square root of

Table 1. - Properties of Bias-Deposited $Be_{0.98}Cu_{0.02}$ Coatings

bias potential (V)	surface rms (nm)	strength (MPa)
0	145 ± 8	25 ± 3
-40	176 ± 62	52
-80	97 ± 16	89 ± 11
-120	49 ± 8	148 ± 49
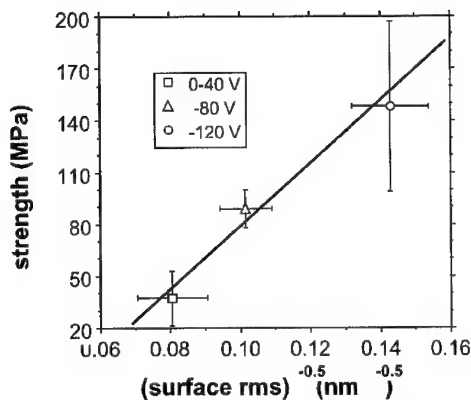
Figure 5. The strength linearly varies with the square root of reciprocal surface roughness for 7-10 μm thick bias deposited, $Be_{0.98}Cu_{0.02}$ coatings.

reciprocal surface roughness yields a linear relationship (with a correlation coefficient of 0.978). This behavior is analogous to the well known Hall-Petch relationship for yield stress with grain size. The analogy is made since the rms surface roughness directly correlates with grain size. A limitation of the epoxy strength did not permit the testing to failure of very thick coatings. For example, a 77 μm thick coating deposited at a -80 V applied bias did not rupture in the capsule but failed within the epoxy joint indicating a coating strength that exceeds 40 MPa (5.7 ksi).

In order for a 0.150 mm thick, $Be_{1-x}Cu_x$ coating deposited on a 2 mm diameter capsule to hold a gaseous-fill (p) of 300 atm (4.4 ksi) at room temperature [7], the material strength (σ_f) must exceed 119 MPa (17 ksi). The application of substrate bias can produce a $Be_{0.98}Cu_{0.02}$ coating with a failure strength that routinely reaches this value. Through the use of cryogenic cooling, the effective gas pressure is reduced and the strength requirement relaxed considerably.

DISCUSSION

Improvements in the material strength and surface finish of $Be_{1-x}Cu_x$ coatings result from an applied substrate bias. However, it appears necessary to develop alternatives to the $Be_{1-x}Cu_x$ alloy in order to achieve a surface finish with less than 2 nm rms roughness. As one alternative, the use of B in substitution for Be forms a binary system that is a potential metallic glass former.[9] Surface roughness values dramatically decrease to less than 3 nm rms for B concentrations above 11 at.%.[8] However, the decrease in roughness found for the 5 μm thick $Be_{1-x}B_x$ (x>0.11) coatings as deposited on stationary flat substrates is lost when thicker coatings are applied to bounced, hollow polymer capsules. This effect is attributed to large compressive stress that arises from the large B addition. As a second alternative, doping impurities as Al, Fe, Ti, and Zr are well known to refine the grain size of Be.[2-5] In combination, the addition of B and Fe refines the Be microstructure to a grain size of only 10 nm and increases the measured hardness as well.[9] The possibility of producing a smooth (Be,B)-based ablator on polymer capsules is evidenced in the 1nm rms surface roughness measured for a 10 μm thick coating of $Be_{0.99-x}B_x(FeCrNi)_{0.01}$ sputter deposited onto a stationary capsule.

In addition to optimizing sputter deposition parameters and material composition, the source-to-substrate geometry is an important consideration. In a typical approach, the substrates randomly bounce and collide with one another in an ultrasonically-vibrated bounce pan. As an alternative to the open bounce pan method, an individual pocket chamber for each substrate (about twice the size of the mandrel diameter) is provided for coating.[9] The opening to each pocket chamber is designed to minimize glancing incident angles of deposition to further reduce roughness as well as to control heating from full exposure to the deposition source. It can be inferred from these findings that a microstructure on the nanoscale is essential to achieve strong and smooth Be-based coatings.

SUMMARY

Coatings of $Be_{1-x}Cu_x$ are prepared by magnetron sputter deposition. The application of a negative bias potential to the substrate induces ionized Ar bombardment during deposition that refines the columnar morphology and surface finish to the nanoscale. A tensile test is developed to load coated capsules under uniaxial tension. A -120 V applied bias produces an increase in strength from 25 MPa to 150 MPa for sputter deposited $Be_{0.98}Cu_{0.02}$ coatings. Concurrently, the surface roughness decreases from 0.15 μm to less than 50 nm. The bias-deposited material exhibits an increase in strength that follows a Hall-Petch type relationship with surface roughness.

ACKNOWLEDGMENTS

REFERENCES

1. S. Haan, Phys. Plasmas **2**, p. 2480 (1995).

2. R. Adams and C. Nordin, Thin Solid Films **181**, p. 375 (1989).

3. L. Tanner, and R. Ray, Acta Metall. **27**, p. 1727 (1979).

4. L. Tanner, Scripta Metall. **145**, p. 657 (1980).

5. C. Severin, C. Chen, A. Belova, and M. Lin, J. Appl. Phys. **52**, p. 1850 (1981).

6. Chen, C.W., and C.S. Alford, J. Vac. Sci. Technol., **A6**, p. 128 (1988).

7. R. McEachern, C. Alford, R. Cook, D. Makowiecki, and R. Wallace, Fusion Technology **31**, p. 4354 (1997).

8. R. McEachern and C. Alford, Fusion Technology **35**, p. 115 (1999).

9. A. Jankowski, P. Ramsey, M. McKernan and J. Morse, in *Amorphous and Nanostructured Carbon*, edited by J. Sullivan, J. Robertson, O. Zhou, T. Allen, and B, Coll, (Mater. Res. Soc. Proc. **593**, Pittsburgh, PA, 2000), pp. 489-492.

Mechanical Properties and Deformation Behavior III—Multilayers

Dislocation Models for Strengthening in Nanostructured Metallic Multilayers

A. Misra, J. P. Hirth, H. Kung, R. G. Hoagland and J. D. Embury,
MST Division, Los Alamos National Laboratory, MS K765, Los Alamos, NM 87545

ABSTRACT

Ultra-high strength metallic multilayers are ideal for investigating the effects of length scales in plastic deformation of metallic materials. Experiments on model systems show that the strengths of these materials increase with decreasing bilayer period following the Hall-Petch model. However, as the layer thickness is reduced to the nm-scale, the number of dislocations in the pile-up approaches one and the pile-up based Hall-Petch model ceases to apply. For nm-scale semi-coherent multilayers, we hypothesize that plastic flow occurs by the motion of single dislocation loops, initially in the softer layer, that deposit misfit type dislocation arrays at the interface and transfer load to the harder phase. The stress concentration eventually leads to slip in the harder phase, overcoming the resistance from the misfit arrays at the interface. A model is developed within the framework of classical dislocation theory to estimate the strengthening from this mechanism. The model predictions are compared with experimentally measured strengths.

INTRODUCTION

Metal-metal composites, synthesized by co-deformation, electroplating or vapor deposition, possess strengths that approach 1/2 to 1/3 of the theoretical limit when the microstructural length scales are on the order of a few nanometers [1,2]. In some cases, the maximum strength of these composites may be an order of magnitude higher than the strength of the soft constituent phases. A fundamental understanding of the deformation mechanisms at nm-length scales is needed to allow optimum microstructural design of these nanostructured materials for desired applications, such as structural components in microelectromechanical systems (MEMS).

For single-phase metals, the increase in yield strength (σ) with decreasing grain size (d) is interpreted by means of the Hall-Petch (H-P) model based on dislocation pile-ups:

$$\sigma = \sigma_0 + kd^{-1/2} \tag{1}$$

where σ_0 represents the lattice friction stress and k (H-P slope) indicates the relative hardening contribution from grain boundaries. This model is also applicable if hardness data is used instead of σ. For lamellar composites, the increase in yield strength with decreasing interphase boundary spacing (h) is also described by the H-P model for the case where h replaces d in eq. (1). Several recent experimental [1,3] and theoretical [4-6] studies have, however, shown that the H-P model may break down at nm-length scales. At μm-length scales, dislocation pile-ups can be treated as a continuum distribution and eq. (1) holds. At the nm-length scales, pile-ups are discrete and the exponent in eq. (1) departs from 0.5. The assumption that the number of dislocations in the pile-up (N) decreases in proportion with decreasing h provides one way to interpret the dependence of strength on h at nm-length scales [4,5]. In this approach, a peak in strength is reached when h is so small that N cannot exceed one [4,5]. This approach assumes that the dislocation sources are such that pile-ups will always form, whether N=2 or significantly greater.

An alternate view is that continuum pile-ups form at large h and, at nm-length scales, deformation behavior is governed by single dislocations [7]. Single dislocations may propagate

in the softer phase by an Orowan bowing process, similar to yielding in thin films on substrates [8], and transfer load to the harder phase till it yields or fractures [7].

In this investigation, we extend the Embury-Hirth [7] model for single dislocation behavior in fine-scale composites to nm-scale semi-coherent metallic multilayers. The roles of the misfit dislocations at the interface and the in-plane coherency stresses in determining the Orowan stress are calculated. Also, calculated is the interface resistance to single dislocation transmission. The model predictions are compared with experimental results on Cu-Ni systems.

RESULTS AND DISCUSSION

Hall-Petch Behavior

We first present experimental results on a number of Cu-based multilayers to determine the length scale limits to which H-P model is valid. These multilayers were all synthesized by physical vapor deposition techniques (sputtering or evaporation), mechanical properties were evaluated by nanoindentation and microstructures were characterized by transmission electron microscopy (TEM). The details of the experimental procedures are described elsewhere [3]. Fig. 1 shows data for Cu-Nb, Cu-Cr and Cu-Ni systems as log-log plots of $(H-H_0)$ vs. h. Here H is the hardness of the multilayer, H_0 is the hardness of a 1μm thick Cu film, and h is the layer thickness (or, one-half of the bilayer period). It follows from eq. (1) that a linear fit with a slope of -0.5 is consistent with H-P model. For all three systems, H increases with decreasing h according to eq. (1) but deviations from the H-P behavior are observed at nm-length scales. Two observations are made from these data. First, in Fig. 1, the y-intercept of the linear fit gives k, the H-P slope. k defines the rate of hardening with decreasing h, i.e., the effectiveness of the boundaries as obstacles to slip transmission. While k correlates with shear modulus for the Cu-Cr and Cu-Nb systems, k for Cu-Ni and Cu-Nb are about the same, even though $\mu_{Ni} > \mu_{Nb}$. This indicates that other factors such as dislocation structure of the interface, yield strength of the harder phase and the misorientation of the slip systems could also be important in determining k. For example, a cube-on-cube orientation relation in the fcc Cu-fcc Ni single crystalline system results in no misorientation between slip systems, and this special orientation boundary would be a relatively weaker obstacle. Second, the H-P break down length scale decreases as the lattice parameter mismatch at the interface increases. Cu-Nb has the highest mismatch of ~10% between the {110}Nb and {111} Cu planes that make the interface plane, and exhibits H-P down to ~10 nm. Cu-Cr and Cu-Ni have mismatch of ~2.5%and exhibit H-P breakdown at h ≈ 40-50 nm. Furthermore, the μ mismatch between layers appears to have no significant effect on the value of h at H-P breakdown.
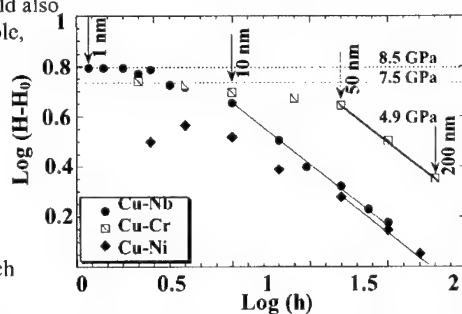
Fig. 1 Plot of log $(H-H_0)$ vs. log h for Cu-based multilayers, where H is the multilayer hardness, H_0 is Cu film hardness and h is one-half of bilayer period. Dotted horizontal lines indicate the maximum H of each of the 3 systems. Linear fits have slope of -0.5 indicating that H increases with decreasing h according to Hall-Petch law, but this model is not applicable at h < ~ 10-50 nm.

These results are consistent with our earlier theoretical work on estimation of H-P breakdown length scales in polycrystalline multilayers [6]. After the H-P model breaks down, in all systems, the hardness continues to increase to a maximum as h is decreased from a few tens of nm to a few nm. A model for strengthening at nm-scales is described next.

Single Dislocation Model

The model developed here applies to multilayers deformed under iso-strain conditions, with one phase significantly harder than the other and the length scale such that dislocation pile-ups do not form. Plasticity initiates in the softer phase when its yield strength is reached (Fig. 2(a)), while the harder phase continues to deform elastically. In this condition, the stress-strain curve deviates from linearity but strain hardening is high as plasticity is confined to only one phase and load is transferred to the harder phase. Yielding in the harder phase occurs at a higher applied stress when dislocations from softer phase can cross over the interface (Fig. 2(b)). In the limited tensile tests conducted on nm-scale multilayers, the stress-strain curves did not reveal a well-defined single yield point, consistent with our hypothesis [9]. Furthermore, multilayers deformed to small plastic strains reveal dislocations predominantly in the softer phase suggesting that the harder phase has not yielded. An example of this behavior is shown Fig. 3 (TEM micrograph) that correlates with the schematic of Fig. 2(a). This free-standing Cu-Nb multilayer was annealed at 600 °C for 1 hour and the thermal stress (calculated strain is ~0.5%) induced during cooling has caused yielding of the softer Cu layer where an array of dislocation loops are observed. No significant dislocation activity is detected in the Nb layer at this strain level.

We first describe the calculation of the Orowan stress for the motion of the hairpin dislocation in layer A of thickness h. This stress is given as follows:

$$\tau_{Orowan} = \frac{2W_D}{bh} \tag{2}$$

where W_D is the energy per unit length of the dislocation, and b the Burgers vector. To calculate W_D, the approach is as follows. Consider the hairpin dislocation loop shown in Fig. 4(a). We assume that it is a 60° dislocation on a {111} glide plane and the interface plane is {100}.
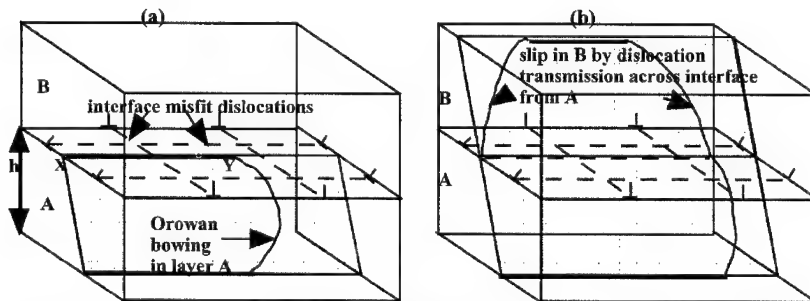
Fig. 2 Schematic illustration of the deformation mechanism in nm-scale multilayers; (a) Orowan bowing of a glide dislocation loop in the softer layer (A) while the harder phase deforms elastically (glide plane is shown shaded). The motion of the glide dislocation leaves behind misfit-type dislocations (e.g., the segment labeled XY) at the interface that already has a cross-grid of misfit dislocations. (b) At higher applied stress, composite yields plastically when single dislocations can transmit across the interfaces.

The bowed segment in Fig. 4(a) is near-screw and the segment deposited at the interface is edge. For this loop, the view with the glide plane edge-on is shown in Fig. 4(b). One can mathematically treat the two edge dislocations deposited at the interface by the motion of the glide loop by creating infinitesimal dislocation dipoles and separating them to the desired positions [10]. If the plastic strain in the layer A is ϵ^A prior to yielding in B, then there will be an array of these glide loops of average spacing (b/ϵ^A). One finds the value of W_D for this array by integrating the Peach-Koehler force $(=\sigma b)$ on the dislocations over the layer thickness:

$$W_D = -\int_0^h \sigma b \, dy \qquad (3)$$

Fig. 3 TEM micrograph of a Cu-Nb multilayer annealed at 600 °C. Thermal strains (~0.5%) result in an array of dislocation loops in the Cu layer, while no significant plasticity is observed in Nb.

The dislocation line energy expressions for simple stretch or shear arrays have been derived by Kreidler and Anderson [11]. Here we have considered 60° glide dislocations and carried out the integration separately for the three resolved components of b (b_y normal to the interface and b_x and b_z along the line directions of the cross-grid of misfit dislocations). For each component, the integration is the sum of integrals over paths I and II shown in Fig. 4(b). We further define an upper bound and a lower bound estimate for W_D. In the upper bound estimate, the work done against the stress fields of both arrays of the misfit dislocations, and the self-energy of the glide loops are included. In the lower bound estimate, we assume that for the h range where this model applies, the misfit dislocation spacing (λ) is greater than the equilibrium value. TEM observations of the Cu-Ni interface have shown that even when h is an order of magnitude higher than the critical thickness (h_c), λ is a factor of 2 above the equilibrium value of ~10 nm [12]. Thus, the glide of the hairpin loops adds the "missing" misfit dislocations at the interface and hence "negative" work is being done as λ is reduced to its equilibrium value. This negative work effectively cancels out the calculated work against the stress field of equilibrium misfit arrays, and to a first approximation, we need only consider the self-energy terms in the lower bound estimate. The result is a sum of the self-energies of the dislocation components b_x, b_y and b_z:

$$W_D = \frac{\mu b^2}{8\pi(1-\upsilon)}\ln\frac{\left(h^2+L^2\right)^{1/2}}{b} + \frac{\mu b^2}{4\pi(1-\upsilon)}\ln\frac{\left(h^2+L^2\right)^{1/2}}{b} + \frac{\mu b^2}{8\pi}\ln\frac{\left(h^2+L^2\right)^{1/2}}{b} \qquad (4)$$

(a)

(b)

Fig. 4(a) Schematic of a glide dislocation moving by an Orowan bowing process in the softer layer A while the harder layer B continues to deform elastically; (b) view of the glide loop shown in (a) with glide plane edge-on. The deposition of two edge dislocations at the interface is equivalent, mathematically, to the creation of infinitesimal dislocation dipoles, followed by separation to the desired positions, along sequential paths I and II.

This result, when substituted in eq. (2), should give a lower bound of the applied shear stress to move the hairpin dislocations in the softer layer, in the absence of any residual stresses. The details of the upper bound calculation and comparison with the lower bound will be presented in a separate article. To account for the effect of residual stress, we consider only the coherency stress here and ignore the intrinsic stress (growth-related stresses in PVD). The maximum bi-axial coherency stress can be estimated from misfit strain by means of Hooke's law [10]. For $h > h_c$, the coherency stress will decrease by a factor of (h/h_c) [13]. We assume that the presence of in-plane coherency stresses (τ_{coh}) will lower the barrier for the motion of hairpin dislocations in the softer layer. The effective applied stress to initiate slip in layer A is:

$$\tau_{applied}^{A} = \tau_{Orowan} - \tau_{coh} \tag{5}$$

Once the array of hairpin loops has caused yielding in the softer phase, the resistance of the interface to single dislocation crossing needs to be computed. The lattice parameter mismatch at the interface (ε_m) when added to the plastic strain accumulated in the softer phase in the elastic-plastic region (ε^A), gives the new misfit dislocation spacing as $b/(\varepsilon_m + \varepsilon^A)$. The stress tensor for this array of edge dislocations is computed from equations by Hirth and Lothe [14], and rotated to the glide system co-ordinates. These stresses vary with distance parallel as well as normal to the edge array. We have calculated the stress tensor at a point that is mid-way between two misfits and a distance of 3b normal to the interface. Once a glide dislocation is pushed out of the interface by a small distance of ~3b, the repulsion from the same-sign dislocations in the array will push it further away. There will be additional attractive and repulsive forces, respectively, from the edge arrays at distances h below and above the array from which the glide dislocation is being pushed out. These forces are roughly equal in magnitude and cancel out. Therefore, the effective applied stress is just what is needed to push the glide dislocation out of the interface by a small distance of ~3b. This calculated stress (τ_{array}) when added to the Orowan stress (eq. 5) gives the composite shear strength:

$$\tau^{*} = \tau_{array} + \tau_{applied}^{A} \tag{6}$$

This shear stress is converted to normal stress by means of the Schmid factor for {111}<110> glide in <100> oriented fcc multilayers, and compared to experimental data on Cu-Ni in Fig. 5. The solid data points in Fig. 5 are hardness values divided by a factor of 3, and the open points are tensile data on electrodeposited materials. For $h > h_c$, the model provides a reasonable fit to the experimental data. At larger h (sub-μm to tens of μm), the pile-up based H-P model will be more appropriate. The single dislocation model incorporates several unit processes involved in the deformation of nm-scale multilayers such as Orowan bowing, coherency stresses, interface misfit dislocations array resistance, etc. Although not discussed here, the dislocation image force (Koehler) effects can be added to eq. (6) as appropriate. Atomistic simulations have shown that the Koehler barrier can be significantly altered by coherency stresses [19]. For $h < h_c$, and in general for $h < \sim 5$ nm, the Orowan bowing stresses are on the order of theoretical strength limit, and this model will not work. We speculate that a saturation in strength will be reached at these length scales corresponding to the transmission of dislocations across interfaces overcoming the coherency and Koehler-type barriers. A drop in strength, as observed in miscible Cu-Ni systems, may occur if the width of the intermixed interface is on the order of h. The deformation mechanisms at these length scales ($h < \sim 5$ nm) may be better studied through atomistic simulations [19,20].
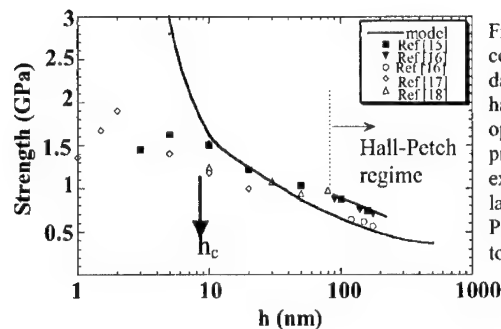
Fig. 5 Single dislocation model compared with Cu-Ni experimental data. The filled data points are hardness divided by 3 and open points are tensile data. Model predictions compare well with the experimental data for $h > h_c$. At large h, the continuum scale Hall-Petch model provides a better fit to the experimental data.

SUMMARY

The Hall-Petch model describes the strengthening in multilayers at near-micron length scales. At nm-scales, plasticity may involve motion of single, rather than piled-up, dislocations, and a model, based on Embury-Hirth [7], is developed to interpret this behavior. We calculate the applied stress for the motion of Orowan loops in the softer layer by incorporating effects of misfit dislocations at the interface and in-plane coherency stresses. This stress when added to the calculated interface resistance to single dislocation transmission gives the composite yield strength that compares favorably with experiments for semi-coherent multilayers.

REFERENCES

1. B.M. Clemens, H. Kung and S.A. Barnett, *MRS Bulletin*, **24**, 20, February (1999).
2. P.M. Anderson, T. Foecke and P.M. Hazzledine, *MRS Bulletin*, **24**, 27, February (1999).
3. A. Misra, M. Verdier, Y.C. Lu, H. Kung, T.E. Mitchell, M. Nastasi and J.D. Embury, *Scripta Mat.*, **39**, 555 (1998).
4. P.M. Anderson and C. Li, *NanoStructured Materials*, **5**, 349 (1995).
5. S.I. Rao, P.M. Hazzledine and D. Dimiduk, *Mat.Res.Soc.Sym.Proc.*, **362**, 67 (1995).
6. A. Misra, M. Verdier, H. Kung, J.D. Embury and J.P. Hirth, *Scripta Mat.*, **41**, p 973 (1999).
7. J.D. Embury and J.P. Hirth, *Acta Met.*, **42**, 2051 (1994).
8. W.D. Nix, *Scripta Mat.*, **39**, 545 (1998).
9. H. Huang and F. Spaepen, *Acta Mat.*, **48**, 3261 (2000).
10. J.P. Hirth and X. Feng, J.Appl. Phys., **67**, 3343 (1990).
11. E.R. Kreidler and P.M. Anderson, *Mat.Res.Soc.Sym.Proc.*, **434**, 159 (1996).
12. T. Yamamoto, LANL, unpublished research.
13. B. Shoykhet, M.A. Grinfeld and P.M. Hazzledine, *Acta Mater.*, **46**, 3761 (1998).
14. J.P. Hirth and J. Lothe, *Theory of Dislocations*, Krieger, p 734 (1992).
15. M. Verdier, M. Niewczas, J.D. Embury, M. Nastasi and H. Kung, *Mat. Res. Soc. Sym. Proc.*, **522**, 77 (1998).
16. R.F. Bunshah *et al.*, *Thin Solid Films*, **72**, 261 (1980).
17. S. Menezes and D.P. Anderson, *J. Electrochem. Soc.*, **137**, 440 (1990)
18. D.M. Tench and J.T. White, *J. Electrochem. Soc.*, **138**, 3757 (1991).
19. R.G. Hoagland, *Phil.Mag.A*, submitted.
20. S.I. Rao and P.M. Hazzledine, Phil. Mag.A, **30**, 2011 (2000).

Correlations of Microstructure and TEM Observations of Plasticity in Metallic Nanolaminates

Donald E. Kramer and Tim Foecke
Metallurgy Division, National Institute of Standards and Technology
Technology Administration, US Department of Commerce
Gaithersburg, Maryland 20899-8553

ABSTRACT

Nanolaminate materials exhibit increases in hardness and yield strength beyond those expected according to rule of mixtures calculations. Several models have been proposed to explain this enhancement of strength, but conclusive experimental verification is hindered by the complex interaction between ingrown defects, in-plane microstructure and compositional modulation. In this study, mechanisms of plastic deformation in nanolaminates are investigated by *in situ* TEM straining of epitaxial Cu/Ni nanolaminates grown on Cu (001) single crystal substrates. Two distinct types of deformation are observed. Initial plastic deformation is accommodated by motion of "Orowan" and threading dislocations in a uniform and random fashion. As the stress levels increase, fracture occurs creating a mixed mode crack. Subsequent observations suggest that intense plastic deformation occurs over many bilayers in the direction of crack growth, but is contained to within one or two bilayers in a direction normal to the crack faces.

INTRODUCTION

The capability of microstructural control on the nanoscale has lead to the development of materials exhibiting significant enhancements in hardness [1], tensile strength [2], and wear properties [3] compared to "bulk" materials fabricated through traditional processing routes. Nanolaminated composites consist of alternating layers of at least two different materials, with each layer being up to tens of nanometers in thickness. Nanometer level modulation in composition may also introduce nanometer scale modulation in elastic modulus, lattice spacing and crystal structure. These effects in turn lead to image forces, interfacial misfit dislocations, alternating residual stresses and variations in Burgers vector, all of which have been proposed as potential interfacial strengthening mechanisms in nanolaminates [1, 4-7].

The lack in understanding of the fundamental deformation mechanisms in nanolaminates has made it difficult to predict, and thereby optimize, their mechanical properties. This is due is part to the paucity of observations of deformation induced structures in these materials. Difficulty in sample preparation and microstructural complexity have made characterization studies difficult to perform. Lu *et al*. have observed threading dislocations crossing multiple interfaces in Cu/Nb nanolaminates deformed under a knife edge contact [8]. Early in-situ straining experiments on Cu/Ni systems have suggested that threading segments deposited at the interfaces can bow into adjacent layers under high stresses [9-11]. One drawback to those studies was that the sample geometry resulted in localization of deformation in a narrow region of the nanolaminate. In this study, *in situ* TEM straining experiments are performed on Cu/Ni nanolaminates with a bilayer thickness of 90 nm and a more uniform stress distribution. Initial plastic deformation is

accommodated by confined layer slip (CLS) and motion of threading dislocations spanning multiple layers. As the stresses increase, a mixed mode crack is initiated inducing localized plastic deformation ahead of the crack tip.

EXPERIMENTAL PROCEDURE

Single crystal nanolaminates composed of alternating layers of copper and nickel were prepared by pulse plate electrodeposition on a 1 inch diameter Cu (001) single crystal substrate disk [12]. The bilayer wavelength was 90 nm, composed of 55 nm Ni layers and 35 nm Cu layers and was repeatedly deposited to a total film thickness of 5 µm. The single crystal disk/ nanolaminate film was subsequently overplated with copper. Slices were cut such that the nanolaminate was viewed in cross-section from the cut surface. Standard 3 mm disks were then mechanically punched from the slice and subsequently dimpled and ion-milled just to the point where the laminate layers were electron transparent but not perforated. The TEM foil was then mounted to a straining blank using cyanoacrylate and loaded into a straining holder. Diffraction studies in the TEM revealed that the crystal was oriented in such a way that the normal to the surface of the TEM foil was along a <100> direction.

In situ straining experiments were performed in a 300 kV TEM with a single tilt, gear driven straining system. All micrographs and video footage are bright field images taken near the (100) zone axis at tilt angles that maximize contrast and minimize layer occlusion. Extension rates were approximately 10 nm/s. Straining experiments were recorded using a mini DV digital video recorder and a CCD camera trained on the phosphor screen. Video was subsequently imported to the computer using commercial video editing software and the brightness and contrast of the images were enhanced to utilize the full grayscale range. Individual frames have been Fourier filtered to remove grids of dots, which were artifacts from the video compression algorithm.

RESULTS AND DISCUSSION

In Situ TEM Observations

The initial microstructure, tensile axis, and crystallographic orientation of the foil are shown in figure 1. Threading dislocations and Orowan-type loops are located in both the Cu and Ni layers. Note also the absence of grain boundaries. The TEM foil is oriented near the (100) zone axis such that the active $\{111\}\langle\overline{1}10\rangle$ slip systems are inclined to the foil surfaces by 45°. Consequently, dislocations move a distance of one or two bilayers before exiting a foil surface.

Initial plastic strain is accommodated by random occurrences of CLS of Orowan-type dislocations, or occasionally through threading dislocations spanning multiple layers. Figures 2 (a) and (b) show two video frames spaced 30 s apart showing the motion and/or disappearance of dislocations due to multiple CLS events and the emergence of dislocations from the foil. The spot in the center of the field of view is an artifact of the phosphor screen. The arrows in each micrograph point to the initial positions of several dislocations and illustrate the occurrence of CLS. Motion and/or disappearance of these dislocations are stochastic and jerky. Occasionally, motion of threading dislocations that span multiple layers is also observed, although this is less common. When a CLS event occurs, it frequently results in a series of CLS events in adjacent
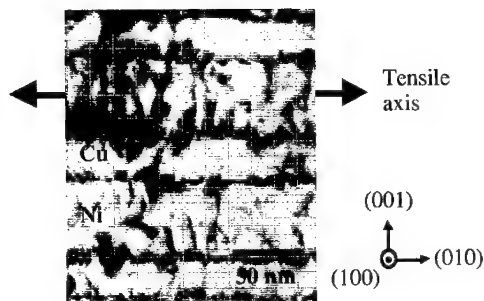
Figure 1. Cross-section TEM micrograph of a 35 nm Cu/55 nm Ni single crystal nanolaminate. Threading and Orowan type dislocation span both layer types.

layers. For this particular foil, the video indicates slip occurring in both the Ni and Cu layers with similar frequency. This is expected as the stress to activate CLS is proportional to $(\mu b/h)\ln(h/b)$, where μ is the shear modulus, b is the Burgers vector, and h is the individual layer thickness [13]. The shear modulus and thickness of the Ni layers are both approximately 1.5 times that of the Cu layers, giving similar threshold stresses for CLS.

Eventually the rising stress level leads to formation of a mixed mode crack. When this occurs, deformation becomes highly localized. Figure 3 shows a micrograph of the crack wake after formation of the crack. Analysis of video footage during straining reveals that the crack was formed during two discrete bursts of deformation spaced 8 s apart. The direction of crack propagation with respect to the tensile axis, combined with out of plane bending in the foil, gives rise to normal, in-plane and out-of-plane shear modes. Inspection of figure 3 reveals that the crack wake consists of two regions that have completely sheared apart, labeled "a" and "b", separated by a bridging ligament. This is consistent with the video observations and suggests that the crack formed in two steps.
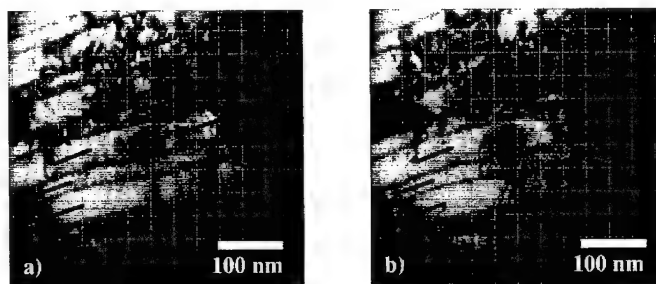
Figure 2. A single crystal Cu/Ni nanolaminate with a 90 nm bilayer thickness showing confined layer slip (CLS). Arrows mark the same location in each frame and highlight regions where CLS has occurred. The dark spot in the center of the frame is an artifact of the phosphor screen. (a) Initial configuration. (b) After 30 s of strain.

Figure 3. A crack formed during *in situ* straining as a result of localized plastic deformation in an epitaxial single crystal Cu/Ni nanolaminate. The crack is growing from right to left and was formed during two discrete events.

Near region "a", the angular projection of the crack faces with respect to the Cu/Ni interface is approximately 45°, consistent with slip along {111} planes projected onto the (100) plane. However, near "b" this angle changes to 56° ± 3°. Selected area diffraction from region "b" indicates the foil has plastically bent causing a rotation from the (100) to the (101) zone axis, thus resulting in the change in projected angle.

The stepped morphology of the fracture surface near "a" and the occurrence of blunting are of particular interest. Fracture within each layer occurs on separate {111} planes and linkage of these regions occurs near the Cu/Ni interfaces. High magnification micrographs reveal that separation does not occur along the Cu/Ni interfaces, but rather within the Cu layers. This process leads to limited ductile tearing and crack tip blunting within the Cu layers. Evidence of nanometer scale blunting can be found by comparing the separation of crack faces in adjacent Ni layers. For instance, in figure 3, the two Ni layers indicated with arrows have projected crack face separations of 15 nm and 30 nm. This may be an opening mode displacement, projected displacement resulting from out of plane shear, or a mixture of the two. The transition in separation between these two Ni layers occurs within the intervening Cu layer.

While initial crack propagation occurs in an unstable manner, subsequent straining produces dislocation activity that is highly localized along slip planes ahead of the crack tip. Figures 4 (a) and (b) are video captures taken 5 min apart during straining. Deformation proceeds from the top to the bottom of the field of view and moves slightly to the left. The tip of the crack is off the top of the viewscreen. Imaging conditions for the dislocations participating in this mode of deformation are extremely weak. However, sudden changes in local strain in the foil due to deformation and crack growth result in variations of diffraction contrast, allowing general observations to be made of how deformation proceeds.

Deformation is observed to proceed on a layer by layer basis. This is inferred from abrupt changes in the location of strain contours and the extent of shear thinning at the interfaces, as seen in figures 4 (a) and (b) and the video footage. Dislocation activity in the nanolaminate is limited to a narrow zone within individual layers provided the crack continues to propagate in the same direction. The width of this zone has been estimated from the video and is indicated in figure 4 (a) as approximately two bilayers. In contrast, dislocation activity occurs over at least 7 adjacent bilayers in the direction of crack propagation, giving the plastic zone a high aspect ratio. For example, in the video sequence from which figures 4 (a) and (b) were taken, localized plastic
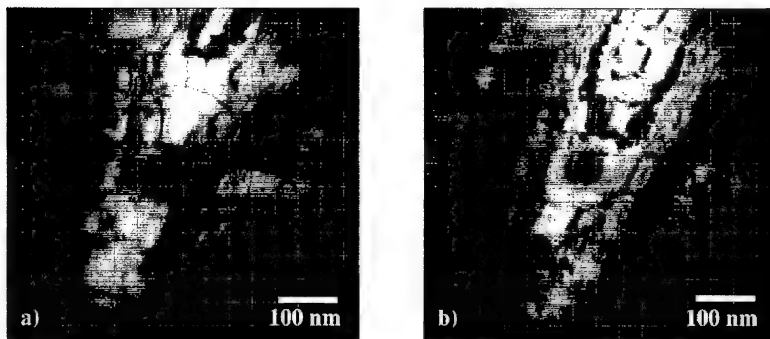
Figure 4. Individual frames taken from *in situ* TEM straining of a Cu/Ni nanolaminate. The video is taken from the plastic zone ahead of the crack tip that is propagating from the top right toward the bottom left. Variations in diffraction contrast indicate the effect of interfaces on plastic deformation. (a) Initial configuration. (b) After 5 min of applied strain.

deformation was seen in all layers on the viewscreen, although the most intense activity occurred within the top four bilayers.

These observations are similar to the initial stages of crack propagation as seen by *in situ* straining of homogenous metals [14], where the thin foil geometry results in a Mode III crack consisting of a coplanar arrays of screw dislocations. However, in the nanolaminate, this deformation structure is not a thin foil effect. When the plastic zone reaches the single crystal substrate, screw dislocations begin to cross-slip, expanding the plastic zone size by more than two orders of magnitude under similar foil thickness and applied stress intensity conditions.

Comparison to Modeling

Observations indicate that initial deformation occurs through CLS in both Ni and Cu layers. Thus, factors such as image forces and other interfacial strengthening mechanisms do not determine the onset of yield at this bilayer thickness. Instead, the layer thickness, shear modulus and Burgers vector determine the line tension that must be overcome to initiate dislocation glide within a layer [13]. For the nanolaminate tested here, this occurs at a similar stress for both Cu and Ni layers and CLS is observed within the entire nanolaminate. The process of CLS involves incorporation of misfit dislocations at the Cu/Ni interfaces. Modeling suggests the gradual increase in misfit dislocation density occurs at a constant stress until the interface is fully saturated [11]. Upon saturation, discrete pileups begin to form within individual layers.

Once the stress to propagate a dislocation at the head of a discrete pileup across the interface is less than that to initiate CLS within a saturated layer, interlayer mechanisms become operational. The stress at which this occurs is dependent upon the mechanisms responsible for the strength of the interface, whether it be modulus mismatch, misfit dislocation grids, differences in crystal structure, etc. Subsequently, Orowan-type dislocations previously confined to a single layer now span multiple layers. These dislocations can now propagate in a CLS mode, under a modified critical configuration where the confined layer thickness is now the combined thickness of two or more adjacent layers. This increase in effective layer thickness decreases the

stress for CLS and increases the number of dislocations that can be incorporated into a pileup configuration. This could concentrate dislocation activity and result in localized deformation. Previous *in situ* TEM studies have hinted at various localizing processes [9-11]. While this study highlights the early stages of slip in nanolaminated structures, investigating the transition from CLS to interlayer deformation mechanisms is the focus of ongoing research.

CONCLUSIONS

Deformation mechanisms in Cu/Ni single crystal nanolaminates have been investigated by *in situ* straining of nanolaminate cross sections in the TEM. Initial plastic deformation is observed to occur by a CLS mechanism in which Orowan-type dislocations glide within their layers and do not penetrate the Cu/Ni interfaces. Upon saturation of the CLS mechanism, a mixed mode crack is initiated. During subsequent crack growth, deformation proceeds on a layer by layer basis. Dislocation activity is limited to within a bilayer thickness of the fracture surface, but extends over at least 7 bilayers in the direction of crack propagation.

ACKNOWLEDGEMENT

REFERENCES

1. X. Chu and S. A. Barnett, *J. Appl. Phys.*, **77**, 4403 (1995).
2. D. Tench and J. White, *Metall. Trans.*, **15A**, 2039 (1984).
3. A.W. Ruff and D.S. Lashmore, *Wear*, **151**, 245 (1991).
4. J. S. Koehler, *Phys. Rev. B*, **2**, 547 (1970).
5. P. M. Anderson and C. Li, *Nanostruct. Mater.*, **5**, 349 (1995).
6. B. J. Daniels, W. D. Nix and B. M. Clemens, *Appl. Phys. Lett.*, **66**, 2969 (1995).
7. A. Misra, M. Verdier, H. Kung, J. D. Embury and J. P. Hirth, *Scripta Mater.*, **41**, 973 (1999).
8. Y-C. Lu, H. Kung, A. J. Griffin, Jr., M. A. Nastasi and T. E. Mitchell, *J. Mater. Res.*, **12**, 1939 (1997).
9. G. S. Was and T. Foecke, *Thin Solid Films*, **286**, 1 (1996).
10. T. Foecke and D. van Heerden, in *Chemistry and Physics of Nanostructures and Related Non-Equilibrium Materials*, edited by E. Ma, B. Fultz, R. Shull. J. Morral and P. Nash (TMS, 1997) pp. 193-200.
11. P. M. Anderson, T. Foecke and P. M. Hazzledine, *MRS Bull.*, **24** (2), 27-33 (1999).
12. T. P. Moffat, *J. Electrochem. Soc.*, **142**, 3767 (1995).
13. J. D. Embury and J. P. Hirth, *Acta metall. mater.*, **42**, 2051 (1994).
14. S.M. Ohr, *Mater. Sci. Engng.*, **72**, 1 (1985).

Superelastic Deformation of Adaptive Nano-Composites

Alexander L. Roytburd[1] and Julia Slutsker
Materials Science & Engineering Laboratory, National Institute of Standards and Technology, Gaithersburg, MD 20899
[1]Department of Materials and Nuclear Engineering, University of Maryland, College Park, MD, 20742

ABSTRACT

An adaptive composite containing a shape memory alloy as an active component is the subject of the paper. The elastically heterogeneous nano-composite containing ultra-thin layers of a passive material and thin layers of an active material is investigated in this paper. The superelastic modulus of the composite depends on the fraction of the active layer and can be negative if relative thickness of the active layer exceeds some critical value depending on the ratio between the elastic moduli of the layers and the characteristics of transformation. The negative superelastic modulus corresponds to the thermodynamic instability of superelastic deformation and results in stress-strain hysteresis. The relation between the elastic properties of the composite's components and relative thickness of the layers, which enable to stabilize the superelastic deformation, is obtained.

INTRODUCTION

A concept of the superelastic polydomain adaptive composite is proposed in the paper. The *adaptive* composite containing a shape memory alloy as an active component utilizes the unique adaptive properties of shape memory alloys to change their crystalline structure in response to the external stimuli such as temperature or stress. In the adaptive *polydomain* composite deformation of an active component proceeds through the evolution of a polydomain martensitic microstructure. Since the microstructure evolution in thin constrained layer can be well controlled, the multilayer composite consisting of thin ($<1\mu m$) active layers separated by ultra-thin ($<100nm$) of a passive material allows one to obtain superelastic material with controlled deformation properties. Under certain constraint conditions the stress-induced transformation and the domain reconstruction of a martensite phase appear as a hysteresisless continuous evolution of an equilibrium microstructure. Thus, the composite should demonstrate large (~0.1) reversible superelastic deformation with the effective modulus much less than the modulus of the composite components. Ultra-thin layers of a passive component of the composites are able to maintain large elastic deformation.

The thermodynamic analysis of the superelastic deformation of the composite is presented below.

MODEL

Microstructures of the composite after the transformation in a polydomain austenite-martensite state are presented in Fig.1. The possible polydomain structures that can be formed in the active layer as a result of martensitic transformation are shown in Fig.2.
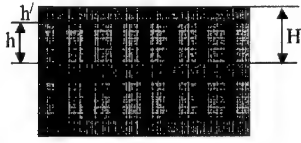
Figure 1. "Elementary cell" of an adaptive nano-composite.
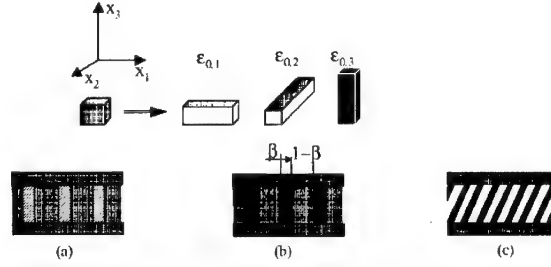
Figure 2. Possible polydomain microstructures in the active layer: (a) two-phase martensite with twin structure inside; (b) single-domain martensite (two-phase polydomain); (c) twin structure.

If the crystallographic symmetry of a product phase is lower than the symmetry of the parent phase, several different variants, or domains, of the product phase can arise. For instance, a transformation of a cubic phase to a tetragonal should give three variants with self-strains (Fig.2).

$$\hat{\varepsilon}_{0,1} = \varepsilon_0 \begin{pmatrix} 1 & 0 & 0 \\ 0 & -\chi & 0 \\ 0 & 0 & -\chi \end{pmatrix} \quad \hat{\varepsilon}_{0,2} = \varepsilon_0 \begin{pmatrix} -\chi & 0 & 0 \\ 0 & 1 & 0 \\ 0 & 0 & -\chi \end{pmatrix} \quad \hat{\varepsilon}_{0,3} = \varepsilon_0 \begin{pmatrix} -\chi & 0 & 0 \\ 0 & -\chi & 0 \\ 0 & 0 & 1 \end{pmatrix} \quad (1)$$

where χ is a coefficient of tetragonality.

The typical two-phase polydomain structure consists of alternation of austenite layers and martensite plates with internal twin structure inside (Fig.2a) [1] . However, because the active layer is thin, the microstructure consisting of martensite plates without internal twins and consequently with lower interface energy may be more preferable (Fig.2b). This degenerated microstructure austenite/single-domain martensite is considered in this paper.

The polydomain microstructure arises as a result of the transformation at cooling or under stress. When the stress increases, the growth of the martensite fraction with stress results in superelastic contribution to the total deformation of composites. Thermodynamic analysis allows us to determine the equilibrium martensite fraction as a function of stress and to construct the superelastic stress-strain relation.

THERMODYNAMICS OF ADAPTIVE NANO-COMPOSITES WITHOUT EXTERNAL STRESS

The free energy of the composite per unit of volume can be presented as following:

$$F = \gamma \beta \Delta f + \gamma \beta (1 - \beta) e_M + \gamma (1 - \gamma) e_C + e_{micro} \quad (2)$$

where $\gamma = h/H$ is a fraction of the active layer, β is a fraction of the martensite phase in the two-phase mixture. The first two terms describe the free energy of the active layer. $\Delta f = f_0^2 - f_0^1$ is the temperature determined difference of the free energies of an austenite phase (f_0^1) and the martensite phase (f_0^2). e_M is and energy due to the misfit between austenite and martensite phases. For the self-strain (Eq.(1)):

$$e_M = \frac{1}{2} E_{100} (\varepsilon_0 \chi)^2 \quad (3)$$

where E_{100} is the Young's modulus along <100> (the cubic elastic anisotropy of the active layer is assumed) [2].

The third term is a constrained energy due to the misfit between layers, where e_C is :

$$e_C = \frac{1}{4}\left[\frac{(\varepsilon_1 + \varepsilon_2)^2}{S(\gamma)} + \frac{(\varepsilon_1 - \varepsilon_2)^2}{\overline{S}(\gamma)}\right]$$

$$S(\gamma) = (1-\gamma)(S_{11}^a + S_{12}^a) + \gamma(S_{11}^P + S_{12}^P)$$ (4)

$$\overline{S}(\gamma) = (1-\gamma)(S_{11}^a - S_{12}^a) + \gamma(S_{11}^P - S_{12}^P)$$

Here $\varepsilon_1 = \varepsilon + \beta\varepsilon_1^0$, $\varepsilon_2 = \varepsilon + \beta\varepsilon_2^0$, where ε is in-plane misfit between the passive layer and the active layer in the austenite state, ε_1^0, ε_2^0 are in-plane components of the self-strain along x_1 and x_2 [3]. It is assumed that the active and passive layers have cubic elastic anisotropy and the layers are parallel to a cubic crystallographic plane, S_{11}^P, S_{12}^P and S_{11}^a, S_{12}^a denote the elastic compliances of the passive and active layers, respectively. The difference between elastic properties of the austenite and the martensite is neglected because it is assumed to be much less than the difference between elastic properties of passive and active layers.

The last term in Eq.(2), the "microscopic" energy, includes the energy of microstresses at the layer interfaces and the energy of the interdomain and interlayer interfaces [3]. In the considered here case of the incompatible phases this term can be omitted because it is small in comparison with the misfit energy between phases.

THERMODYNAMICS OF ADAPTIVE NANO-COMPOSITE UNDER EXTERNAL STRESS

Consider the composite under uniaxial external stress along x_3, σ_3. In this case the martensite with the self-strain $\varepsilon_{0,3}$ is preferable. Under external stress the thermodynamic of the composite is characterized by the minimum of the free enthalpy [4]:

$$\Phi = \Delta f \beta \gamma + \gamma\beta(1-\beta)E^a\frac{1}{2}(\varepsilon_0\chi)^2 + \gamma(1-\gamma)e_C(\sigma_3) - \frac{1}{2}[(1-\gamma)S_{11}^P + \gamma S_{11}^a]\sigma_3^2 - \sigma_3\beta\gamma\varepsilon_3^0$$ (5)

The expression for the free enthalpy is deduced from the expression for the free energy by adding the last two terms in Eq.(5) taking into account the work of external stress and renormalization of constrained energy which becomes

$$e_C = \frac{(-\beta\varepsilon_0\chi + (S_{12}^a - S_{12}^P)\sigma_3)^2}{S(\gamma)}$$ (6)

Here it is taken into account that $\varepsilon_1 = \varepsilon_2$ and assumed $\varepsilon = 0$ (Eq.(4)).

The equilibrium fraction of the martensite phase, β_0, is determined by the equilibrium equation $\partial\Phi/\partial\beta = 0$. The average strain is equal to

$$\varepsilon_3 = -\frac{d\Phi}{d\sigma_3}\bigg|_{\beta_0}$$ (7)
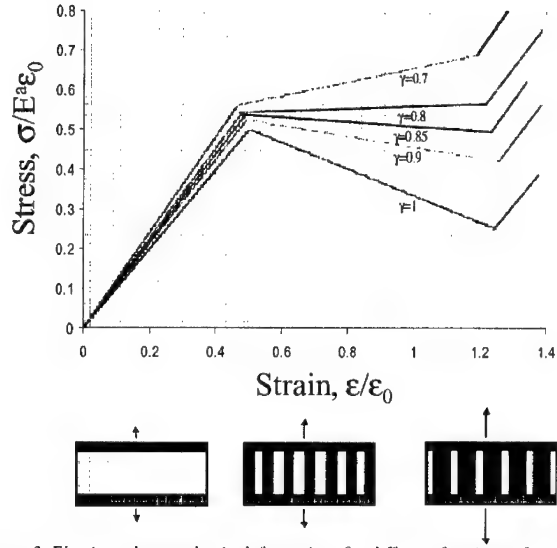
Figure 3. Elastic and superelastic deformation for different fractions of an active layer and the evolution of an equilibrium. Ratio between Young's moduli of active and passive layers, $\xi=S_{11}^{a}/S_{11}^{p}=E^{p}/E^{a}=2$, $S_{12}^{a}/S_{11}^{a}=S_{12}^{p}/S_{11}^{p}=-\nu=-0.33$, $\chi=0.5$.
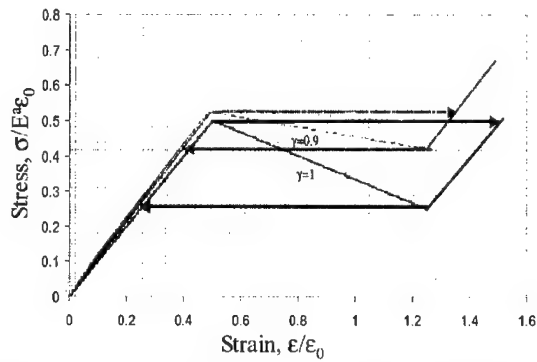
Figure 4. Thermodynamic hysteresis corresponding to the negative slopes on stress-strain curves.

And the superelastic compliance of the composite is

$$S_{33}^{*} = -\frac{d^{2}\Phi}{d\sigma_{3}^{2}}\bigg|_{\beta_{0}} \tag{8}$$

As an example, the superelastic deformation of the composite with isotropic elastic properties of the layers with different relative thicknesses is shown in Fig.3. The negative slope of the curve
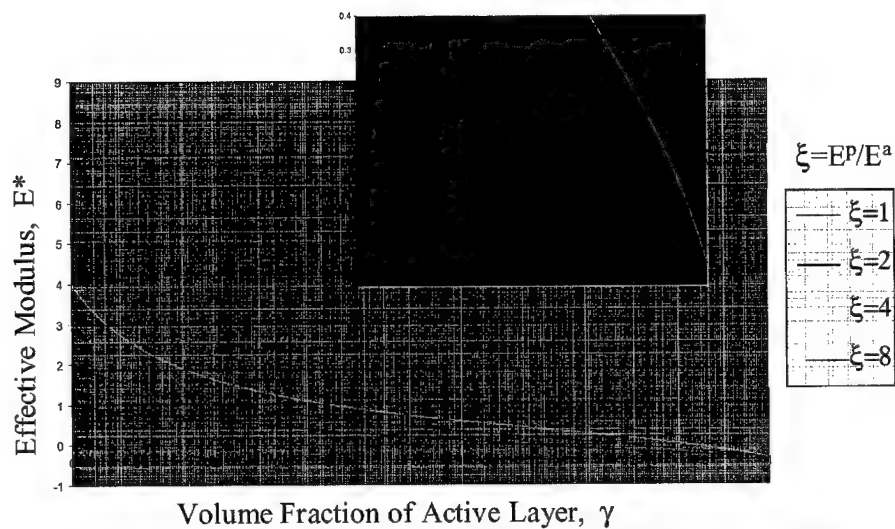
Figure 5. Superelastic modulus $(1/S_{33}^*)$ of the composite for different fractions of an active layer at different ratios between elastic moduli of a passive and active layer.
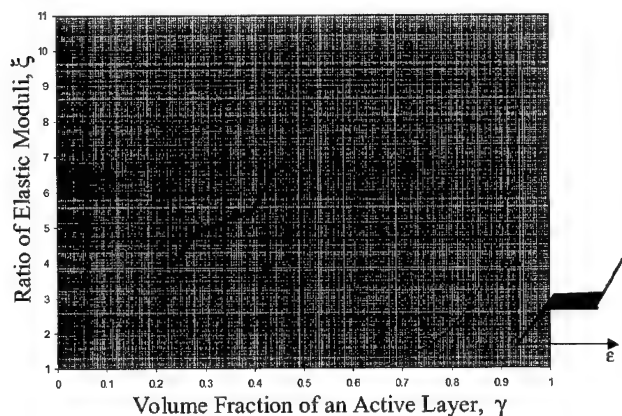
Figure 6. Boundary between areas of stable and unstable superelastic deformation of a composite.

corresponds to the stress-strain hysteresis (Fig.4). This hysteresis decreases and eventually disappears as a fraction of the active layer decreases. The positive and negative superelastic modulus at different fractions of an active layer, γ and at different ratios between elastic moduli of an active and a passive layers, ξ, is shown in Fig.5. Figure 6 shows the optimal relation between ξ and γ which allows one to create the composite without the hysteresis (positive effective Young's modulus of the composite). The boundary $(1/S^*=0)$ which separates the areas of stable and unstable deformation is determined by the equation:

$$\frac{(1-\gamma)\xi}{(1-\gamma)\xi+\xi} = \frac{1-\nu}{2} \qquad (9)$$

Different components of the superelastic compliance can be obtained analogously. However, it is necessary to select the most preferable variant of the martensite phase at different stress states. It results in the change of elastic compliances with change of sign of external stress.

DISSCUSSION AND CONCLUSIONS

As shown in our previous research [2,5] the superelastic deformation of a transforming crystal is intrinsic instable due to incompatibility between phases. This instability is a main source of stress-strain hysteresis of superelasticity. The engineering of the composite including shape memory alloy as a component allows one to eliminate the thermodynamic instability of the two-phase state and to decrease the hysteresis. This problem has been discussed before neglecting the difference of the elastic properties of the composite components [6]. However, it is necessary to note that the constraint imposed by the composite architecture making the evolution of the microstructure more reversible simultaneously decreases the accessible superelastic strain. Therefore, taking into account the difference between elastic properties of the composite's components is necessary for optimization of the deformation properties of the adaptive composites. This important step to design adaptive nano-composites is done in the present paper.

The analysis of the composite with the simplest microstructure presented here can be expanded to more complex hierarchical microstructures including twinned martensite [7] as well to ultra-thin multilayers where the effect of microscopic energy is essential. The effect of the microscopic energy has been taking into account in the analysis of *superplastic* deformation of the adaptive composites with polytwin active layer (Fig.2c) [6, 8].

ACKNOWLEDGMENTS

REFERENCES

1. A.L. Roitburd, *Solid-State Physics*, **33**, 317, 1978.
2. A.L. Roytburd and J. Slutsker, *J.Mech.Phys. Solids*, **47**, 2299,1999.
3. A. L. Roytburd, *J.Appl.Phys.*, **83**, 228, 1998; ibid., 239.
4. A.L. Roitburd, *Soviet Physics-Solid State*, **25**, 17, 1983.
5. A.L. Roytburd and J. Slutsker, *J.Appl. Phys.*,**77**, 2745 ,1995; *J. Mech. Phys. Solids* in press
6. A.L. Roytburd and J. Slutsker, *J.Mech.Phys. Solids*, **47**, 2331, 1999.
7. J. Slutsker and A.L. Roytburd, *J .Mech, Phys. Solids*, submitted
8. A.L. Roytburd, J. Slutsker and M.Wuttig, in *Advances in Twinning*, eds. S.Ankem and G.S. Pande, TMS, 1999, p.313.

Atomistic Simulations of Steps in Bimetallic Interfaces as Barriers to Interface Slip Transmission

Charles H. Henager, Jr.*, Howard L. Heinisch, Jr, Richard J. Kurtz, and Richard G. Hoagland
Pacific Northwest National Laboratory[1]
Richland, WA 99335-0999

ABSTRACT

Atomistic models of coherent interfaces in the CuNi system with and without (111)-steps were used to study slip transmission across interfaces in CuNi metallic bilayers. The lattice mismatch of the CuNi system results in large coherency stresses at the interface. The (111)-steps afford a larger barrier to slip than the flat, coherent interface. The coherent flat interface dislocation barrier is largely due to the large compressive stresses in the Cu layer that must be overcome by applied tensile stresses. Additional Koehler forces are present as the dislocation in the elastically softer Cu approaches the stiffer Ni layer. The step, however, possesses a small residual edge dislocation with a Burgers vector equal to the difference of b_{Cu} and b_{Ni} times the height of the (111)-step in (111)-layers. We find that these steps are potent slip barriers, which suggests that homogeneous slip is preferred in such systems.

INTRODUCTION

Nanolayered materials can have strengths approaching theoretical strengths and empirical laws, such as the Hall-Petch relation, can be used to estimate these strengths as a function of layer spacing. However, the Hall-Petch formalism neglects important mechanisms that begin to become important at small sizes for which single dislocation motion is critical and, therefore, strength estimates may be erroneous. These mechanisms include glide dislocation interactions with coherency strains, Koehler forces due to elasticity differences, and dislocation core structure changes in passing from one layer to another. The mechanical behavior of these materials suggests the term "interface strengthening" as a better description than that given by the Hall-Petch model. Interface strengthening not only describes the yield behavior but subsequent deformation as well since the onset of deformation can change the nature of the interface, which, in turn, can have significant effects on continued deformation processes.

Deformation of cast CuCr eutectics provides indirect evidence that interface steps play a significant role in deformation of interface strengthened materials. Drawn samples of CuCr material containing Cr fibers exhibit rather homogeneous deformation such that the fibers undergo rather uniform shape changes [1]. Extracted Cr fibers exhibit surface slip steps but also show uniform elongation and homogeneous shape changes. These observations suggest that slip is occurring uniformly along the fiber length with dislocations shuttling between the CuCr interfaces [1]. This suggests that surface steps inhibit continued deformation and prevent fiber necking and local shear banding within the Cr fibers.

The size scale of nanolayered materials allows detailed atomistic modeling of deformation behavior. We determine the force required for a dislocation to transect an interface with and without atomic-scale steps. This information can be used to develop detailed mechanistic understanding of deformation nanolayered materials.

DESCRIPTION OF MODEL

Many of the details of our approach are described elsewhere [2]. Briefly, we employ rectangular atomistic models containing an interface parallel to the x-z plane (normal to the y-axis) and having two regions; region 1 is an inner region containing moveable atoms and region 2 is an outer semi-rigid rectangle containing fixed atoms. The two crystals on either side of the interface are free to move and undergo homogenous strain in all three directions and this movement occurs during the relaxation via a viscous drag algorithm, i.e., the velocities and strain rates associated with such motions are proportional to the net forces acting on each of the two crystals within region 1. In addition, we employed a mapping scheme whereby average displacements within region 1 were used to adjust the positions of individual atoms near the interface but within the surrounding region 2. Periodic boundary conditions were employed parallel to the z-axis. Embedded atom method (EAM) potentials that were used to describe the energetics of atomic interactions in the Cu-Ni system are of the Voter-Chen type [3,4].

For this study, we constructed a coherent {010}-interface (cube-on-cube) between Cu and Ni with no interdiffusion or mixing across the interface. The x-axis of the model is [101] and the z-axis is [$\bar{1}$01]. Large coherency strains are present without the misfit dislocations such that σ_{11} in the Cu layer is -2.38 GPa (compression) based on the 2.7% misfit between Cu and Ni. This situation applies to that portion of the CuNi interface lying between the misfit dislocations where the coherency strains are not cancelled by the dislocation strain fields and represents, therefore, the "hard" portion of the interface [5].

Interface steps were created and relaxed during the lattice generation part of the model construction. Dislocations were subsequently created in the Cu layer by applying the anisotropic displacement field(s), the Volterra field, to the atoms in both regions 1 and 2. The dislocation lines were parallel to the z-axes in all cases. The dislocated lattice is then relaxed and incremental tensile strains of 0.002 are applied (quasi-static) to the model using $\varepsilon_{11} = 0.002$, $\varepsilon_{22} = -.0015085$, and $\varepsilon_{33} = 0.00018168$ for the Cu layer and $\varepsilon_{11} = 0.002$, $\varepsilon_{22} = -.00131802$, and $\varepsilon_{33} = 0.00018168$ for the Ni layer to maintain mechanical equilibrium during straining. A molecular dynamics algorithm moves the atoms in response to the nonzero forces acting on them. The relaxation process is stopped when the root mean square of the forces acting in region 1 drops below a set value, about 3×10^{-4} eV/Å. The lattice temperature at relaxation is about 0.01K. Repeated straining and relaxing gradually finds the level of applied strain at which the glide dislocation transects the CuNi interface.

{111} CuNi Step

The lattice mismatch between Cu and Ni of 2.7% gives rise to the large coherency strains in the portion of the interface lying between misfit dislocations [5]. There is a corresponding misfit along <110>{111} since $b_{Cu} = 0.25562$ nm and $b_{Ni} = 0.248902$ nm. Therefore, a {111}-step at the CuNi interface will have a mismatch of $b_{Cu} - b_{Ni} = 0.006718$ nm, which is a residual Burgers vector pointing from Cu to Ni along <110>{111}. For our specific geometry, however, we find that this residual Burgers vector is given by

$$\vec{b}_R = \frac{a_{Cu}}{6}[1\bar{2}1] - \frac{a_{Ni}}{6}[1\bar{2}1] = \left(\frac{a_{Cu}}{6} - \frac{a_{Ni}}{6}\right)[1\bar{2}1] = \frac{0.0095}{6}[1\bar{2}1] \qquad (1)$$

where $a_{Cu} = 0.3615$ nm and $a_{Ni} = 0.352$ nm so that the magnitude of $b_R = 0.003878$ nm. Since our interface is parallel to the x-z plane and is periodic in z, the only direction along which relaxation is allowed in the plane of the (111)-step is in the [1$\bar{2}$1] direction. Therefore, our mismatch Burgers vector must lie along the [1$\bar{2}$1] direction on the (111) plane (Fig. 1).
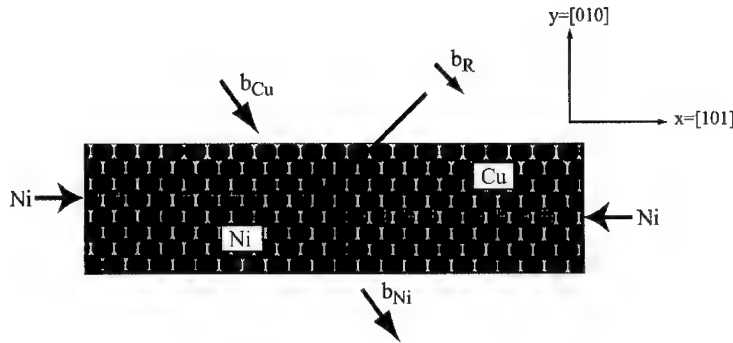
Figure 1. Atomic model of 1-high (111) step in CuNi system. The plane of the step is the (111) plane and the residual b (b_R) lies in the ($\bar{1}11$)-plane along the [$1\bar{2}1$] direction.

Glide Dislocation

We place a pure edge partial $\delta A = a_{Cu} / 6[1\bar{2}1]$ in the Cu layer near the CuNi interface and on the same (111) plane as the step. We use the full anisotropic field for this and place that field in the region 1 and 2 atoms. The large compressive σ_{11} in the Cu layer pushes δA up to the edge of the model (Fig. 2a). Then we apply the strain tensor listed above in 0.002 increments and relax. As the strain increases, we observe the dislocation approaching closer to the boundary and eventually passing through (Fig. 2b). We use the edge partial since it is the leading partial of the **CA** dislocation and experiences the maximum resolved shear stress on the (111) plane. The trailing partial is the **Cδ** partial, which is a 30° dislocation, and it experiences less of the resolved force. Dislocation δA will be the first one to transect the interface and will require the smallest stress to do so.

RESULTS AND DISCUSSION

Flat interface

At an applied strain level of 0.020 the dislocation δA is able to pass through the CuNi interface. Hoagland et al. [5] showed that the following nonlinear stress-strain relation was required to calculate the stresses in the Cu layer:

$$\sigma_{11} = 133.14\varepsilon_{11} - 946.85\varepsilon_{11}^2 \qquad (2)$$

since the strains are large. From this relationship we find that the applied tensile stress is about 3 GPa. Since the Cu layer starts out at −2.4 GPa this means that the tensile stress in the Cu layer at transection is about 0.6 GPa. We also show the distance in the y-direction (height) of δA as a function of applied strain and plot that with the applied stress in the Cu layer (Fig. 3a) as a function of the applied strain.

1-high (111) step

At an applied strain level of 0.024 the dislocation δA is able to pass through the CuNi interface containing a one atomic layer high (111) step. For this case the dislocation is on the same (111) plane containing the step. We show an atomic model of the critical position just

before transection (Fig. 2b). From Eq. (2) we find that the applied tensile stress is about 3.5 GPa, or about 1.1 GPa tensile stress in the Cu layer. We compare results for the flat interface and the 1-high (111) step in Fig. 3a. The stress to transect the interface is significantly higher than for the flat interface. Note that the dislocation approaches closer to the interface for a given strain level compared to that for the flat interface.

(a)   (b)

Figure 2. (a) Atomic model of stepped interface (1-high) with pure edge partial, δA, at top of model. Dislocation was introduced near CuNi interface but was pushed to edge of model by coherency stresses, (b) Model just prior to transection, applied strain equal to 0.022. Dislocation has approached boundary and strained Ni lattice is visible across the interface.

2-high (111) step

At an applied strain level of 0.026 the dislocation δA is able to pass through the CuNi interface containing a two atomic layer high (111) step. Again, the dislocation is on the same (111) plane containing the step. We find that the applied tensile stress is about 3.7 GPa, or about 1.3 GPa tensile stress in the Cu layer. We compare results for the flat interface and both steps in Fig. 3a. The 2-high step has twice the b_R of the 1-high step and the transection stresses are correspondingly higher.

Slip Proximity to the 1-high (111) step

The location of dislocation δA relative to the 1-high (111) step was varied to help understand the range of influence of the step. The dislocation was moved over one plane (1-off) and two planes (2-off) and the strain to push it through the boundary was calculated. The results are shown in Fig. 3b relative to the 1-high (111) step on-plane. We see that the stress to transect the boundary is reduced as the dislocation moves away from the step, as we might expect. However, even at two planes from the step the transection stress is higher than that for the flat interface.

General Discussion

We find that even small steps at the CuNi interface have significant effects on slip transmission. The stress to push a glide dislocation through a flat interfaces increases by about 0.5 GPa for the case with a 1-high (111) step. This stress is increased by 0.8 GPa for the 2-high

step. Although the residual b is very small, it is not expected to be glissile and, therefore, it acts as a strong glide barrier. Although we were not able to determine the stress field of the step from this study (we do plan to do this), we also find that the step has a range of influence at least 2 planes away from the plane of the step. This may be due to the field of the small residual b or it may be due to the elastic field of the step itself.

The main implication of this study is that these slip steps are potent glide barriers and that subsequent deformation is likely prohibited. That is, work hardening is high and subsequent deformation would more likely occur on adjacent planes rather than localized shear banding. Rather, homogeneous deformation is encouraged and this agrees with the general observations in the CuCr system [1].

(a)   (b)
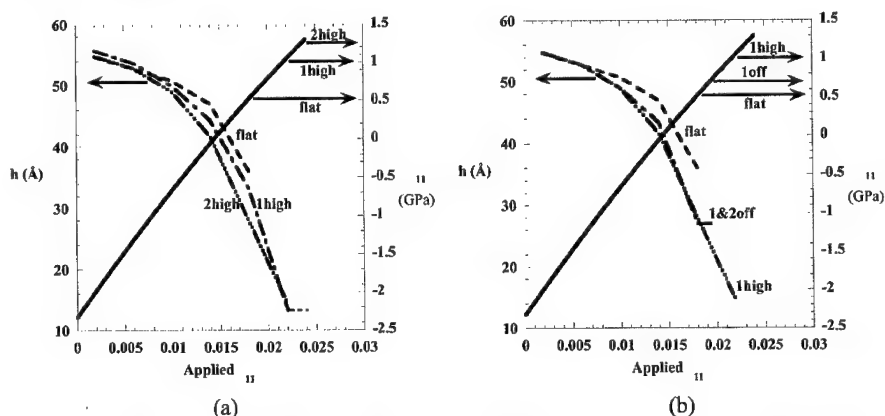
Figure 3. (a) Plot showing dislocation height (y-direction) and σ_{11} as a function of applied strain for flat, 1-high, and 2-high (111) steps. The labeled arrows mark the stress at which δA was able to transect the indicated boundary, (b) Dislocation height and σ_{11} as a function of applied strain for flat, 1-high, and 1-high, 1- and 2-off cases. Glide plane of δA was moved over either one or two planes. The two cases give the same stress level for transection.

CONCLUSIONS

Slip steps, or (111) steps, on CuNi coherent interfaces are a potent glide barrier relative to the flat interface. Dislocations in the highly compressive Cu layer require large applied stresses that overcome the coherency stresses in order to transect the CuNi interface in the case of flat interfaces. These applied stresses must be increased significantly in order to push dislocations through atomic height steps at this interface. Such glide barriers argue for homogeneous slip in these nanolayered materials, which agrees with general findings in the CuCr eutectic system.

References

1. C. W. Sinclair, J. D. Embury, and G. C. Weatherly, *Mater. Sci. Eng., A*, 1999, **A272** 90.
2. R. J. Kurtz, R. G. Hoagland, and J. P. Hirth, *Phil. Mag. A*, 1999, **79** 683.
3. A. F. Voter and S. P. Chen, *Mater. Res. Soc. Symp. Proc.*, 1987, **186** 175.
4. A. F. Voter, , , 1993, 77.
5. R. G. Hoagland, H. Kung, A. Misra, and J. D. Embury, *Mater. Sci. Res. Soc. Symp. (submitted to this proceedings)*, 2001, **634** .

Interaction Between Dislocations and Misfit Interface

A. Kuronen, K. Kaski, L. F. Perondi[1], and J. Rintala

Helsinki University of Technology, Laboratory of Computational Engineering
P.O.Box 9400, FIN-02015 HUT, FINLAND
[1]Permanent address: Instituto Nacional de Pesquisas Espaciais – INPE
P.O.Box 515, 12–227–010 São José dos Campos – SP, Brazil

ABSTRACT

Mechanisms responsible for the formation of a misfit dislocation in a lattice-mismatched system have been studied using Molecular Dynamics simulations of a two-dimensional Lennard-Jones system. Results show clearly how the strain due to the lattice-mismatched interface acts as a driving force for migration of dislocations in the substrate and the overlayer and nucleation of dislocations in the overlayer edges. Moreover, we observe dislocation reactions in which the gliding planes of dislocations change such that they can migrate to the interface.

INTRODUCTION

Dislocations play an essential role not only in strength properties of ductile materials but also in strain relaxation processes of lattice-mismatched hetero-structures [1–3], that are central in todays nanotechnology. When in a lattice-mismatched hetero-structure the thickness of the overlayer is small enough, the mismatch is accommodated by elastic deformation of the overlayer. When the thickness increases, the elastic energy of the overlayer becomes larger and at a certain critical thickness it becomes favorable to relieve the strain by misfit dislocations at the interface.

Various mechanisms of dislocation migration and nucleation have been found to affect the strain relaxation process [1, 3]. These mechanisms include the migration of threading dislocation to the interface, nucleation of dislocations, and dislocation multiplication [4–7]. In all these mechanisms the underlying atomic level cause of the misfit dislocation formation is the attractive force exerted by the interface on dislocations with Burgers vector orientation appropriate for the relaxation of misfit energy.

In the present work, we investigate the migration of dislocations and their effect on strain relaxation in an atomistic model of a hetero-structure. We will study the effect of the misfit interface on the migration of dislocations initially present in the system, nucleation of dislocations in the overlayer edges, and the effect of the interface on the interaction between dislocations, by using Molecular Dynamics (MD) simulations. In order to explore the qualitative behavior of dislocation dynamics and for simplicity inter-atomic interactions have been modeled by Lennard-Jones (LJ) potentials. We have restricted our investigations to two-dimensional (2D) systems, thus avoiding the geometrical complexities involved in the simulation of three-dimensional dislocations while retaining salient features of the problem under consideration.

COMPUTATIONAL DETAILS

In order to get better insight to the dislocation dynamics we have constructed a computational model that is based on an interactive simulation program with a graphical visual-
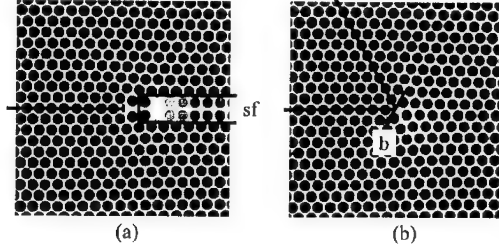
Figure 1. *Dislocations in a close-packed 2D system. (a) A partial dislocation and a stacking fault (sf) formed by removing one atomic row. (b) A perfect dislocation formed by removing two atomic rows. The Burgers vector* **b** *of the dislocation is also shown. The shading of the atoms is coded according to their potential energy (light: high energy, dark: low energy).*

ization environment, described in detail in ref. [8]. The interaction between a pair of atoms is described by the Lennard-Jones potential

$$V(r) = \epsilon_{\alpha\beta}[(\sigma_{\alpha\beta}/r)^{12} - (\sigma_{\alpha\beta}/r)^6], \tag{1}$$

where r is the interatomic distance. Potential parameters $\epsilon_{\alpha\beta}$ and $\sigma_{\alpha\beta}$ depend on the species (α and β) of the interacting atoms. The lattice mismatch is defined as $f = (a_f - a_s)/a_s$, where a_f and a_s are the lattice constants of the film and the substrate, respectively. This mismatch can be incorporated into the simulations by assigning a different index for the atoms in the upper layers as compared to the atoms in the rest of the system and changing the equilibrium distance parameter σ for these atoms accordingly. The cross-interactions between different types of atoms are calculated by an interpolation scheme [9] as follows:

$$\epsilon_{\alpha\beta} = (2(\epsilon_{\alpha\alpha}\epsilon_{\beta\beta})^{1/2}\sigma_{\alpha\alpha}^3\sigma_{\beta\beta}^3)/(\sigma_{\alpha\alpha}^6 + \sigma_{\beta\beta}^6) \tag{2}$$

$$\sigma_{\alpha\beta} = ((\sigma_{\alpha\alpha}^6 + \sigma_{\beta\beta}^6)/2)^{1/6} \tag{3}$$

The values of parameters ϵ and σ from ref. [8] – fitted to describe copper – were used for the substrate atoms. The range of the potential is limited by the cut-off distance r_c chosen here to be $r_c = 2.1 \times r_{NN}$, where r_{NN} is the nearest neighbor distance. The effect of the discontinuity in the potential at the cut-off radius was compensated by subtracting a linear term of the form $(r - r_c)dV/dr|_{r=r_c}$ from the potential. The simulation system consists of atoms placed in a densely packed hexagonal lattice.

Dislocations can be introduced into the system by removing a part of a densely packed row of atoms from the system (see figure 1). This can be done in three orientations, which introduces into the system two partial dislocations with a stacking fault between them. Such a high energy configuration quickly relaxes and the stacking fault disappears, thus two perfect dislocations with Burgers vector equal to the shortest lattice vector are formed. In some simulations where only one dislocation was initially needed, it was introduced by applying the deformation field of elastic continuum theory [10].

RESULTS AND DISCUSSION

In the simulations described below, the bottom layer of the substrate atoms is fixed in the vertical direction while the other boundaries of the system are free to move in any direction.
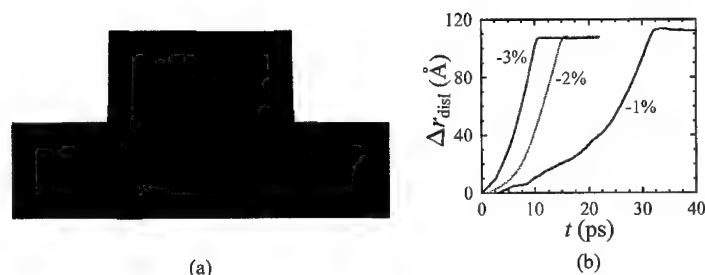
Figure 2. Migration of a dislocation from the overlayer to the interface. (a) The simulation system used in migration studies. (b) The distance of the dislocations from their position in the beginning of the simulation as a function of time plotted for misfits -1%, -2%, and -3%.
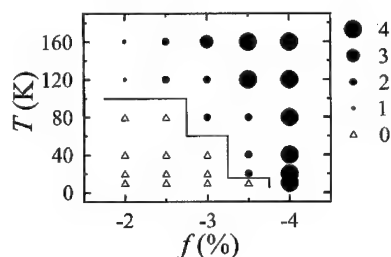
Figure 3. Results of the nucleation simulations. The number of dislocations nucleated from the overlayer edges during the 130 ps simulations is plotted for different misfits and simulation temperatures. The size of the circles denotes the number of dislocations. Open triangles designate runs where no dislocations were observed. The thin line separates pseudomorphic and relaxed regions.

The system sizes varied from 3442 to 34667 atoms.

In figure 2 are shown the results of the dislocation migration simulations. The system consisted of 11590 overlayer atoms and 23076 substrate atoms [see figure 2(a)]. The system size was 722 Å× 361 Å. The initial dislocation was introduced into the center of the overlayer by deforming the lattice according to elastic continuum theory. After relaxing the system [11] the velocities of the atoms were scaled for 100 fs to reach a temperature of 20 K after which the simulation was continued in constant energy mode. Figure 2(b) shows the distance of the dislocation from its initial position as a function of time for three different misfits. The velocities are averages of a statistics of 20 simulation runs. In all cases the final position of the dislocation is at the interface as can be seen in figure 2(b): the distance of the dislocation saturates after a long enough time. The amount misfit has a strong effect on the dislocation migration. The final velocities of dislocations estimated from the last 5 ps before reaching the interface were 936, 1338, and 1654 m/s for the misfits of -1.0, -2.0, and -3.0%, respectively.

Dislocation nucleation was studied using the same system as above but without the initial dislocation in the overlayer. Simulations were performed for misfits -2.0% – 4.0% at
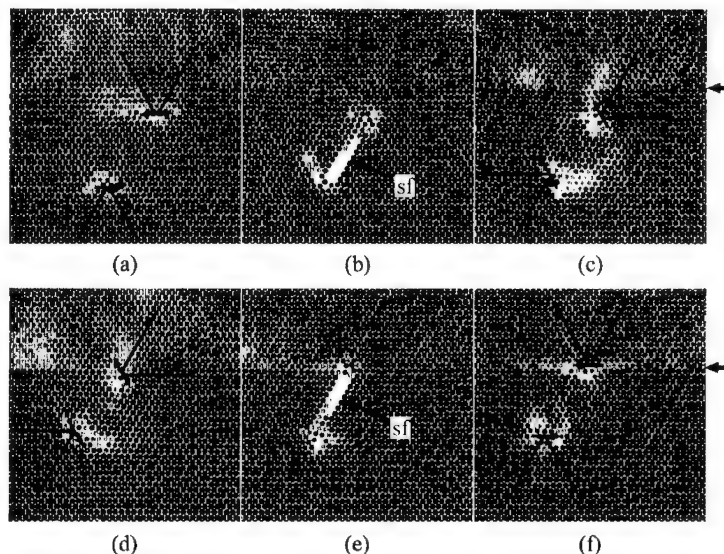
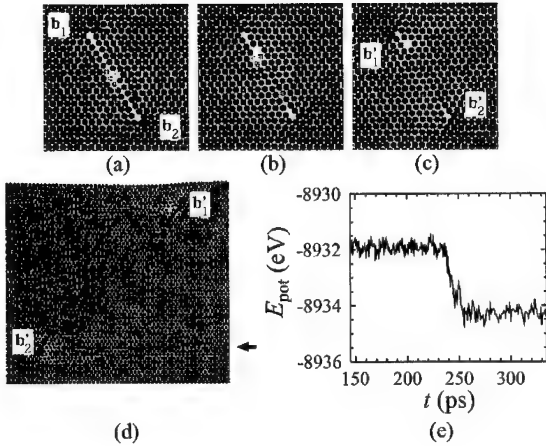**Figure 4.** *Reaction between dislocations and the misfit interface. The lattice mismatch between the overlayer and the substrate is $f = 4\%$ (a) [Elapsed time from the beginning of the simulation $t = 12.1$ ps] Two dislocations with horizontal Burgers vectors are introduced to the system. (b,c) [$t = 15.1, 16.1$ ps] These interact with each other first forming a stacking fault (sf) between them and then dislocations with Burgers vectors oriented 60° relative to the x-axis. (d) [$t = 18.8$ ps] The upper dislocation migrates to the interface. (e,f) [$t = 33.5, 34.2$ ps] The dislocations interact once again and turn their Burgers vectors horizontally. The small arrows show the position of the interface.*

temperatures 10–160 K. The simulation time was 130 ps. Results are shown in figure 3. In the region of low misfit and low temperature no dislocations were seen. In this region, the strain is relieved by elastic deformation of the overlayer and substrate. By increasing the temperature dislocations are seen to nucleate from the overlayer edges. In all other cases except the -2.0% misfit the highest temperature of 160 K was enough to reach the equilibrium configuration (number of dislocations of 4, 4, 3, 2, and 1 for the misfits -4.0%, -3.5%, -3.0%, -2.5%, and -2.0%, respectively). In the case of misfit of -4.0%, dislocations were observed even in simulations with zero initial temperature, indicating that the activation barrier for nucleation disappears.

Figure 4 depicts an example of the effect of an interface on dislocation interactions, when the lattice mismatch is set to $f = -4\%$. The simulation system consisted of 1340 atoms in the overlayer and 2102 atoms in the substrate. Simulation runs were also performed using a four times larger system with qualitatively similar results. In order to introduce a pair of dislocations into the system an initial crack was introduced first. Then the system was let to heal for 10 ps at the temperature of 15 K. After this the simulation was continued in constant energy mode. The upper dislocation – having two extra planes in the positive y-direction – has the maximum capability to relieve stress formed at the interface [see figure 4(a)]. However, this dislocation cannot glide to the interface because its Burg-

Figure 5. Reaction between dislocations and the misfit interface. The lattice mismatch between the overlayer and the substrate is $f = 2.5\%$ (a,b) [Elapsed time from the beginning of the simulation $t = 230.0, 235.2$ ps] A stacking fault is formed between dislocations b_1 and b_2 by slip of atomic rows (dashed arrows). (c) [$t = 235.2$ ps] Burgers vector of dislocations change orientation. (d) [$t = 250.4$ ps] Dislocation migrate to the interface and overlayer surface. (e) Potential energy of the simulation system as a function of time.

ers vector is horizontal. Figure 4(b) shows how the interaction between the dislocations induces a reaction that results in changes in the Burgers vectors. The fact that the sum of Burgers vector does not change in this reaction can be easily verified. After the reaction, the upper dislocation is able to glide to the interface. However, its Burgers vector is not ideal for relieving stress at the interface. In figures 4(d) and 4(e) a further reaction can be seen which gives rise to dislocations with horizontal Burgers vectors [figure 4(f)]. The upper dislocation is now located at the interface and it has the optimum orientation – i.e. parallel to the interface – as regards to the stress relief. The lower dislocation finally glides to the free boundary of the system, where a step is created.

Reactions between dislocations proceed through creation of two partial dislocations and a stacking fault between them, and thus a slip of two adjacent atomic rows with respect to each other, as can be seen in figure 5(a). For this reaction to take place the dislocation cores have to lie at the same densely packed row of atoms. Figures 5(a)-5(c) show how the reaction changes the orientation of the Burgers vectors of the dislocations. Also shown is the potential function of the simulation system [figure 5(e)] during the reaction and migration of the dislocations to the overlayer surface and the interface [figure 5(d)].

CONCLUSIONS

In conclusion, our results show clearly how the strain due to the lattice-mismatched interface acts as a driving force for dislocation migration, nucleation, and reactions between dislocations.

The stress caused by the lattice-mismatched interface exerts an attractive force on existing dislocations that are able to relieve misfit strain. In case there is initially no dislocations

in the system, strain relaxation proceeds through dislocation nucleation from the overlayer edges, assuming that the misfit and the temperature are large enough to overcome the nucleation barrier.

In the hexagonal lattice dislocations that are able to glide from the substrate towards the interface do not have optimal Burgers vector for strain relief. However, interaction between the dislocation at the interface and the one left in the substrate causes changes in their Burgers vectors that result in an optimal strain for relieving dislocation at the interface.

ACKNOWLEDGMENTS

REFERENCES

1. E. A. Fitzgerald, *Mat. Sci. Rep.* **7**, 87 (1991).
2. R. Hull and J. C. Bean, *Crit. Rev. Solid State. Mat. Sci.* **17**, 507 (1992).
3. R. Hull and E. A. Stach, in *Thin Films: Heteroepitaxial Systems*, Vol. 15 of *Series on Directions in Condensed Matter Physics*, edited by A. W. K. Liu and M. B. Santos (World Scientific, Singapore, 1999), Chap. 7, pp. 299–367.
4. J. W. Matthews, *J. Vac. Sci. Technol.* **12**, 126 (1975).
5. W. Hagen and H. Strunk, *Appl. Phys.* **17**, 85 (1978).
6. H. Strunk, W. Hagen, and E. Bauser, *Appl. Phys.* **18**, 67 (1979).
7. F. K. LeGoues, B. S. Meyerson, and J. F. Morar, *Phys. Rev. Lett.* **66**, 2903 (1991).
8. J. Merimaa, L. F. Perondi, and K. Kaski, *Comp. Phys. Comm.* **124**, 60 (1999).
9. M. Diaz Peña, C. Pando, and J. A. R. Renuncio, *J. Chem. Phys.* **76**, 325 (1982).
10. J. P. Hirth and J. Lothe, *Theory of Dislocations*, 2 ed. (Krieger Publishing Company, Malabar, 1992).
11. Relaxation was performed by scaling down the velocities of all those atoms that satisfied the condition $\mathbf{v}_i \cdot \mathbf{F}_i < 0$ where $\mathbf{v}_i$ and $\mathbf{F}_i$ are the velocity and total force of atom i at all time steps for a few picoseconds.

Coherency Strain and a New Yield Criterion

N.B. Jayaweera, J.R. Downes, D.J. Dunstan, A.J. Bushby,[1] P. Kidd and A. Kelly[2]
Department of Physics, Queen Mary, University of London, London E1 4NS, UK.
[1]Department of Materials, Queen Mary, University of London, London E1 4NS, UK.
[2]Department of Materials Science and Metallurgy, University of Cambridge, Pembroke St.,
Cambridge CB2 3QZ, UK.

ABSTRACT

We have studied the onset of plasticity in coherently-strained semiconductor superlattices, using nano-indentation with spherical indenter tips to observe the full stress-strain curve. The yield pressure is reduced by as much as a factor of two by the presence of the coherency strain. By varying the thicknesses and strains of the superlattice layers, we provide a proof that yield commences over a finite volume. It is properties averaged or summed over this volume which determine the yield pressure. We show that the relevant yield criterion for our experimental data is the rate of change of elastic strain energy with plastic relaxation, integrated over a volume of the order of a micron across. This result is expected to be valid for other systems with highly inhomogenous strain fields, and hence to be applicable to modelling of point contact, and to the design and understanding of structural materials which have coherently-strained microstructure.

INTRODUCTION

The classic yield criteria are those of Tresca and von Mises. They are scalar functions of the stress tensor at a point, such that if the value exceeds a critical value, plastic yield will occur. Pointwise criteria are satisfactory for homogeneous stress, since the same scalar value will be reached simultaneously at all points within the material. However, it has long been realised that inhomogenous stress fields are not adequately treated by pointwise criteria, since for physical reasons plastic yield must initiate throughout some finite volume. Thus, in 1931, Cook [1] suggested that the yield point should be higher in cases of inhomogeneous stress. For a discussion, see Kelly [2]. For want of a satisfactory yield criterion for inhomogeneous stress, finite-element modelling of point contact fails rather badly, with serious implications for our understanding of phenomena such as wear and single-point machining. Semiconductor strained layer structures represent a very powerful tool for investigations of yield in the presence of inhomogeneous stress. Strains up to 1% and more can readily be incorporated into layers of thicknesses of a few tens of nanometres, and multilayer structures can be grown with total thicknesses of a few microns. These structures are epitaxial single crystals with atomically flat interfaces. The coherency strain is introduced by small changes in composition, in an alloy system in which other physical properties change little. So departures from bulk behaviour can be attributed unambiguously to effects of the inhomogeneous stress field alone.

EXPERIMENTAL DETAILS

Superlattices of InGaAs bilayers, repeated to obtain a total thickness of 2.5 μm were grown on InP substrates by molecular beam epitaxy. Each bilayer consists of two layers of different

strain, usually compressive and tensile. For an $In_yGa_{1-y}As$, lattice-match to the substrate, and hence zero strain, is achieved at $x = 0.53$, while for other compositions the strain is related to the composition through Vegard's Law and is $\varepsilon = 0.07 \times (0.53 - x)$. Structures were designed with: a) equal layer thickness and equal but opposite strains (i.e. strain balanced symmetric), b) with equal layer thickness and unequal stains (i.e. with a small net strain in the sample), and c) with unequal layer thicknesses and strains (i.e. asymmetric), Figure 1.

Structures are characterised after growth by high-resolution X-ray diffraction and comparison of the rocking curves or reciprocal space maps with simulations generated by proprietary dynamical diffraction simulation packages. The degree of control in molecular beam epitaxy is such that the structures did not have significant deviations from the nominal (designed) layer thicknesses, strains and compositions. The X-ray diffraction also yields information on the crystallinity. The dislocation densities in the epitaxial layers are not significantly higher than in the InP substrates, in the range $10^2 - 10^4$ cm^{-2} [3,4].

Nanoindentation with spherical tipped indenters was chosen to study the layers using a UMIS 2000 machine. With tip radii in the range $2 - 35$ μm plastic deformation is expected to initiate within the epitaxial superlattice. Spherical tipped indenters allow the transition from elastic to plastic behaviour to be readily observed.

(a) Strain balanced   (b) Net strain   (c) Asymmetric
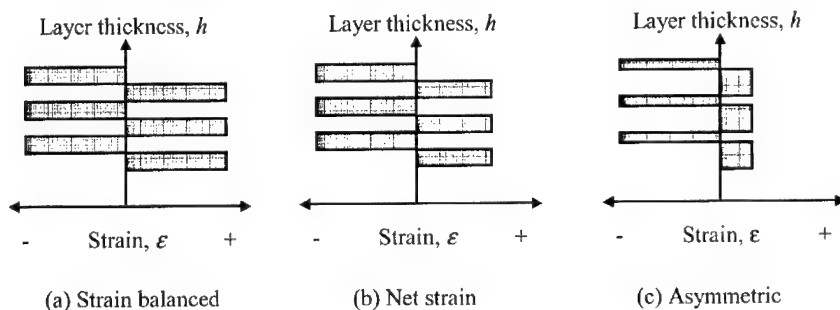
Figure 1. Types of multilayered structures grown.
Range of layer parameters used $(0\% < \varepsilon < \pm1.5\%,\ 17nm < \text{layer thickness} < 125nm)$.

Indentation stress-strain curves ($P/\pi a^2$ vs a/r, where P is the applied force, r is the radius of the indenter tip and a is the radius of the circle of contact between the indenter and surface) were generated using the partial-unloading method of Field and Swain [5], Fig. 2a. In this form, the elastic part of the response is a straight line with a slope corresponding to an appropriate modulus. The departure from this straight line is identified as the yield point. Replotting in the form of Fig.2b, the yield point is the apex of the inverted 'V'. In some samples, a large proportion of indents displayed the behaviour known as 'pop-in', in which the sample remains elastic to a higher stress and then undergoes discontinuous plastic deformation [3]. As shown in Fig.1b, the yield point can still be identified by extrapolation of the plastic curve back to the elastic part; data obtained in this way agrees well with data from indents in which pop-in did not occur. The yield point is therefore defined as the departure from purely elastic behaviour in the presence of a suitable dislocation source.
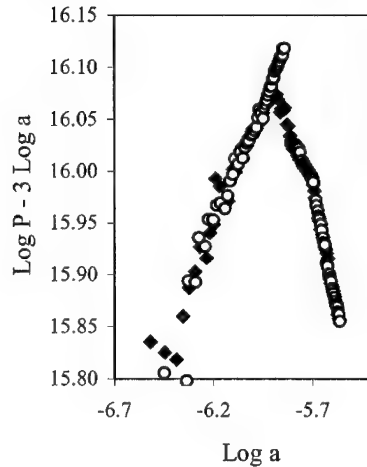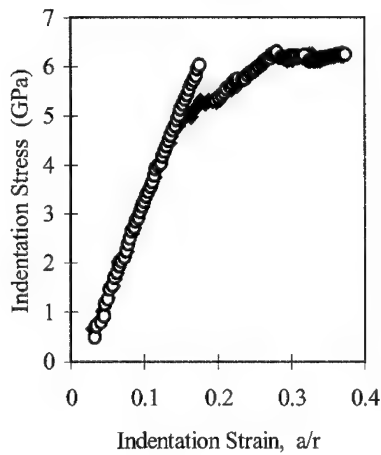
Figure 2a. Indentation stress-strain curves for 'pop-in' O and continuous yield ◆

**Figure 2b.** Data of Figure 2a replotted to identify the yield pressure.

RESULTS

The yield pressure of the superlattice structures decreased very significantly with the introduction of coherency strain. For example, from 6GPa in bulk material to as little as 3GPa in the structure with the highest strains. However, we do not find a good correlation between the extent of the drop in yield pressure and any single design parameter (Fig. 3). In structures with equal layer thickness of 50nm (bilayer thickness 100nm) we previously reported a good correlation with the strain difference between the compressive and tensile layers [3]. However, the structures with asymmetrical layer thicknesses and strains do not obey the same correlation (Fig.3c) and show that none of the parameters in Fig 3 are appropriate yield criteria.

For all the structures studied, we find an excellent correlation with the factor F, (Fig. 4) defined as

$$F = \frac{\varepsilon_t h_t - \varepsilon_c h_c}{h_t + h_c} \qquad [1]$$

where ε_t is the strain in the tensile layers of thickness h_t and ε_c is the strain in the compressive layers of thickness h_c. In the next section we shall derive this factor theoretically and show how it implies a new yield criterion. Here we wish to emphasise that it proves that plasticity begins throughout a volume which incorporates at least one whole bilayer. This is because the formula for F contains parameters describing both layers of the bilayer, yet the parameters of a layer in which no plastic deformation takes place at the yield point could not be relevant. This observation is sufficient to show that plasticity begins in a volume of at least 0.150 μm, our largest bilayer period.
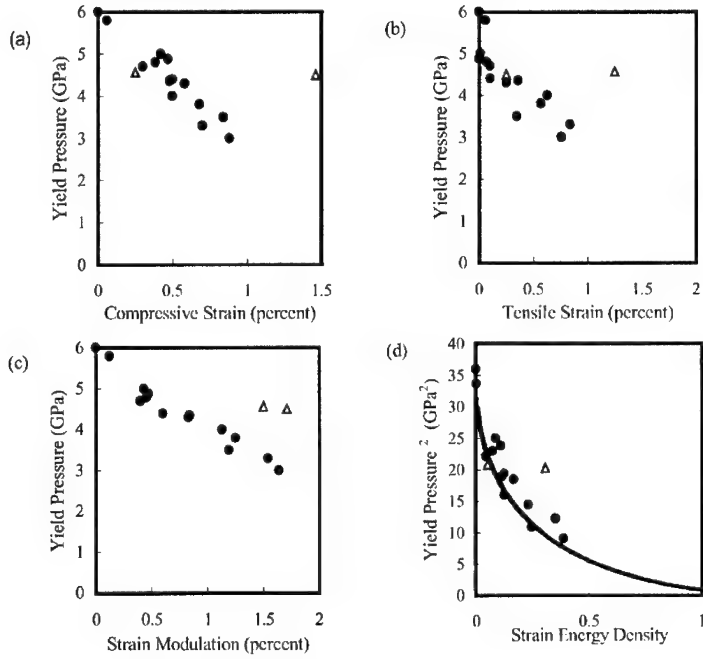
Figure 3. Yield pressure plotted as a function of various multilayer design parameters. Open symbols denote the asymmetric samples (Figure 1c). Data for the 10μm radius indenter.

THEORY

There are three strains in this system which may contribute to the initiation of plastic flow. These are the non-uniform applied strain from the indenter, ε_{ind}, and the uniform biaxial internal coherency strains, ε_c and ε_t, in the compressive and tensile layers respectively. It might be natural to suppose that one of these strains (most likely the tensile strain) adds to the indenter strain to promote plastic yield, which would then start in the tensile layers. The compressively strained layers would be irrelevant to the yield point. It would then be appropriate to apply a conventional yield criterion such as that of von Mises, a function of the stress tensor at a point. However, the plots against compressive and tensile strain, Figs. 3(a) and 3(b), are conclusive evidence that this is not so, and the plots against energy E, Fig. 3(d) and against F, Fig. 4, show that all three strains are relevant. Our central conclusion is that it follows that a pointwise-valid yield criterion is not applicable.
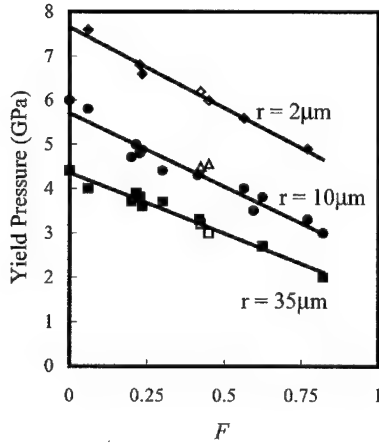
Figure 4. Yield pressure as a function of F (as defined by equation 1) for all the types of structure shown in Figure 1. Open symbols denote the asymmetric samples (Figure 1c).

Data for various radius spherical indenter tips, showing the size effect.

We now give an interpretation of F as an expression of the rate of change of the elastic energy as plastic deformation occurs. Equation 1 and Figure 4 emphasize that all three strain fields in the system, the indenter strain ε_{ind}, ε_c, and ε_t, all contribute to inducing plasticity. This is only plausible if all three strains are reduced by plastic relaxation, and this requires us to consider some finite volume V including both tensile and compressive layers. Assuming linear elasticity, the average elastic energy per unit volume within V is

$$E = \frac{1}{V}\int_V \frac{1}{2}\varepsilon_{ind}\sigma_{ind}\,dV + \frac{1}{2}\varepsilon_t\sigma_t\,\frac{h_t}{h_t+h_c} + \frac{1}{2}\varepsilon_c\sigma_c\,\frac{h_c}{h_t+h_c}$$

$$= \frac{1}{2}I\varepsilon_{ind}^2 + \frac{1}{2}M_t\varepsilon_t^2\,\frac{h_t}{h_t+h_c} + \frac{1}{2}M_c\varepsilon_c^2\,\frac{h_c}{h_t+h_c} \qquad [2]$$

where I and $M_t = M_c$ are appropriate elastic moduli. The compressive and tensile layers make independent contributions to the energy, which are weighted according to their thicknesses. Normally one might expect Eqn.2 to contain cross terms between the indenter strain field and the individual strains in the superlattice. However, the internal strains in the superlattice produce no tractions or normal forces at the surface. In this case, the energies of the indenter strain field and the superlattice strain field are simply additive. So, to a first approximation using linear elasticity, the work done by the indenter is the same regardless of the presence of internal strains. Thus, the cross terms are either zero or very small and can be neglected.

Without being specific as to mechanism, we may define R as a general measure of strain energy release via plastic flow. Elastic deformation is thermodynamically reversible, while plastic deformation is dissipative. The magnitude of plastic deformation within a specimen, R, may therefore be defined quantitatively as the work done irreversibly on the specimen, or the energy dissipated in it, per unit volume. Differentiating Eqn.2 with respect to R we get

$$\frac{dE}{dR} = I\varepsilon_{ind}\frac{\partial\varepsilon_{ind}}{\partial R} + \frac{M}{h_t+h_c}\left(\varepsilon_t h_t\frac{\partial\varepsilon_t}{\partial R} + \varepsilon_c h_c\frac{\partial\varepsilon_c}{\partial R}\right) \qquad [3]$$

The dimensionless quantities dE/dR are to be such that all elastic strains in the system decrease initially with R. Since ε_t and ε_c are of opposite signs, if they are both reduced by relaxation (at the same rate) then $\dfrac{\partial \varepsilon_t}{\partial R} = -\dfrac{\partial \varepsilon_c}{\partial R}$ and arbitrarily setting them to $\pm k \dfrac{\partial \varepsilon_{ind}}{\partial R}$ gives

$$\frac{dE}{dR}\left(\frac{\partial \varepsilon_{ind}}{\partial R}\right)^{-1} = I\varepsilon_{ind} + kM\left(\frac{\varepsilon_t h_t - \varepsilon_c h_c}{h_t + h_c}\right) = I\varepsilon_{ind} + kMF \qquad [4]$$

The terms in Eqn.4 have the dimensions of stress, and so we may write

$$\sigma_Y^0 = \sigma_Y + kMF \qquad [5]$$

to express the observed yield pressure σ_Y in terms of the critical value σ_Y^0 observed at $F=0$ and the linear dependence on F seen in Fig.4.

CONCLUSIONS

A finite volume over which the yield criterion is met is necessitated by our evidence that both compressive and tensile layers influence the yield point. With large indenters, the indenter stress field will be essentially constant across this volume. For sufficiently small indenters, the indenter stress field will vary significantly across this volume. The peak value must then be higher to reach the yield criterion over the whole volume. This is sufficient to account for the size effect seen in Fig.4. In a companion paper [6] we show that in our materials the critical volume is expected to be of the order of $1 \mu m$ across.

The above results are expected to be valid for other systems with highly inhomogenous strain fields, and hence to be applicable to modelling of point contact, and to the design and understanding of structural materials which have coherently-strained microstructure.

ACKNOWLEDGEMENTS

REFERENCES

1. G.Cook, *Engineering*, **132**, 343 (1931).
2. A.Kelly, and N.H.Macmillan, *Strong Solids* (Clarendon Press, Oxford, 1986) 3rd edition, p. 116 and Sect. 4.3.4 – 4.3.5.
3. N.B.Jayaweera, A.J.Bushby, P.Kidd, A.Kelly and D.J.Dunstan, *Phil. Mag. Lett.* **79**, 343 (1999).
4. M.E.Brenchley, M.Hopkinson, A.Kelly, P.Kidd, and D.J.Dunstan, *Phys. Rev. Lett.* **78**, 3912 (1997).
5. J.S.Field, and M.V.Swain, *J. Mater. Res.*, **8**, 297 (1993); *ibid.* **10**, 101 (1995).
6. A.J.Bushby, J.R.Downes, N.B.Jayaweera, P.Kidd, A.Kelly and D.J.Dunstan , in, , *Mat. Res. Soc. Symp. Proc*, 'Fundamentals of nanoindentation and nanotribology II' (2001)

Mechanical Properties and Deformation Behavior IV— Softening at Very Small Grain Sizes

The Inverse Hall-Petch Effect—Fact or Artifact?

Carl C. Koch and J. Narayan
Department of Materials Science and Engineering
North Carolina State University
Campus Box 7907
Raleigh, NC 27695-7907

ABSTRACT

This paper critically reviews the data in the literature which gives softening—the inverse Hall-Petch effect—at the finest nanoscale grain sizes. The difficulties with obtaining artifact-free samples of nanocrystalline materials will be discussed along with the problems of measurement of the average grain size distribution. Computer simulations which predict the inverse Hall-Petch effect are also noted as well as the models which have been proposed for the effect. It is concluded that while only a few of the experiments which have reported the inverse Hall-Petch effect are free from obvious or possible artifacts, these few along with the predictions of computer simulations suggest it is real. However, it seems that it should only be observed for grain sizes less than about 10 nm.

1. INTRODUCTION

Nanocrystalline materials have attracted increasing attention in the research community since they were recognized as an identifiable activity in materials science as stimulated by the work of Gleiter and his collaborators in the 1980s [1]. Among the various properties studied, nanocrystalline materials have exhibited promising mechanical behavior. In elemental metals in particular, extremely high values for room temperature hardness and strength have been observed when the grain size is reduced to the nanoscale (10-20 nm diameter) [2].

Because of the difficulties in preparing artifact free nanocrystalline materials of sufficient size, in fact the most measured mechanical property of nanocrystalline materials as a function of grain size is hardness. However, while significant increases in hardness and, where measured, strength, have been documented in a number of nanocrystalline materials there is no general agreement on the mechanism(s) for this hardening. For conventional grain size materials (1-100 μm diameter) the empirical Hall-Petch equation [3, 4] predicts that

$$\sigma_y = \sigma_o + kd^{-\frac{1}{2}}$$

where σ_y is the yield strength, σ_o is a friction stress below which dislocations will not move in a single crystal, k is a constant and d is the grain size. A similar expression is given for hardness. If such an empirical plot is extrapolated to the nanoscale grain size of about 10 nm, extremely high strengths and hardness are predicted. However, to date, experimental measurements of hardness and strength fall well below the Hall-Petch extrapolations. At the finest grain sizes a

variety of behavior is observed with typically a decrease in k, the slope of the Hall-Petch plot, or a leveling out to about zero slope, or in some cases, albeit still controversial, an actual negative slope. Differences from the classic Hall-Petch behavior at the nanoscale are not unexpected since the traditional explanations [5] for this behavior involve a large array of dislocations piled up at a grain boundary. The length of such a pile-up is of the order of magnitude of the grain diameter. At the nanoscale grain sizes, applied stresses required approach or exceed theoretical strength. At these small grain sizes the dislocation image forces are sufficient to eliminate dislocations by moving them into the grain boundaries. In addition, dislocation multiplication mechanisms such as the Frank-Read source would require stresses of the order of theoretical strength. It is predicted, therefore, that dislocations are absent in the smallest nanocrystals and deformation must involve other than conventional dislocation creation and motion. This is consistent with in situ TEM studies [6]. Ke et al. [6] studied nanocrystalline Au and Ag films by straining in an electron microscope. They observed dislocation-based plasticity for 100 nm grain size samples. However, in 10 nm grain size films, no dislocations were observed. Fracture was seen to occur along the grain boundaries, and the approximately 30% strain at the crack tip was believed to occur by grain boundary sliding. This was consistent with observations of relative grain rotation as measured by the angular changes among the lattice fringes of the individual grains.

All the experiments and theoretical predictions suggest conventional dislocation deformation mechanisms are not applicable to the finest nanocrystalline grain size materials. The role of dislocation activity, if any, grain boundary sliding, diffusion and other deformation processes have yet to be clearly identified. Therefore it is reasonable to expect different plastic deformation behavior at the nanoscale. The first report of an apparent inverse Hall-Petch effect was given by Chokshi et al. [7] on nc Cu and Pd prepared by the gas condensation method. A clear inverse Hall-Petch behavior was observed for both nc Cu and nc Pd for grain sizes less than 16 nm or 14 nm, respectively, as shown in Figure 1. The authors rationalized these results as due to the occurrence of diffusional creep at room temperature. It was suggested that an "equicohesive" grain size demarcates low temperature behavior (positive Hall-Petch) from high
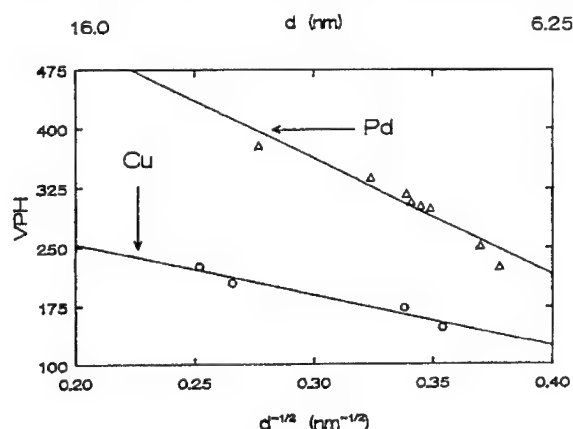

Figure 1. Hardness vs. grain size, $d^{-0.5}$ for nanocrystalline Cu and Pd. After Chokshi et al. (7).

temperature behavior (inverse Hall-Petch) analogous to the well-known equicohesive temperature at a given grain size. While other instances of an inverse Hall-Petch effect were subsequently observed by other investigators it was also noted that in most of these reports nc grain size was varied by annealing the smallest grain size samples to obtain grain growth and therefore a range of grain sizes. It is suggested [8] that thermally treating nanophase samples in the as-produced condition may result in such changes in structure as densification, stress relief, phase transformations, or grain boundary structure, all of which may lead to the observed inverse Hall-Petch behavior. Only a small number of reports of the inverse Hall-Petch effect have been for as-produced nanocrystalline samples with a range of grain sizes. Other problems with experimental verification of the inverse Hall-Petch effects include the accurate measurement of grain sizes and grain size distribution at the nanoscale.

The goal of this paper is to critically review the reports of the inverse Hall-Petch effect and the difficulties associated with obtaining artifact free data for hardness or strength vs. grain size at the nanoscale. The simulation studies which predict inverse Hall-Petch behavior will also be noted. Various models for deformation behavior of nanocrystalline materials will be reviewed with emphasis on their explanations for a possible inverse Hall-Petch effect.

2. EXPERIMENTAL DIFFICULTIES FOR HARDNESS AT THE NANOSCALE

Many studies of nanocrystalline materials have used a "two-step" process to obtain bulk samples. The inert gas-condensation method pioneered by Gleiter and co-workers [1] used the compaction of nanoscale particulates to obtain bulk samples. However, in the early nanocrystalline research the densities of the compacts often gave values ranging from as little as 70% to over 90% [1, 9] of the theoretical density. It has been concluded that the major cause of the lower densities is due to incomplete removal of porosity. Mechanical attrition is also a popular method for preparing nanocrystalline microstructures. In most cases, however, the product is a fine powder which must be compacted. Incomplete compaction can also lead to porosity and to poor powder-to-powder bonding. Since most compaction methods involve application of both pressure and temperature, a balance between densification/compaction and grain growth exists as the processing temperature is raised. That is, lower temperatures, which minimize grain growth also provide less likelihood of complete compaction. Therefore, porosity and incomplete particulate bonding are more likely at the lower processing temperatures which in turn results in the finest grain sizes. Thus the use of "two-step" processes which require compaction of particulates is susceptible to the possible artifacts of porosity and/or incomplete particulate bonding. These artifacts can lead to the apparent "softening" at the finest grain sizes.

"One-step" methods for processing nanocrystalline materials have the advantage of not needing a compaction step. These include selective pulsed laser deposition, controlled crystallization of amorphous phases, and electrodeposition. Some of these methods also have the possibility of artifacts, however. For example, crystallization of amorphous precursors can leave residual amorphous phase for the production of the finest grain sizes, thus providing a softer, difficult to detect phase which can lead to softening and an apparent inverse Hall-Petch effect. This effect has been clearly demonstrated by Alves et al. [10]. Another possible problem with crystallization of amorphous precursors is the crystalline product can be multiphase and composition and morphology can change on annealing. An example of this problem is noted for

crystallized Ni-P glass [11] wherein an inverse Hall-Petch effect is seen but nanocrystalline Ni and Ni_3P phases result from the crystallization anneal.

Another experimental problem with analysis of hardness/strength with grain size is accurate determination of the grain size and grain size distribution at the nanoscale. While most measurements of grain size and lattice strain in nanocrystalline materials have been carried out by analysis of XRD line broadening there are clearly problems with the results of such methods. In some cases significant differences in grain sizes have been calculated from the Scherrer equation in comparison to the Warren-Averbach method [12]. Similar discrepancies have been reported among the modified Williamson-Hall method, integral breadths, the modified Warren-Averbach, and unmodified Warren-Averbach [13]. Mitra et al. [13] also measured grain sizes of nanocrystalline Cu by TEM as well as XRD line broadening. Fitting both the XRD data and the TEM data by a log normal relationship allowed for a comparison. Distributions of both number and volume fractions of grain sizes were presented. The mode of the volume distribution was found to be much larger than that for the number distribution. The results for XRD and TEM matched closely for the finer mean grain sizes and narrow distributions. However, significant discrepancies were observed for samples with somewhat larger grain sizes and broader distributions. For example, a sample prepared by inert gas condensation, compacted at 180°C, deformed 20% by compression, and aged at room temperature for 6 months had values for the peak of the distribution (mode) of 41 nm (number fraction) by XRD compared to 74 nm by TEM. Similarly the mean values for XRD were 89 nm compared to 115 nm for TEM. The volume fraction mode by TEM was 205 nm.

Recent XRD and TEM studies of nanocrystalline Zn prepared by mechanical attrition also illustrate the need to use extensive TEM to provide accurate measurements of grain size and distribution [14]. At short milling times (≤3h) a bimodal distribution of grain sizes is observed by TEM for both number and volume fractions. The average grain size from XRD (Williamson-Hall method) is 24 nm. After 12 h of milling a monotonic distribution in both number fraction and volume fraction is observed. Here the mode is about 17 nm comparing closely with the 20 nm average from XRD. Grain size dispersity is a variable which must be considered carefully in descriptions of mechanical behavior since there is an apparent change from dislocation controlled deformation for the larger end of the distribution (50-100 nm) compared to the as yet ill-defined mechanism or mechanisms operative in the finer grain size regime (10-30 nm). Selective pulsed laser deposition can be used to produce porosity-free nc thin films up to 1.0 μm thick with fairly uniform grain size. In this technique, monolayers of insoluble elements are used to start the renucleation process, for example, W for nc copper and zinc films.

3. INVERSE HALL-PETCH OBSERVATIONS

In this section, the various reports of the inverse Hall-Petch effect as determined experimentally will be presented and discussed. These results are summarized in Table 1. In the case of the first examples of an inverse Hall-Petch effect by Chokshi et al. [7] on Cu and Pd it is now clear that porosity removal or other structural changes on the grain growth anneals were responsible for this observation. Hardness measurements on as-prepared nanocrystalline Cu and Pd [15] showed no inverse Hall-Petch effect in the same range of grain sizes.

Palumbo et al. [16] observed a negative Hall Petch effect in electrodeposited Ni-P. However, the authors suggest that there is a continuous transition from crystalline to the

Table I. Possible Inverse Hall-Petch Effect

Material	Preparation method	Grain Size varied by annealing	Counter example in same material	Possible artifacts	Reference
Cu	IGC	yes	yes	porosity	Chokshi et al. (1998) (7)
Pd	IGC	yes	yes	porosity	Chokshi et al. (1998) (7)
Ni-P	Electrodeposition	no		amorphous regions	Palumbo et al (1990) (16)
Ni-P	Crystallization of amorphous alloy	yes		changes in chemistry, morphology	Lu et al (1990) (11)
Ti-Al-Nb	Mechanical attrition	yes		changes in chemistry, porosity	Christman and Jain (1991) (11)
NbAl$_3$	Mechanical attrition	yes		chemistry, particle bonding	Kim and Okasaki (1992) (19)
TiAl	Sputtering, variation of IGC	yes		porosity	Chang et al. (1992) (19)
Fe$_{80}$Ni$_{20}$	Electrodeposition	no			Cheung et al. (1994) (20)
(Fe, Co)$_{23}$Zr$_{67}$	Crystallization of amorphous alloy	yes		amorphous regions	Alves et al. (1996) (10)
Fe	Mechanical attrition	yes	yes	porosity	Khan et al. (2000) (21)
Ni	Electrodeposition	no			Erb (1995) (25)
Zn	Laser ablation	no			Narayan (2000) (26)

amorphous phase as the grain size decreases with a smooth increase in the (triple line) disclination content. Therefore, the smallest grain size samples (<10 nm) are assumed to contain some amorphous phase which results in the observed softening.

Lu et al. [11] used crystallization of the amorphous Ni-P phase to nanocrystalline Ni_3P in a two-phase mixture where the composition as well as the morphology of the phases changes during annealing. Therefore, structural and chemical changes accompanied the grain growth such that the softening is unlikely to be due to the grain size decreases.

Christman and Jain [17] prepared a Ti-rich Ti-Al-Nb alloy by ball milling. The as-milled powders were multiphase bcc and orthogonal phases and x-ray line broadening gave a very small 3 nm grain size. Hot rolling of the canned powders at 900°C (for less than 1 minute) compacted the powders to near theoretical density. After compaction and heat treatment the grain size grew to about 20 nm and the hardness was 521 VHN compared to 498 VHN for the as-compacted, smaller grain size sample. Clearly, this preliminary data is not sufficient to judge the validity of an inverse Hall-Petch effect, but given the processing rate and possible structural/compositional changes it is unlikely.

Kim and Okazaki [18] prepared nanocrystalline $NbAl_3$ by mechanical alloying of Al and Nb powder followed by consolidation by electric discharge compaction. However, the grain size was varied by annealing which presumably also changed the structure/chemistry. It is also likely that incomplete compaction occurred at the finest grain sizes.

Chang et al. [19] prepared nanophase TiAl by magnetron sputtering in an inert gas atmosphere followed by in situ consolidation. This is a variation of the inert gas condensation method pioneered by Gleiter and co-workers. The initial compacted powders had grain sizes of 10-20 nm and were a mixture of amorphous and crystalline phases. Compaction at 250°C maintained the grain size and still had an unknown volume of amorphous phase and 12% porosity. Grain growth occurred on subsequent annealing. After sintering at temperatures above 450°C the porosity decreased to 4% along with grain growth. While this study has often been quoted by those modeling the inverse Hall-Petch effect the softening at small grain sizes can not be unambiguously attributed to grain size changes alone.

Alves et al. [10] used the crystallization of an amorphous $(Fe, Co)_{33}Zr_{67}$. This material crystallizes isomorphously so that a single phase crystalline phase results. An inverse Hall-Petch effect was noted with softening on decreasing grain size from about 140 nm to 5 nm grain size as shown in Figure 2. However, the authors point out that this apparent effect of decreasing grain size in hardness is clearly due to residual amorphous phase. The volume fraction of the softer amorphous phase decreases with annealing along with the grain growth and the softening with smaller grain sizes can be accounted for by a rule of mixtures of the amorphous and crystalline phases.

Khan et al. [20] prepared nanocrystalline Fe by mechanical attrition and compaction. An inverse Hall-Petch effect was observed. However, grain size was varied by annealing and porosity was present in the as-compacted powders. Furthermore, no inverse Hall-Petch effect has been observed in nanocrystalline Fe over some range of grain sizes by others [21, 22]. Erb and his colleagues (e.g. [24, 25]) have observed an inverse Hall-Petch effect in a number of studies of electrodeposited Ni. A deviation from positive linear Hall-Petch behavior is seen for grain sizes less than about 10 nm as shown in Figure 3. The variation in grain size in these cases was by changes in the electrodeposition variables; not by annealing for grain growth. Pure Ni can not be made amorphous by any known method at room temperature so partial amorphization is an unlikely possibility.
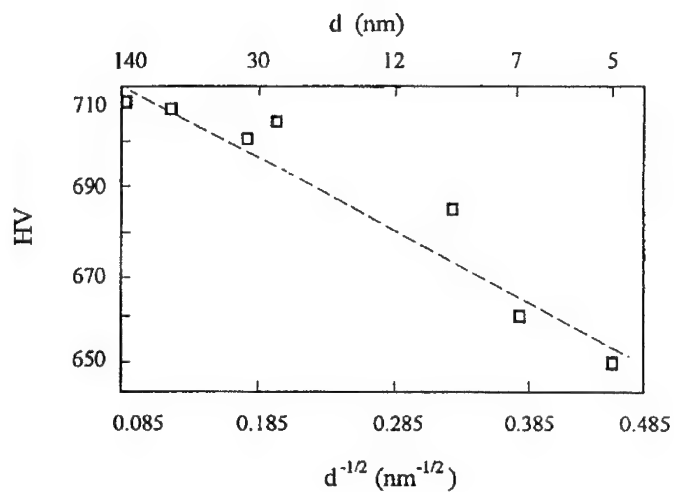
Figure 2. Hardness vs. grain size, $d^{-0.5}$ for nanocrystalline $(Fe, Co)_{33}Zr_{67}$ alloys. After Alves et al. (10).
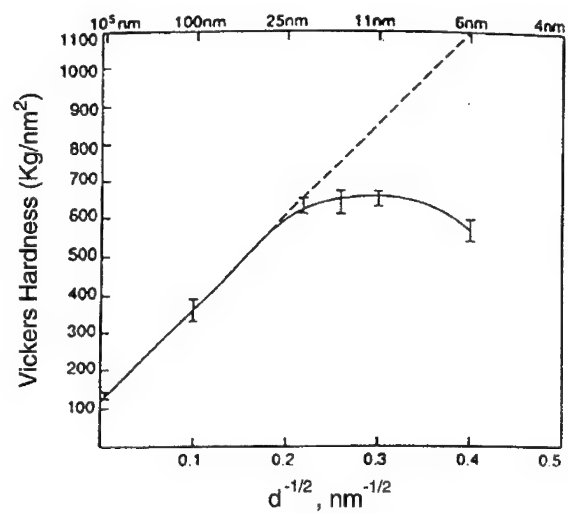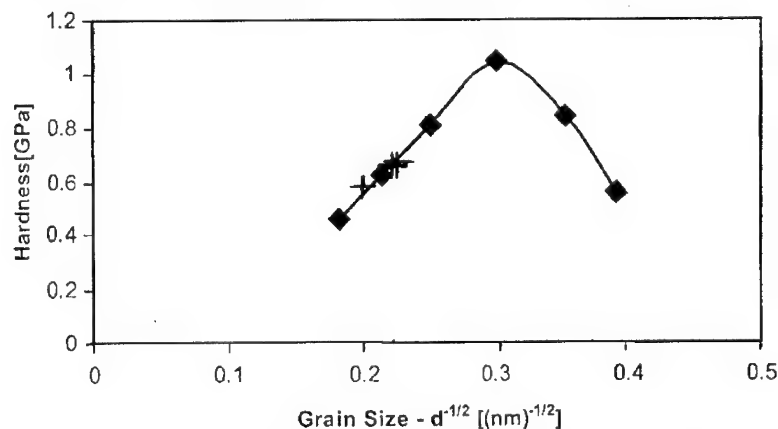

Figure 3. Hardness vs. grain size, $d^{-0.5}$ for electrodeposited Ni. After Erb (25).

Recently, Narayan and co-workers [26, 27] have prepared nanocrystalline Cu and Zn by the method of pulse laser ablation. They deposited layers of the metal with monolayers of W. The W apparently blocks grain growth of the deposited layers and allows for nucleation of new grains to provide a nanocrystalline grain structure. The total W percentage in the thin films (~0.5 μm) formed is $\leq$1 at. %. Hardness measurements were carried out on the nanocrystalline films using a nanoindentation method. Hardness vs. (grain size)$^{-1/2}$ is plotted in Figure 4 for the nanocrystalline Zn films along with values from bulk nanocrystalline Zn prepared by mechanical attrition and compaction. Conventional microhardness measurements were made on the bulk nanocrystalline Zn. An inverse Hall-Petch is observed for the nanocrystalline Zn for grain sizes less than about 9 nm. Except for the small quantities of W which acted as nucleation agent, no obvious artifacts are present to induce the inverse Hall-Petch effect. In fact, we expect W to enhance hardness by increasing resistance to grain boundary sliding.

4. COMPUTER SIMULATION RESULTS

While the experimental studies of hardness/deformation of nanocrystalline materials are complicated by material and analytical problems, considerable progress has been made in recent years by computer simulation of the deformation behavior of fcc metals such as Cu and Ni have been carried out by several investigators [28-30]. Schiøtz et al. observed most of the plastic deformation which occurred in simulations for nanocrystalline Cu was due to a large number of small "sliding" events of atomic planes at the grain boundaries with only a small fraction of the deformation being caused by dislocation motion within the grains. Softening is observed at the smallest grain sizes due to the larger number of atoms at grain boundaries. The results of this simulation for Cu with grain sizes from about 7 to 3 nm exhibit the inverse Hall-Petch effect. Van Swygenhoven and her colleagues (e.g. [29]) also carried out computer simulations which

Figure 4. Hardness vs. grain size, d$^{-0.5}$ for nanocrystalline Zn made by laser ablation or mechanical attrition. After Narayan et al (26).

indicate a change from intra-grain dislocation activity to deformation in the grain boundaries as the grain size is reduced. They reveal an intermediate grain size range in which deformation is due to a combination of intra-grain as well as inter-grain plasticity and therefore the transition between the conventional Hall-Petch behavior and grain boundary sliding.

5. MODELS FOR THE INVERSE HALL-PETCH EFFECT

As pointed out in the Introduction, the Hall-Petch effect is traditionally explained by a model for dislocation pileups at grain boundaries. At nanoscale grain sizes this model breaks down. Nieh and Wadsworth [31] calculated the minimum grain size that could support two dislocations (the smallest pileup) from the yield strength of some nanocrystalline materials. Below this size the strength was predicted to stay constant or decrease. A number of models for deformation of nanocrystalline materials have been developed which address the inverse Hall-Petch effect. Most of these models are based on a two component or multi-component approach. The two components are typically the grain boundaries and the crystalline grain interiors. Carsley et al. [32] carried out a rule-of-mixtures calculation wherein the hardness of the grain boundary region was assumed to be that for the amorphous state where the hardness (based on shear modulus) was taken as about one half the crystalline value. This model predicted a peak in hardness at about 4 nm in Ni, with softening for smaller grain sizes. Other models, e.g. [33], have included grain boundaries, grain edges, and grain corners as components which increase relative to the crystalline grain interior as grain size decreases. Masumura et al. [34] have proposed a two-component model that takes into account the dispersion in grain sizes that appears to be common in actual nanocrystalline materials. They assume that above a critical grain size conventional deformation by dislocation activity is controlling but below this grain size a Coble creep mechanism dominates. Models based on grain boundary sliding (e.g. [35, 36]) have also been proposed as the deformation mode at grain sizes below the critical size where normal dislocation activity ceases.

In a model which considered dislocation motion over the entire grain size range, Scattergood and Koch [37] assume a drop in dislocation line tension at the smallest grain sizes which gives rise to the negative Hall-Petch effect. They suggest that at large grain size dislocations get past obstacles by cutting of dislocation forests, while at small grain sizes the expression for dislocation line tension T,

$$T = \left(\frac{Gb^2}{4\pi} \right) \ln \frac{R}{r_o}$$

becomes sensitive to R, the long range stress screening distance. (Here G is the shear modulus, b is the Burgers vector and r_o is the dislocation core cutoff radius.) R is scaled with the grain size d. The stress needed for a dislocation to get past obstacles by Orowan looping becomes favored over the cutting stress at a critical grain size and is the dominant mechanism for smaller grain sizes leading to softening. While the model gave a good fit to data for the inverse Hall-Petch effect it assumed that dislocation motion is responsible for plastic flow both above and below the critical grain size in conflict with experimental [6] and theoretical [28, 29] observations. The data on the inverse Hall-Petch effect used for comparison with the above model [37] is also now suspect. This is generally the case where the authors of the various models have used

experimental hardness data to compare with the predictions of their models. In almost all cases the experimental data is questionable.

6. SUMMARY

There are many problems associated with measurement of hardness as a function of grain size for nanocrystalline materials. These include the preparation of artifact free samples. If the grain size is varied by annealing the finest grain samples for grain growth, it is possible that other structural and/or compositional effects may occur on annealing. Most of the experiments that report the inverse Hall-Petch effect have samples which exhibit clear artifacts or are at least questionable. However, there are reports where no obvious artifacts or other problems exist. We have identified at least three such apparently artifact-free examples of the inverse Hall-Petch effect. Computer simulations also predict softening at grain sizes below some critical value. Both the simulations show this critical grain size to be of the order of 10 nm or smaller. While it has been difficult to access the hardness of the smallest nanocrystalline samples unambiguously it appears that the inverse Hall-Petch effect is real. Models which describe the deformation of nanoscale materials should use only three few experimental sets of data that are clearly artifact free to test their predictions.

ACKNOWLEDGEMENTS

REFERENCES

1. H. Gleiter, "Nanocrystalline Materials," Progress in Materials Science, 33 (1989), 223-315.
2. J. R. Weertman, D . Farkas, K. Hemker, H. Kung, M. Mayo, R. Mitra, H. Van Swygenhoven, MRS Bulletin, 24 (1999), 44.
3. E. O. Hall, Proc. Roy. Soc. (London) 364 (1951) 474.
4. N. J. Petch, J. Iron Steel Inst. 174 (1953) 25.
5. A. H. Cottrell, Trans. TMS-AIME, 212 (1958) 192.
6. M. Ke, S. A. Hackney, W. W. Milligan, and E. C. Aifantis, NanoStructured Mater. 5 (1995) 689.
7. A. H. Chokshi, A. Rosen, J. Karch, and H. Gleiter, Scripta Metall. 23 (1989) 1679.
8. D. G. Morris, "Mechanical Behavior of Nanostructured Materials," Material Science Foundations, No. 2, ed. M. Magini and F. H. Wohlbier, (Uetikon-Zurich, Switzerland: Trans. Tech. Pubs., 1998) 43-44.
9. G. W. Nieman, J. R. Weertman, and R. W. Siegel, J. Mater. Res., 6 (1991), 1012.
10. H. Alves, M. Ferreira, U. Köster, and B. Müller, Mater. Sci. Forum 225-226 (1996) 769.
11. K. Lu, W. D. Wei, and J. T. Wang, Scripta Metall. Mater. 24 (1990) 2319.

12. G. W. Nieman and J. R. Weertman, <u>Morris E. Fine Symposium</u>, (Warrendale, PA: The Minerals, Metals & Materials Society, 1991), 243-250.

13. R. Mitra T. Ungar,. T. Morita, P. G. Sanders, J. R. Weertman, "Assessment of Grain Size Distribution in Nanocrystalline Copper and their Effect on Mechanical Behavior," Advanced Materials for the 21st Century: The 1999 Julia R. Weertman Symposium, ed. Y.-W. Chung et al., (Warrendale, PA: The Minerals, Metals & Materials Society, 1999), 553-564.

14. X. Zhang, H. Wang, J. Narayan, and C. Koch, "Evidence for Formation Mechanism of Nanoscale Microstructures in Cryomilled Zn Powder," (Submitted for publication, 2000).

15. G. W. Nieman, J. R. Weertman, and R. W. Siegel, Scripta Met. Mater., 23 (1989), 2013.

16. G. Palumbo, U. Erb, and K. T. Aust, Scripta Met. Mater. 24 (1990) 2347.

17. T. Christman and M. Jain, Scripta Met. Mater., 25 (1991) 767.

18. D. K. Kim and K. Okazaki, Mater. Sci. Forum, 88-90 (1992) 553.

19. H. Cheung, C. J. Altstetter, and R. S. Averback, J. Mater. Res. 7 (1992) 2962.

20. C. Cheung, G. Palumbo, and U. Erb, Scripta Met. Mater. 31 (1994) 735.

21. A. S. Khan, H. Zhang, L. Takacs, Inter. J. Plasticity, 16 (2000) 1459.

22. J. S. C. Jang and C. C. Koch, Scripta Metall. Mater. 24 (1990) 1599.

23. T. R. Mallow and C. C. Koch, Metall. and Mater. Trans. A 29 (1998) 2285.

24. A. M. El-Sherik, U. Erb, G. Palumbo, and K. T. Aust, Scripta Met. Mat. 27 (1992) 1185.

25. U. Erb, NanoStructured Mater. 6 (1995) 533.

26. J. Narayan, C. C. Koch, X. Zhang, and R. Venkatesan, unpublished results, 2000.

27. J. Narayan, J. Nanoparticle Research 2(1) (2000) 91.

28. J. Schiøtz, F. D. DiTolla, and K. W. Jacobsen, Nature 391 (1998) 561.

29. H. Van Swygenhoven, A. Caro, M. Spaczer, "Atomistic view of plasticity in nanophase materials," Advanced Materials for the 21st Century: The 1999 Julia R. Weertman Symposium, ed. Y.-W. Chung et al., (Warrendale, PA: The Minerals, Metals & Materials Society, 1999), 399.

30. S. Yip, Nature 391 (1998) 532.

31. T. G. Nieh and J. Wadsworth, Scripta Met. Mat. 25 (1991) 955.

32. J. E. Carsley, J. Ning, W. W. Milligan, S. A. Hackney and E. C. Aifantis, NanoStructured Mater. 5 (1995) 441.

33. N. Wang, Z. Wang, K. T. Aust, and U. Erb, Acta Met. Mat. 43 (1995) 519.

34. R. A. Masumura, P. M. Hazzledine, and C. S. Pande, Acta Mat. 46 (1998) 4527.

35. H. Hahn and K. A. Padmanabhan, Phil. Mag. B 76 (1997) 559.

36. H. Conrad and J. Narayan, Scripta Mater. 42 (2000) 1025.

37. R. O. Scattergood and C. C. Koch, Scripta Met. Mat. 27 (1992) 1195.

Atomistic Studies of Plasticity in Nanophase Metals

H. Van Swygenhoven [1], P. Derlet [1], A. Caro [2], D. Farkas[3], M. Caturla[4], and T. Díaz de la Rubia[4]

(1) Paul Scherrer Institute, CH-5232 Villigen-PSI, Switzerland
(2) Centro Atmico Bariloche, 8400 Bariloche, Argentina
(3) Dept. of MS & E, Virginia Polytechnic Inst. & State Univ. Blacksburg, VA
(4) Lawrence Livermore National Laboratory, Livermore, CA

Abstract

Molecular dynamics computer simulation of nanocrystalline Ni and Cu with mean grain sizes ranging from 5 to 20 nm show that grain boundaries in nanocrystalline metals have structures similar to most grain boundaries found in conventional polycrystalline materials. Moreover, the excess enthalpy density in grain boundaries and triple junctions appears to be independent of grain in both, computer generated and experimental measured samples. Simulations of deformation under constant uniaxial stress demonstrate a change in deformation mechanism as function of grain size: at the smallest grain sizes all deformation is accommodated in the grain boundaries, at higher grain sizes, intragrain deformation is observed

Introduction

The reduction of the grain size down to the nm regime opened new avenues for research in several aspects of materials science, including mechanical properties. At the lower end of the grain size range obtainable nowadays, half of the atoms belong to, or are affected by, the interfaces. Grain boundaries are believed to play a predominant role in plastic deformation of such materials, although the details of how precisely deformation occurs are still uncertain.

The relation between yield stress and grain size has been the subject of intensive research in recent years due to the complex behavior observed in nanophase materials. Most of the results confirm the validity of the classical Hall-Petch (H-P) relation down to grain sizes of the order of a few tens of nanometers, eventually with a different slope in the sub-micron range but keeping the classical exponent $d^{-1/2}$. Overviews of experimental data are given in [1-3]. At smaller grain sizes (below 20 nm) the results are controversial: whereas some results indicate a yield stress independent of grain size, or even a reverse H-P relation, others confirm an increasing yield stress with decreasing grain size [4,5]. At these small grain sizes the difficulty in the sample preparation plays an increasing role. It has recently been shown that controversial results can in some cases be ascribed to sample imperfections that have particular influence depending on the measurement technique [6]. Samples obtained from compaction of nano-powder particularly suffer from grain boundary (GB) imperfections. For instance, a reverse HP relation is obtained in Cu nanophase synthesised by inert gas condensation, when yield stress is obtained from tensile experiments, whereas an increase in yield stress is obtained from hardness measurements and compressive stress-strain curves. Another uncertainty in the results on yield values is the measurement of the grain size and the influence of its distribution. Nanophase samples often

contain heavily twinned regions [7]. Determination of the mean grain size by TEM or XRD using the Warren-Averbach [8] method results in a much smaller grain size if the structure is represented by the size of the twinned regions [4,6].

Molecular Dynamics (MD) computer simulations provide an atomistic view of the grain boundary structure and the deformation process through the embedded atom type models for the atomic interactions. It is simple enough to deal with several million atoms allowing computer-generated samples to be in a one-to-one scale with real nano-grains.

In this paper we give an overview of our molecular dynamics computer simulations of nanocrystalline Ni and Cu, two model fcc materials, with high and low values for the stacking fault energy respectively [9-14]. Samples are constructed with mainly high angle grain boundaries and mean grain size between 5 and 20 nm. We first focus on the study of the grain boundaries on the atomic level, providing their structural characterization in the nanocrystalline state. The boundaries studied provide examples of the most ordered and the most disordered found in our samples, representing different misorientations ranging from 9 to 75 degrees.

We then investigate the excess enthalpy of the computer generated samples, coming from grain boundaries and tri- or higher order- junctions. We show that the excess enthalpy per unit volume (excess enthalpy density) at the triple joints, TJ's, is essentially the same as that found in the grain boundaries GB. It implies that, energetically, TJ's and GB are a kind of matter with equivalent departures from the perfect crystal structure. By a proper account of the amount of GB's and TJ, we show that the reported observations on decreasing GB energy with decreasing grain size in nanocrystallized amorphous Se are a consequence of neglecting the relation between the grain boundary width d and the grain size Δ, which in the nanophase regime may be of the same order of magnitude.

Finally we deform the samples under constant uniaxial stress, and evaluate their strain rate as a function of grain size. We report the presence of a critical grain size below which all deformation is accommodated in the grain boundary. We provide a quantitative explanation of the results in terms of a non-linear viscosity originated by sliding at the interfaces. Above a critical grain size a departure from this regime is observed and dislocation activity appears. Partial dislocations are emitted from grain boundaries, travel across the grain, and are absorbed in opposite grain boundaries

Computational techniques

Cu and Ni nanocrystalline samples containing at least 15 grains, with mean grain size ranging from 5 to 20 nm, are created using a stochastic procedure and the Voronoi construction [15]. The location of the center of the grains and their crystallographic orientation are chosen randomly, resulting in samples with mainly high angle grain boundaries. The Voronoi procedure gives irregular Wigner-Seitz polyhedra, whose faces, the grain boundaries, result randomly oriented as well. The samples are then relaxed for 50-100 picoseconds at 300K using molecular dynamics, giving a metastable equilibrium state with final density between 96 and 97% of the perfect crystal value. Further relaxation at this temperature does not change the overall density and does not induce significant grain growth or rotation. The density is related to the grain boundary type and mean grain size and is quite insensitive to the relaxation procedure. Simulations done under hydrostatic pressure up to 10 GPa and 500K followed by relaxation still do not produce an increase in density [16].

To study grain size effects, a series of samples were constructed using the same set of random location of grain centers inside the simulation cell and orientations, but different cell sizes. Therefore the same microstructure appears in both series, differing only in their scale. This comparison allows us to study the same grain boundary for different grain sizes, isolating in this way the possible grain size effects on the measured properties.

As a description of the interatomic interaction we use the second moment (tight binding) potentials for Ni and Cu [17] in the Parrinello-Rahman [18] approach. In order to assess the dependence of our results on the interatomic potentials used, we have also tested samples relaxed using two other interatomic potentials. The first one is the EAM potential for Ni developed by Baskes [19]. The second one is a more recent interatomic potential for Ni developed on the basis of ab-initio calculations and also using the EAM framework [20]. The latter potentials accurately reproduce many experimental properties, including the stacking fault energy as well as ab-initio calculations of structural energies of metastable configurations. This latter feature helps insure that the potential will perform well in situations far from equilibrium. We choose Cu and Ni as model materials because with the potentials used they have very different stacking fault energies, enabling us to study the effect of stacking fault energy on the observed grain boundary structure.

We use periodic boundary conditions in all three directions and sample sizes between 10^5 and 6.10^6 atoms. Strain-time curves were recorded at 300 K and snapshot configurations were regularly stored for detailed analysis at several values of applied constant uniaxial stress between 1 and 2.6 GPa.

Since it is not possible to analyze all boundaries present is a sample, we started with a two-dimensional visualization of cross sections of the sample every 0.5 nm and chose a number of representative boundaries. The selected grain boundaries represent different misorientations between the grains, ranging from 9 to 75 degrees.

As an analysis tool, we investigate the coordination environment of each atom in the sample using the topological medium range order analysis developed by Honeycutt et al. [21], which is based in the classification of atom pairs. This technique is based on determining the configuration of the common neighbors of a selected atom pair, and associating each possible configuration with a four-digit number. This procedure provides a distinction between the fcc and hcp structures even taking into account only nearest neighbor pairs. Using this analysis we define categories of atoms and usually present them with different colors: atoms having local fcc order, atoms having local hcp order, atoms having other 12 coordinated combinations, and finally atoms having non-12 coordination. In this paper we present only black and white pictures, and there we choose light gray for fcc atoms, dark gray for other-12 and non-12 coordinated atoms and black for hcp atoms . For colored pictures we refer to our papers [9-14]. This tool proved to be very important in the visualization of the grain boundary structures and helps identify regions typical of a twin boundary as well as regions including stacking faults that may result from dislocation dissociation into Shockley partials.

Grain boundary structures

A detailed direct visualization technique at the atomic scale is used to study the grain boundary structural features. A significant degree of crystalline order is found for all boundaries studied. For boundaries with deviations within about 10 degrees from the perfect twin, a

repeated building structure was found consisting of structural units typical of the Σ−3 symmetrical tilt twin boundary, and highly disordered steps between them. Figure 1 shows such a grain boundary in the 12 nm Ni sample which appears as a sequence of structural building blocks, each one formed by a portion of a (111) twin boundary plane (black atoms), and a step between them, which is a disordered region (dark-gray atoms). This twin-and-step block is repeated several times forming a stair with the twins in parallel - but not consecutive - (111) planes. The view in Figure 1 is along a common axis, which is close to a <110> direction. The block is repeated 5 times in a direction close to the <112> direction. We note that the stair structure is a way to accommodate the approximately 12 degrees difference between the common (111) plane and the actual boundary plane, as well as the 4.5 degrees difference between the perfect twin misorientation and the actual misorientation for this boundary.

The corresponding grain boundary in the 5.2 nm sample shows a similar structural block as found in the 12 nm sample [9]. In this case however, there is no clear repetition of this unit due to the restriction imposed by the smaller grain size, even though the tendency to form a portion of a perfect twin is evident. Hence, the structural features of the boundary observed are basically independent of grain size in this range.

Figure 2 (left) shows another grain boundary in the Ni-12nm sample. The angular deviation between the [100] directions is about 50 degrees. The common axis for this grain boundary was also close to a <110> axis. The grain boundary is not amorphous. A significant degree of structural coherence across the grain boundary plane can be observed between the crystallographic planes. The misfit due to the different inter-planar distance for the different types of planes is accommodated by more disordered region every three planes [9].

For some of the boundaries studied, the atomic structure reveals clear evidence of dislocation networks, with some degree of decomposition of the dislocations into Shockley partials as is shown in Figure 2 (right). In this plot a section of a grain boundary in Ni 8.0 nm with
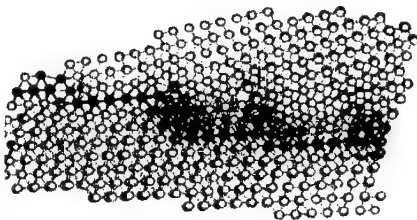
Figure 1 View of a grain boundary in a 12 nm sample with a misorientation between the grains of 75 degrees. The view is along a common axis, which is close to a <110> direction.

misorientation of about 17 deg around an axis close to <110> is shown. The boundary plane is close to a {112} type plane. Figure 2 (right) shows a section perpendicular to the common <110> direction. To accommodate the misfit between the grains, a periodic array of 1/2<110> dislocations is formed, with dislocation lines along <110>. These dislocation networks are the usual expected mechanism of misfit accommodation in low angle boundaries in large grain

polycrystals. For detailed analysis of grain boundaries with other types of misfit and colored pictures we refer to [9].
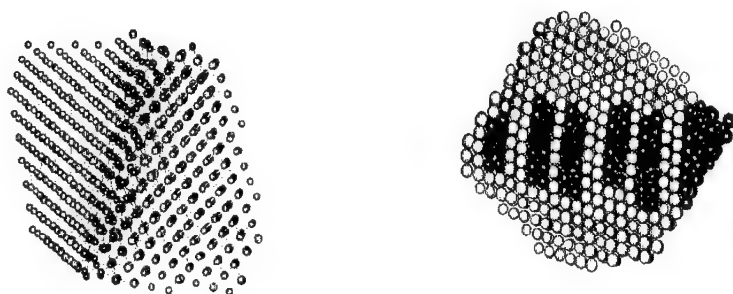
Figure 2 Left: View of a grain boundary in a 12 nm grain size sample with a misorientation between the grains of 75 degrees. Right: Section of a grain boundary in the Ni 8.0 nm grain size sample with misorientation of about 17 deg around an axis close to <110>.

The observation of structural units, similar to those observed in coarse grained samples provides evidence against the proposed model of these boundaries in terms of highly disordered, amorphous or cement-like interfaces in nano-phase bulk materials [22].

Grain boundary energy

We now analyze the interfaces using energetic considerations. NC materials have an excess enthalpy per unit volume, ΔH, defined as the difference between the enthalpy of the NC state minus the enthalpy of the perfect crystalline state at the same temperature and pressure. This difference is proportional to the energy stored in structural defects, like GB's, and triple joints, TJ's. To calculate the excess energy the same set of NC samples used in the previous section will be used here is. We focus our attention into their dependence on average grain size, and compare our results with a recent paper that claims a decrease on excess enthalpy as the grain size decreases [23].

Although real as well as computer generated NC samples are formed by grains of arbitrary shape, to evaluate the amount of GB area and TJ length when the only macroscopic parameter is the average grain size, it is convenient to assume a particular shape and distribution of sizes. It is customary to take an average of the actual distribution of shapes and sizes that translates into a geometric factor representing the average surface-to-volume ratio. This factor alters the quantitative results of defect energies, but not their dependence on relevant variables like grain

size. For simplicity in our analysis of the computer generated samples, instead of an average, we shall assume two extreme geometries, namely spherical (with minimum surface to volume ratio) and cubic (with large surface to volume ratio); the real case will very probably be in between these two cases. This simplification allows us to calculate the amount of defect surface or length with precision. We consider then a NC formed by perfect equal cubes, with grains repeating in all 3-dimensions. The grain size d is the sum of the size of the perfect crystal portion of the grain, d-Δ, plus the GB width Δ. We assume (and justify below) that as d changes, Δ remains constant.

The TJ is the intersection of 3-grain boundaries. For this particular example of cubic grains, all intersections are four-junction lines. A six-junction point may be identified in the intersection of 6 four-junction lines; for each particular geometry considered there are different types of intersections. In our analysis, we shall classify the defects in such a way that the volume associated to the six-junction points will be included in the four-junction lines, so they will not be considered as independent defects; moreover, we shall call them all TJ's. We note that there are several options to count the amount of defects: for the cubic shape example they can be GB alone, GB plus four-junctions, and GB plus four-junctions plus six-junctions. These options are not all equivalent: the results depend significantly on them as we show below

With these definitions, the grain density n_g, that is the number of grains per unit volume, is the reciprocal of the grain volume V_g. For a general shape, $V_g = g\, d^3$, with $g = 1$ for cubic and $g = 0.52$ for spherical shapes. Then for cubes, $n_g = 1/V_g = 1/d^3$. The GB surface per unit volume, s_{GB}, is the surface of a grain, S_g, times the number of grains per unit volume n_g, times ½ for double counting (each surface is shared by two grains). The surface of a grain is $g'(d-\Delta)^2$, with $g'= 6$ for cubic and $g' = 3.14$ for spherical shapes; then $s_{GB} = ng\, S_{GB} = 6(d-\Delta)^2/2d^3$.

The TJ's length per unit volume (including six-point junctions for our simplified geometry), l_{TJ}, is the product of the amount of TJ per grain, times the number of grains per unit volume. The first quantity is proportional to the linear dimensions of the grain, $g''d$. In the case of cubic grains $g'' = 12$, and multiple counting (in cubic grains the TJ's are four-junctions, shared by four nearest neighbor grains) adds a factor 1/4, then $l_{TJ} = n_g g''d = 3/d^2$.

Note here that if we want to explicitly make the six-joints appear in the analysis as a separate term, $g''d$ should be replaced by $g''(d-\Delta)$ in the expression for l_{TJ}, and an additional expression for the amount of six-joints should be considered. With these definitions, the excess enthalpy per unit volume is, $\Delta H = \gamma_{GB}\, s_{GB} + \gamma_{TJ}\, l_{GB}$, where γ_{GB} and γ_{TJ} are the surface energy density of the GB and the length energy density of the TJ; replacing the surface and length densities by the expressions above, $\Delta H = 3\gamma_{GB}(d-\Delta)^2/d^3 + \gamma_{TJ}\, 3/d^2$

Neglecting terms in Δ^2/d (because $\Delta < d$), a plot of $1/3\,\Delta H\, d^2 \cong \gamma_{GB}\, d + (\gamma_{TJ} - 2\,\Delta\,\gamma_{GB})$ gives a straight line with slope γ_{GB}. To be able to determine the other two unknowns, γ_{TJ} and Δ, let's also assume that the state of matter in the GB and in the TJ is the same. This state may be characterized by an excess enthalpy per unit volume h. Then, the enthalpy per unit surface of GB is the enthalpy per unit volume of the defect matter, h, times the GB width Δ. Similarly for the four-joints, its enthalpy per unit length is $h\,\Delta^2$, therefore $\gamma_{GB} = h\,\Delta$ and $\gamma_{TJ} = h\,\Delta^2$; then now, $\Delta H = 3h\Delta/d^2(d-\Delta)$; here again we neglect terms higher than linear in Δ/d. Now multiplying ΔH times d^2 we get a linear dependence on d with slope $3h\Delta$ and intersection $-3h\Delta^2$ (note the negative sign). It allows us to determine both unknowns h and Δ.

We apply this expression to our computer simulation results on Ni samples at different grain sizes, reported in [9-11]. The left ordinate axis of Figure 3 shows $\Delta H \, d^2$ vs d, together with a linear fit with: $3h\Delta = 38.0$ (± 0.1) eV/nm^2 and $3h\Delta^2 = 26.4$ (± 9) eV/nm. From these values, we determine $\Delta = 0.7$ nm and $h = 18$ eV/nm$^3 = 0.21$ eV/at, $\gamma_{GB} = h\,\Delta = 12.6$ eV/nm$^2 = 2.0$ J/m^2, and $\gamma_{TJ} = h\Delta^2 = 8.8$ eV/nm $= 14.1 \; 10^{-10}$ J/m.
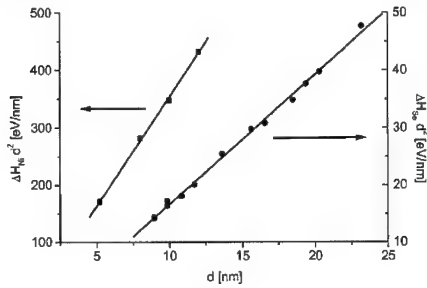
Figure 3: The function ΔH times d^2 versus d. Left axis: our data for Ni ; right axis: Lu's data from Ref. [23]. Linear fits according to Eq. detailed in text.

The value of Δ is compatible with the observed width of the GB determined in the simulations, and h is close to the latent heat of melting of this potential (0.18 eV/at), which is a measure of the energy necessary to loose the crystalline order.
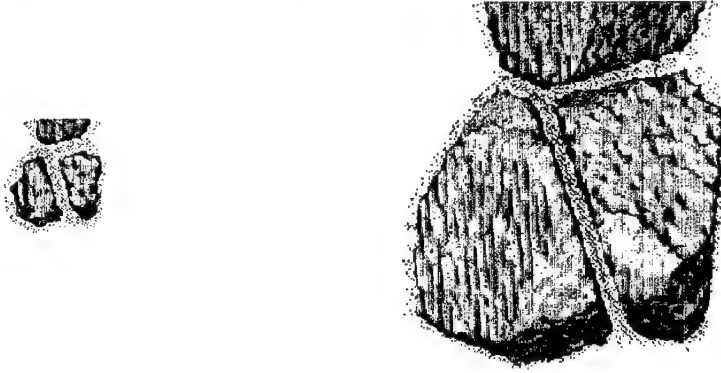
Figure 4: Grain boundaries and triple joints between three grains in computer generated 5.2 nm (left) and 12 nm (right) Ni NC samples. The surface of the grains has been taken as the frontier between perfect and non-perfect fcc-coordinated atoms. Small dots represent atoms with potential energy greater than the perfect crystal value plus 1.5 times the latent heat of melting, as a way to visualize the excess energy stored in defects. The scale of both figures is the same.

The quality of the linear fit provides support to the defect accounting assumptions made, and determines unambiguously the GB energy.

The assumption that the nature of the defect matter in the GB and the TJ is similar gives us values for the TJ energy and GB width, this last being compatible with the observations in the computer generated samples, as shown below.

An additional test of these assumptions is the visual observation of the GB's and TJ's in the simulated samples. As we described previously, a series of samples were created starting from the same set of random grain locations and crystallographic orientations, but with different grain sizes, in such a way that the same set of boundaries appears in different samples, differing only in the length scale. In Figure 4 we show a partial view of two of these samples: three grains with the same orientation parameters in a 5.2 nm and a 12 nm Ni samples. As it becomes apparent, grains in both samples have equal shape but different size. As a way to visualize the perfect crystal component of the grain we plot a closed surface containing in its interior all atoms with fcc co-ordination up to fourth neighbors. In the schematic representation of cubic grains and used in the calculations, this region has a characteristic linear dimension d-Δ. This is an arbitrary but sound definition of the frontier between a grain and a grain boundary, useful for visualization purposes.

The perspective used in Figure 4 clearly shows that the GB's are planar, constant in width and that they intersect in a triple joint whose cross section dimension is comparable to the GB width. In addition to these surfaces, we also plot in Figure 4 those atoms with energy higher than 0.27 eV above the perfect crystal value. This value is 1.5 times the latent heat of melting and is an arbitrary value that gives an adequate density of atoms in the figures to represent the distribution of excess enthalpy. It appears evident that these atoms are evenly distributed in the GB and TJ volumes, with no distinction between flat surface (what we associate to GB planes) and dihedral vertex (what we associate to TJ). Also clear is the fact that for both grain sizes (12 and 5.2 nm), the width of the GB, that we call Δ, and the density of energetic atoms, that is related to h, are similar.

This average analysis suggests then that the nature of the GB in NC metals is quite independent of grain size. However it is only a small portion of the information that can be obtained from computer simulations. In fact, in a previous paper we show an exhaustive analysis of particular GB's showing their structure and energetics depending on the misorientation parameters. In real experiments, however, it is this kind of average which is obtained from DSC measurements, while direct observation requires more sophisticated techniques. These observations justify the assumptions made in the previous section.

In a recent paper Lu et al. determine the excess enthalpy of NC selenium [23] obtained by recrystalization from the amorphous phase. Using the simple relation $\Delta H = \gamma_{GB}S_{GB}$, and $S_{GB} = 3.34/d$, the authors determine γ_{GB} as, $\gamma_{GB} = \Delta H/S_{GB} = \Delta H d / 3.34$. If γ_{GB} is independent of d, a plot of ΔH times d versus d, should give a constant horizontal line at $y = \gamma_{GB}$. Instead they obtain a line that has a negative curvature and positive slope. They arrive at the conclusion that a significant decrease of the GB enthalpy as the grain size decreases indicates that the GB's nature depends on the grain size. In view of the calculations presented in the preceding sections, we can interpret the conclusions of Lu et al. as a consequence of a wrong account of GB area and energy balance in the NC phase. For a proper determination of Se parameters, we represent the Lu's data on the right ordinate axis in Figure 3, together with a fit to our expression for $\Delta H d^2$. We obtain for these amorphous-Se annealed samples, that the GB width is 2.5 nm, and the GB energy is

0.4 J/m^2 assuming their geometric factor, and 0.36 J/m^2 assuming cubic grains. The GB width is significantly larger than in the metallic sample but the difference may be in fact that Se samples are originally amorphous and grains grow by re-crystallization. This procedure does not guarantee that the crystalline nuclei fill up all the volume. It is interesting to note that in the linear representation their data points show much less dispersion than in the non-linear one (See Figure in Lu's paper). We believe that this provides support to the assumptions made in deriving our expression for $\Delta H\, d^2$, that is: the nature of the GB is independent of grain size.

Mechanism of plastic deformation

At high load, after a transient period following the application of the load, the strain increases almost linearly with time for all the grain sizes. Figure 5 shows the strain rate versus the inverse of the grain size for the Ni and Cu samples. The strain rates under these conditions are high compared with actual experimental values, but for these small sample sizes (10nm-25nm) any relative velocity is still four orders of magnitude smaller then the velocity of sound.

At the smallest grain sizes explored the strain rate for a given applied stress increases with decreasing grain size. This behavior indicates that the Hall-Petch slope is negative at these very fine grain sizes. An energy balance indicates that at these sizes the total amount of grain boundary remains constant during deformation. These observations suggest an important characteristic of plasticity in nanophase metals under the present conditions: there is no damage accumulation during deformation, similar to the case of superplasticity. Careful examination of the samples confirms the absence of intra-grain defects.
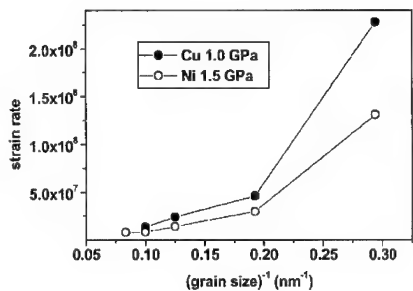
Figure 5: Strain rate versus the inverse of the grain size for the Ni and Cu samples

The deformation mechanism can be discussed in terms of a model based on GB viscosity controlled by a self-diffusion mechanism at the disordered interface, activated by thermal energy and stress [11]. With a set of simple assumptions based on these observations, we arrived at a picture of a standard stress-assisted activation process. In qualitative terms, it means that when a homogeneous shear stress is applied across the interface between two grains, the local

heterogeneous stress field makes each atom feel a different value of the net force (external plus internal) acting on them. At every instant of time, and depending both on the environment each of these atoms have and on thermal fluctuations, one atom at a time will get the conditions to reach and pass its saddle point configuration separating two possible locations, contributing in this way with a minute amount to the total plastic strain. The combination of all these localized, random processes, leads to a homogeneous slide of grains with respect to each other.

When similar load is applied on samples with larger average grain sizes, the deformation rate is much smaller. These observations indicate a transition to another deformation mechanism. We analyzed the atomic structure of Ni and Cu samples with larger grain sizes, deformed at those stress levels that give approximately the same strain rate as in the sample with the very small grain sizes, and compare the structures at similar values of plastic deformation. In this way we take into account the different elastic contribution in very fine-grained samples due to the reduction of the Young's modulus. Figure 6 shows a section of the Ni 12 nm sample, deformed to a total deformation level of 2.7%, which means a plastic deformation level of 1.4 %. using a tensile load of 2.6 GPa. The stacking fault observed in this section is produced by motion of Shockley partial dislocations generated and absorbed in opposite grain boundaries. The dislocation velocity estimated from sections made at different deformation times is 4 Å/psec, a tenth of the speed of sound.
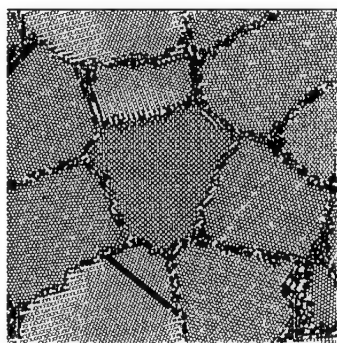
Figure 6 Slice of the 12 Ni sample, deformed until a plastic deformation level of 1.4%. The stacking fault is represented by the black atoms.

Evidences of stacking faults inside the grains in Ni are observed at a slightly higher grain size (11nm) compared to Cu (8nm), probably due to the higher stacking fault energy. In Cu all the observed slip belongs to the {111}<110> system. The first slip event we observe in Cu is in a (1, 1, -1) plane with slip direction is <1, -1, 0>. Its Schmid factor is only 0.12, which is the highest for this slip plane, but not the highest possible for that grain orientation. The same is observed in other grains reflecting the presence of significant internal stress. Increased dislocation activity is observed with increasing grain sizes. Figure 7 (left) shows a particular grain boundary in the 12 nm sample where a partial is emitted, travels trough the grain and is absorbed in the opposite grain boundary, leaving behind two hcp planes.

The glide plane is (1,1,-1). In this plot only atoms other then fcc are plotted. After further deformation, no second partial is observed. During deformation in the 20 nm sample, Figure 7 (right), two partials are emitted from the same grain boundary, both on parallel glide (1,1,-1) planes.
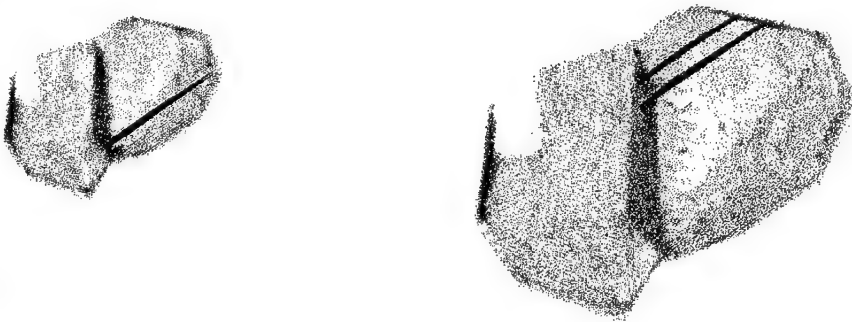

Figure 7: Partial dislocation emitted in a grain boundary in the 12 nm sample (left) and in the 20nm sample (right).

Concerning the microscopic view of sliding, it is well know that slide occurs preferentially in high energy interfaces due to the high local stress already acting on each atom that helps providing the enthalpy necessary for the activation process. Our samples contain a distribution of GB, including low energy-dislocation structured boundaries as well as high energy-less structured ones; we can therefore identify several cases: sliding plus dislocation glide, sliding plus GB migration, and pure GB migration.

GB migration is an accommodation process that may accompany GB sliding. This effect is always present in a deformation test and is particularly relevant in superplasticity, as GBS favors the formation of slide channels in the grain's mantles. In our simulations, GB migration is always present to some extent in all grains.

Conclusions

MD gives clear evidence that GB in nanocrystalline fcc metals have the short range structure of GB found in conventional polycrystalline materials. It also provides GB enthalpies; the total excess enthalpy approach used here allows a direct comparison with experimental measurements on nanocrystalline samples.

Our calculation suggests that since in the nanometer regime the GB width and grain size are of the same order of magnitude, a proper account of the amount of defects appearing in the enthalpy balance is essential to give the correct picture of the energetics involved. Moreover, our results show that the energy stored in the TJ's is the same kind of energy stored in the GB's and is related to the disorder that characterizes these regions.

With decreasing grain size a change in deformation mechanism is observed: at the smallest grain sizes all deformation is accommodated in the grain boundaries as the grains slide. A process based on mechanical and thermally activated single atomic jumps dominates the contribution to deformation. At larger grain sizes, a combination of sliding and intra-grain dislocation activity is observed.

Accurate analysis of the atomic configurations shows that the stacking faults are produced by the passage of partial dislocations generated and absorbed in opposite grain boundaries. In Cu we observe dislocation activity appearing at smaller grain sizes than in Ni (8 nm in Cu, 12 nm in Ni). Dislocation activity becomes increasingly more important as grain size increases. This trend has been observed in grain sizes up to 20nm.

References
1. R. Siegel. Materials Science Forum 235-238, 851 (1997).
2. R. A. Masumura, P. M. Hazzledine, and C. S. Pande. Acta Mater. 46, 4527 (1998)
3. V. Y. Gertsman, M. Hoffmann, H. Gleiter, and R. Birringer, Acta metall. mater. 42, 3539 (1994).
4. S.R. Agnew, B. R. Elliot, C. J. Young'sdahl, K. J. Hemker, and J. R. Weertman, in Modelling of Structure and Mechanics from Microscale to Product, edited by J. V. Carstensen, T. Leffers, T. Lorentzen, O. B Pedersen, B. F. Sorensen, and G. Winther (Risø National laboratory, Roskilde, Denmark, 1998, p. 1
5. M. El-Sheiric, U. Erb, G. Palumbo, K. T. Aust. Scripta Metall. Mater. 27, 1185 (1997)
6. J.R. Weertman, D. Farkas, K. Hemker, H. Kung, M. Mayo, R. Mitra, and H. Van Swygenhoven, MRS Bulletin, 24(2), January 1999
7. P. G. Sanders, M. Rittner, E. Kiedaisch, J. R. Weertman, H. Kung, and Y. C. Lu. Nanostr. Mater 9, 433 (1997).
8. E. Warren, X-ray diffraction, Edited by Dover, NY 1990.
9. H. Van Swygenhoven, D. Farkas, and A. Caro. Phys. Rev. B 62, 831 (2000).
10. Caro, H. Van Swygenhoven. To appear in Phys. Rev. B.
11. H. Van Swygenhoven, M. Spaczer, and A. Caro. Acta Mater. 47, 3117 (1999).
12. H. Van Swygenhoven, M. Spaczer, and A. Caro. Phys. Rev. B 58, 11246 (1998).
13. H. Van Swygenhoven, M. Spaczer, and A. Caro. Nanostr. Mater 10, 819 (1998).
14. H. Van Swygenhoven ,A. Caro. Appl. Phys. Lett. 71, 12 (1997).
15. G. Z. Voronoi. Reine Angew. Math. 134, 199 (1908).
16. H. Van Swygenhoven, M. Spaczer, and A. Caro. NanoStructured Mater. 12, 629 (1999).
17. F. Cleri and V. Rosato. Phys. Rev. B 48, 22 (1993).
18. M. Parrinello and A. Rahman. J. Appl. Phys. 52, 12 (1981).
19. M. I. Baskes, X. Sha, J. E. Angelo, and N. R. Moody. Modelling and Simul. In Mater. Sci. Eng, 5, 651 (1997).
20. Y. Mishin , D. Farkas, M.J. Mehl and D.A. Papaconstantopoulos . Phys. Rev. B 59, 5 (1999).
21. J. Honneycutt and H. C. Andersen. J. Phys. Chem. 91 4950 (1987).
22. P. Keblinski, D. Wolf, S.R. Phillpot, H. Gleiter, Scr. Mater. 41,631 (1999)
23. Lu and N. X. Sun. Phil. Mag. Lett. 75, 389 (1997).

Poster Session

NOVEL TUNGSTEN CARBIDE NANOCRYSTALLINE COMPOSITES BY PULSED LASER DEPOSITION

Ravi K. Venkatesan, A.Kvit, Q.Wei, J.Narayan
Department of Materials Science & Engineering,
North Carolina State University, Raleigh, NC 27695-7916, USA

ABSTRACT

We have developed a novel processing technique to fabricate *"artifact free"* tungsten carbide (WC) nanocomposites. In this method, pulsed laser deposition of WC in conjunction with a few monolayers of nickel aluminide (NiAl) is used to control the grain size of nanocrystalline composites. The grain size of WC was controlled by the thickness of tungsten carbide and the substrate temperature. The role of NiAl is to ensure the nucleation of tungsten carbide islands, and it is also insoluble in WC. Using this approach, we have fabricated nanocomposites of grain sizes ranging from 6 nm to 35 nm. The hardness of the composite increases with the decrease in grain size, following approximately Hall-Petch relationship. The role of NiAl in grain boundary deformation is of particular interest in strengthening the nanocrystalline composites. The potential of this technique to go to even lower grain sizes is discussed.

INTRODUCTION

Nanocrystalline materials having grain sizes between 1-50 nm exhibit interesting physical and mechanical properties, which are different than that of their bulk counterparts [1-3]. These properties include improved hardness, increased ductility & toughness and reduced elasticity modulus compared to their coarse grained counterparts. At grain size dimensions less than 10 nm, a large volume fraction of atoms are located at the grain boundaries; consequently, the interface provides a very large number of high diffusivity paths. A rough estimate shows that the volume fraction at the grain boundaries is given by 6 δ/D, where, D is the grain size(diameter) and δ ,the width of the grain boundary, thus with δ =1 nm, the volume fraction equals unity for D=6 nm. The yield strength and hardness of nanocrystalline materials increase with decrease in grain size, which is qualitatively described by the Hall-Petch relationship [3-4]. It is also observed that this relationship holds good up to a certain grain size, below which softening is observed with decreasing grain size, thus exhibiting a negative Hall-Petch effect[1-2,4].

In the present investigation, we have used a modified pulsed laser deposition technique to control three-dimensional nucleation or island growth by introducing a few monolayers of insoluble elements with high surface energy. Here, we have used a few monolayers of NiAl during the deposition of WC to control the island growth and grain size. Using this approach, we initially obtained a grain size of 35 nm and have reached a grain size of 6 nm. This grain size refers to the size of the WC grains alone and does not include NiAl, which is present at the WC grain boundaries. The potential is to reach a lower grain size by playing with the parameters. The hardness of the WC films on Si(001) substrates was also investigated using a nanoindentation technique.

EXPERIMENTAL DETAILS

The tungsten carbide nanocrystals with alternating layers of NiAl were grown on a Si(001) substrate using a modified Pulsed Laser Deposition technique. In this technique, the nucleation of islands/grains was controlled by the interfacial energy and the amount of materials that are deposited. A rotating target holder with four different slots is used which provides capability for depositing four different materials. Two of these four slots are occupied in this experiment by tungsten carbide and nickel aluminide. The insitu deposition chamber was evacuated to a base pressure of 2.0×10^{-7} torr and the depositions were carried out using a high power KrF laser ($\lambda=248$ nm, $\tau = 25$ ns, energy density 2-4 Jcm^{-2}, repetition rate 10 Hz). One of the unique features of this technique is that the average density of the laser-ablated species is considerably higher (10-1000 kT) than the equilibrium value kT. Therefore, this excess energy can be used in crystallization and formation of nanocrystalline islands on the substrate. Here, NiAl is introduced to enhance the nucleation sites of WC and the grain size of WC can be controlled by the relative amounts of WC and NiAl deposited in each layer. In the present experiments, the substrate temperature was maintained at room temperature.

The hardness measurements on these films were made using a nanoindentation technique, where Hardness is given by

$$H = \frac{P}{A} \qquad \text{----(1)}$$

where, P – Applied load. The contact area A is given by

$$A = 24.5h_c^2 + \sum_{i=0}^{7} C_i h_c^{1/2i} \qquad \text{----(2)}$$

where, C_i = experimentally determined constant. The contact displacement h_t. is given by

$$h_c = h_t - 0.75\frac{P}{S} \qquad \text{----(3)}$$

where, stiffness is measured as a function of h

$$\frac{dP}{dh}\bigg|_{P_{max}} = S \qquad \text{----(4)}$$

The tungsten carbide nanocrystals were characterized using High Resolution TEM. Plan view TEM of the WC film on Si(001) substrate gave a good estimate of the grain size and grain size distribution of nanocrystalline tungsten carbide. During the preparation of the sample for TEM, ion beam modulation technique was employed in the Ar+ ion-milling machine in addition to cooling the sample with liquid N2. This was used to prevent recrystallization of WC nanocrystals as grain growth in WC occurs at relatively low temperatures.

RESULTS AND DISCUSSION

We achieved a significant reduction in grain size by depositing the WC thin film on Si(001) substrate in the form of multilayers of WC and NiAl. The TEM studies of WC/NiAl samples reveal a significant reduction in grain size. The plan view study of multilayered WC/NiAl structure deposited on Si(001) substrate at 10 Hz reveals a grain size of 35 nm for WC/NiAl #1. The bright field TEM micrograph is shown in Figure 1. The grains are very

uniform and artifact-free. Further reduction in grain size was obtained by varying the relative thickness of the alternating WC and NiAl layers. The corresponding bright field TEM micrographs are shown in Figures 2-5. Grain Sizes of 24nm, 14nm, 10nm and 6nm were obtained. Tungsten Carbide nanocrystals with a grain size of 6 nm have been obtained by adjusting the deposition time of WC and the potential is to go to even lower grain sizes. High Resolution TEM studies were done on these WC nanocomposite samples and the corresponding micrographs are shown in Figures 7. Figure 7(a) & 7(b) shows that NiAl is present as an amorphous layer at the WC grain boundaries. The ratio of WC to NiAl remains constant as the grain size reduction occurs in all the TEM micrographs shown below This is also clearly seen in the diffraction patterns that were obtained. The nanohardness measurements as a function of depth were made on all the samples using the nanoindentation technique. The average hardness of coarse grain Tungsten Carbide was found to be 15.8 GPa, which agrees with the literature values. The hardness values increased with decreasing grain size attaining the highest value of 21.7 GPa for the 10 nm specimen. The hardness decreased to 17.69 GPa as the grain size was reduced to 6 nm. These results are summarized in Table 1.
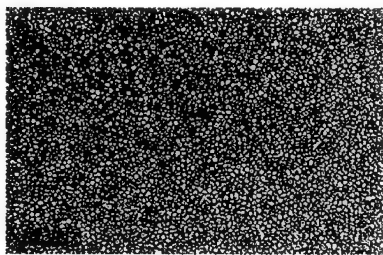
Figure 1 - HRTEM Micrograph of WC nanocomposites
with NiAl at the grain boundaries
Average grain size = 6 nm
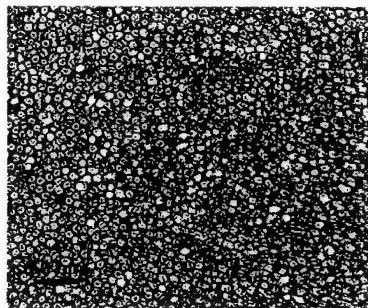
Figure 2 - HRTEM Micrograph of WC nanocomposites
with NiAl at the grain boundaries
Average grain size = 10 nm
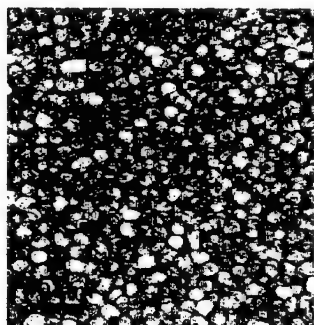
Figure 3 - HRTEM Micrograph of WC nanocomposites
with NiAl at the grain boundaries
Average grain size = 14 nm
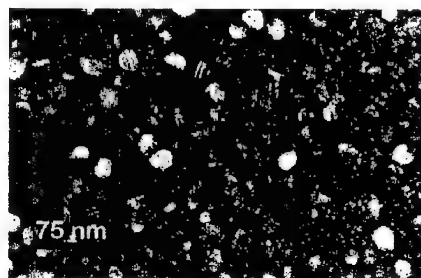
Figure 4 - HRTEM micrograph of WC nanocomposites
with NiAl at the grain boundaries
Average grain size = 24 nm
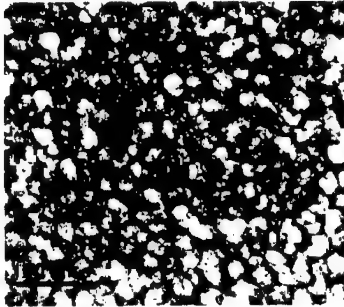
Figure 5 - HRTEM Micrograph of WC nanocomposites
with NiAl at the grain boundaries
Average grain size ~ 35 nm

Figure 6 - Hardness vs Grain Size($d^{-1/2}$)
- Tungsten Carbide Nanocrystals

Hardness[GPa]

Grain Size - $d^{-1/2}$ [$(nm)^{-1/2}$]

WC grains
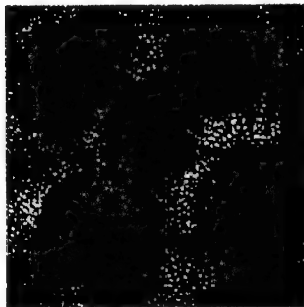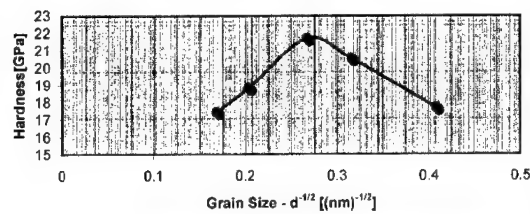
amorphous NiAl

Figure 7(a) - HRTEM Micrograph showing
WC grains and amorphous NiAl phase
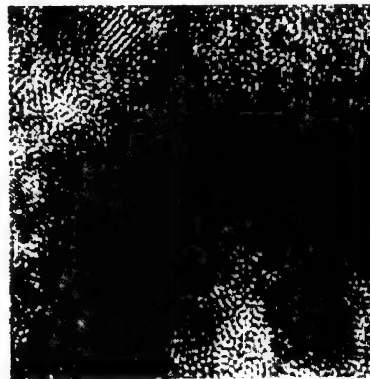
Figure 7(b) - HRTEM Micrograph showing
WC grains and amorphous NiAl

The grain size of WC was controlled by introducing a few interposing monolayers of NiAl, which is insoluble in WC and has a high surface energy with little or no interaction with the film [5]. According to the phase diagram, NiAl is insoluble in WC, and NiAl satisfies the above criteria for three-dimensional island growth. The grain size of WC nanocrystals grown using PLD depends on the number of nucleation sites available. Therefore a material, which provides more nucleation sites can reduce the grain size in the thin film nanostructures to significantly low values. The size of the island and hence the grain size of the nanocrystals is primarily controlled by amount of tungsten carbide and relative amounts of WC and NiAl in each layer of the multilayers formed.

We emphasize that it is possible to reduce the grain size of WC nanocrystals by introducing insoluble NiAl layers, which have little or no interaction with WC. The presence of

NiAl is seen in the TEM diffraction patterns as an amorphous layer. Thus, the amount of W was enough to affect nucleation and reduce the grain-size of WC to very low values. This present technique provides a self-assembling approach, where grain size is controlled by the amount of WC and the relative amounts of WC and NiAl in each layer of the multilayers that were obtained.

Table 1 : Details of Deposition Conditions for WC/NiAl multilayers – WC nanocrystals

Sample No.	Growth Conditions	Grain Size (nm)	Hardness(GPa)
WC/NiAl #1	E = 600 mJ WC = 8 min NiAl= 30 sec 10 Hz	30	17.44
WC/NiAl #2	E = 600 mJ WC = 6 min. NiAl – 20 sec 10 Hz	24	18.82
WC/NiAl #3	E = 600 mJ WC = 4 min. NiAl = 15 sec 10 Hz	14	21.67
WC/NiAl #3	E = 600 mJ WC = 2.5 min. NiAl = 10 sec 10 Hz	10	20.52
WC/NiAl #3	E = 600 mJ WC = 1.5 min. NiAl = 8 sec 10 Hz	6	17.69

The hardness increases with grain size, which is predicted by Hall-Petch relationship. Figure 6 shows a plot of Hardness as a function of grain size ($d\frac{1}{2}$), where we obtain a linear behavior with decreasing grain size up to a certain value. In this region intra-grain deformation mechanisms predominate. As the grain size decreases, intergrain deformation becomes increasingly important. Below a certain grain size, $d < d_c$, grain boundary sliding takes over, which leads to softening[6-7]. In this regime, the deformation is dominated by grain boundary sliding as a large fraction(majority) of atoms resides at the boundaries. NiAl being insoluble in WC and having high interfacial energy with WC increases the number of heterogeneous nucleation sites. The high surface energy between WC and NiAl reduces the number of atoms in a nucleus. This increases the number of nucleation sites of tungsten carbide. The NiAl pins down the WC grain boundary and prevents the grain growth. The NiAl at the grain boundary pins them and prevents their recrystallization. This reduces the grain size of WC. The interface between NiAl and WC hinders the dislocation movement and increases the sample hardness. Thus NiAl serves a two-fold purpose - first it may help reduce the grain size of the WC nanocrystals formed ; second, NiAl also prevents grain boundary sliding. Thus, this technique can be used to significantly improve the mechanical properties of thin film nanocomposites.

CONCLUSIONS

In the present study, we fabricated nanocrystalline WC without artifacts using pulsed laser deposition. The aims were to process, characterize and study the mechanical properties of nanocrystalline materials. By a series of experiments, we were able to obtain artifact free nanocrystalline WC with grain sizes of down to 6 nm using a novel pulsed laser deposition technique. Alternate layers of WC and NiAl was deposited on Si(001) substrates. The presence of NiAl reduces the grain size of WC. The NiAl present at the grain boundary also pins the grain boundaries preventing their movement during the deformation. The presence of NiAl at the interface also hinders the dislocation motion. These factors in conjunction improve the hardness values of the fabricated nanocrystalline WC from 15.8 GPa for coarse grain WC to 21.7 GPa for WC/NiAl multilayer nanocrystalline thin film heterostructures.

ACKNOWLEDGEMENTS

REFERENCES

1. J.Narayan, Y.Chen and R.M.Moon, Phys. Rev. Lett. **46,** 1491(1981)
2. J.Narayan and Y.Chen, Phil. Mag. **A49,** 475(1984); U.S. Patent #4,376,455(March 15,1983)
3. J.Narayan, Y.Chen and K.L.Tsang. Phil. Mag. **A55,** 807(1987)
4. Suryanarayana, C International Materials Review, **vol. 40 No.2,** (1995), 41
5. R.W.Siegel, Ann. Rev. Materials Science, **21,** 559(1991)
6. R.Armstrong, I.Codd, R.M.Douthwaite and N.J.Petch, Phil. Mag. **7,** 45(1962)
7. R.O.Scattergood and C.C.Koch, Script. Met. **27,** 1195(1992)
8. L.Vitos, A.V.Ruban, H.L.Shriver and J.Knollar, Surface Science **411,** 186(1998)
9. H.Conrad and J.Narayan, Scripta Mat(2000)
10. J.Narayan, J.Nanoparticle Research **10,** 1-6(2000)
11. Sanders-PG et al, Nanostructured-materials. **Vol. 8,** no. 3; May-June 1997; 243-52
12. G.W.Nieman, J.R.Weertman and R.W.Siegel, J.Materials Research, **6,** 1012(1995)
13. L.Riester, M.Ferber, J.R.Weertman & R.W.Siegel, Materials Science & Engineering. **A 204,** 1(1995)

New Ceramic Composite from a Multioxide Eutectic Melt

Jose M. Calderon-Moreno and Masahiro Yoshimura
Center of Materials Design, Tokyo Institute of Technology
Nagatsuta 4259, Midori-ku, 226-8503 Yokohama, Japan.

ABSTRACT

New high temperature ceramic eutectic composites have been obtained. The composite is self-assembled in one quick step by rapid supercooling of the multioxide alumina-YAG-zirconia eutectic in an arc-image lamp furnace. The new material will find applications as in-situ coating and component for use at ultra-high temperature. Periodic self-assembled layered structures kinetically forced to solidify with interspacing in the submicron range will result in very interesting properties and applications for high temperature multioxide oxide eutectic composites, offering the challenge of design of layered nanostructures tailored to specific applications by kinetic control during solidification.

INTRODUCTION

Oxides ceramics have intrinsic properties such as oxidation resistance, chemical and thermal stability. However, they also have poor resistance to thermal shock and in general to crack propagation and growth, which results in rapid material degradation and catastrophic fracture. One successful approach to improve the thermo-mechanical stability of ceramic oxide composites has been their fabrication by solidification from eutectic melts. Eutectic composites fabricated by unidirectional solidification have excellent strength and creep resistance at high temperature. The strengthening of grain boundaries characteristic of eutectics is especially required for long-term service in high temperature applications. The refining of the microstructure in eutectic composites with thinner lamella size will result in higher strength by reduction in flaw size, inhomogeneities and stress accumulation points.

However the fabrication of oxide eutectics by more rapid solidification techniques has yielded moderate success, producing partially amorphous or inhomogeneous samples, because it is difficult to maintain a homogeneous heat transfer at high cooling rates [1-6]. Therefore rapid solidification methods have been used to fabricate eutectic powders, but not layered eutectic crystals. The smaller lamella sizes in eutectic composites by unidirectional solidification are in the few microns range. The aim of this work is to obtain a eutectic composite with lamella size in the sub-micron range, by using rapid solidification in an arc-image furnace.

EXPERIMENTAL

Starting materials were prepared from high purity (>99.9%) ZrO_2, Y_2O_3 and Al_2O_3 powders by dry and wet mixing in methanol using an alumina mortar. A constant alumina to zirconia ratio of 79:21 and different yttria contents were used for the initial powders mixtures. Pellets of the mixed powders were placed on a copper plate cooled by water and melted in air in an arc-image lamp furnace by the radiation of a Xe lamp (Ushio UF-10001). The spherical arc-melted

specimen was quenched by rapidly moving the copper plate from the focal point. The cooling rate using the described method is estimated to be higher than $10^3\,Ks^{-1}$ [7]. Arc-melted materials were white spheres with diameters from a few mms to the focal size of the focal point (~ 15 mm). The white color indicates good stoichiometry of the oxides formed; oxygen vacancies would be revealed by their activity as color centers. Surfaces of melted samples were prepared by diamond polishing and Pt-Pd coated before observation by scanning electron microscopy (SEM).

Powder X-ray diffraction patterns were obtained from arc-melted samples after grinding in ethanol using an agate mortar, using CuK_α radiation in a curved graphite-beam monochromator (MXP^{3VA}, MAC Science Company, Ltd, Tokyo, Japan). Surfaces of melted samples were prepared by diamond polishing and Pt-Pd coated before observation by scanning electron microscopy (SEM) in the back scattering mode.
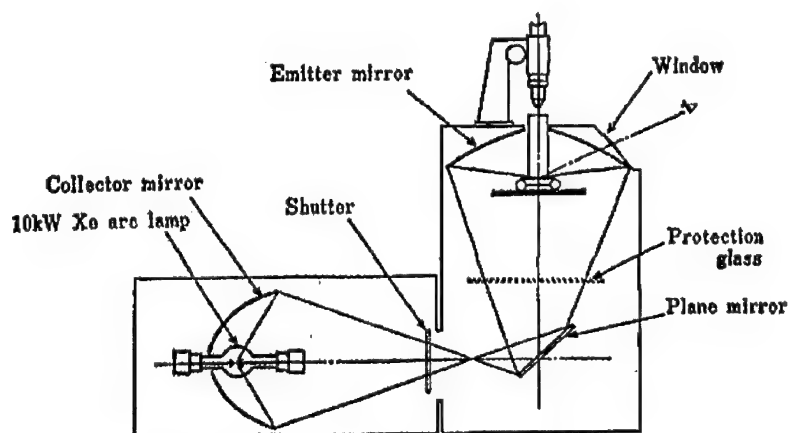
Figure 1. *Optical system of the arc-image lamp furnace. The sample is placed in the focus of the emitter mirror.*

RESULTS AND DISCUSSION

An as-solidified pellet can be observed in Fig. 2.The bulk as-solidified samples (ϕ ~ 1 cm) present good homogeneity and are free of surface flaws, cracks and porosity. As-solidified surfaces show waves associated with periodic lamella entanglement of aligned eutectic colonies.
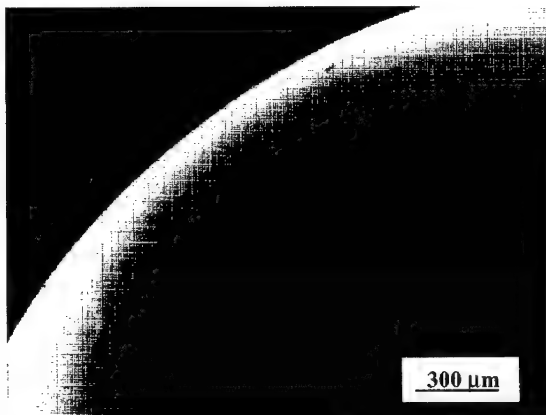
Figure 2. *Surface of a solidified pellet as-quenched. The surface is smooth and free of cracks.*

The XRD pattern in Fig. 3 corresponds to a ternary composite with three crystalline phases: alumina, YAG and cubic fluorite-type zirconia-yttria solid solution.
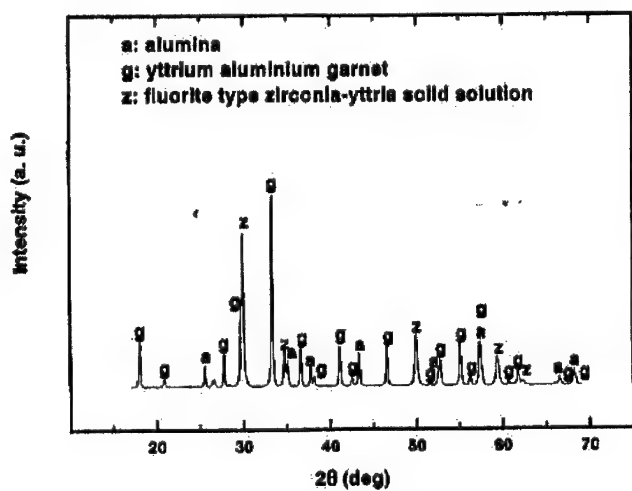
Figure 3. *XRD pattern from a solidified pellet as-quenched.*

The smooth surface corresponds to the as-solidified bulk ceramic composite, without any machining or polishing, with the interface shape theoretically predicted by Jackson & Hunt [8]. The curvature of the boundary offsets the effect of the compositional changes across the interface in the liquid in front of the lamella, caused by lateral diffusion of the components during phase separation.

Lamella sizes are homogeneous thorough the solidified sample. Theoretical predictions and experimental data of characteristic interlayer spacing in directionally solidified binary eutectic composites in the system indicate that this lamella size corresponds to cooling rates higher than $10^{4o}Cs^{-1}$. In spite of the rapidness of the process, the kinetics is homogeneous because the simplicity of the heat-transfer and the absence of thermal inertia by thermal image heating. We use the most simple heat transfer conditions. Heating in a solar furnace with an ellipsoidal mirror offers the advantages of very low thermal inertia, direct heating without using a container, uniform radial temperature distribution and good stability. Cooling by contact with a copper plate with high thermal conductivity allows rapid heat transfer in the sample through a positive thermal gradient. In those conditions homogenous and reproducible microstructures are obtained.

CONCLUSIONS

Ceramic composites have been obtained as bulk solid spheres by rapid solidification in an arc-image lamp furnace, in the alumina-YAG-zirconia system. The nanostructured material will find applications as ultra-high temperature thermal barrier coatings.

ACKNOWLEDGEMENTS

REFERENCES

[1] Vil'k YN, Il'in EA, Timofeev AY, Semenov SS, Niss VS, Alekseev YG, Kovalevskij VN. *Ogneupory*. 1992;5:11-12.

[2] Lakiza SN, Shevchenko AV, Zaitseva ZA, Knysh YA. *Soviet Powder Metallurgy & Metal Ceramics*. 1990;29:3-6.

[3] McKittrick J, Kalonji G. *Materials Science & Engineering A*. 1997;1-2: 90-97.

[4] McKittrick J, Kalonji G, Ando T. *Journal of Non-Crystalline Solids*. 1987;94:163-174.

[5] Claussen N, Lindemann G, Petzow G. *Ceramics International*. 1983;9:83-86.

[6] Glasser FP, Jing X. *British Ceramic Transactions & Journal* 1992;91:195-198.

[7] Ohtake K, Yashima M, Arashi M, Kakihana M, Yoshimura M. *Trans. Mat. Res. Soc. Jpn*. 1994;14A:717-720.

[8] Jackson, KA, Hunt JD, *Trans. Met. Soc. AIME*. 1966;236:1129

Calculating Surface Energies of Lead Magnesium Niobate Using Density Functional Theory

George Kavarnos[1] and Roger Richards
Submarine Sonar Department, Naval Undersea Warfare Center Division,
Newport, Rhode Island 02841
[1]EGG, Inc.,
Groton, Connecticut 06340

ABSTRACT

Computations involving density functional theory have been performed on lead magnesium niobate (PMN) single crystal models in an effort to calculate their surface energies, which are believed to play a role in brittle fracture mechanisms. To establish credibility of this approach, test calculations were performed on MgO and SiC single crystal models. The surface energy of MgO was determined to be 1.2 J/m^2, which is in close agreement with the experimental value. Similarly, the value for SiC, 8.03 J/m^2, supported a level of confidence with this methodology. Surface energies were calculated for several simple perovskites and several PMN models. The calculated values suggest that changes in the A-site ion of PMN do not result in any significant changes in the surface energies.

INTRODUCTION

Lead magnesium niobate (PMN) is well-known as a relaxor ceramic distinguished by its large strain and high energy density [1]. Addition of lead titanate, barium titanate, or strontium titanate to PMN leads to an improvement in relaxor properties [2]. However, these compositions are still relatively brittle materials, hindering attempts to collect reliable strain data. The brittleness of the ceramic has been attributed to processing conditions and impurities in the materials used in processing. In an attempt to understand the root origin of brittleness in PMN ceramics, we have used density functional theory to model the surface energies of model crystals. The objective of this work was to demonstrate that a quantum mechanical approach can be used to calculate the surface energy, which is an invaluable parameter for investigations of brittle fracture.

THEORY

The approach is based on Griffith's theory where crack formation is viewed as a thermodynamic balance between the reduction in mechanical energy on crack extension and the resulting increase in surface energy of the surface created by the extension of the crack [3]. Crack propagation is a thermodynamic process, i. e., during propagation, energy stored in the material is constantly released [4,5]. When a crack is initiated in a material such as a ceramic or crystal, the area generated by crack propagation is approximately proportional to the square of length of the crack, which implies that the relief of strain energy should be proportional to the square of the crack length or depth. At the same time, the energy expended to form the surfaces of the newly-formed crack

(surface energy) is proportional to only the first power of the crack depth. Thus, a critical Griffith crack length, l_g, is defined as the critical length of a crack beyond which more energy is released so that crack propagation is highly favorable. A simple formulation of the Griffith crack length is [4]:

$$lg = \frac{2GE}{\pi s^2} \qquad (1)$$

Where G is the free surface energy, E is the Young's modulus, and s is the strength of the material. Thus, the surface energy is one of the key parameters that controls crack propagation, i. e., the larger the surface energy, the greater the critical crack length, and thus the more stable the material is to crack propagation. To investigate the molecular mechanisms underscoring cracking in PMN crystals, we focused on the effect of composition on the surface energy. Density functional theory (DFT) was used to calculate G for simple models. Electronic energies of bulk crystals were first calculated. Superlattice surface structures were then constructed by separating the lattice planes. After the electronic energies of the "separated" lattice structures were calculated, the surface energies were estimated from the differences in the electronic energies and surface areas of the bulk and separated lattice structures. The model PMN crystals consisted of 3 x 3 x 1 PMN pseudocubic superlattices constructed with experimental lattice dimensions of 12.12 Å x 12.12 Å x 4.04 Å [6]. The stoichiometry of this perovskite cell is $Pb_9Mg_3Nb_6O_{27}$. Mg^{2+} and Nb^{5+} were distributed randomly on the B-sites (figure 1). Two (001) surfaces were created from this cell by greatly expanding the a-dimension. The plane of one (001) surface, the B-site surface, is coincident with the B-O lattice bond. The second surface, the A-site surface, contains the A-site ion (Pb^{2+}) and oxygen.. Bulk crystal and surface superlattices $Pb_6Ba_3Mg_3Nb_6O_{27}$ and $Pb_6Sr_3Mg_3Nb_6O_{27}$ with the same lattice dimensions were also built. In these structures, Ba^{2+} and Sr^{2+} replaced A-site Pb^{2+} within the lattice plane that forms the A-site surface.

A

B

Oxygen
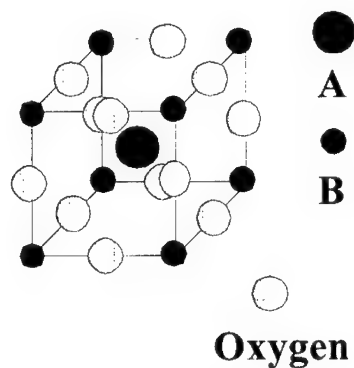
Figure 1. *Structure of a simple perovskite*

Density functional theory treats the dependence of the total ground-state energy E_{GS} of an electronic ensemble as a function of the density distribution of these electrons, $\rho(x)$, which represents the concentration of electrons at position x [7]. Consider that these interacting electrons are in a Coulombic field of fixed nuclei. Since E_{GS} is a *unique* functional of $\rho(x)$, we write the familiar Kohn-Sham equation describing the exact ground-state energy functional of a system of electrons in an external field as:

$$E_{GS} = T_S[\rho(x)] + E_{ES}[\rho(x)] + E_{XC}[\rho(x)] + E_{EXT}[\rho(x)] \qquad (2)$$

$T_S[\rho(x)]$ is the kinetic energy of non-interacting electrons with density $\rho(x)$, $E_{ES}[\rho(x)]$ is the electrostatic energy, $E_{XC}[\rho(x)]$ is the exchange-correlation energy, and $E_{EXT}[\rho(x)]$ is the potential energy of non-interacting electrons. The kinetic energy term is estimated using a one-particle equation:

$$T_S[\rho(x)] = \sum_n a_n \int dx \psi_n(x) \left\{ -\frac{\nabla^2}{2m} \right\} \psi_n(x) \qquad (3)$$

Where ψ_n is a single particle orbital that produces a charge density $\rho(x)$. The minimized ground-state energy of a crystal was calculated by solving the Schrödinger equation [7]:

$$\left\{ -\frac{\nabla^2}{2m} + V_{EFF}(x) - \varepsilon_n \right\} \psi_n(x) = 0 \qquad (4)$$

Where V_{EFF}, the effective potential of each electron, can be represented as:

$$V_{EFF}(x) = V_{EFF}(x) + e^2 \int dx' \frac{[\rho(x)]}{|x - x'|} + \mu_{XC}[\rho(x)] \qquad (5)$$

In equation 5, μ_{XC} is defined as a Coulomb potential:

$$\mu_{XC} \equiv \frac{d}{d\rho}[\rho \varepsilon_{XC}(\rho)] \qquad (6)$$

The local density approximation (LDA), where the density of exchange-correlation in a nonuniform system is assumed to vary with $\rho(x)$ regardless of the nature of the density distribution, was used to facilitate the calculations [8]. In practice, equation 2 is written as a function of a "starting" charge density. Equations 2 and 4 are then used to recalculate the "final" charge density. The calculation is performed until self-consistency is achieved [7].

The strategy used in this investigation was to first optimize the geometries and determine the total energies of the relaxed crystals. The only exception was in the case of the PMN models where experimental lattice dimensions were used (the computation would have been quite demanding). The energies of the "separated" crystals were calculated under the assumption that surface ion positions do not shift appreciably after cleavage when generating the surfaces.

The calculations were performed using the CASTEP (Cambridge Serial Total Energy Package) interface provided by Molecular Simulations (MSI) [9]. This program is installed on NUWC's Silicon Graphics ONYX 2 Platform in NUWC's Advanced Scientific and Engineering Computational Center. Periodic models were constructed using MSI's Cerius^2 package [9]. The pseudopotential approach was performed and k-point sampling over the Brillouin zone was calculated using the Monkhorst-Pack scheme to generate a uniform mesh of k-points in reciprocal space [10].

RESULTS AND CONCLUSIONS

The surface energies for several model crystals including MgO and SiC as test cases are listed in table I.

Table I. Surface energy (G) of model crystals calculated using density functional theory

Crystal	G (J/m^2)
MgO	1.02
SiC	8.03
PbTiO$_3$	1.24
BaTiO$_3$	1.12
SrTiO$_3$	1.33
PMN	1.23
PMN-Ba	1.31
PMN-Sr	1.41

The values found for MgO and SiC are in close agreement with literature values (1.2 and >3 J/m^2, respectively) [11,12]. The calculated value for SiC is consistent with the extreme hardness of this material [13]. The values calculated for simple perovskite structures, PbTiO$_3$, BaTiO$_3$, and SrTiO$_3$, were included to provided a basis of comparison with the PMN model crystals. It is evident that for both the simple perovskites and the PMN crystals, there are only slight and in fact no particularly noticeable trends depending on the nature of the A-site ion. This would appear to support a conclusion that replacements of A-site ions in simple and complex perovskites should not influence the propensity for brittle fracture. Given their slightly higher surface energies, the simple perovskites as well as the PMN models would appear to be slightly more stable to brittle fracture than an oxide such as MgO. This work suggests that the approach using density functional theory can be applied to studies of brittle fracture most notably in systems where surface energies are difficult to determine by experiment. To further strengthen the conclusions of this study, it will be desirable to perform relaxation of ionic positions on the surfaces to determine the magnitude of differences, if any, between unrelaxed and relaxed surfaces [14]. It is also recommended that studies be performed to determine the effects of model lattice size, volume, and surface separation on the calculated energies before this approach is applied to the study of cracking behavior in solutions of PMN and PbTiO$_3$, which possess excellent electromechanical properties yet are known to suffer from a strong propensity to cracking. Another area where this approach has promise is in studies of lattice trapping, which is believed to play a role in stabilizing cracks [15].

ACKNOWLEDGMENTS

REFERENCES

1. L. E. Cross, *Ferroelectrics*, **76**, 241 (1987).
2. S. M. Pilgrim, M. Massuda and A. E. Sutherland, *J. Ameri. Cer. Soc.*, **75**, 1970 (1992).
3. A. A. Griffith, *Philos. Trans. R. Soc. London, Ser. A*, **221**, 163 (1921).
4. P. Gumbsch and R. M. Cannon, *Mater. Sci. Bull.*, **25**, 15 (2000).
5. K. Hellan, *Introduction to Fracture Mechanics* (McGraw-Hill, 1984) pp.163-168.
6 . I. G. Ismailzade, *Soviet Phys.*, **5**, 292 (1960).
7. W. Kohn and L. J. Sham, *Phys. Rev.*, **140A**, 1133 (1965).
8. M. J. Gillan, *Cont. Phys.*, **38**, 115 (1997).
9. Molecular Simulations, Inc., San Diego, CA 92121-3752
10. M. C. Payne, *Phase Transitions*, **61**, 41 (1997).
11. P. Tasker, *Adv. Ceram.*, **10**, 176 (1984).
12. C. J. Gilbert, J. J. Cao, L. C. DeJonghe and R. O. Ritchie, *J. Am. Ceram. Soc.*, **80**, 2253 (1997).
13. F. A. Cotton and G. Wilkinson, *Advanced Inorganic Chemistry*, 4th edition (Wilcy, 1980), pp.362-3.
14. P. J. Lawrence and S. C. Parker, Computer Modelling of Oxide Surfaces and Interfaces, *Computer Modelling of Fluids, Polymers, and Solids*, 293, NATO ASI Series, ed. C. R. A. Catlow, S. C. Parker, and M. P. Allen (Kluwer, 1990), pp.219-48.
15. R. Thomson, C. Hsieh and V. Rana, *J. Appl. Phys.*, **42**, 3154 (1971).

Sol-gel synthesis and characterization of mesoporous organosilicas by using block copolymer templates

Eun-Bum Cho, Kwan-Wook Kwon and Kookheon Char
School of Chemical Engineering, Seoul National University,
Seoul 151-742, Korea.

ABSTRACT

Mesoporous organosilicas based on a bridged organosilicate have been synthesized using a triblock PEO-PLGA-PEO copolymer containing more hydrophobic poly(DL-lactic acid-co-glycolic acid) block and the structural difference between mesoporous organosilicas prepared from PEO-PLGA-PEO and PEO-PPO-PEO block templates is discussed.

INTRODUCTION

Surfactant-templated mesoporous silica materials have attracted great interest since the discovery of hexagonally ordered mesoporous silica material (M41S) by Mobil Corp [1]. Structures and pore sizes of the mesoporous silica materials have been varied by several surfactants and polymeric templates. Particularly, non-ionic poly(ethylene oxide) surfactants or triblock poly(ethylene oxide)-poly(propylene oxide)-poly(ethylene oxide) (PEO-PPO-PEO) copolymers as structure directing templates have been widely used for preparing mesoporous silicas such as SBA-15 [2-4], SBA-16 [4] and MSU-X [5,6]. The synthetic route of employing non-ionic block copolymers has advantages for forming thicker walls, nontoxicity, and easy removal of the polymer during calcination. The block copolymer templates obviously yield larger structural features compared with the structural size obtained with low molecular weight surfactants.

Recently, a new class of mesoporous materials has been reported such as the periodic mesoporous organosilicas (PMOs) [7-11]. These materials are so unique in containing organic functional groups inside the channel wall. The organic modification of the silica framework provides diverse variation of optical, electrical and mechanical properties. However, the organosilicas prepared by block copolymer templates have not yet been reported extensively in literature.

We have investigated a new synthetic method of incorporating organosilicates in the basis reaction between a PEO-PPO-PEO triblock copolymer and tetraethyl orthosilicates (TEOS). The synthesis using non-ionic block copolymer templates generally utilizes the electrostatic forces

mediated by strong acid to allow for the counter ion mediated interactions of the type $(N^0H^+)(X^-I^+)$, where N^0 is the non-ionic surfactant, X^- is the counter anionic and I^+ is the protonated silicic acid from the silicon alkoxide precursors. In present study, we describe the synthesis of mesoporous organosilicas from the co-condensation of TEOS and 1,2-bis(trimethoxysilyl)ethane (BTMSE) by using PEO containing triblock copolymer templates such as F127 ($EO_{106}PO_{70}EO_{106}$; BASF) and poly(ethylene oxide)-poly(DL-lactic acid-co-glycolic acid)-poly(ethylene oxide) (PEO-PLGA-PEO). In our study, more hydrophobic PLGA block, compared with the PPO block in the PEO-PPO-PEO block templates, was chosen in order to give more contrast between hydrophilicity and hydrophobocity of a block template yielding tighter micelles to confine more amount of organosilicate in the aqueous matrix phase.

EXPERIMENTAL DETAILS

We have studied the cubic morphologies using a commercial Pluronic F127 and a $EO_{43}(L_{23}G_6)EO_{43}$ (M_n= 7,550 gmol^{-1}; LGE76) triblock copolymer synthesized in our laboratory through the ring opening polymerization of a mixture of lactide and glycolide onto mono-methoxypoly(ethylene oxide) [13]. In a typical synthesis of mesoporous organosilicas, a mixture (3.75 g) of BTMSE and TEOS was added to a 1.5 M HCl aqueous solution (160 g) containing LGE76 (1 g; 0.6 wt%) maintained at 30 ℃. The mixture was stirred vigorously for about 0.5 h, then the solid products were aged for 24 h at 100 ℃. The products were isolated, washed, and filtered off. Solvent extraction of the polymeric surfactants was carried out by a solution of 10 g of HCl (37 wt%) and 70 g of methanol, and dried at room temperature. Calcination was carried out in a furnace by employing stepwise temperature increase from 30 ℃ to 450 ℃ for 10 h under N_2 flow. The synthetic method of organically modified SBA-16 with F127 was similar to the procedures described above and the quantities of reactants are reported elsewhere [3]. Mesoporous organosilica materials obtained with the F127 template were prepared with BTMSE:TEOS weight ratios of 0:100 (SBA-16), 5:95 (S16-B5), 10:90 (S16-B10) and 15:85 (S16-B15). Also, the organosilicas prepared with the LGE76 template were 0:100 (LGE-B0), 10:90 (LGE-B10), 30:70 (LGE-B30), 50:50 (LGE-B50) and 60:40 (LGE-B60).

DISCUSSION

In the case of employing the F127 triblock template and BTMSE as an organosilicate source, we found that the organosilica materials do not maintain their cubic ($Im\overline{3}m$) morphologies when BTMSE quantity exceeds 15 wt% as shown in the scattering pattern of Figure 1(a) (trace D).
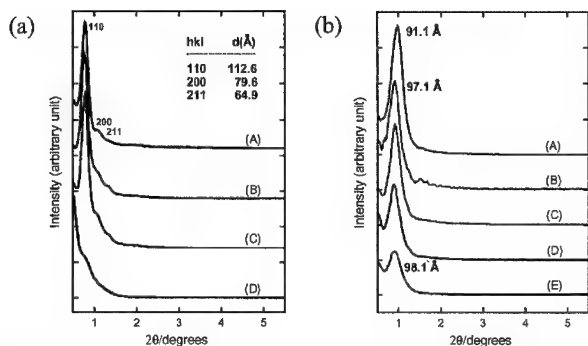
Figure 1. *Powder small angle X-ray scattering patterns of mesoporous ethanesilicas containing different weight proportions of TEOS and BTMSE. (a) As-synthesized samples of SBA-16 (trace A), S16-B5 (B), S16-B10 (C) and S16-B15 (D) (b) Calcined ethanesilicas prepared with LGE76 ($EO_{43}(L_{23}G_6)EO_{43}$) of LGE-B0 (trace A), LGE-B10 (B), LGE-B30 (C), LGE-B50 (D) and LGE-B60 (E). Scattering patterns were obtained with a Bruker 2D-GADDS diffractometer using Cu-Kα radiation with λ = 1.5418 Å.*

Moreover, in a typical experimental scheme of preparing the SBA-16, we found that solid precipitates could not be obtained in the case when the BTMSE content is above 15 wt% in the total silica. However, we observed that the cubic mesoporous ethanesilicas containing small quantities of BTMSE have high periodicity, high surface area and pore volume as shown in transmission electron micrograph [Figure 2(a)] and N_2 adsorption data (Table 1). As-synthesized ethanesilicas modified from the SBA-16 show well resolved SAXS patterns with large d-spacing (110) values of 113 Å (2θ = 0.78) and two additional reflections appeared in the range between 1 and 1.5°. After calcination, their cubic ($Im\overline{3}m$) structures are well maintained and the first diffraction peak is shifted to a d-spacing value of 97 Å (2θ = 0.90). The unit cell parameter values (a) of these cubic structures are estimated to be 160 and 137 Å for as-synthesized and calcined samples, respectively. The N_2 adsorption-desorption isotherm on the S16-B15 sample containing 15 wt% of BTMSE in the total silica source exhibits a mixed form of type I and II, which are the characteristics of microporosity and nonporosity [14]. We also noted that the pore size distribution of the S16-B15 sample is too polydisperse to be evaluated by the N_2 adsorption isotherm. From several experiments, we conclude that the PEO-PPO-PEO structure directing template with small difference between hydrophilicity of the PEO block and hydrophobicity of the PPO block are not so effective for forming new mesoporous organosilicas containing a large quantity of the organosilicate precursor.

Figure 1(b) illustrates the powder small angle X-ray scattering patterns of calcined ethanesilicas obtained with the LGE76 triblock template containing more hydrophobic PLGA block than the PPO block as a function of BTMSE content in the total silica. Scattering patterns
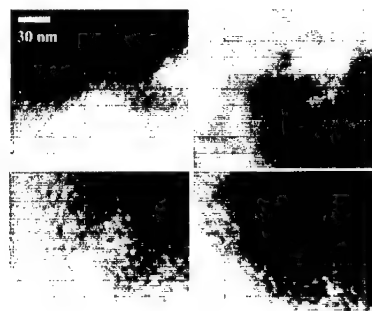
Figure 2. TEM images of calcined mesoporous ethanesilicas: (a), (b) are the images of S16-B5 and S16-B15 prepared with F127 ($EO_{106}PO_{70}EO_{106}$) and (c), (d) are LGE-B30 and LGE-B60 obtained from LGE76 ($EO_{43}(L_{23}G_6)EO_{43}$), respectively. TEM images were obtained with a JEOL JEM-200CX operated at an accelerating voltage of 120 kV.

show a single intense reflection with a d-spacing value near 98 Å ($2\theta = 0.91$). TEM [Fig. 2(c,d)] and N_2 adsorption-desorption data (Table 1) also represent that a large amount of mesopore is still maintained even after the addition of 60 wt% BTMSE in the silica although the samples are found to be less ordered in the long range as shown in Figure 2(d). These results imply that the LGE76 triblock template is so effective for forming the mesoporous organosilica materials. The decrease in the main peak intensity with increasing BTMSE content in the scattering data shown in Figure 1(b) agrees with the decrease in the BET surface area data shown in Table 1.

Table 1 also shows that the BJH average pore size slightly increases as the BTMSE content is increased. These data indicate that the electrostatic attractive force between the PEO chain and the silica source is weakened or the hydrophobic compatibility between the PLGA block and the ethane moiety of BTMSE slightly increases as the BTMSE content is increased. However, we also found that the pore size having the maximum portion of pore volume in all the samples prepared with the BTMSE precursor yields almost the same values of 3.7 nm irrespective of the BTMSE content, as also verified in the TEM micrographs of Figure 2(c,d). We note that the pore size is quite similar to that obtained with the modified SBA-16 shown in Figure 2(a) and Table 1. N_2 adsorption-desorption isotherms of the mesoporous ethanesilica materials prepared with the LGE76 template exhibit typical type IV behavior, which is the characteristic of mesoporous materials with a sharp inflection at $P/P_0 \approx 0.42$ (H_2 hysteresis).

To verify BTMSE incorporated into the silica solids prepared with the LGE76 template, ^{13}C and ^{29}Si CP-MAS NMR experiments on the solvent extracted samples were performed. The ^{13}C CP-MAS NMR spectra represent a resonance assigned to ethane carbon at δ −4 and a resonance at δ −70 corresponding to unremoved carbons originating from polymeric surfactants.

Table 1. Physicochemical properties of mesoporous ethanesilicas[a]

Sample code	Block copolymer	BET surface area/ m^2g^{-1}	Pore volume/ cm^3g^{-1}	Average pore diameter /nm	Max. pore diameter[b]/nm
S16-B5	$EO_{106}PO_{70}EO_{106}$	933	0.65	3.4	3.5
S16-B10	$EO_{106}PO_{70}EO_{106}$	640	0.44	3.2	3.5
S16-B15	$EO_{106}PO_{70}EO_{106}$	432	0.64	7.0	44.2
LGE-B10	$EO_{43}(L_{23}G_6)EO_{43}$	666	0.48	3.1	3.7
LGE-B30	$EO_{43}(L_{23}G_6)EO_{43}$	595	0.41	3.4	3.7
LGE-B50	$EO_{43}(L_{23}G_6)EO_{43}$	572	0.49	4.2	3.7
LGE-B60	$EO_{43}(L_{23}G_6)EO_{43}$	470	0.47	4.5	3.6

[a] N_2 adsorption-desorption isotherm data were measured on a Micromeri-tics ASAP 2010 analyzer. Samples were pre-degassed at 200 °C and 30 µmHg for 6 h and pore size distributions were calculated from the desorption branch of the isotherm by the BJH method. [b] Maximum pore diameter represents the pore diameter having the largest portion of pore volume in all measured pore size.

The ^{29}Si CP-MAS NMR of the LGE-B0 sample shows the characteristic signals assigned to $Si(OSi)_4$ (Q_4 δ −110), $(HO)Si(OSi)_3$ (Q_3 δ −101) and $(HO)_2Si(OSi)_2$ (Q_2 δ −92), respectively [Figure 3(a)]. In contrast, the ethanesilicas obtained from the BTMSE precursor represent another characteristic signals assigned to $CSi(OSi)_3$ (T_3 δ −65) and $CSi(OSi)_2(OH)$ (T_2 δ −57) as shown in Figure 3(b,c) confirming the presence of the ethane moieties inside the silica framework. Integration of ^{29}Si MAS NMR signals also confirms the successful quantitative incorporation of the BTMSE into the mesoporous silica materials.
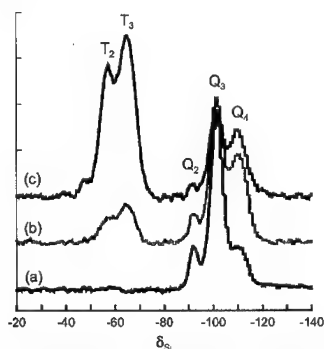
Figure 3. ^{29}Si CP-MAS NMR spectra of mesoporous ethanesilicas prepared with a LGE76 triblock copolymer. The spectra are for; (a) LGE76-B0, (b) LGE76-B10 and (c) LGE76-B50, respectively and obtained with a Bruker DSX400 spectrometer.

CONCLUSION

We concluded that more hydrophobic PLGA containing PEO-PLGA-PEO triblock copolymer was more effective in incorporating organosilicate precursors into the mesoporous silica materials than PEO-PPO-PEO triblock copolymer template.

ACKNOWLEDGEMENTS

REFERENCES

1. C. T. Kresge, M. E. Leonowicz, W. J. Roth, J. C. Vartuli and J. S. Beck, *Nature*, **359**, 710 (1992).
2. D. Zhao, J. Feng, Q. Huo, N. Melosh, G. H. Fredrickson, B. F. Chmelka and G. D. Stucky, *Science*, **279**, 548 (1998).
3. D. Zhao, Q. Huo, J. Feng, B. F. Chmelka and G. D. Stucky, *J. Am. Chem. Soc.*, **120**, 6024 (1998).
4. D. Zhao, P. Yang, N. Melosh, J. Feng, B. F. Chmelka and G. D. Stucky, *Adv. Mater.*, **10**, 1380 (1998).
5. S. A. Bagshaw, E. Prouzet and T. J. Pinnavaia, *Science*, **267**, 865 (1995).
6. S.-S. Kim, T. R. Pauly and T. J. Pinnavaia, *Chem. Commun.*, 1661 (2000).
7. T. Asefa, M. J. MacLachlan, N. Coombs and G. A. Ozin, *Nature*, **402**, 867 (1999).
8. C. Yoshina-Ishii, T. Asefa, N. Coombs, M. J. MacLachlan and G. A. Ozin, *Chem. Commun.*, 2539 (1999).
9. B. J. Melde, B. T. Holland, C. F. Blanford and A. Stein, *Chem. Mater*, **11**, 3302 (1999).
10. Y. Lu, H, Fan, N. Doke, D. A. Loy, R. A. Assink, D. A. LaVan and C. J. Brinker, *J. Am. Chem. Soc.*, **122**, 5258 (2000).
11. J. Joo, T. Hyeon and J. Hyeon-Lee, *Chem. Commun.*, 1487 (2000).
12. C. Yu, Y. Yu and D. Zhao, *Chem. Commun.*, 575 (2000).
13. B. Jeong, Y. H. Bae and S. W. Kim, *Colloids Surf.: B: Biointerfaces*, **16**, 185 (1999).
14. S. J. Gregg and K. S. W. Sing, *Adsorption, surface area and porosity*, Academic Press, London, 1982.

Millimeter-Wave Driven Polyol Processing of Nanocrystalline Metals

L. K. Kurihara[1, 3]*, D. Lewis[1], A. M. Jung[2], A. W. Fliflet[2] and R. W. Bruce[4]
Naval Research Laboratory, Washington, DC 20375
*Email: kurihara@anvil.nrl.navy.mil
1. Multifunctional Materials Branch, Code 6350
2. Beam Physics Branch, Code 6790
3. Also at Potomac Research Int., Fairfax, VA
4. LET Corp., Washington, DC

ABSTRACT

Nanocrystalline metallic powders and coatings have been synthesized using a millimeter wave driven polyol process. We have been able to prepare powders of single elements, alloys, metastable alloys, composites and coatings. Examples of a few of the metals processed in this study include Fe, Co, Ni, Cu, Ru, Rh, Pt, Au, FePt, Fe_xCo_{100-x}, NiAg and Cu-Ni. The polyol experiment was set up in the millimeter wave processing chamber, the beam was directed into the center of the solution and it was brought to reflux, using the millimeter wave beam as a heat source. Varying the power input easily controlled the rate of reflux.

INTRODUCTION

Fine metal particles have many uses in pigments, magnetic materials, catalysts, electromagnetic shielding, ferrofluids, sensors, biomedical, electronics and advanced-engineered materials. Among the various preparative techniques used to prepare nanoscale particles, chemical routes provide a practical route for preparing fine and ultrafine powders. The polyol method, in which the polyol acts as a solvent and as the reducing agent, and also acts as a surfactant, is a suitable method for preparing nanophase and micron size particles with well-defined shapes and controlled particle sizes (1-10).

The high intensity millimeter-wave beams (10^2–10^5 W/cm^2) that can be generated by powerful gyrotron oscillators have unique capabilities for rapid, selective heating of many materials to high temperatures. Previous work by the authors has demonstrated the efficacy of such rapid heating for both production of nanophase materials and processing of such materials into useful components (11-13). The advantages of using a millimeter wave beam as the heat source includes rapid heating and cooling, volumetric heating, elimination of thermal inertia effects, and spatial control of heating. Using the millimeter wave as the heating source in the polyol process allows for very short processing times; high heating rates due to bulk heating of the solution, which results from direct coupling of the beam energy to the solution elements; the ability to selectively coat substrates where the beam has been focused; as well as working in a superheated liquid region. By working in this regime, it is possible to suppress the growth process and to promote nucleation. Millimeter wave driven polyol processing has been used to prepare nanocrystalline powders of Fe, Fe_xCo_{100-x}, FePt, Co, Ni, NiAg, Cu, Cu_xNi_{100-x}, Ru, Rh, Ag, Pt and Au. Nanostructured coatings of copper have been deposited on AlN.

EXPERIMENTAL

A new continuous-wave (CW) gyrotron-based material processing system has been set up at the Naval Research Laboratory (NRL). The system is comprised of a Gycom, Ltd. industrial 15-kW CW gyrotron and associated superconducting magnet, power supplies, cooling system, control system, and a work chamber. A schematic of the complete system is shown in Fig. 1.
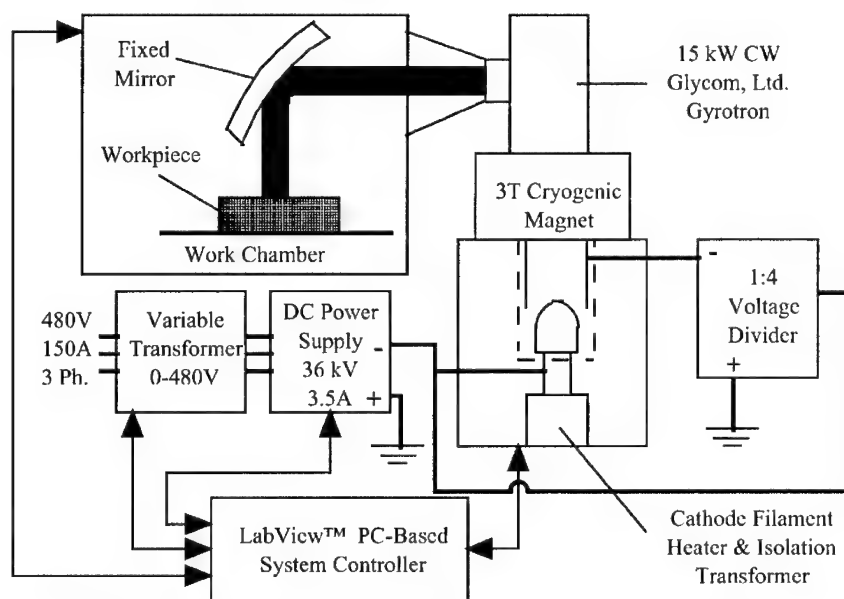
Fig. 1. Schematic of 83 GHz Millimeter-Wave Beam Processing Facility

The gyrotron operates near 83 GHz, and the output is produced in the form of a free-space quasi-Gaussian beam, which is directed into the work chamber. The gyrotron can be operated over a wide range of output powers (0.1–15 kW) by varying the cathode voltage from 22 to 28 kV, the cathode current from 1 to 2 A, and by making small changes in the applied magnetic field to vary the interaction efficiency. The gyrotron can be operated in the CW mode or for pulses as short as 1 second.

After exiting the gyrotron boron nitride output window, the microwave beam is injected into a cylindrical stainless steel work chamber (length = 100 cm, diameter = 60 cm) via a 60-cm conical transition. The beam waist diameter is about 3 cm at the window and it spreads to about 6 cm by the end of the work chamber. In the work chamber, the beam is directed down onto the flask containing the polyol solution by a 6-in-diam. concave mirror (48 cm radius of curvature).

The beam was approximately 3 cm in diameter at the flask. The reaction flask was placed in the work chamber. The flask was set up with an air-cooled reflux condenser and the beam was centered on the glycol-metal solution (Figure 2.)

The general procedure for the synthesis of different metallic powders and coatings involved preparing a mixture of the metal precursor in ethylene glycol or 1,2- propanediol and
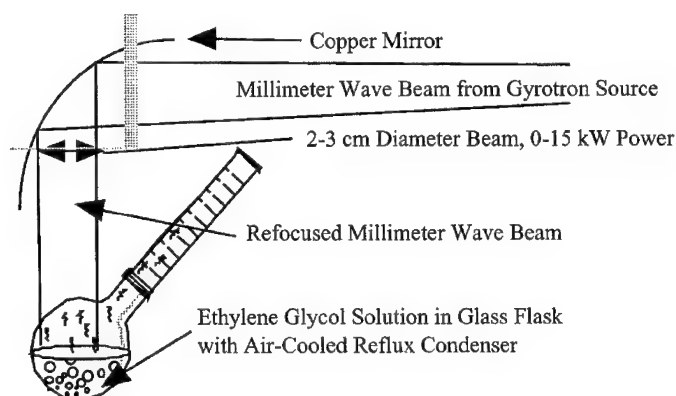
Fig. 2. Schematic of Millimeter Wave-Driven Polyol Process for Nanophase Material Production and Coating with Rapid Direct Heating with Millimeter Wave Beam Source

bringing the mixture to reflux. In most cases, refluxing of the glycol solution was observed within a minute of turning on the millimeter-wave beam. Details of the experimental procedure will be published elsewhere (13). However, some of the typical values used in the experiments were a metal precursor concentration ranging from 0.01-0.3M, and reaction times ranging from 1 minute to 60 minutes. The gyrotron was operated at relatively low voltages of 23.5–25 kV, and the electron beam current and applied magnetic field were held fixed at 1 A and 30.73 kG, respectively. Under these conditions the output power scaled with voltage as:

$$P(V) = 100V^2 - 4370V + 47,500.$$

The nominal gyrotron operating frequency was 82.6 GHz. During the processing, the gyrotron power was increased to the point that continuous refluxing could be maintained. After the reaction was completed, the metal–glycol mixture was cooled to room temperature. For film deposition experiments, an AlN substrate was placed in the metal-glycol solution . The crystal structure of the powders and coatings were studied using X-ray diffraction (XRD). Line broadening of XRD peaks was used to estimate the average crystallite size. The morphology of the particles was investigated using scanning electron microscopy (SEM) and transmission electron microscopy (TEM).

RESULTS AND DISCUSSION

Powders of a variety of transition metals have been synthesized by reducing metal precursors in a millimeter wave driven polyol solution. The precursors used in our study included: acetates, oxides, hydroxides, chlorides and carbonates.

Cu powder

Table I shows the relationship between the processing parameters of power and time for copper. With power at 100 W, and processing time of 9 minutes, the predominant phase of copper by XRD is Cu_2O, although there was a small amount of copper metal present (~20%). Increasing the average power lead to formation of copper metal. However, after 60 minutes with the beam on, copper was present, but now agglomerated. The average agglomerate size was 1-3 microns, with an average crystallite size of 500 nm. Further increasing the power output, while decreasing the time and concentration, also produced copper metal. In this case, (power = 220 W, time =10 minutes) the average crystallite size dropped to 150-200 nm. Increasing the power further to 330 W produced copper with an average crystallite size of 80-90 nm. Experiments are currently underway to further decrease the particle size. When copper acetate is reduced using a conventional heating mantle, the trend appears to show that the millimeter wave driven reactions take shorter times. One hour of refluxing under conventional conditions leads to Cu_2O (14) and when the solution is refluxed for only 15 minutes, just copper acetate is present (9).

Table I. Millimeter-Wave Processing Parameters for Polyol Process Copper

Copper Acetate concentration (M)	Time (min)	Power (W)	Results
.215	9	100	Cu_2O, Cu
.215	60	120*	Cu
.1	7	220	Cu
.1	10	220	Cu
.1	15	330	Cu
.1	20	688	Cu

*average power

CONCLUSIONS

The millimeter wave driven polyol approach has been used to synthesize metallic nanocrystalline powders and coatings. The results of this study show that there are two promising trends in processing with millimeter waves. First, is that an increase in power decreases the time needed to reduce the metallic precursor, and also leads to a decrease in particle size. Secondly, that the millimeter wave process produce materials with smaller crystallite sizes than those prepared by the conventional thermal method, at the same processing

times. Experiments are currently underway to optimize the processing parameters relative to particle size.

ACKNOWLEDGEMENTS

REFERENCES

1. P. Tonguzzo, G. Viau, O. Archer, F. Guillet, E. Bruneton. *J. Mater. Sci.*, **35**(2000).
2. P. Tonguzzo, G. Viau, O. Archer, F. Fievet-Vincent, and F. Fievet, *Adv. Mater.* **10**, 1032 (1998)
3. H. -O. Jungk and C. Feldmann, *J. Mater. Res.* **15**, 2244(2000).
4. J. Merikhi, H. -O. Jungk, and C. Feldmann, *J. Mater. Chem.* **10**, 1311(2000).
5. P. Tonguzzo, O. Archer, G. Viau, A. Pierrard, F. Fievet-Vincent, F. Fievet and I. Rosenman, *IEEE Trans. Magn.* **35**, 3469(1999).
6. L. K. Kurihara, G. M. Chow and P. E. Schoen, *Nanostruct. Mater.* **5**, 607(1995).
7. G. M. Chow, L. K. Kurihara, K. M. Kemner, P. E. Schoen, W. T. Elam, A. Ervin, S. Keller, Y. D. Zhang, J. Budnick, and T. Ambrose, *J. Mater. Res.* 10, 1546(1995).
8. G. M. Chow, L. K. Kurihara, and P. E. Schoen, U.S. Patent 5,759,230(1998).
9. L. K. Kurihara, D. Lewis, A. M. Jung, A. W. Fliflet, unpublished results 2000.
10. D. Lewis, R. J. Rayne, B. A. Bender, L. K. Kurihara et al. *Nanostruct Mater*, **9** , 97(1997)
11. L. K. Kurihara, G. M. Chow, D. Lewis, B. Bender, M. 1. Baraton, and P. E. Schoen,, to be published in *J. Am. Ceram. Soc.*
12. A. W. Fliflet, R. W. Bruce, R. P. Fischer, D. Lewis L.K. Kurihara., and B. Bender, to be published in *IEEE Transactions on Plasma Science*, (2001).
13. L. K. Kurihara, D. Lewis, M. A. Imam, A. M. Jung, A. W. Fliflet, and R. W. Bruce, unpublished results.
14. L. K. Kurihara, G. M. Chow, S. H. Lawrence, and P. E. Schoen, Processing and Properties of Nanocrystalline Materials, C. Suryanarayana, J. Singh and F. H. Froes, Eds., TMS Minerals, Metals, Materials, Warrendale PA **49**,235 (1996).

Ceramic Materials

Processing and Properties of Ceramic Nanocomposites Produced from Polymer Precursor Pyrolysis, High Pressure Sintering and Spark Plasma Sintering

Julin Wan*, Matt J. Gasch*, Joshua D. Kuntz*, Rajiv Mishra[+], and Amiya K. Mukherjee*
* Department of Chemical Engineering and Materials Science, University of California Davis, CA 95616
[+] Department of Metallurgical Engineering, University of Missouri, Rolla, MO 65401

ABSTRACT

Silicon nitride/silicon carbide nanocomposites and alumina-based nanocomposites were investigated in an effort to produce materials with high structural integrity and service properties. Bulk nano-nano composites of silicon nitride and silicon carbide were processed by crystallization of amorphous Si-C-N ceramics that were consolidated in-situ during pyrolysis of a polymer precursor. This material was developed for the purpose of examining the creep behavior of covalent ceramics when there is no oxide glassy phase at grain boundaries. Si_3N_4/SiC micro-nano composites were sintered by spark plasma sintering (SPS), aiming at better microstructural control and improved creep resistance. Composites of alumina with diamond, silicon carbide and metal (Nb) were developed by high pressure sintering and SPS. These composites maintain microstructures with a nanometric alumina matrix and are targeted for studying the toughening mechanisms and superplastic deformation mechanisms.

INTRODUCTION

Nanocrystalline materials, with their many unique properties related to small grain size and a very large number of grain interfaces, have raised expectations in both the scientific and the industrial communities [1]. The effort to employ nanocrystalline materials in some of the potential application fields, e.g., as structural materials, faces a major challenge that has been proven in the past decades to be a rather difficult one — how to produce bulk materials and yet retain a nanometric grain size. This problem is especially evident for nanocrystalline ceramics, and in particular, the hard-to-sinter ceramic systems such as silicon nitride and alumina.

Although certain skepticism about the expectation of silicon nitride ceramics (mainly its potential application in gas turbine engines) has been accumulating over the years [2], this system remains a major candidate for high temperature structural applications. The glassy grain boundary phase (GBP) in sintered silicon nitride is, on one hand, the dominant microstructural factor that accounts for the property degradation at elevated temperatures [3]. On the other hand, it is also important and in most cases indispensable for high-density sintering and also superplastic deformation [4]. Controlling the amount and properties of the glassy grain boundary phase has been, and also will be, the most effective way to improve the high temperature properties of silicon nitride and its composites.

Polymer precursor pyrolysis was originally developed for the fabrication of low-dimension ceramic materials such as coatings and fibers. Nowadays the consolidation of bulk Si-C-N amorphous ceramics is emerging as a new frontier for precursor-derived materials [5, 6]. Since densification happens in-situ during the polymer pyrolysis process, without relying on either solid-state diffusion in the ceramic network (which is negligible due to high covalent bonding in the silicon nitride/carbide systems) or solution-reprecipitation in liquid phase (which leads to oxide glassy GBPs), polymer precursor pyrolysis might open a window for consolidating silicon nitride ceramics without sintering aids. This approach, therefore, has the potential to produce

materials with high creep resistance and provides us with the first opportunity to study creep behavior and mechanisms without the interference of GBPs.

Among the types of nanocrystalline ceramic-based composites, the system of nano Al_2O_3-based composites is one of the most difficult to produce, since Al_2O_3 possesses one of the highest homologous temperatures for full-density sintering [7]. Superplasticity is difficult to realize in alumina, largely for the same reason. The successful suppression of Al_2O_3 grain growth depends on the utilization of nano-sized powders, application of lower sintering temperature and/or shorter sintering time than conventional processing. The mutual growth restriction from second phases can also suppress grain growth during sintering [8].

In this paper, a brief introduction will be given on the processing and microstructural features, along with some primary mechanical property results.

POLYMER PRECURSOR DERIVED Si_3N_4/SiC NANO-NANO COMPOSITES

The raw material we used to fabricate silicon nitride ceramic composites is a commercially available polyureasilazane precursor (Ceraset SN), supplied in liquid form. The polymer was first thermally cross-linked and crushed into powders. Two approaches were used for consolidation. Route 1: Warm-pressing/pyrolysis. Cross-linked polymer powders were compacted by uniaxial pressing at certain temperatures, followed by pyrolysis at a controlled heating-rate in a nitrogen atmosphere for ceramization. Route 2: Pre-pyrolysis/binding/pyrolysis. Cross-linked polymer powders were subjected to a pre-pyrolysis treatment then mixed with an appropriate amount of liquid polymer and compacted to form green bodies, which were then pyrolyzed. Detailed description of the processing routes can be found elsewhere [9].

Both of these approaches produce amorphous Si-C-N bulk materials without cracks. The densification behavior is well demonstrated by the porosity evolution during the pyrolysis of the materials of Route 1, as illustrated in Figure 1. Porosity increases with the pyrolysis temperature up to 450°C due to oligomer evaporation, then decreases with further pyrolysis, featured by
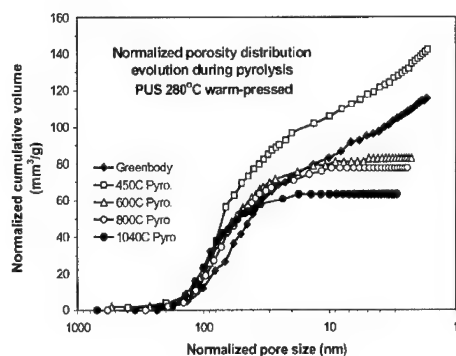
Figure 1 – *Pore size distribution during polymer pyrolysis.*
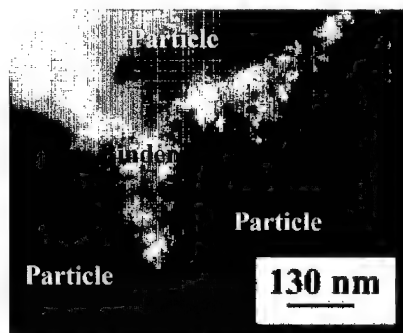
Figure 2 – *Structure of a compacted amorphous sample with particles and binder phase illustrated.*
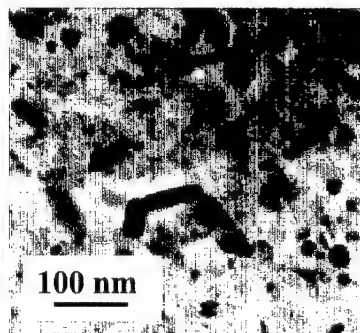
Figure 3 – *Crystallized Si_3N_4/SiC nano-nano composite.*

complete elimination of intrinsic pores (nano-sized pores, exist within the polymer particles due to phase-separation and volatile evaporation) and shrinkage of extrinsic pores (larger pores are the result of powder compaction) after 800°C. Pyrolysis is usually completed at about 1000°C, leaving behind consolidated amorphous material containing a certain amount of open porosity.

The amorphous Si-C-N ceramics made by Route 2, as compared with those produced by Route 1, are better in that they have higher density, lower volume shrinkage, and larger viable material size. Therefore, Route 2 is considered to be a more attractive method for industrial production. Furthermore, these materials, as long as they stay amorphous, can be free of open porosity, which is an important feature for application in oxidizing or corrosive environments. The structure of the amorphous ceramic, as shown in Fig. 2, is composed of a particle phase (which is originally the pre-pyrolyzed powder) surrounded by a binder phase containing nanometric pores. The nano-pores, although they are generally closed pores in the pyrolyzed ceramics, were not eliminated during pyrolysis, owing to the restriction from the particle phase. Amorphous Si-C-N materials were crystallized into nanocrystalline ceramics, by heat-treating at temperatures between 1550-1700°C. Two types of crystallization behavior can be observed. One is heterogeneous crystallization that happens at the surfaces (outer surface of the material or inner surfaces such as pore walls), and is believed to be closely linked to gaseous phase reactions and starts at lower temperatures (1400-1450°C) than the crystallization of the overall material. Depending on the type of atmosphere (inert gas or nitrogen) and the nature of the surface (open or closed pores), α- Si_3N_4 whiskers or β-SiC particles or whiskers, can be found on the surfaces. Heterogeneous crystallization seen in Route 2 derived materials is manifested by crystallization of the binder before crystallization of the particle phase. Homogeneous crystallization of the interior of the amorphous material involves conversion of SiC_xN_{4-x} tetrahetra to SiN_4 and SiC_4 tetrahetra, and is believed to be preceded by the forming of carbonic basic unit cells (BSUs) and then the nucleation and growth of silicon carbide and silicon nitride grains. Ultimately, Si_3N_4/SiC nanocomposites with both Si_3N_4 and SiC grains within a nanometric size range (~30nm) can be obtained, as shown in Fig. 3. Closer look at this microstructure revealed that although it can be highly crystalline, certain regions of carbon-rich amorphous regions are retained (Fig. 4(a)). Nonetheless, as long as the grains reach close contact, GBP-free grain boundaries can be achieved (Fig. 4(b)), which suggests possible high creep resistance in these kind of materials.
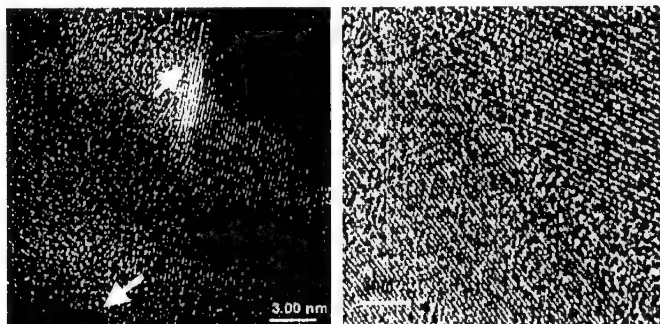
Figure 4a – *Illustration of S-N-C polymer that has been crystallized. Arrows show regions of non-oxide amorphous material.* **4b** – *Illustration of a grain boundary completely free of amorphous material.*

MICRO-NANO Si$_3$N$_4$/SiC COMPOSITES FROM SPS OF POLYMER-DERIVED AMORPHOUS POWDERS

In the SPS process, due to the combined effects of (1) spark plasma, (2) spark impact pressure, (3) Joule heating, and (4) an electrical diffusion field generated by an ON-OFF DC pulse, the powder particle surfaces are easily cleaned and activated, and material transfer at both the micro and macro levels is promoted, so a high quality sintered compact is obtained at a lower temperature and in a shorter time compared to conventional processes. 2-5wt% MgAl$_2$O$_4$ or 5-8wt% Y$_2$O$_3$ additives were mixed with the amorphous Si-C-N powder derived from 1450°C pyrolysis of polymer precursor by high energy ball-milling. Successful sintering by SPS was realized at low temperature (~1600°C) and very short sintering time (<10minutes), as compared with 1750-1850°C/2-4hrs for conventional methods. It was found that, by changing the amount or type of the sintering additives, the phase composition could readily be changed in large span. With lower additive content, the microstructure is composed almost entirely of microcrystalline silicon carbide. While with higher additive contents, micro-nano composite microstructures were achieved. Silicon nitride and silicon carbide grains 100-200nm in size were found to co-exist in the microstructures. SiC nano-particles (10-30nm) were found in most of the Si$_3$N$_4$ grains. Grain boundaries which are only partially wetted by glassy phase were observed (leaving part of the grain boundary free of GBP. This kind of grain boundary hasn't been found in conventional silicon nitride. In conventional Si$_3$N$_4$ ceramics, the equilibrium GBP thickness has been established to be 0.5-2.0nm, while in the SPS derived samples, GBPs thinner than or at least at the lower limit of this range are abundant. Investigation on statistical basis is yet to be conducted to confirm this observation. In the triple junction pockets where most of the glassy phase is located, graphitic free carbon was observed. This is a result of the decomposition of the amorphous Si-C-N phase during sintering and crystallization. The partially wetted grain boundaries and thinner GBP layers predict higher creep resistance for the materials. Furthermore, the graphitic free carbon has the possibility to increase the viscosity of the glassy phase, which might also contribute to increased creep resistance.

NANOMETRIC ALUMINA AND ALUMINA-BASED NANOCOMPOSITES

Nanocrystalline alumina and alumina matrix nanocomposites were produced using different sintering routes; HPS and SPS. A Boyd-England piston-cylinder apparatus, capable of sintering conditions in excess of 2 GPa and 1450°C, was used for the HPS. SPS was performed in Dr. Sinter® 1050 spark plasma sintering system (Sumitomo coal mining company, Ltd.) This equipment is capable of pulsing 5000 A at 63 MPa and 2000°C.

Nanometric γ-Al_2O_3 powder was consolidated through HPS at 1 GPa in the temperature range 650-1050°C. The smallest grain size obtained for fully dense (>99% theoretical density) alumina was 93 nm sintered at 950°C for 10 minutes. It was observed that the $\gamma \rightarrow \alpha$ phase transformation during HPS is lowered from 1200°C to about 750°C. This phase transformation helps produce equiaxed morphology during sintering (γ-Al_2O_3 usually assumes a vermicular structure) which promotes accelerated sintering. The effect of plasma on alumina sintering kinetics was studied using SPS processing. Densification to >98.6% theoretical density was achieved in less than 10 minutes at 1300°C. This is obviously more effective than conventional sintering of alumina, which usually requires 3 hours at 1500°C to obtain the same density. It was also observed that for a given set of sintering conditions α alumina starting powder leads to higher final density than γ alumina powder.

Nano-nano composites of alumina with diamond, silicon carbide, and niobium as the second phases were also sintered by high pressure sintering with Boyd-England piston-cylinder apparatus. Sample microstructures of HPS processed nanocomposites are shown in Figure 5. The toughness and hardness of nanocomposites show promising improvements, as indicated in Table 1. The alumina nanocomposite with 10vol.% diamond deserves special attention

Fig. 5   *Microstructure of (a) alumina-diamond and (b) alumina-niobium nanocomposites synthesized by high pressure sintering.*

Table I – Mechanical properties of 'nano-nano' alumina composites

Material	Grain Size (nm)	Hardness (GPa)	Indentation Toughness (MPa m$^{1/2}$)
Al_2O_3-10 vol. % SiC	101±32	19.6±0.22	2.96±0.91
Al_2O_3-10 vol. % Diamond	106±17	24.7±0.56	3.49±0.97
Al_2O_3-10 vol. % Nb	40-50	20-23	>8
Microcrystalline Al_2O_3	3000	20.1	2.32±0.07

(microstructure shown in Fig 5(a)). Along with good hardness (24.7GPa), it exhibits a toughness of 3.49 MPa√m which is 50% higher than that of coarse alumina. Fully dense nanocrystalline Al_2O_3/10vol.%Nb composite was achieved by HPS at 900°C and 2GPa for 10 minutes. The average grain-size of the sintered material was in the range of 40-50nm. The microstructure, as shown in Fig. 5(b), has the nano-nano layer nanocomposite morphology with Nb forming an approximately continuous phase. Such a microstructure is different from most of the reported metal phase –toughened "nanocomposites" (usually nanometric metal particles embedded in microcrytalline alumina matrix), and it has the potential of more effectively generating a plastic deformation zone at the crack tips. The Al_2O_3/Nb nanocomposite exhibits significantly improved toughness of >8 MPa $\sqrt{m}$, along with well-retained hardness values (20-23 GPa).

CONCLUSION

Bulk silicon nitride/silicon carbide nanocomposites were synthesized by polymer precursor pyrolysis. Composites with both silicon nitride and silicon carbide grains in the nanometer range was achieved by in-situ consolidation followed by crystallization, without sintering aids. Micro-nano composites were sintered with oxide additive by fast-sintering with SPS. Both these composites show grain boundary conditions different from that of conventionally produced ceramics. Alumina based nanocomposites were sintered by high pressure sintering and SPS, some of the composites show significant improvement in mechanical properties.

REFERENCES

1   H. Gleiter, Nanostructured Materials: Basic Concepts and Microstructure, *Acta Mater.*, **48**, 1-29 (2000).

2   K. H. Jack, Nitrogen Ceramics for Engine Application, Nitrides and Oxynitrides, Proceedings of the Second International Symposium on Nitrides, ed. S. Hampshire and M. J. Pomeroy (Limerick, Ireland, 1998) pp. 255-262.

3   S. Hampshire, Nitride Ceramics, *Materials Science and Technology: A Comprehensive Treatment*, ed. R. W. Cahn, P. Haasen and E. J. Kramer (VCH, 1992) pp. 120-171.

4   F. Wakai, N. Kondo and Y. Shinoda, Ceramics Superplasticity, *Curr. Opinon in Solid St. and Mat. Sci.*, **4**, 461-465 (1999).

5   J. Bill and F. Aldinger, Precursor-Derived Covalent Ceramics, *Precursor-Derived Ceramics*, ed. J. Bill, F. Wakai and F. Aldinger (Wiley-VCH, 1999) pp. 33-51.

6   R. Riedel and W. Dressler, Chemical Formation of Ceramics, *Ceram. Inter.*, **22**, 233-239 (1996).

7   R. S. Mishra, J. A. Schneider, J. F. Shackelford and A. K. Mukherjee, Plasma Activated Sintering of Nanocrystalline γ–Al2O3, *NanoStructured Materials*, **5**, 525-544 (1995).

8   K. Nakano, T. S. Suzuki, K. Hiraga and Y. Sakka, Superplastic Tensile Ductility Enhanced by Grain Size Refinement in a Zirconia-dispersed Alumina, *Scripta Mater.*, **38**, 33-38 (1998).

9   J. Wan, M. J. Gasch and A. K. Mukherjee, Silicon Carbonitride Ceramics Produced by Pyrolysis of Polymer Ceramic Precursor, *J. Mat. Res.*, **15**, 1657-1660 (2000).

Initial Stages of Sintering of TiO₂ Nanoparticles: Variable-Charge Molecular Dynamics Simulations

Shuji Ogata,[1] Hiroshi Iyetomi,[2] Kenji Tsuruta,[3] Fuyuki Shimojo,[4] Aiichiro Nakano,[5] Priya Vashishta,[5] Rajiv K. Kalia,[5] and Chun-K. Loong[6]

[1]Department of Applied Sciences, Yamaguchi University, Ube 755-8611, Japan

[2]Department of Physics, Niigata University, Niigata 950-2181, Japan

[3]Department of Electrical and Electronic Engineering, Okayama University, Okayama 700-8530, Japan

[4]Faculty of Integrated Arts and Sciences, Hiroshima University, Higashi-Hiroshima 739-8521, Japan

[5]Concurrent Computing Laboratory for Materials Simulations, Louisiana State University, Baton Rouge, LA 70803-4001, U.S.A

[6]Argonne National Laboratory, Argonne, IL 60439, U.S.A.

ABSTRACT

Variable-charge molecular dynamics simulation of 32 TiO₂-nanoparticles with diameter 60Å is performed for 40 ps at 1 GPa and 1,400 K for both rutile and anatase phases, to investigate their phase-dependent sintering mechanisms. In the rutile case, the nanoparticles rotate around their centers during the first 20 ps. Varying degrees of neck formation between neighboring rutile-nanoparticles are found at ~ 40 ps. In the anatase case, the nanoparticles maintain their original orientations. Similar degrees of neck formation are observed at contacting regions of the anatase nanoparticles.

INTRODUCTION

TiO₂ is well known for its wide range of applications including photocatalysts [1-3], capacitors [3], and pigments [3]. Those useful applications stem from its high electric permittivity [3], $\varepsilon \approx 200$ along $\langle 001 \rangle$ direction and $\varepsilon \approx 90$ along $\langle 100 \rangle$ direction, indicating large degrees of dynamic charge-transfer between the atoms. The TiO₂ assumes the rutile structure at the ground state; the anatase structure, at a metastable state [3].

TiO₂ nanoparticles are synthesized by several methods. In the gas-condensation method [4], rutile nanoparticles with size ~ 14 nm are formed [5]. Anatase nanoparticles with 3 – 10 nm can be formed in the sol-gel method [6,7]. Those anatase-nanoparticles sinter at lower temperatures [8] (~ 900 K) than the sintering temperature (~ 1,300 K) of rutile nanoparticles. During the sintering of anatase nanoparticles, an anatase-to-rutile phase transformation has been found at grain boundaries [8]. Such low sintering temperatures are desirable for technical applications since grain growth is significantly suppressed during the sintering. Theoretical understanding of the different sintering mechanisms between the rutile and anatase nanoparticles will offer valuable information for improved production of nanophase materials.

We have recently developed a variable-charge inter-atomic potential [9] for molecular dynamics (MD) simulations of TiO₂ systems. In the potential, atomic charges vary dynamically depending on their environment to minimize the total potential energy [9,10]. The calculated

pressure- and orientation-dependent dielectric constants and surface energies of low-index planes for the rutile crystal as well as its cohesive energy, elastic moduli, and melting temperature, agree well with experimental values [9]. Experimental values of the dielectric constants, cohesive energy, and lattice constants for the anatase crystal are reproduced as well by the potential [9].

In this paper we perform variable-charge MD simulation of 32 TiO_2-nanoparticles at 1 GPa and 1,400 K for both rutile and anatase phases to understand their phase-dependent sintering behaviors. We thereby find substantial differences in rotational motions of the nanoparticles and in neck formation mechanisms between the rutile and anatase cases.

VARIABLE-CHARGE MD SIMULATIONS

Initial configurations for the present simulations are prepared as follows. First a nanoparticle with diameter ~ 60 Å is cut out from the bulk crystal. Variable-charge MD simulation of the nanoparticle is performed at 1,400 K with free boundary conditions for equilibration. We then place 32 copies of the nanoparticle with random orientations at the face-centered-cubic positions in the cubic MD-box under the periodic boundary conditions; initial value of the nearest neighbor distances of the nanoparticles is 70 Å. Total number of atoms $N = 334,274$ for the rutile system; $N = 331,296$ for the anatase system.

We perform NPT-MD simulations of the rutile and anatase systems at 1,400 K and 1 GPa using the variable-charge inter-atomic potential on a 8-node PC-cluster in Yamaguchi University consisted of Intel Pentium III/600MHz processors interconnected by FastEthernet. The fast-multipole method [11] is used for fast computations of the Coulomb interaction potentials. Multiple time-steps [12] are used in the simulations; the smallest time-step is 0.15 fs.
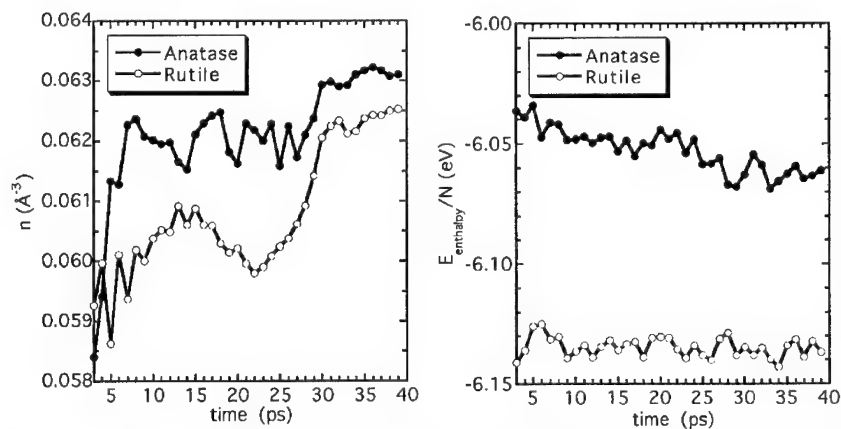
Figure 1. *Time evolution of density and normalized enthalpy in the present simulations for rutile and anatase nanoparticles.*

Figure 1 depicts time evolution of density $n = N/V$ and normalized enthalpy in the rutile and anatase cases. The enthalpy of the anatase system decreases linearly as a function of time as shown in Fig. 1 (right). The n increases toward $n = 0.062\text{Å}^{-3}$ after ~ 6 ps in the anatase case (Fig. 1 (left)). During 5 – 25 ps, $n = 0.060\text{Å}^{-3}$ in the rutile case, which is substantially smaller than $n = 0.062\text{Å}^{-3}$ in the anatase case. The n increases after ~ 30 ps in the rutile case as seen in Fig. 1 (left).

Time evolution of the normalized radial-distribution function between Ti atoms $g_{\text{TiTi}}(r)$ is depicted in Fig. 2 for the rutile and anatase systems. No significant differences are seen between $g_{\text{TiTi}}(r)$'s at 3 ps, 15 ps, 27 ps, and 39 ps in both rutile and anatase cases, which indicate that the crystalline structures at the interiors of the nanoparticles are maintained. In the anatase case, height of the first peak of $g_{\text{TiTi}}(r)$ at time $\geq 15\text{ps}$ is smaller by about 10 % from the height at 3 ps. For further analyses, we consider atomic configurations of boundary regions of the nanoparticles.

We cut out a thin slab with thickness 6 Å from the system, which is terminated by two planes parallel to the close-packed plane of the nanoparticle-centers. Atomic configurations of the slab at 15 ps and 39 ps are plotted in Fig. 3 for the rutile system, and in Fig. 4 for the anatase system. Rotation angles of the nanoparticles at 3 ps, 15 ps, 27 ps, and 39 ps defined as $\cos^{-1}(\vec{n}_{[100]} \bullet \vec{n}_{[100]}^{\text{init}}) + \cos^{-1}(\vec{n}_{[010]} \bullet \vec{n}_{[010]}^{\text{init}}) + \cos^{-1}(\vec{n}_{[001]} \bullet \vec{n}_{[001]}^{\text{init}})$ using the normalized lattice-vectors ($\vec{n}$) and the vectors at the initial ($\vec{n}^{\text{init}}$), are plotted in Fig. 5 for both rutile and anatase cases. Numbers typed on the nanoparticles in Fig. 3 (right) correspond to the nanoparticle ID's.
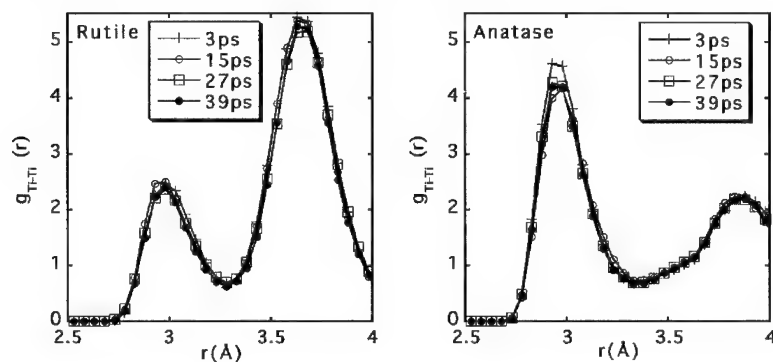
Figure 2. Time evolution of normalized radial-distribution function between Ti atoms in the present simulations for rutile and anatase nanoparticles.

Until around 22 ps, the rutile nanoparticles are rotating as depicted in Fig. 5 (left). No substantial degrees of neck formation between the rutile nanoparticles are therefore found at 15 ps as seen in Fig. 3 (left). We may consider that the delayed densification in the rutile case, observed in Fig. 1 (left), has resulted from such rotational motions of the rutile nanoparticles. The anatase nanoparticles, on the other hand, maintain their original orientations (Fig. 5 (right)). Substantial degrees of neck formation are observed at 15 ps in Fig. 4 (left) at all the contacting

regions of the anatase nanoparticles. No further rotations of the rutile nanoparticles exist after ~ 25 ps. During 27 – 39 ps, total volume of the rutile system decreases accompanied by varying degrees of neck formation at contacting regions of the nanoparticles (Fig. 3 (right)). Such rotational motions and unisotropic neck-formation of the rutile nanoparticles, observed in Figs. 3 and 5, may be related to large difference in the dielectric constants of the rutile crystal [3], i.e., $\varepsilon_{\langle 001\rangle} \approx 200$ and $\varepsilon_{\langle 100\rangle} \approx 90$.
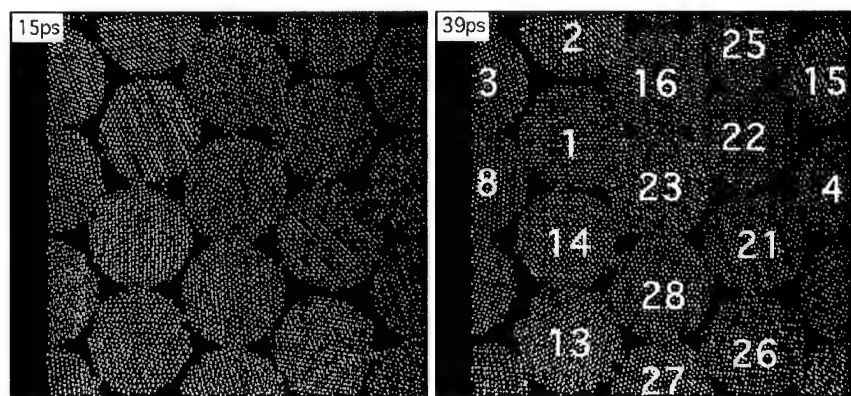
Figure 3. *Atomic configurations of a 6Å-thickness slab at 15 ps and 39 ps in the present simulation for rutile nanoparticles.*
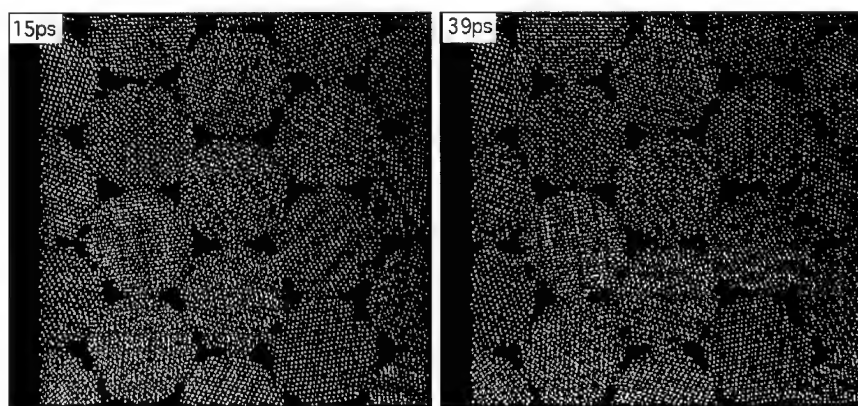
Figure 4. *Atomic configurations of a 6Å-thickness slab at 15 ps and 39 ps in the present simulation for anatase nanoparticles.*
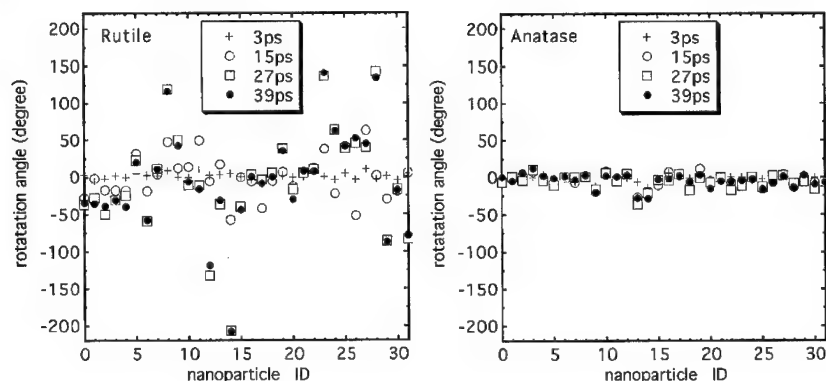
Figure5. *Time evolution of the rotation angles of nanoparticles in the present simulations for rutile and anatase nanoparticles.*

We analyze crystalline orientations of mutually contacting nanoparticles to investigate their possible relation to the degrees of neck formation. Let us consider 3 nanoparticles with ID=1, 23, and 21 in alignment (scc Fig. 3 (right)). Nanoparticles with ID=1 and 23 sinter well with each other, while no substantial neck formation is observed between nanoparticles with ID=21 and 23 in Fig. 3 (right). Crystalline orientations along the connecting line of their centers are ⟨112⟩, ⟨124⟩, and ⟨112⟩ within errors of ±7 degrees for nanoparticles with ID=1, 23, and 21, respectively. Despite same set of crystalline orientations in the two cases of contact, different degrees of sintering has resulted in Fig. 3 (right).

CONCLUSIONS

We have performed variable-charge molecular dynamics simulations of TiO_2-nanoparticles (diameter 60 Å) for 40 ps at 1 GPa and 1,400 K for both rutile and anatase phases, to investigate their phase-dependent sintering behaviors. We thereby found that the rutile nanoparticles rotate around their centers during the first 20 ps (Fig. 3 (left)). Degrees of neck formation between the nanoparticles varied in the rutile case. The anatase nanoparticles maintained their original orientations (Fig. 5 (right)), resulting in similar degrees of neck formation between the contacting nanoparticles (Fig. 3 (right)).

REREFENCES

1. *Nanomaterials Synthesis, Properties, and Application*, edited by A.S. Edelstein and R.C. Cammarata (IOP Pub., London, 1996).

2. Y.-M. Chiang, D. Birnie III, W.D. Kingery, *Physical Ceramics* (Wiley & Sons, New York, 1997).
3. *Concise Encyclopedia of Advanced Ceramic Materials*, edited by R.J. Brook (Pergamon, Cambridge, 1991), pp. 486-488.
4. R.W. Siegel, S. Ramasamy, H. Hahn, L. Zongquan, L. Ting, and R. Gronsky, J. Mater. Res. **3**, 1367 (1988).
5. H. Hahn, J. Logas, and R.S. Averback, J. Mater. Res. **5**, 609 (1990).
6. Q. Xu and M.A. Anderson, Mat. Res. Soc. Symp. Proc. **132**, 41 (1989).
7. T.J. Trentler, T.E. Denler, J.F. Bertone, A. Agrawal, and V.L. Colvin, J. Am. Chem. Soc. **121**, 1613 (1999).
8. K.-N.P. Kumar, K. Keizer, A.J. Burggraaf, T. Okubo, H. Nagamoto, and S. Morooka, Nature **358**, 48 (1992).
9. S. Ogata, H. Iyetomi, K. Tsuruta, F. Shimojo, R.K. Kalia, A. Nakano, and P. Vashishta, J. Appl. Phys. **86**, 3036 (1999).
10. F.H. Streitz and J.W. Mintmire, J. Adhes. Sci. Technol. **8**, 853 (1994).
11. L. Greengard and V. Rokhlin, J. Comp. Phys. **73**, 325 (1987).
12. G.J. Martyna et al., Mol. Phys. **87**, 1117 (1996).

Structural Disorder in the Anion Lattice of Nanocrystalline Zirconia and Hafnia Particles

Dieter Vollath[1], Manfred Forker[2], Michael Hagelstein[3], D. Vinga Szabó[1]
[1] Forschungszentrum Karlsruhe, Institut für Materialforschung III, D-76021 Karlsruhe,
   Germany, P.O.Box 3640, Germany, E-mail: dieter.vollath@imf.fzk.de
[2] Universität Bonn, Institut für Strahlen- und Kernphysik, Nußallee , D-53115Bonn, Germany
[3] ANKA GmbH, Hermann-von-Helmholtz-Platz, D-76344 Eggenstein-Leopoldshafen, Germany

ABSTRACT

Nanoparticles of ZrO_2 and HfO_2 with sizes around 5 nm are – depending on the production route - found in the cubic or tetragonal or monoclinc phase. To shed some light into this difference, an analysis of crystal structure, distances, and symmetry around the cations was performed on alumina coated nanoparticles prepared by the microwave plasma process. Within the range of accuracy, electron-diffraction and -microscopy revealed a possibly cubic cation lattice for both materials. In the case of ZrO_2, the evaluation of the amplitude of the modified radial distribution function derived from extended x-ray absorption fine structure (EXAFS) data lead to a structure with a narrow distribution of oxygen ions in the first shell of neighbors. This is expected for the cubic structure. Comparing the imaginary part with model calculations, a distinct similarity with the cubic structure is obvious. In the second shell of neighbors, consisting of metal ions, one radial distribution peak is expected and found experimentally. Perturbed angular correlation measurements indicate a pronounced disorder of the positions of the first neighbors of the metal ions. Together with the EXAFS observation of a narrow radial distribution of the first neighbor oxygen ions, these measurements provide evidence for a random distribution of Zr-O bond angles in the vicinity of their crystallographic positions. Above 500°C a partially reversible transformation to almost perfect tetragonal symmetry is observed. Therefore, one has to conclude that the cubic structure with disordered anion lattice is more stable than the tetragonal one at room temperature. Structural relationships like this are unknown in coarse-grained material.

INTRODUCTION

Undoped zirconia, ZrO_2 and hafnia, HfO_2, undergo a series of phase transformations. The first solid phase at high temperatures is the cubic fluorite structure with the highest density, lowering the temperature the tetragonal phase occurs, and finally, at room temperature, the stable structure is the monoclinic one exhibiting the lowest density [1]. In general, compressive stresses promote the stability of the phases with higher density. Therefore, decreasing grain size lowers the temperature of the phase transformations. This behavior is well proven for zirconia and expected for hafnia, too [1].

The materials used in this study, undoped nanocrystalline zirconia and hafnia with particle size around 5 nm with and without alumina, Al_2O_3, coating were synthesized using the microwave plasma process [2,3]. As in this process the particles leave the reaction zone with electric charges of equal sign, coagulation or agglomeration of the particles is thwarted. This leads to extreme narrow particle size distributions and makes it possible to coat each individual particle. Coating the zirconia respectively hafnia particles with alumina has two consequences:

i) The particles are kept apart avoiding sintering and grain growth of the kernels at elevated temperatures. ii) Due to the differences in the thermal expansion the alumina coating causes a mechanical constrain on the kernel during the phase transformation.

High-resolution electron microscopy and electron diffraction are sensing the lattice in toto, giving information on global symmetries. Perturbed angular correlation (PAC) measurements [4,5] provide information on strength and symmetry of the charge distribution related to the next neighbors around the Zr^{4+} and Hf^{4+} ions. The extended x-ray absorption fine structure (EXAFS) is created by the interference of the x-rays scattered at the different neighboring ions. As a result this leads to a function, similar to a pair distribution function, containing information on the distance of the absorbing atom to the neighbors in the different shells and the co-ordination number. Additionally, the width of the pair distribution function gives indications on the perfection of the arrangement of the ions in the lattice. EXAFS senses primarily the distance between the ions; it is rather insensitive with respect to the angular distribution of the ions in the neighboring shells. Therefore these three complementary techniques were applied to analyze the material.

Electron microscopy of earlier experiments revealed that zirconia nanoparticles crystallize within the margins of accuracy in the cubic structure [2]. An additional study using electron microscopy and perturbed angular correlation (PAC) spectroscopy indicated that the anion sublattice in this cubic structure is disturbed [6]. Similar results were found in hafnia [7]. In the present study the co-ordination of the oxygen and zirconium shells around a Zr^{4+} ion are determined by EXAFS and correlated with the results from electron microscopy and PAC.

EXPERIMENTAL DETAILS

Electron microscopy

Morphology and structure of the materials in question were studied by electron microscopy and electron diffraction. Within the limited accuracy of the method electron microscopy revealed for coated and uncoated zirconia crystallized material with cubic structure. Hafnia particles, both uncoated and coated, were also well crystallized. Uncoated hafnia particles were found in the monoclinic structure, whereas the coated ones were in the cubic or tetragonal structure. A well-founded decision was impossible because of the even smaller differences between the a and c value of the lattice parameters. Additionally, a faint indication of the monoclinic phase was observed. The size of the zirconia or hafnia particles was around 5 nm.

Extended x-ray absorption fine structure (EXAFS)

The EXAFS experiments have been performed on the beam line BM29 at the European Synchrotron Radiation Facility in Grenoble, France. The synchrotron x-rays passed a Si(311) double crystal monochromator. To suppress higher harmonics, the second crystal was detuned. The measurements were performed in an energy range from 17.75 keV to 19.0 keV. The spectra were calibrated setting the maximum inflection point of the Zr-K edge of ZrO_2 to 17.998 keV. In addition to the nanocrystalline material, yttria doped zirconia with cubic structure was used as reference material.

The experimental EXAFS data were analyzed using the analysis program WinXAS [8]. The application of the cumulant expansion including the third cumulant parameter takes care of the

deviation from a Gaussian pair distribution function. After Fourier transformation over a wavenumber range from $k = 0.25$ to 0.14 nm and a Bessel window, each shell has been fitted individually in real space [9]. The Fourier transformed function $FT(\chi(k)k^3)$ represents a modified pair distribution as it is depicted in figure 1.
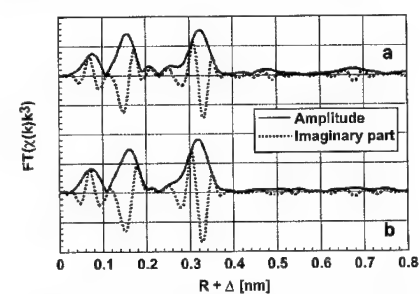
Figure 1: *Radial distribution function for Al_2O_3 coated ZrO_2 (a) and Y_2O_3 doped coarse grained cubic ZrO_2 (b).*
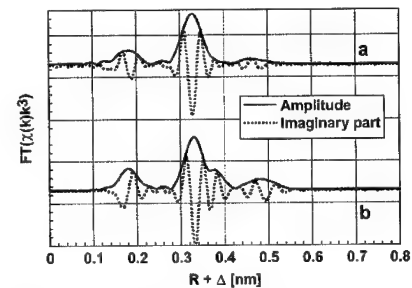
Figure 2: *Calculated radial distribution functions for tetragonal (a) and cubic (b) ZrO_2.*

In this figure the abscissa values are not corrected for phase shift due to scattering on the atomic potential of the absorbing atom and the scattering neighbors. For both, the nanocomposite and the yttria stabilized ZrO_2, the first prominent peak can be fitted using a single O^{2-} shell with a $Zr^{4+} - O$ distance of 0.214 nm. The second prominent peak reflects a single Zr^{4+} shell with a $Zr^{4+} - Zr^{4+}$ distance of 0.365 nm. In figure 1, there is actually a "first peak" at 0.07 nm. This is an artifact caused by scattering of the photons on the absorbing potential or the background removal procedure during data reduction.

Table 1: Results from the evaluation of the first two EXAFS peaks.

	Nano- ZrO_2/Al_2O_3		Coarse $ZrO_2(Y_2O_3)$		Cubic ZrO_2 theoretical		Tetragonal ZrO_2 theoretical	
Shell	Zr - O	Zr- Zr	Zr - O	Zr- Zr	Zr - O	Zr- Zr	Zr - O	Zr- Zr
Radial distance $\pm \sigma$ [nm]	0.214 ± 0.0076	0.365 ± 0.0089	0.219 ± 0.0087	0.360 ± 0.010	0.2238	0.365	0.207/ 0.245	0.364/ 0.368
Coordination number	4.1	6.4	5.4	10.5	8	12	4/ 4	4/ 8

The results summarized in table 1 are to some extent puzzling. On the one hand the width σ of the first O^{2-} shell and the first Zr^{4+} shell is narrower for the nanoparticles as compared to the coarse grained cubic material, on the other hand, the coordination numbers are significantly too small for the nanomaterial in the cubic structure. This is valid even under the assumption that coordination numbers determined by EXAFS are often up to 20% too small [10]. Also the fact that a significant amount of the ions in the nanoparticles is on the surface cannot explain these small coordination numbers. Therefore, a significant disorder has to be assumed. The reduced coordination numbers and the large shell width in the case of $ZrO_2(Y_2O_3)$ may be explained by the lattice disorder introduced by the yttria doping. Two further peaks at 0.477 nm and 0.677 nm

are significantly stronger for the nanocomposite as compared to the yttria-stabilized compound.

Theoretically determined functions, analogous to those presented in figure 1, calculated using the multiple scattering code FEFF [11] on the basis of model compounds for cubic and tetragonal zirconia, are presented in figure 2. It is obvious that in special the experimentally determined imaginary part of the nano-ZrO_2/Al_2O_3 is very similar to the one calculated for the cubic phase. The shoulder on the second peak of the cubic zirconia in figure 2 stems from multiple scattering between Zr^{4+} and O^{2-} ions. This phenomenon is possible only in the case of a perfect lattice, it was never found experimentally, neither for the coarse nor for the nano-material. From figure 2 it is obvious, that the third peak is strongest for the cubic phase and weakest for the monoclinic one. Looking at the imaginary part of the first peak of the amplitudes, one realizes that both experimental data sets are more similar to the ones calculated for the cubic structure as compared to the tetragonal structure.

Perturbed angular correlation (PAC) spectroscopy

PAC spectroscopy allows measurements of the electric quadrupole interaction between the nuclear quadrupole moment of a probe nucleus and the electric-field gradient caused by the surrounding charge distribution. Because of the r^{-3} dependence of the electric-field gradient, the dominant contribution to the quadrupole interaction comes from the nearest neighbor charges. PAC measurements therefore provided information on the local probe environment.

These measurements [6,7] were performed in the temperature range from 290 K to 1400 K. For these measurements, [181]Hf, a β-emitter with a half-life time of 45 d, produced by thermal neutron irradiation of [180]Hf, was used as nuclear probe. In the case of zirconia, the material was doped with ca. 2% Hf [6]. Zirconium and hafnium are chemically very similar, and their ionic radii are nearly equal. Therefore, doping zirconia with Hf^{4+} ions does not lead to a significant distortion of the lattice. For phase identification, the PAC spectra of the nanocrystalline compounds were compared to those of the coarse-grained material.

Perturbed angular correlation spectra, i.e. the modulation of the anisotropy $-A_{22}G_{22}(t)$ with time, reflect the symmetry and strength of the perturbing electrical quadrupole interaction. The electric quadrupole interaction of an axially symmetric lattice, as the tetragonal phase of ZrO_2, leads to a periodic modulation of $-A_{22}G_{22}(t)$. The monoclinic structure of ZrO_2 without axially symmetry results in a non-periodic modulation. In cubic symmetry, the quadrupole interaction vanishes leaving the angular correlation unperturbed. This leads to an un-modulated spectrum. Figure 3 displays PAC spectra of coarse-grained zirconia at different temperatures used as fingerprints for the identification of the different phases. The non-periodic and the periodic modulation of $-A_{22}G_{22}(t)$ at 290 K and 1383 K, respectively, characterize the monoclinic and the tetragonal phase, respectively. The spectrum measured at 2160 K represents the cubic phase of ZrO_2. The weak decrease of the function $-A_{22}G_{22}(t)$ with time is due to slight deviations from perfect cubic symmetry caused by lattice defects and impurities.

Figures 4 and 5 show the PAC spectra obtained on uncoated and coated zirconia nanoparticles at some characteristic temperatures. Obviously, the spectra obtained after neutron activation, both for the uncoated and the coated material, at room temperature have no similarities with any of the spectra for the coarse-grained material. They display the typical features of a broad frequency distribution of the quadrupole interaction reflecting a high degree of disorder. The nearest neighbors of the nuclear probes on Zr^{4+} sites are the O^{2-} anions. Therefore, the distribution of quadrupole interaction implies a random distribution of the anion
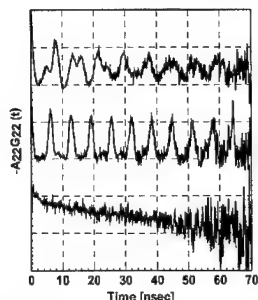
Figure 3: *PAC spectra of coarse-grained zirconia. a) monoclinic, b) tetragonal, c) cubic.*
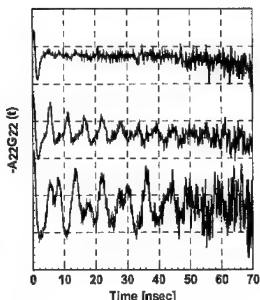
Figure 4: PAC spectra of nanocrystalline zirconia. a) 290 K, b) 600 K, 1300 K.
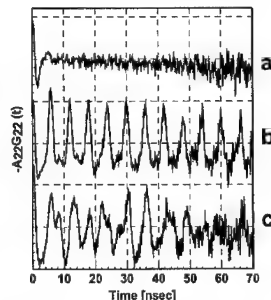
Figure 5: PAC spectra of nanocrystalline alumina coated zirconia. a) 290 K, b) 1200 K, 1300 K.

positions. As this phase exhibits – according to electron diffraction and EXAFS data – a cubic lattice, this phase is called "disturbed cubic phase". Heating the specimen, both, the coated and the uncoated ones, above 500 K, initiates the transformation to the tetragonal structure. At higher temperatures the two types of specimen behave differently. Uncoated nanocrystalline ZrO_2 starts to transform from the tetragonal to the monoclinic phase at about 800 K, whereas the coated specimen remains tetragonal up to 1200 K. At still higher temperatures the transformation of the coated material to the monoclinic phase is observed. According to the phase equilibrium, both specimens transform back to the tetragonal structure at 1400 K. Cooling both types of specimen from elevated to room temperature, the fraction of the tetragonal phase decreases forming the disturbed cubic one. The monoclinic phase does not undergo any phase transformation during cooling.

The room temperature PAC spectra obtained after neutron-activation of coated and uncoated nanocrystalline HfO_2, are also characterized by a broad distribution of quadrupole frequencies. Although electron diffraction reveals different lattice structures, monoclinic for the bare and cubic (or tetragonal) for the coated material, the quadrupole interaction parameters of this component are very similar for both types of specimen. With increasing temperature the broadly distributed component, dominating at room temperature, transforms to the monoclinic phase which can be identified from its quadrupole interaction parameters. In non-coated HfO_2 the monoclinic fraction grows more or less continuously with temperature, whereas in coated HfO_2 the transition of the disordered to the monoclinic phase is suppressed up to about 800 K. In the spectra of bare HfO_2 one finds no indication for the presence of the tetragonal phase. The data of coated HfO_2, however, are compatible with a small content of the tetragonal component in the range of 10-15 vol%. The preliminary data analysis suggests that upon cooling to room temperature, the monoclinic component in coated and non-coated HfO_2 transforms back to the disordered phase.

CONCLUSIONS

At a first glance, the results of the three methods to obtain structural information seem to be inconsistent in the view of classical crystallography and material sciences. To explain these

results, for zirconia the following model was developed: Based on the electron diffraction data and the narrow width of the first O^{2-} and the Zr^{4+} shell determined with EXAFS a nearly perfect cubic lattice of the cations is assumed. EXAFS measurements give a clear indication that the disturbed structure, observed in the as produced zirconia, has a cubic cation lattice. The distance between the two O^{2-} ion shells in the tetragonal structure is – in the ideal case –0.038 nm, whereas the width σ of the oxygen shell was determined to be $\pm$ 0.0076 nm. The distance of the two Zr^{4+} shells is to small to be used for comparison. Additionally, the comparison of the calculated distribution functions with the experimental ones gives a strong indication in this direction. Different experimental findings of Li et al. [12] that a strong third peak indicates the tetragonal structure may be misleading because the coarse-grained material used by these authors was doped in contrast to the nanoparticles described in this paper. The PAC data indicate a random distribution of the O^{2-} positions around the Zr^{4+} ions in the vicinity of their lattice positions. According to the EXAFS results, the O^{2-} shells have a very narrow radial distribution. Together, PAC and EXAFS observations provide evidence for a random distribution of O^{2-} ions in the vicinity of their lattice sites on the surface of a sphere.

The fact that the radial distribution of O^{2-} and the Zr^{4+} shells are broader in the case of cubic $ZrO_2(Y_2O_3)$ may be explained by the significant larger ionic radius of Y^3 as compared to Zr^{4+} and the O^{2-} vacancies caused by the Y doping. The transformation of the tetragonal zirconia to the monoclinic phase is retarded in the case of the coated nanocrystalline material. This can be explained easily by the volume expansion during this transformation. The coating acts as a mechanical confinement. The same delay for the transformation from disturbed phase occurring directly after synthesis to the monoclinic one is observed in the case of hafnia. In the case of zirconia, it was observed that the transformation from the distorted cubic phase to the tetragonal one is partially reversible. Similarly, monoclinic hafnia shows a partial back-transformation to the distorted phase.

REFERENCES

1. Massalski, T. B., Binary Alloy Phase Diagrams, ASM-International (1990)
2. Vollath, D., Sickafus, K. E., *Nanostr. Mater.*, **1**, 427 (1992)
3. Vollath, D., Szabó, D. V., *Nanostr. Mater.*, **4**, 927 (1994)
4. Frauenfelder, H., Steffen R. M., Alpha, Beta, and Gamma Spectroscopy. Amsterdam 1965
5. Catchen, G. L. *MRS Bull.*, **20** 37 (1995)
6. Forker, M., Schmidberger, J., Szabó, D. V., Vollath, D., *Phys. Rev. B*, **61**, 1014 (2000)
7. Vollath, D., Forker, M., Szabó, D. V., *Scripta Mater.*, (2001) (in press).
8. Ressler, T., *J. of Synchrotron Radiation*, **5**, 118 (1998)
9. Hagelstein, M., Moser, H. O. Vollath, D., Ferrero, C., Borowski, M. *J. of Synchrotron Radiation,*, accepted
10. Sayers, D. E., Bunker, B. A. in *X-Ray Absorption*, editors Konigsberger, D. C., Prins R,, John Wiley & Sons, New York (1988)
11. Mustre de Leon, J., Rehr, J. J., Zabinsky, S. I., Albers, R. C., *Phys. Rev. B*, **44**, 4146 (1991)
12. Li, P., Chen, L.-W., Penner-Hahn, J. E., *Phys. Rev. B*, **48**, 10063 (1993)

Clusters and Other Nanostructures

Atomic Scale Modelling of Supported and Assembled Nanoparticles

E.Zhurkin[1], M.Hou[2] , H.Van Swygenhoven[3], B.Pauwels[4], M.Yandouzi[4],
D.Schryvers[4], G.Van Tendeloo[4], P.Lievens[5], G.Verschoren[5], J.Kuriplach[6], S.Van Peteghem[7], D.Segers[7] and C.Dauwe[7]

[1] St.Petersbourg State Technical University, Department of experimental Nuclear Physics, Polytechnicheskaya 29, 195251, St.Petersbourg, Russia
[2] Physics of Irradiated Solids C.P.234, Free University of Brussels, B-1050 Brussels, Belgium
[3] Paul Scherrer Institute, Ch-5232 Villligen PSI , Switzerland
[4] EMAT, University of Antwerp, RUCA, Groenenborgerlaan 171, B-2020 Antwerp, Belgium
[5] Laboratory for Solid State Physics and Magnetism, Catholic University of Leuven, Celestijnenlaan 200 D, B-3001 Leuven, Belgium
[6] Department of Low temperature Physics, Charles University, V. Holesovickach 2, CZ-18000 Prague 8, Czech Republic
[7] NUMAT, Subatomic and Radiation Physics Department, Ghent University, Proeftuinstraat 86, B-9000 Ghent, Belgium

Abstract

The properties of elemental and bimetallic free, supported and assembled nanoclusters are modeled at the atomic scale and the models are discussed on the basis of experimental observations. This way, the memory of some free cluster properties in nanostructured materials may be evaluated.

The combination of molecular statics with High Resolution Transmission Electron Microscopy (HRTEM) allows to predict fine detail of the lattice relaxation of a truncated octahedral gold cluster deposited on MgO. Metropolis Monte Carlo (MC) predicts that a lattice mismatch may contribute to disordering in deposited Cu_3Au nanoclusters. In both Cu-Au and Ni-Al free clusters, offset of equilibrium stoichiometry may result in segregation of Au or Al at the cluster surface. An ordered stoichiometric core is surrounded by a disordered mantle where the excess species resides. Different modeling methods predict different nanometer scale textures. Therefore, cluster assembled Ni_3Al alloys formed by condensation and pressing are modeled in two different ways. Both make use of a combination of Molecular Dynamics and MC. Whatever the model nanostructure, the segregation properties of free clusters remain in the nanostructured material. This segregation is one possible cause that can inhibit the formation of a metastable martensitic phase as observed in bulk Ni-Al alloys.

The occurrence of vacancy clusters and voids is hardly identified by HRTEM. On the other hand, their distribution and sizes are sensitive to the nanostructure modeling. Therefore, a new characterization method is developed, which combines positron lifetime spectroscopy with the calculation of positron lifetimes from selected areas of the model samples.

1. Introduction

Cluster assembled systems represent an original class of nanostructured materials which properties are studied on atomic level atomic level both experimentally and by numerical

modeling. One of the major motivations in studying cluster assembled materials is to establish the relation between the nano-, meso- and macroscopic properties and those of the nanoclusters forming them, as primarily synthesized in free space. This broad question is narrowed and limited here to nanoscopic characterization. The systems considered have sizes ranging from 10^2 to 10^5 atoms, that is, covering three orders of magnitude.

Configurational and thermodynamic modeling of selected systems will allow to establish the relation between free and constraint clusters. The simplest constrain considered is the consequences of a lattice mismatch between elemental or bimetallic clusters and a substrate surface after Low Energy Cluster Beam Deposition (LECBD) [1]. Since nanoclustered films formed by LECBD are discussed elsewhere [2], we here focus on the systems which can be fabricated by means of condensation and pressing [3] or by fast quenching [4]. These are predicted to display fairly different nanoscale morphologies which may result in different mechanical properties. Bimetallic nanostructured alloys are used as a case study to emphasize thermodynamic properties in relation to those of free clusters.

Molecular dynamics (MD) and Metropolis Monte Carlo (MC) are natural methods for studying nanosize systems. A general review of these methods is given in [5]. In addition, in the present work, use is made of MD according to the scheme of Rahmann and Parinello [6] and MC sampling in the semi grand canonical ensemble according to the algorithm described in [7]. Second moment tight binding potentials are used, that are described in detail elsewhere [8].

II. Free, supported and assembled clusters

The initial configuration of a gold cluster on MgO for the MD simulation is deduced from the HREM observation after LECBD deposition [1] and the corresponding geometrical model is shown in Fig.1.
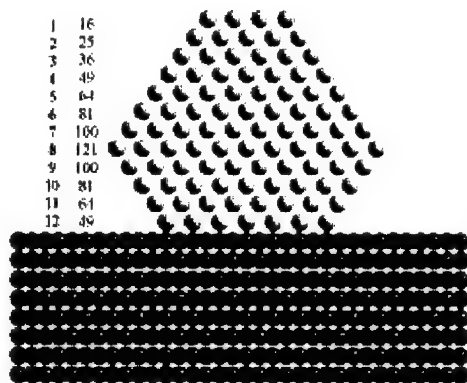
Figure 1 *Projection of a truncated octaedron delimited by {111} and {100}facets supported by a MgO(100) substrate. It represents the initial configuration of a* Au_{786}/MgO(100) *combination. The layer number is given in the first column and the number of atoms in each layer in the second column.*

At the cluster-substrate interface, as a first approximation, the Au-MgO interfacial gold atom positions are initially adjusted to exactly match the MgO (100) surface lattice. The strain at the interface is modeled by means of simple harmonic forces on the interfacial cluster atoms, characterized by a force constant k. At the Au-MgO interface, k is taken as a parameter which magnitude is around k_{bulk} $(3.84 \cdot 10^2$ J/m^2). Values between k=0 and k=2.0$\cdot 10^2$ J/m^2 are considered. The case k=0 corresponds to a free cluster with the same morphology. A comparison with k>0 will help us to understand the influence of the substrate on the strain internal to the cluster. The mean d_{220}, d_{200} equidistances parallel to the substrate surface are estimated layer by layer, as well as the spacing between these layers. Results are shown in Fig.2 for four force constant values. For the discussion, it is useful to section the cluster into two areas at layer 8 in fig.1 and represented by an arrow in fig.2. This partition is at the intersection between the {111} facets of the cluster. In the area close to the substrate, the lattice spacing is expanded with respect to the free cluster while it contracts in the other. This is the direct consequence of the MgO surface which lattice parameter is larger than bulk gold, shown as a horizontal line in Fig.2. The atomic spacing in the eighth layer is independent of k. The convergence of the results in the facets intersection obtained with constraints of different strengths shows that its stiffness is rather pronounced. As a consequence, it acts as the fulcrum of a lever: the increase of the equidistance on the one side, subsequent to the constraint imposed by the substrate, is balanced by their decrease on the other side. A close analysis shows that the deformation happens at constant volume, the change of the equidistance parallel to the substrate surface being balanced by a decrease in the lattice spacing normal to this surface.

The question now arises to know how a realistic strain may modify the cluster properties. This is discussed for the example of a Cu_3Au cluster, which core is predicted to be ordered in free space. We consider a distortion, as it could happen when the Cu_3Au cluster is deposited on a crystalline surface. Again, we select a morphology similar to that in fig.1, as observed by HRTEM for a cluster containing 454 atoms.
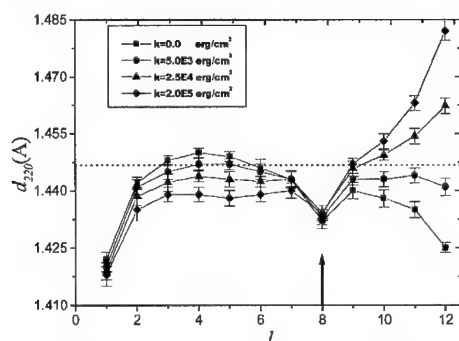
Figure 2. *Interatomic distance, layer by layer in the cluster, starting from the top layer in the cluster (see fig.1). The results are shown at 300K for four k-values. The dashed line represents the bulk Au value at 300K, as predicted by MD. The arrow shows the position of the fulcrum lever.*

The mismatch is particularly large at the Cu_3Au (001) / MgO (001) interface, and we now explore its consequence on the cluster structure and order. The same technique as above is used to model the interfacial strain, but the modeling is done at non-zero temperature by means of semi-grand canonical Metropolis Monte Carlo. The effect of the interface distortion is found to decrease the stability of the $L1_2$ phase in the core. The segregation state in the surrounding mantle is not significantly affected. The cluster disorders continuously as k is increased, which demonstrates that external constrains may contribute to disordering in the cluster. Other factors determine disorder, which are discussed in [1].

The question addressed so far, namely, the sensitivity of free cluster properties to an external constraint is of course most relevant to nanostructured materials. It was already shown for Au clusters deposited on gold [2] that the deposition energy in LECBD is a critical factor in determining the nanostructure. It was also shown in [9] that different nanostructures may induce totally different macroscopic mechanical properties. Here, we focus on two different ones, as they could be obtained either by condensation and pressing, or by fast quenching. The Ni-Al system is considered therefore, where no order disorder transition is known in the bulk system, but surface segregation is expectable.

Free Ni-Al clusters have the same stable phases as the bulk material, namely $L1_2$ and B2 [7]. A distinction however appears between the core and the surrounding disordered mantle in case of deviations from overall ideal stoichiometries. No disordered mantle is found in elemental clusters. The bimetallic core then keeps stoichiometric while the mantle may be subjected to Al segregation. On the one hand, at a given overall chemical potential difference, aluminium segregation decreases with increasing cluster size while on the other, provided more than one thousand atoms form the cluster, the relative thickness of the mantle is not significantly size dependent. Finally, because of this partition between the ideal core and the surrounding mantle in which aluminium may accumulate, no metastable martensitic phase is predicted in the core. The possible occurrence of a critical size for the austensitic/martensitic phase transition is plausible and its discussion is planned for further work.

We now address the question to know whether these properties remain once clusters are assembled.

The nanostrucure of materials depends on their synthesis method and these methods can be modelled. We consider two of them.

The first synthesis model is applied to the Ni_3Al alloy. It consists in simulating the growth of perfect Ni_3Al grains around 15 randomly located and oriented seeds in a limited box with periodic boundary conditions. The grains are grown until the whole space in the box is filled. The sample thus contains 15 grains of different sizes, orientations and morphologies. In the present case, they contain from 3500 to 10000 atoms. This initial sample is compressed by an external pressure of 2GPa by means of the Rahman Parinello MD technique. Interface segregation is than modelled by MC for two different values of the chemical potential difference, corresponding to the $L1_2$ stable phase and the largest possible offset from stoichiometry allowing the phase to remain stable. In all that follows we shall refer to this sample as "SF (Space Filling) sample". The second sample is simulated by assembling free Ni-Al clusters with the same size distribution as for the previous one. First, we simulate the 15 clusters, each in two thermodynamic equilibrium states determined by the same values of the chemical potential difference as for the SF sample. The procedure is repeated for clusters with a B2 core arrangement. They are then pressed by MD in the same conditions as above. In this pressure

range (2 GPa), because of the occurrence of large holes between assembled clusters, the density is a sharply increasing function of pressure.

In what follows, we shall refer to these samples as "CA (Cluster Assembled) samples". The SF and CA model samples are shown in fig. 3. The nanostructures obtained are clearly different. After relaxation of the CA and SF samples at 0K and zero pressure, the equilibrium atomic density relative to a bulk single crystal is 91% and 85.7 % for the CA and SF samples respectively.

No excess Al is found in the core while segregation in the interfaces may be substantial. For a given chemical potential difference value, the segregation state is found similar for isolated clusters, CA and SF samples. The maximal excess Al ranges about 30-40 percent at room temperature and zero external pressure. This indicates that the segregation state of the nanostructured Ni-Al alloys is not very sensitive to the synthesis method and is primarily determined by the thermodynamic conditions.

Since, in contrast with segregation, the mechanical properties of nanostructured metals are predicted to be most nanostructure dependent [9], it is worthwhile to check the above model predictions experimentally, in order to insure an accurate knowledge of the nanostructures. A specific non destructive technique is designed therefore, based on positron annihilation spectroscopy. Positron lifetimes are calculated for trapping in vacancy clusters of various sizes and also from selected areas of the modelled samples (shown in fig. 3.). This allows for a comparison between models and real undamaged samples. The method and first results are described in this proceedings [10].
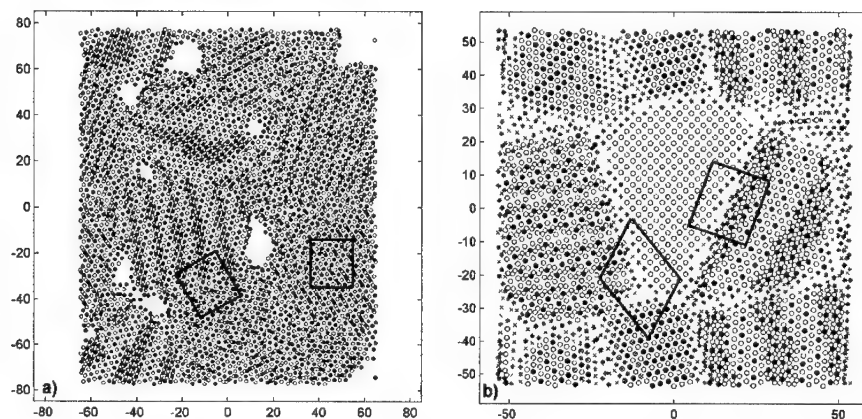
Figure 3: *Slabs in NiAl CA (a) and Ni_3Al SF (b) model samples after MD relaxation and MC sampling at 300K in order to account for Al segregation. Open circles represent Ni atoms and black circles represent Al atoms (in (b) '*' and 'x' represent Ni and Al atoms, respectively, with the coordination number not equal to 12). The Al segregation at grain boundaries and at internal void surfaces is visible. The numbers on axes are in units of Å.*

III. Conclusion

Nanoclusters and nanostructured materials are studied at the atomic scale among various situations. The analysis converges toward general rules applying to all cases studied.
Free bimetallic clusters may be subjected to pronounced surface segregation, which may prevent the formation of metastable phases observed in bulk materials. Lattice mismatch with a substrate induces overall cluster distortions, which may strongly affect the structural properties of deposited clusters.
When clusters are assembled to form nanostructured materials, their structural and mechanical characteristics are strongly affected by the assembling conditions. Segregation, however, depends on the cluster size but is not quite sensitive to assembling induced constrains.

References

1. B. Pauwels, G. Van Tendeloo, W. Bouwen, L. Theil Kuhn, P. Lievens, H. Lei and M. Hou; Phys. Rev. **B62**, 15 (2000) 10383. B. Pauwels, G. Van Tendeloo, E.E. Zhurkin, M. Hou, G. Verschoren, L. Theil Kuhn, W. Bouwen and P. Lievens; submitted for publication.
2. Q. Hou, M. Hou, L. Bardotti, B. Prével, P. Mélinon and A. Perez; Phys. Rev. **B62**, 4 (2000) 2825; L. Bardotti, B. Prével, P. Mélinon, A. Pérez, Q. Hou and M. Hou; Phys. Rev. **B62**, 4 (2000) 2835
3. H. Gleiter, Prog. Mater. Sci, **33** (1989) 223
4. see *e.g.* A.S. Edelstein, R.C. Cammarata in "Nanomaterials: Synthesis, properties and Applications" (Inst. of Physics Publ., Bristol and Philadelphia, 1996)
5. see *e.g.* D. Frenkel and B. Smit; "Understanding Molecular Simulation" (Academic Press, San Diego, 1996)
6. M. Parinello and A. Rahman; J. Appl. Phys., **52** (1981) 7182
7. E.E. Zhurkin and M. Hou; J. of Physics **C12** (2000) 6735
8. G.J. Acjland and V. Vitek; Phys. Rev. **B41** (1990) 10324; F. Gao, D. Bacon and G.J. Ackland; Phil. Mag. **A67** (1993) 275
9. Q. Hou, J-M. Cayphas and M. Hou; *in* "Advances in mechanical behaviour, plasticity and damage", ed. By D. Miannay, P. Costa, D. François and A. Pineau (Elsevier, Amsterdam, 2000) 287.
10. J. Kuriplach *et. al.* this conference; S. Van Peteghem *et. al*; this conference

Atomic Scale Characterization of Supported and Assembled Nanoparticles

B. Pauwels, M. Yandouzi, D. Schryvers, G. Van Tendeloo, G. Verschoren[1], P. Lievens[1], M. Hou[2] and H. Van Swygenhoven[3]

EMAT, University of Antwerp (RUCA), Groenenborgerlaan 171, B-2020 Antwerp, Belgium.
[1] Laboratory of Solid State Physics and Magnetism, Catholic University of Leuven, Celestijnenlaan 200D, B-3001 Leuven, Belgium.
[2] Physics of Irradiated Solids-C.P. 234, Free University of Brussels, B-1050 Brussels, Belgium.
[3] Paul Scherrer Institute, Ch-5232 Villigen PSI, Switzerland.

ABSTRACT

Different structural configurations of nanoparticles have been investigated by advanced transmission electron microscopy (TEM) techniques. The cluster-surface interaction of Au clusters, produced in a laser vaporization source and deposited with low energy on MgO cubes, is investigated by high-resolution transmission electron microscopy (HRTEM). A dilation of the Au lattice that perfectly accommodates the misfit with the MgO lattice is measured and modeled with Molecular Dynamics (MD). To study the chemical ordering in bimetallic clusters, Au-Cu alloy clusters with different stoichiometries are produced and deposited in the same way as the Au clusters. Electron diffraction (ED) ring patterns obtained from these alloy clusters lying on amorphous carbon, are indexed as face-centered cubic, which is confirmed by HRTEM. This indicates that clusters of Au-Cu alloys are solid solutions, i.e. no ordering takes place in these clusters. Assembled nanoclusters of Ni_3Al, produced by the inert gas condensation (IGC) technique and pressed under high pressure (2 GPa), are investigated by HRTEM. These studies indicate that nanocrystalline Ni_3Al consists of small crystallites of random crystallographic orientations separated by grain boundaries, with the presence of several nanoscaled voids. From the selected area electron diffraction (SAED) ring pattern, an incomplete $L1_2$ ordering is concluded.

INTRODUCTION

In the past, materials research mainly focused on single crystal or microstructured bulk materials and thin films in order to understand and model their behavior under different external conditions. Recently a lot of attention, both from theoretical and from applied points of view, is devoted to nanoparticles and nanocrystalline materials (NCMs), i.e. polycrystalline materials with grain sizes in the nanometer range.

Nanosized clusters, deposited on a surface, can be regarded as building blocks for nanostructures and nanostructured materials. To obtain insight in the physical properties of such nanosystems, it is necessary to understand the physical and chemical properties of individual clusters as well as of the assembled configurations.

In bimetallic clusters, processes like segregation, chemical ordering and crystal structure are of importance in many applications. With HRTEM and ED, not only the morphology and the crystal structure of clusters can be determined, but also the epitaxial relation and possible lattice dilations due to a lattice mismatch between clusters and substrate can be derived. The nanostructural features of importance in assembled materials include the lattice structure, the grain size distribution and morphology, the nature of grain boundaries and interfaces and the existence of voids.

The most reliable results are obtained by a combination of experimental and theoretical techniques. This contribution describes the experimental results obtained with TEM. These results are compared with data obtained by MD and Monte Carlo (MC) simulations [1].

METHODS

Pure Au clusters and alloyed Au-Cu clusters are fabricated in a laser vaporization source using targets of the respective composition [2]. The free clusters are deposited at room temperature by low energy cluster beam deposition (LECBD) [3] on amorphous carbon and MgO cubes, simultaneously. The low cluster kinetic energy ($E_{kin} < 1$ eV/atom) prevents fragmentation of the clusters and minimizes the interaction with the substrate upon impact.

The nanocrystalline Ni_3Al samples were produced by the inert-gas condensation (IGC) technique [4]. Polycrystalline Ni_3Al (75 at. % Ni) is thermally evaporated from a tungsten boat in a 10^{-6} Pa pressure vacuum system filled with 100 Pa of 99.999% pure He gas. After re-evacuation to the initial pressure of 10^{-6} Pa, pressing at a pressure of 2 GPa at room temperature consolidates the powder. The samples are disk-shaped with a diameter of 8 mm and a thickness of 200-300 μm. These nanocrystalline materials are sliced and punched into 3 mm TEM discs. Thin foils transparent for the electron beam are prepared by ion-milling using Ar^- ions.

Diffraction experiments are performed with a Philips CM20 microscope (200 keV). HRTEM images are obtained with a JEOL 4000 EX and are carried out at low electron beam irradiation density (17 pA/cm^2) to avoid structural changes and reorientations of the small clusters. The local composition of the Ni_3Al grains is measured by energy dispersive X-ray analysis (EDX) using a Si(Li) detector in a Link QX-2000 system. Precise measurements of the lattices of Au and MgO are obtained using the DaLi program (Digital Analysis of Lattice Images) [5]. Simulations of HRTEM images are obtained using the EMS program [6].

RESULTS

Au clusters

The morphology of pure Au clusters deposited on (001) MgO is determined by projections of the clusters parallel to the Au/MgO interface (cross section) in two different orientations: <011> and <001>. In the <011> zone axis, also observations perpendicular to the interface (i.e. top view) helped to determine the morphology. Figure 1a shows a 2.5 nm cluster in cross section in the [011] orientation. The profile of the particle is limited by 4 <112> directions and 2 <011> directions. This indicates that the cluster has an octahedral shape and is asymmetrically truncated at the top and the interface. HRTEM images taken in the <001> orientation also show truncations at the corners of the Au octahedrons. Smaller clusters (around 1 nm) are half octahedron shaped. The epitaxial relation between Au clusters and MgO could be derived from the HRTEM-images as $(001)_{MgO}$ // $(001)_{Au}$ and $[100]_{MgO}$ // $[100]_{Au}$.

Figure 1b shows the (220) lattice distances of a Au cluster and the MgO substrate as observed in the [011] orientation. From this graph, it is clearly seen that the interface between Au and MgO is located between the layers 11 and 12. The (220) distances in the Au layers close to the interface decrease from 1.472 ± 0.013 Å (in layer 11) to 1.451 ± 0.010 Å (in layer 9). For the layers above (n<9) it reaches the bulk value of Au, i.e. 1.442 Å. The dilations of the (220) lattice in layers 1 and 2, layers close to the top of the particle, are delocalization effects of the microscope image and are also observed in other studies of metal clusters [7]. The same behavior as shown in figure 1b is also seen for clusters in the <001> orientation. Here the d_{200} distance
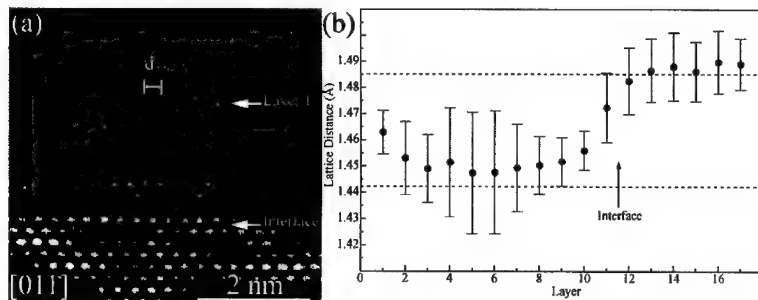
Figure 1. (a) HRTEM image of a Au cluster deposited on MgO. (b) Graph of the 220 distances through the cluster shown in (a). The accommodation in the cluster is clearly seen. Layer 1 and the interface are both indicated on the photo and on the graph.

accommodates to the MgO substrate [8]. These lattice dilations are modeled by MD and a good agreement between experiment and model is found [1, 8].

Au-Cu clusters

The diffraction patterns of the different Au-Cu alloy clusters deposited on amorphous carbon can all be indexed as face-centered cubic; only the lattice parameter differs for the three materials: 3.87 Å (Au_3Cu), 3.82 Å (CuAu) and 3.76 Å (Cu_3Au), respectively (see figure 2). For these three materials, no evidence for a chemical ordering of Au and Cu atoms is found in the diffraction data.

The lattice parameter of Au-Cu alloy clusters apparently diminishes with increasing Cu-content in the same way as the bulk lattice parameter does. Since also the magnitude of the lattice parameters fits, it is therefore assumed that the chemical composition of the clusters corresponds to the chemical composition of the target material in the source. We can thus state that with laser vaporization of an alloy target material, clusters of the same overall chemical composition are formed. The fact that the overall concentration of both elements in the clusters, deposited by LECBD, corresponds to the concentration of the elements of the target material was already observed for other bimetallic clusters (see e.g. [9]).

Neither by HRTEM nor in the corresponding fast Fourier transforms (FFTs), any evidence is found for a chemical ordering between Au and Cu. Simulations of HRTEM images indicate that the superstructure should be visible when ordering is taken into account in the
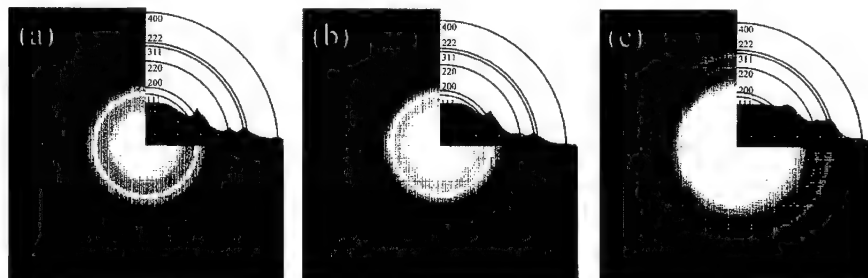
Figure 2. Diffraction ring patterns of Au_3Cu (a), CuAu (b) and Cu_3Au (c) clusters. The rotational average of the diffraction pattern is shown.

model. None of the HRTEM images taken from clusters -deposited on amorphous carbon or on MgO- of Au_3Cu, CuAu or Cu_3Au show any superstructure in the <200> or <022> directions, which should occur in case of chemical ordering. In the FFTs, the chemical ordering would give rise to extra reflections as e.g. 100 and 011, which are extinct in an fcc diffraction pattern. All the FFTs give evidence of a regular <011> face-centered cubic crystal (see figure 3). For clusters deposited on (001) MgO, the same morphologies and epitaxial relation as for the pure Au clusters were found.

Ni-Al assembled material

The Bright Field (BF) image of figure 4a shows the polycrystalline arrangement in the Ni_3Al nanocrystalline sample. The bright areas are voids with sizes less than 5 nm in diameter (black arrows in figure 4a). A majority of grains have a size ranging between 8 and 14 nm. In the corresponding SAED ring pattern (figure 4b) the diffracted intensity along the rings is very homogeneous indicating a random orientation of the grains, i.e., no texturing is observed. According to the phase diagram, room temperature bulk Ni-rich Ni-Al materials with a Ni content of 72-76 at.% are expected to consist exclusively of the Ni_3Al $L1_2$ phase [10]. As seen from the schematic representation of the $L1_2$ powder electron diffraction simulation in figure 4c the present ring pattern can be indexed as 'fcc based' (h,k,l all even or odd). Note that the intensity of the visible superstructure rings existing in these SAED patterns [e. g., (210) and (211)] is very weak, indicating that the $L1_2$ structure is not totally chemically ordered. From the SAED pattern a lattice parameter of the Ni_3Al nanostructure was measured as (3.60 ± 0.05) Å which is compatible with the bulk value. EDX measurements at different locations of the sample reveal an average composition of 74 ± 2 at.% Ni.

The above results are confirmed by HRTEM. A lower magnification HRTEM image (figure 5a) shows the nanostructure containing a number of nanometer-sized crystallites (C) and grain boundaries (I). Note also the presence of some small amorphous areas (A). High-resolution images of some nanocrystalline grains along different zone axes confirm the $L1_2$-structure and the local lattice parameters measured are in agreement with the SAED pattern measurements. In many cases sharp interfaces, which can be coherent, incoherent or semicoherent, as well as triple points were detected.

In figure 5b, a HRTEM image of a grain boundary between two $L1_2$ grains (C1 & C2) is shown, together with the respective image simulations. Both grains are viewed close to their respective [110] zones, although grain C2 is slightly tilted yielding lattice fringes, rather than a dot pattern as in C1. The present grain boundary can be considered as a high angle grain boundary, close to the (111) $L1_2$ plane. Due to the small misorientation a single interface
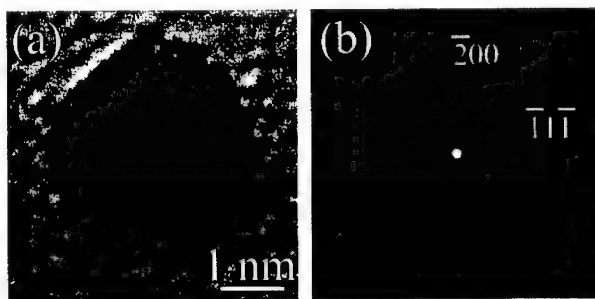
Figure 3. *HREM image of a AuCu cubo-octahedron in <011> zone axis orientation (a) and the FFT (b).*
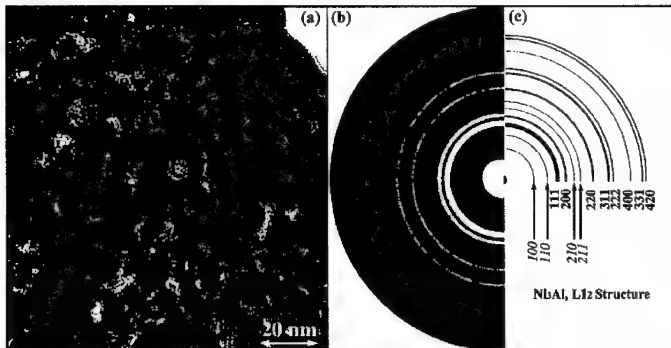
Figure 4. (a) BF image of Ni3Al (NCMs) (b) corresponding SAED pattern revealing a L12 microstructure and (c) schematic representation indicating that the L12 structure is not totally chemically ordered.

dislocation is observed (see figure 5b). Inside the grains generally only few dislocations are observed. Another apparent feature in the observations is the presence of amorphous regions in between the nanocrystalline grains. The existence of nanoscale voids can be related to the compaction technique, but the origin of the filling is unclear. The compaction could lead to amorphization of contacting particle surfaces, or the free surfaces could be amorphizised by the ion-milling treatment [11]. These findings are compared with positron lifetime annihilation measurements on the same materials [12, 13].

CONCLUSIONS

It is concluded that all Au clusters deposited on MgO are single crystals exhibiting the fcc structure. From cross section and plan view images, it is determined that clusters with a size of 2 nm have a truncated octahedral shape. For smaller particles (1 nm) a truncated half-octahedral shape is observed. These morphologies are only limited by {111} and {001} faces, which are energetically the most stable ones. From the HRTEM images of clusters in <001> and <011> orientations the epitaxial relation is determined as $(001)_{MgO} // (001)_{Au}$ and $[100]_{MgO} // [100]_{Au}$.
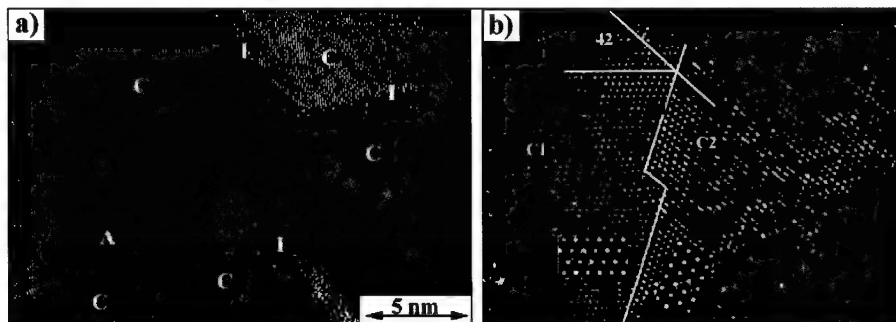
Figure 5. (a) HRTEM image of a Nanocrystalline Ni_3Al sample containing a number of nanometer-sized crystallites (C), amorphous areas (A) and grain boundaries (I). (b) HRTEM image of a high angle grain boundary.

From precise measurement of the (220) lattice distances in the deposited clusters, it is concluded that near the interface between Au and MgO, the Au lattice dilates in the first two or three contact layers to adapt to the lattice of MgO.

These conclusions about morphology and epitaxial relation also hold for Au-Cu clusters of different stoichiometry. Both from diffraction data as well as from HRTEM images and their corresponding FFTs it is concluded that for Au-Cu clusters deposited at room temperature on amorphous carbon as well as on crystalline MgO, the crystal structure is disordered fcc which contrasts with phase diagram predictions for the corresponding bulk material.

The assembled Ni_3Al nanocrystalline material reveals incomplete $L1_2$ ordering inside the clusters, nanosized voids in between different clusters and a variety of grain boundary structures.

ACKNOWLEDGEMENTS

REFERENCES

1. E. Zhurkin, M. Hou, H. Van Swygenhoven, B. Pauwels, M. Yandouzi, D. Schryvers, G. Van Tendeloo, P. Lievens, G. Verschoren, J. Kuriplach, S. Van Peteghem, D. Segers and C. Dauwe, MRS fall meeting (2000), Symposium B8.2.
2. W. Bouwen, P. Thoen, F. Vanhoutte, S. Bouckaert, F. Despa, H. Weidele, R.E. Silverans, and P. Lievens, Rev. Sci. Instrum., **71**, 54-58 (2000).
3. W. Bouwen, E. Kunnen, K. Temst, M.J. van Bael, F. Vanhoutte, H. Weidele, P. Lievens, and R.E. Silverans, Thin Solid Films, **354**, 87-92 (1999).
4   P. G. Sanders, G. E. Fougere, L.J. Thompson, J. A. Eastman and J. R. Weertman, Nanostruct. Mater., **8**, 243- 252 (1997).
5. A. Rosenauer and D. Gerthsen, Advances in Imaging and Electron Physics, **107**, 121-230 (1999).
6. P.A. Stadelman, Ultramicroscopy, **21**, 131-145 (1987).
7. S. Giorgio, C. Chapon, C.R. Henry, and G. Nihoul, Phil. Mag. B, **67**, 773-785 (1993).
8. B. Pauwels, G. Van Tendeloo, W. Bouwen, L. Theil Kuhn, P. Lievens, H. Lei, and M. Hou, Phys. Rev. B, **62**, 10383-10393 (2000).
9. J.L. Rousset, A.M. Cadrot, F.J. Cadete Santos Aires, A.J. Renouprez, P. Mélinon, A. Perez, M. Pellarin, J.L. Vialle, and M. Broyer, J. Chem. Phys, **102**, 8574-8585 (1995).
10. M. F. Singleton, J. Murray and P. Nash, in *Binary alloy phase diagrams*, edited by T. B. Massalski (American Society for Metals, 1986) p. 140.
11. C. Suryanarayana, Int. Mat. Rev., **40**, 41-64 (1995)
12. M. Yandouzi, D. Schryvers, J. Kuriplach, S. Van Petegem, D. Segers, A. L. Morales, C. Dauwe, E. E. Zhurkin, M. Hou, H. Van Swygenhoven and G. Van Tendeloo, to be published.
13. S. Van Petegem, D. Segers, C. Dauwe, F. Dalla Torre, H. Van Swygenhoven, M. Yandouzi, D. Schryvers, G. Van Tendeloo, J. Kuriplach, M. Hou, E.E. Zhurkin, MRS fall meeting (2000), Symposium B3.9.

Simulation of Surface Morphology and Defect Structure
in Copper Nanoparticles

Yoshiaki Kogure and Masao Doyama
Teikyo University of Science & Technology
Uenohara, Yamanashi 409-0193, Japan

ABSTRACT

Molecular dynamics simulation for the morphology and the defect structure in nanoparticles has been performed. The nanoparticles are consisted of 1300 – 5000 atoms and the EAM potential developed by the present authors is adopted to calculate the interactions between atoms. The atom consisting the surfaces or defects are selected thorough the potential energy of individual atoms and structure is investigated by calculating the local crystalline order. A relation between the cooling rate and the particle morphology is also investigated.

INTRODUCTION

The nanoparticles or fine particles are known to have peculiar properties due to confined volume and large surface effects. The quantum mechanical energy level intervals in electronic and phonon states are larger than bulk materials due to strongly confined spaces, then the thermal, the mechanical, the electric, and the magnetic properties are different from the bulk materials. These characteristic properties of nanoparticles have large potentiality for the industrial materials. On the other hand, the confined system is suitable to the molecular dynamics simulation studies, because the number of atoms are manageable by a computer and the results can be compared with experiment. Structure and atomistic processes during the nanoparticle formation is simulated in this paper.

METHOD OF SIMULATION

The embedded atom method (EAM) potential can express the many body interaction of atoms in metals and the potential is suitable for the simulation of the surface and the defects [1,2]. The EAM potential functions developed by the present authors are used in the present study [3]. The potential function was characterized on the point of anharmonicity and defect energy [4]. The potential has been adopted in the molecular dynamics simulations [5].
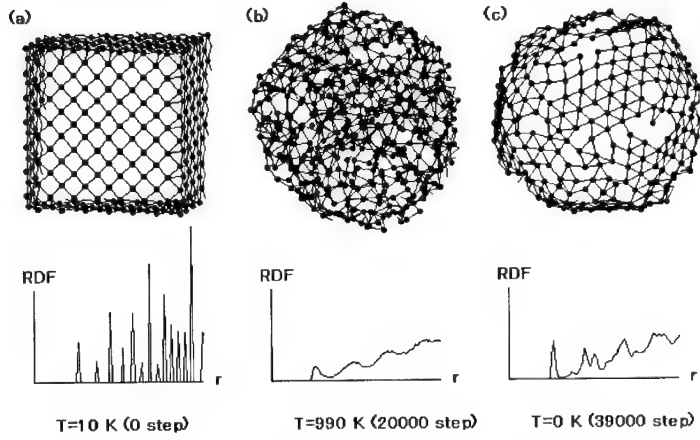
Figure 1. Formation of nanoparticles. Shape of outer surface and the radial distribution function at 0, 20000 and 39000 MD step are shown.

. The potential energy of *i*-th atom is expressed as

$$E_i = F(\rho) + \sum_j \phi(r_{ij}),\qquad (1)$$

where, $F(\rho)$ is the embedding energy, ρ the electron density, and r_{ij} the distance between *i*-th and *j*-th atoms and the function $F(\rho)$ is expressed as

$$F(\rho) = D\rho \log \rho, \quad \rho = \sum_j f(r_{ij})\qquad (2)$$

Functions $f(r_{ij})$ and $\phi(r_{ij})$ are

$$f(r_{ij}) = A(r_c - r)^2 \exp(-cr_{ij}),\qquad (3)$$

$$\phi(r_{ij}) = B(r_c - r)^2 \exp(-c_2 r_{ij}).\qquad (4)$$

The potential functions contains five parameters (A, B, C_1, C_2, D) and these are determined by fitting the potential functions to the experimental values of the cohesive energy, the elastic constants and the vacancy formation energy in copper crystal

As an initial condition $1000 - 5000$ atoms are arranged in fcc structure. Then the particle velocity of individual atom is gradually increased until the corresponding temperature becomes 1800 K, where the model crystals are in liquid state. After that the
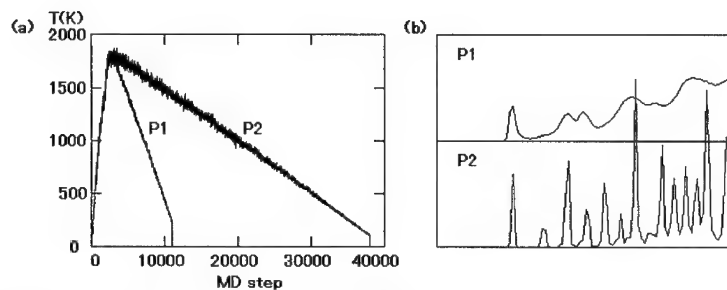
Figure 2. (a) Temperature change in particle formation for two cooling modes (P1 and P2) . (b) RDF of the particles formed by different cooling mode.
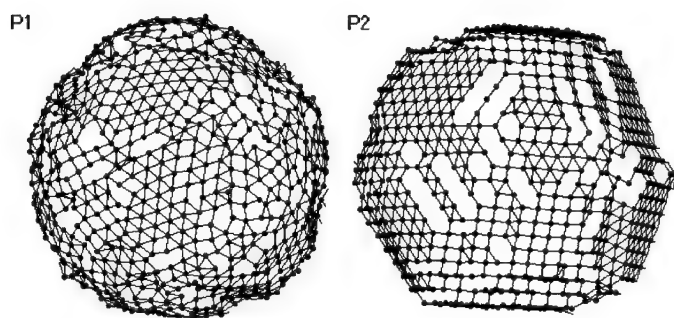
Figure 3. Surface morphology of nanoparticles formed by different cooling rate.

system temperature is gradually decreased by removing the atomic velocity and the systems are solidified. The time interval of molecular dynamics simulation is

chosen as $\Delta t = 2.0 \times 10^{-15}$ sec. An example of the process to form a nanoparticle

consisted of 1372 atoms is shown in figure 1. Where the atoms consisting the particle surface are selected by the potential energy. As the coordination number of atoms at the surface is small, the potential energy is large. The radial distribution functions (RDF) of atoms in the particle are also shown in the figure. RDF for (a) 0 and (b) 20000 MD step shows characteristic nature of crystal and liquid state. At the final state (figure1 (c)) the particle shows crystal-like characters.

RESULTS AND DISCUSSION

The structure and the morphology are found strongly to depend on the cooling process. The nanoparticles of 5324 atoms are produced by two cooling mode. They are
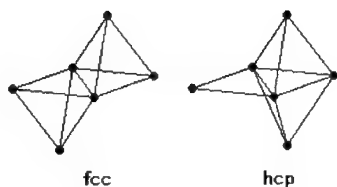
Figure 4. Elementary configuration for local crystalline order.
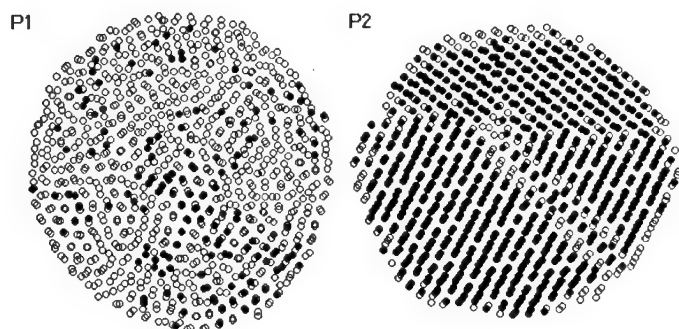
Figure 5. Cross sectional view of particle P1 and P2. Solid circles show the atoms of fcc structure and open circles show the atoms of other local crystalline structures.

labeled P1 and P2, which correspond to fast and slow cooling, respectively. The temperature change of these processes are shown in figure 2 (a). The cooling rate of P1 is about four times of P2 particle. The radial distribution functions of these particles at final state are shown in figure 2 (b). The RDF of P2 shows sharp peaks and these are characteristic to the crystal, whereas the peaks in P1 particle is rather broad and seems to be amorphous state. The sprit second peak is commonly observed in amorphous materials. The surface morphologies of these particles are also shown in figure 3. It is seen that most of faces are [111] crystal surfaces and particle P2 is surrounded by flat surfaces and forming a polyhedron. The surface energy by the present potential is calculated. Results are -3.0689 eV/atom for [111], -3.0057 eV/atom for [100], -2.8117 eV/atom for [110] surfaces. Namely [111] surface has lowest energy in these 3 surfaces. A part of surfaces on particle P2 in figure 3 shows [100] configuration, which. has secondly lowest energy. The nanoparticles of the shape of polyhedron of [111] and [100] surfaces are experimentally observed in gold.

Table I. Number of atoms of fcc, hcp and other structure in particle P1 and P2.

Particle	fcc	hcp	others	total
P1	829	1094	3401	5324
P2	4045	340	939	5324

The mean potential energy in the initial crystal is −3.3791 eV/atom, which is higer than the cohesive energy −3.5433 eV/atom due to the [100] surface energy. After the heat treatment, quickly cooled particle P1 has the mean potential energy −3.3434 eV/atom, and slowly cooled particle P2 has a energy −3.3901 eV/atom. The particle P2 has a lower energy than initial state, because the most of the [100] surfaces are changed to [111] after the heat treatment. The energy of P1 is rather larger than the initial state. This may be due to quenching of liquid state and the particle contains large number of imperfections.

To investigate the crystal structure of internal particles, the local crystalline order is calculated. The elementary configuration for fcc and hcp structure is shown in figure 4. For an atom in the particle, relative positions of five nearest neighbor atoms are investigated, and local crystalline order is determined, which distinguish the fcc and the hcp structures from others. The intersectional view of the two particle is shown in figure 5, where atoms belong to fcc structure is shown by solid circle and the atoms of other structure is shown by open circles. It can be seen that P2 particle is consisted of several fcc crystal grains. The disordered atomic configuration is observed in grain boundaries. No periodic structure is seen in the particle P1. The calculated number of atoms, which belong to fcc, hcp or other structure are summarized in the table I. Most of atoms are classified to the fcc structure in P2 particles, whereas most of atoms are not in fcc or hcp structures in P1 particles. Judging from surface morphology, RDF and the local crystalline order, particle P2 may be intermediate between amorphous or partially crystallized state .

CONCLUSION

A molecular dynamics simulation for the structure and the surface morphology of copper nanoparticles has been performed. An EAM potential shown by equations (1)-(4) is successfully applied in the simulation. The morphology of the particles are strongly influenced by the cooling rate. Slowly cooled particles are well crystallized, and rapidly cooled particles are intermediate between amorphous and crystal state. A simulation for the dynamics of atoms in the particles is a future subject.

REFERENCES

1. M.S. Daw and M.I. Baskes, Phys. Rev. B **29**, 6443 (1984)
2. M.W. Finnis and J.E. Sinclair, Philos. Mag. A **50**, 45 (1984)
3. M. Doyama and Y. Kogure, Radiation Efects and Defect in Solids **142**, 107 (1997)
4. Y. Kogure and M. Doyama, in *Tight-Binding Approach to Computational Materials Science*, edited by P.E.A. Turchi, A. Gonis and L. Colombo, (Materials Res. Soc. Symposium Proc. **491**, Warrendale, PA, 1998) pp. 359-364.
5. Y. Kogure and M. Doyama, in *Bulk Metallic Glasses*, edited by W.L. Johnson, A. Inoue and C.T. Liu, (Materials Res. Soc. Symposium Proc. **554**, Warrendale, PA, 1999) pp. 37-42.

Achieving Superplasticity and Superplastic Forming through Severe Plastic Deformation

Minoru Furukawa[1], Zenji Horita[2] and Terence G. Langdon[3]
[1]Department of Technology, Fukuoka University of Education,
Munakata, Fukuoka 811-4192, Japan
[2]Department of Materials Science and Engineering, Faculty of Engineering,
Kyushu University, Fukuoka 812-8581, Japan
[3]Departments of Aerospace & Mechanical Engineering and Materials Science,
University of Southern California, Los Angeles, CA 90089-1453, U.S.A.

ABSTRACT

The application of severe plastic deformation to metals provides a convenient procedure for achieving nanometer and submicrometer microstructures. Several different processing methods are available but Equal-Channel Angular Pressing (ECAP) is especially attractive because it provides an opportunity for preparing relatively large bulk samples. This paper describes the use of ECAP in preparing materials with ultrafine grain sizes and the subsequent properties of these materials at elevated temperatures. It is demonstrated that, provided precipitates are present to retain these small grain sizes at the high temperatures where diffusion is reasonably rapid, it is possible to achieve remarkably high superplastic elongations in the as-pressed materials and there is a potential for making use of this processing procedure to develop a superplastic forming capability at very rapid strain rates.

INTRODUCTION

Superplasticity refers to the ability of some crystalline materials to exhibit very high strains when pulled in tension [1]. In general, two significant conditions must be fulfilled in order to achieve superplastic elongations. First, since flow occurs through a diffusion-controlled mechanism, it is necessary that the testing temperature is sufficiently high that diffusion occurs reasonably rapidly. This generally means that the temperature must be of the order of at least $\sim 0.5 \, T_m$, where T_m is the melting temperature of the material in degrees Kelvin. Second, the dominant flow mechanism in superplasticity is grain boundary sliding [2] and this requires that the grain size is very small and, typically, not larger than $\sim 10 \, \mu m$. When both of these conditions are met, there is a potential for making use of these materials in developing a superplastic forming capability.

The superplastic forming of aluminum sheet metals is now well established for the fabrication of complex parts for a wide range of applications including in the aerospace, automotive, electronic and architectural industries [3,4]. Nevertheless, any further development and expansion of the superplastic forming technology has been limited by the relatively slow strain rates associated with the forming process. For example, the production forming rates of conventional aluminum sheet metals are typically within the range of $\sim 10^{-3} - 10^{-2} \, s^{-1}$ so that the forming times are generally of the order of $\sim 20 - 30$ minutes for the fabrication of each individual component. Since grain boundary sliding is the dominant flow mechanism in superplasticity, and theory suggests the rate of sliding varies inversely with the grain size of the material raised to a power of ~ 2 [5,6], it follows that it may be possible to displace the

superplastic regime to faster strain rates by making a substantial reduction in the grain size [7]. There are some experimental results demonstrating this trend [8] but in practice it is not generally possible to reduce the grain size of an alloy below ~1 μm using conventional thermomechanical processing. As a result of this limitation, an interest has arisen in developing alternative procedures for reducing the grain size of crystalline metals to the submicrometer or even the nanometer range.

Substantial reductions in grain size may be achieved by making use of processing methods incorporating the application of severe plastic deformation [9-11]. Several different methods are now available for imposing very high strains but the primary procedures are High-Pressure Torsion (HPT) [12] and Equal-Channel Angular Pressing (ECAP) [13,14]. Although HPT is capable of producing material with extremely small grain sizes, this processing technique has the disadvantage that the samples are very small, typically in the form of disks with a diameter of ~10 mm, and there appears to be no simple procedure for scaling HPT to produce large bulk material. By contrast, ECAP is capable of producing reasonably large samples and, as will be demonstrated, there is no subsequent diminution in the mechanical properties if the as-pressed material is subsequently rolled into sheets. Accordingly, this paper describes recent developments in fabricating and testing aluminum alloys using ECAP with the objective of achieving a superplastic forming capability at high strain rates.

PRINCIPLES OF EQUAL-CHANNEL ANGULAR PRESSING
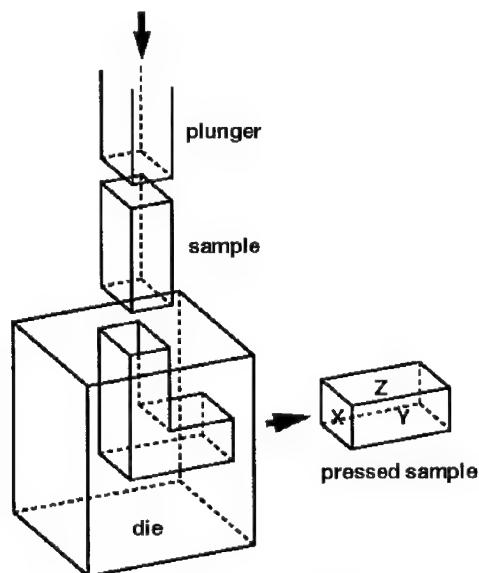
Figure 1. Schematic illustration of the principle of ECAP.

The principle of ECAP is illustrated schematically in figure 1. The ECAP die contains two channels, equal in cross-section, intersecting near the center of the die at an angle that is generally close to 90°. The sample is machined to fit within the channel and it is pressed through the die using a plunger. Thus, a strain is imposed on the sample as it passes through the shearing plane at the intersection of the two channels. Unlike more conventional metal-working processes, such as rolling and extrusion, it is apparent that the sample emerges from the die with the same cross-sectional dimensions as in the unpressed sample. Three separate planes are defined in figure 1: X is the plane perpendicular to the pressing direction and Y and Z are the side plane and the top plane at the point of exit from the die, respectively.
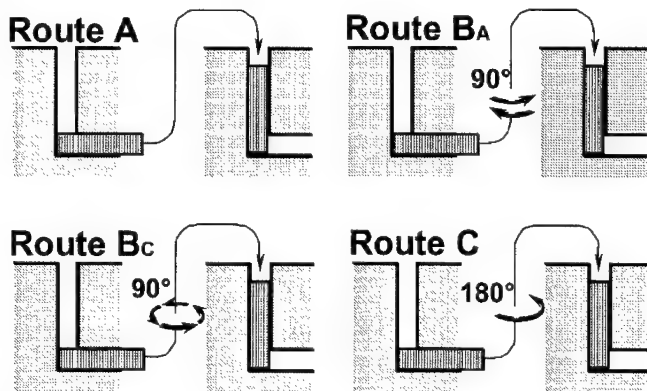
Figure 2. *The four different processing routes for ECAP.*

The strain imposed on the sample during passage through the ECAP die is dependent upon both the angle, Φ, between the two channels and the angle, Ψ, representing the outer arc of curvature where the two channels intersect. However, it can be shown that the angle Ψ has only a relatively minor influence on the overall strain so that the total strain is close to ~1 for each separate pass through the die when the internal die angle is given by $\Phi = 90°$ [15].

Since the sample emerges from the die without any reduction in the cross-sectional dimensions, it is apparent that repetitive pressings may be undertaken in order to achieve very high total strains. This provides an opportunity to rotate the sample between consecutive pressings in order to change the shearing characteristics within the material [14]. Four distinct processing routes have been defined and these are illustrated schematically in figure 2 [16]. In route A the sample is pressed repetitively without any rotation, route B refers to a rotation of 90° between each pressing and route C denotes a rotation of 180° between pressings. Route B may be further subdivided into route B_A where the rotations are by 90° in alternate directions between each pass and route B_C where the rotations are by 90° in the same sense between each pass. Several investigations have shown these different processing routes lead to different microstructures within the material [17-20]. In general, it appears that, at least when using a die with an internal angle of $\Phi = 90°$, route B_C leads most expeditiously to an array of essentially equiaxed grains separated by boundaries having high angles of misorientation [21] but there is some evidence that route A may be more effective in refining the grain size and producing high-angle boundaries when using a die with an internal angle of 120° [20]. An explanation for this apparent difference when using die angles of 90° and 120° has been developed through an analysis that incorporates the interaction of the shear plane with the texture and the crystal structure of the sample [22]. In practice, it is found experimentally that the development of an ultrafine microstructure in ECAP requires a very intense plastic straining on each separate passage through the die and this suggests that a die angle of $\Phi = 90°$ probably represents the optimum pressing condition [23].

THE PROCESS OF GRAIN REFINEMENT THROUGH ECAP

Repetitive pressings through an ECAP die lead to very substantial grain refinement and significant changes in the properties of the materials [9]. The effect of ECAP may be illustrated by considering the pressing of samples of pure Al at room temperature where the initial grain size was ~1.0 mm and the samples were pressed through a die having an internal die angle of Φ = 90° [17,19].

In general, the first pass serves to divide the large grains into arrays of subgrains that are well delineated but separated by boundaries having low angles of misorientation. These subgrains are elongated and they tend to lie in a banded structure that is oriented essentially parallel to the shearing direction at 45° to the upper and lower surfaces when viewed in the Y plane. In the second pass, following a rotation of 90°, the subgrain structure is broken into an array of ultrafine grains and there is some increase in the misorientations across the boundaries. After a total of three passes using processing route B_C, the subgrain bands are no longer visible and instead the microstructure consists of an essentially equiaxed array of grains with some boundaries having high angles of misorientation. The situation after four passes for route B_C is shown in figure 3 for each of the three planes, X, Y and Z, together with the selected area electron diffraction (SAED) patterns appropriate to each plane and taken from regions having a diameter of 12.3 μm [19]. In this condition, at a strain of ~4, the SAED patterns reveal the presence of boundaries having high angles of misorientation on each plane of sectioning and the microstructures on each plane consist of equiaxed grains with an average size of ~1.3 μm. Careful measurements have shown this final grain size is of the same order as the separation between the subgrain bands after the first pass through the die [17].

The development of an array of equiaxed grains having a size close to ~1 μm suggests the possibility of using this material to achieve superplastic elongations in tension. In practice, however, these small grains are not stable at the high temperatures needed for rapid diffusion and superplastic flow. This is illustrated in figure 4 where the measured grain size is plotted as a function of the annealing temperature for samples annealed for one hour at each selected temperature. For pure Al, it is apparent that the grains with an as-pressed size close to 1 μm grow very rapidly at temperatures above ~500 K [24]. A similar effect is shown also for an Al-3% Mg alloy, where the as-pressed grain size is significantly smaller than in pure Al because of the slower rate of recovery but, nevertheless, these ultrafine grains are again unstable at temperatures exceeding ~500 K [24]. These results lead to the conclusion that ECAP may be used to achieve very substantial grain refinement in pure metals and solid solution alloys but the as-pressed materials cannot exhibit superplasticity because of the grain instability at elevated temperatures.

A possible procedure for overcoming this problem is to use ECAP with alloys containing precipitates. Two examples are shown in figure 4. First, there is significant grain refinement in an Al-3% Mg-0.2% Sc alloy from an initial size of ~1.2 mm to a final size of ~0.2 μm after either 8 or 12 passes using route B_C at room temperature [25]. Furthermore, these small grains are extremely stable because of the presence of a fine dispersion of Al_3Sc precipitates and it is apparent from figure 4 that a grain size of <1 μm is retained to temperatures as high as ~700 K. Figure 4 also includes data for a commercial Al-5.5% Mg-2.2% Li-0.12% Zr alloy where the initial grain size was ~400 μm and the material was pressed at 673 K to a strain of ~3.7 to give a grain size of ~1.2 μm [26]. In this material, these small grains are stable up to ~750 K because of the presence of a dispersion of fine β'-Al_3Zr precipitates.
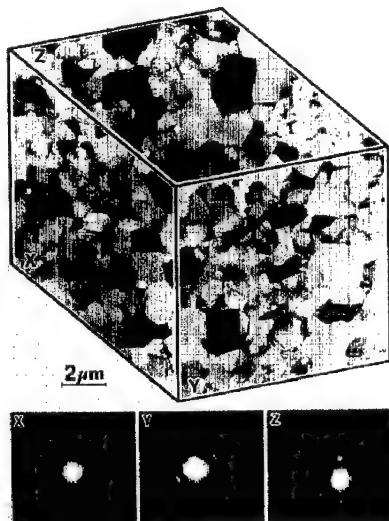
Figure 3. Microstructures produced on the X, Y and Z planes in pure Al after ECAP at room temperature to a total of 4 passes using route B_C: the selected area electron diffraction patterns were taken for each plane from regions having diameters of 12.3 μm [19].
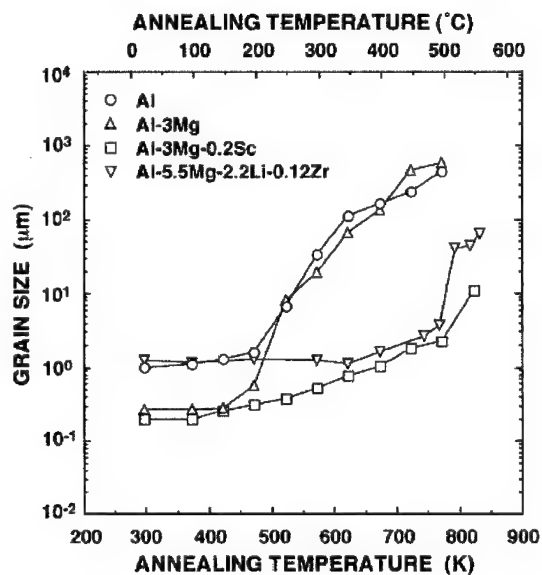
Figure 4. Variation of grain size with annealing temperature for pure Al [24], Al-3% Mg [24], Al-3% Mg-0.2% Sc [25] and Al-5.5% Mg-2.2% Li-0.12% Zr [26]: each sample was held for one hour at the annealing temperature.
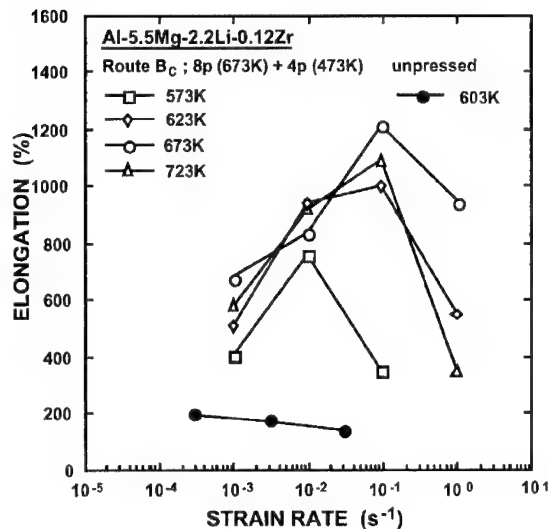
Figure 5. Elongation versus strain rate for a commercial Al-Mg-Li-Zr alloy in the unpressed condition and after ECAP for 8 passes at 673 K and 4 passes at 473 K to a total strain of ~12 using route B_C [27].

The dramatic increase in the superplastic capability that may be achieved through the use of ECAP is illustrated in figure 5 for the commercial Al-Mg-Li-Zr alloy [27]. The solid points at the lower left show the relatively modest ductilities attained in this alloy at a testing temperature of 603 K when testing without ECAP. The upper open points demonstrate the much larger elongations exhibited by specimens of the same alloy after ECAP using route B_C through a total of eight passes at 673 K and an additional four passes at 473 K to give a total imposed strain of ~12. These points cover tests conducted at temperatures from 573 to 723 K where, as is evident from figure 4, the grain size remains reasonably small. Inspection shows the ductilities are now exceptionally high and, in addition, these high elongations are achieved at very rapid strain rates: for example, the elongations to failure at 673 K are up to >1000% at testing strain rates of ~10^{-1} s^{-1}. These elongations are more than sufficient to meet the requirements for use in superplastic forming operations. Thus, results of this type serve to establish the possibility of using ECAP as a viable processing tool for attaining the ultrafine grain sizes needed to achieve superplasticity at very high strain rates.

Figure 4 gave results also for an Al-Mg-Sc alloy that was prepared by casting and this material provides an excellent opportunity to make a direct comparison between materials subjected either to ECAP or to cold rolling [28]. Figure 6 shows the microstructures produced in this alloy after two different processing conditions. In figure 6(a), the Al-Mg-Sc alloy was subjected to ECAP at room temperature for a total of eight passes using route B_C and then it was held at a temperature of 673 K for ~10 minutes. In figure 6(b), the as-fabricated alloy was subjected to cold rolling (CR) at room temperature to an equivalent strain of ~2.4 and again annealed at 673 K for ~10 minutes. Careful inspection shows the grain sizes in these two conditions are similar with values of ~1.1 and ~0.9 μm after ECAP and CR, respectively,
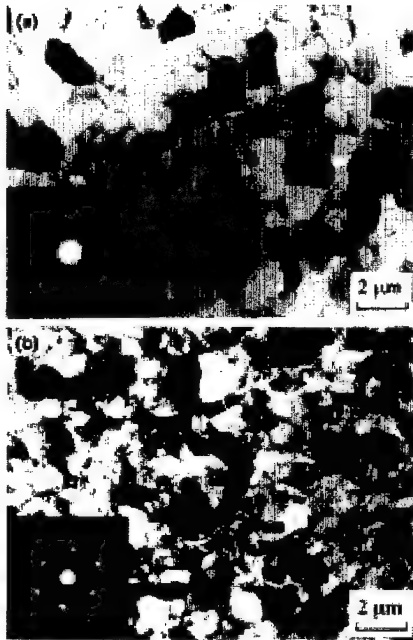
Figure 6. Microstructures in an Al-3% Mg-0.2% Sc alloy after holding at 673 K for ~10 minutes following (a) ECAP for 8 passes at room temperature using route B_C and (b) cold rolling at room temperature to a strain of ~2.4 [28].

but the SAED patterns reveal the presence of high angle grain boundaries in figure 6(a) after ECAP whereas the boundaries have low angles of misorientation in figure 6(b) after CR. From these observations, it is reasonable to conclude that ECAP and CR both have the potential for refining the microstructure but in CR these new boundaries do not evolve, at least over the range of strains examined experimentally, to produce the high angle boundaries needed for easy grain boundary sliding and consequently for the occurrence of superplastic elongations.

The effect of ECAP and CR on the mechanical properties of the Al-Mg-Sc alloy may be examined directly by preparing samples of the alloy using both procedures and then testing in tension over a range of strain rates. The results are shown in figure 7 for a testing temperature of 673 K where the data are plotted in the form of the measured flow stress against the imposed strain rate. Thus, the alloy processed by ECAP exhibits a strain rate sensitivity, m, close to ~0.5 at strain rates in the range of ~10^{-2} to 10^{-1} s^{-1} and this is consistent with the expectations for superplasticity, whereas the alloy processed by CR exhibits a strain rate sensitivity of ~0.3 which is consistent with dilute Al-Mg alloys [28]. These differences in the values of m lead to very significant differences in the measured elongations to failure, as shown in figure 8 for the same set of specimens [28]. As expected, the alloy showing m ≈ 0.3 after CR exhibits modest elongations of <300% whereas the same alloy after ECAP, where m ≈ 0.5, exhibits elongations up to >1000% at very rapid strain rates at and above 10^{-2} s^{-1}.
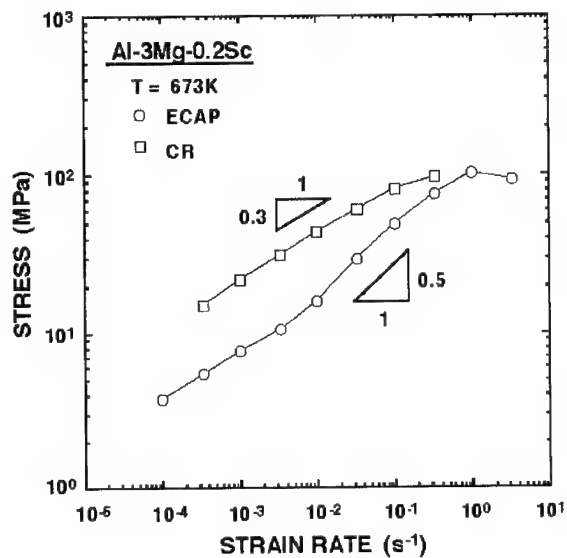
Figure 7. Flow stress versus strain rate at 673 K for an Al-3% Mg-0.2% Sc alloy after ECAP or cold rolling (CR) [28].
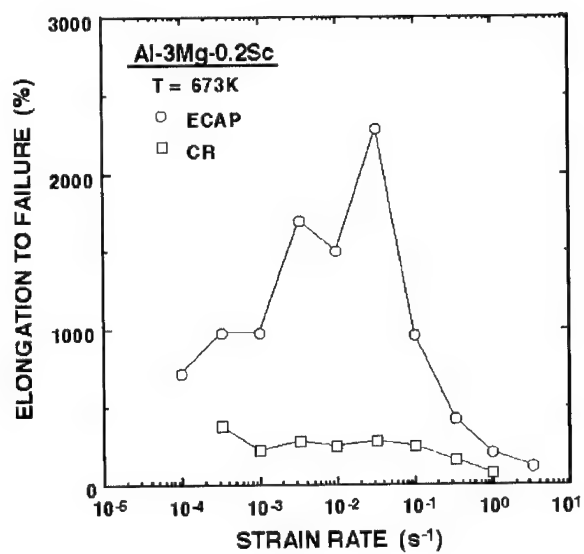
Figure 8. Elongation to failure versus strain rate at 673 K for an Al-3% Mg-0.2% Sc alloy after ECAP or cold rolling (CR) [28].
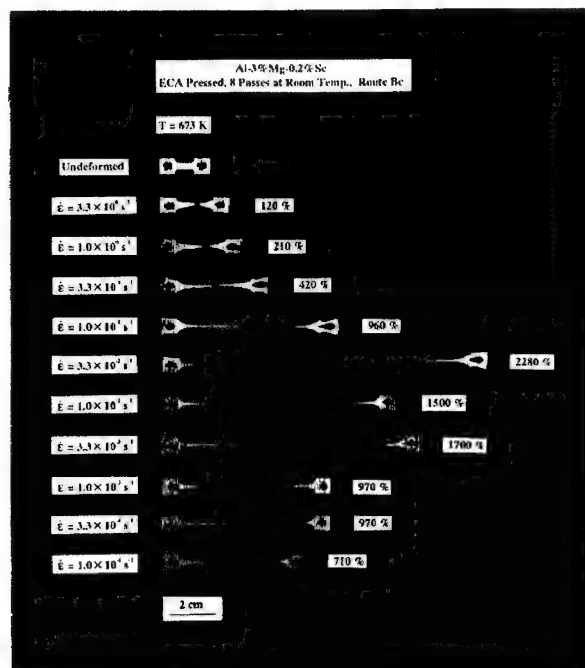
Figure 9. Samples of an Al-3% Mg-0.2% Sc alloy after ECAP for 8 passes at room temperature using route B_C and then pulling to failure at 673 K [28]: the upper specimen is untested.

Figure 9 shows the specimens of the Al-Mg-Sc alloy after ECAP and pulling to failure as documented in figure 8 [28]. The uniformity of deformation within the gauge lengths of specimens giving high tensile elongations confirms the occurrence of true superplasticity and an absence of any significant localized necking.

The exceptionally high tensile ductilities evident in figure 9 suggest it should be possible to use the as-pressed material for rapid superplastic forming. This suggestion is confirmed in figure 10 where disks were cut from the rods of the as-pressed Al-Mg-Sc alloy, inserted into a biaxial gas-pressure forming facility, heated to 673 K and then subjected to an argon gas pressure of 10 atmospheres, equivalent to 1 MPa, for periods up to a maximum of 60 s: disk (a) on the left is untested and the disks labeled (b) and (c) were formed for periods of 30 and 60 s, respectively [29]. Following forming, these two disks were sectioned and measurements were taken to determine the local thickness at angular positions around each dome, where 0° corresponds to the pole of the dome at the highest point. These measurements are shown in figure 11 and they confirm the uniformity of thinning associated with true superplasticity [29].

The demonstration in figure 10 confirms the potential for using small disks cut from the as-pressed rods for rapid forming but in practice the superplastic forming industry uses materials in the form of thin sheets. To evaluate whether the superplastic characteristics are retained if the
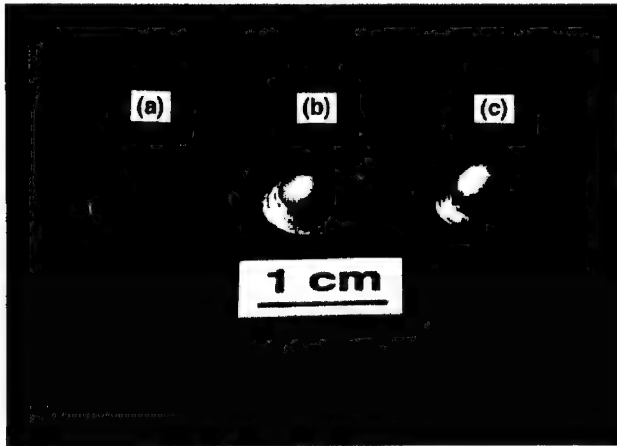
Figure 10. *Disks cut from rods of the Al-Mg-Sc alloy after ECAP for 8 passes at room temperature using route B_C. Disk (a) is in the as-pressed condition and the other disks were heated to 673 K and subjected to a gas pressure of 1 MPa for periods of (b) 30 s and (c) 60 s [29].*
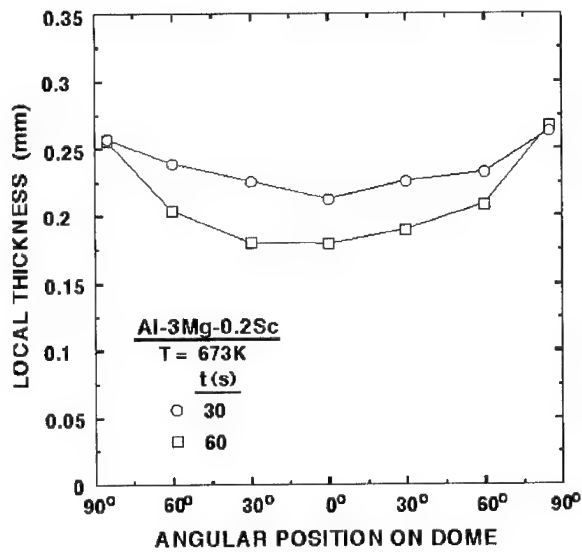
Figure 11. *Variation of the local thickness with the angular position around the dome for the two domes shown at (b) and (c) in Fig 10 [29].*
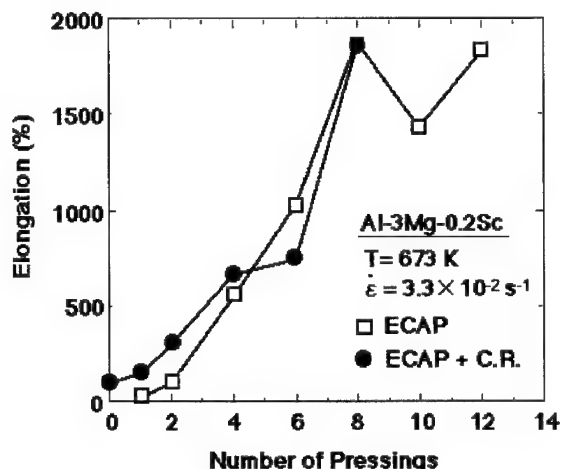
Figure 12. Elongation to failure at
673 K versus number of passes in
ECAP for samples of an Al-3% Mg-
0.2% Sc alloy after ECAP and after
ECAP + cold rolling (CR) [30].

as-pressed alloy is subjected to cold rolling, figure 12 shows the elongations recorded at 673 K
after both ECAP through different numbers of passes and ECAP + CR [30]. It is evident that the
superplastic properties remain essentially unchanged when cold rolling is used to prepare the
material as a sheet after processing by ECAP, thereby providing additional support for the utility
of the ECAP procedure as a tool for fabricating materials for potential use in superplastic
forming applications.

SUMMARY AND CONCLUSIONS

1. Equal-channel angular pressing (ECAP) is a useful processing technique involving the
application of severe plastic deformation to achieve a very substantial refinement in the grain
size of conventional metals and alloys. If ECAP is continued to a sufficiently high strain, it is
possible, at least in pure aluminum and aluminum-based alloys, to achieve an array of ultrafine
grains separated by boundaries having high angles of misorientation.

2. The ultrafine grains produced by ECAP are reasonably stable at elevated temperatures
when there are precipitates in the material. Under these conditions, the high angle grain
boundaries produced by ECAP lead to grain boundary sliding and superplastic ductilities at high
strain rates and thus they give the potential for achieving a rapid superplastic forming capability.

REFERENCES

1. T.G. Langdon, *Metall. Trans.*, **13A**, 689 (1982).
2. T.G. Langdon, *Mater. Sci. Engng*, **A174**, 225 (1994).
3. A.J. Barnes, *Mater. Sci. Forum*, **304-306**, 785 (1999).
4. A.J. Barnes, *Mater. Res. Soc. Symp. Proc.*, **601**, 207 (2000).
5. A. Ball and M.M. Hutchison, *Metal Sci. J.*, **3**, 1 (1969).
6. T.G. Langdon, *Acta Metall. Mater.*, **42**, 2437 (1994).
7. Y. Ma, M. Furukawa, Z. Horita, M. Nemoto, R.Z. Valiev and T.G. Langdon, *Mater. Trans. JIM*, **37**, 336 (1996).
8. F.A. Mohamed, M.M.I. Ahmed and T.G. Langdon, *Metall. Trans.*, **8A**, 933 (1977).
9. R.Z. Valiev, R.K. Islamgaliev and I.V. Alexandrov, *Prog. Mater. Sci.*, **45**, 103 (2000).
10. T.C. Lowe and R.Z. Valiev, *JOM*, **52** (4), 27 (2000).
11. T.C. Lowe and R.Z. Valiev (eds), *Investigations and Applications of Severe Plastic Deformation*, Kluwer, Dordrecht, The Netherlands (2000).
12. N.A. Smirnova, V.I. Levit, V.I. Pilyugin, R.I. Kuznetsov, L.S. Davydova and V.A. Sazonova, *Fiz. Met. Metalloved.*, **61**, 1170 (1986).
13. V.M. Segal, V.I. Reznikov, A.E. Drobyshevskiy and V.I. Kopylov, *Russian Metall.*, **1**, 99 (1981).
14. V.M. Segal, *Mater. Sci. Engng*, **A197**, 157 (1995).
15. Y. Iwahashi, J. Wang, Z. Horita, M. Nemoto and T.G. Langdon, *Scripta Mater.*, **35**, 143 (1996).
16. M. Furukawa, Y. Iwahashi, Z. Horita, M. Nemoto and T.G. Langdon, *Mater. Sci. Engng*, **A257**, 328 (1998).
17. Y. Iwahashi, Z. Horita, M. Nemoto and T.G. Langdon, *Acta Mater.*, **45**, 4733 (1997).
18. S. Ferrasse, V.M. Segal, K.T. Hartwig and R.E. Goforth, *Metall. Mater. Trans.*, 28A, 1047 (1997).
19. Y. Iwahashi, Z. Horita, M. Nemoto and T.G. Langdon, *Acta Mater.*, **46**, 3317 (1998).
20. A. Gholinia, P.B. Prangnell and M.V. Markushev, *Acta Mater.*, **48**, 1115 (2000).
21. K. Oh-ishi, Z. Horita, M. Furukawa, M. Nemoto and T.G. Langdon, *Metall. Mater. Trans.*, **29A**, 2011 (1998).
22. Y.T. Zhu and T.C. Lowe, *Mater. Sci. Engng*, **A291**, 46 (2000).
23. K. Nakashima, Z. Horita, M. Nemoto and T.G. Langdon, *Acta Mater.*, **46**, 1589 (1998).
24. H. Hasegawa, S. Komura, A. Utsunomiya, Z. Horita, M. Furukawa, M. Nemoto and T.G. Langdon, *Mater. Sci. Engng*, **A265**, 188 (1999).
25. P.B. Berbon, S. Komura, A. Utsunomiya, Z. Horita, M. Furukawa, M. Nemoto and T.G. Langdon, *Mater. Trans. JIM*, **40**, 772 (1999).
26. M. Furukawa, Y. Iwahashi, Z. Horita, M. Nemoto, N.K. Tsenev, R.Z. Valiev and T.G. Langdon, *Acta Mater.*, **45**, 4751 (1997).
27. S. Lee, P.B. Berbon, M. Furukawa, Z. Horita, M. Nemoto, N.K. Tsenev, R.Z. Valiev and T.G. Langdon, *Mater. Sci. Engng*, **A272**, 63 (1999).
28. S. Komura, Z. Horita, M. Furukawa, M. Nemoto and T.G. Langdon, *Metall. Mater. Trans.*, in press.
29. Z. Horita, M. Furukawa, M. Nemoto, A.J. Barnes and T.G. Langdon, *Acta Mater.*, **48**, 3633 (2000).
30. H. Akamatsu, T. Fujinami, Z. Horita and T.G. Langdon, *Scripta Mater.*, in press.

Size-dependent melting of matrix-embedded Pb-nanocrystals

H. Ehrhardt,[1] J. Weissmüller[1,2] and G. Wilde[1]

[1] Institut für Nanotechnologie , Forschungszentrum Karlsruhe, Karlsruhe, Germany
[2] Technische Physik, Universität des Saarlandes, Saarbrücken, Germany

Abstract

We report calorimetric data for the size-dependence of the melting temperature as well as the enthalpy and entropy of melting for nanoscale Pb particles in an Al matrix, prepared by high energy ball-milling. The results are discussed with respect to various models for the melting of small confined systems. We can rule out models based on a temperature-independent Gibbs excess free energy of the particle-matrix interface, and a model based on an increased mean-square displacement of the interfacial layer. The best agreement to the data is provided by modeling the interface as an inert layer of finite thickness, which does not participate in the phase transition.

Introduction

It is well known that a decrease of the size D of a particle leads to a shift of the melting temperature, T_M, [1-4], both for free and for matrix-isolated particles [5-7]; a recent review is given in Ref. [8]. There is as yet no single generally accepted model for the size dependence, and the individual models yield different predictions for the variations of measurable quantities, such as the temperature and enthalpy of melting, on the particle size.

Since Pb has a conveniently low bulk melting point and is insoluble in Al, size-effects on the melting of Pb nanoparticles in Al has been repeatedly studied. Al-Pb nanocomposites have been prepared by melt spinning [9] and by high energy ball milling [10], the former technique leading to an increase of T_M with decreasing size, whereas the latter results in a decrease with decreasing size. More recently, a melting point increase was also reported for Pb in Al-Pb multilayers [11].

Besides T_M, calorimetry measures the heat of melting, and provides estimates for the entropy of melting. The proposed models make different predictions on the size-dependence of these quantities, and the purpose of our paper is to assess the models by comparing their predictions to experimental data. The data were obtained by a calorimetric investigation of the melting of Pb particles, with sizes ranging from 2 to 100 nm, embedded in an Al matrix by means of high energy ball milling.

Theory

We denote by g, h and s the free energy, enthalpy, and entropy, respectively, of the Pb particles per volume of Pb (e.g., total enthalpy over total volume); the subscript '0' refers to the properties of the bulk material in the absence of interfaces, and we denote by Δ and the subscript M the change upon solidification (e.g., Δh_M denotes the volumetric latent heat of melting, liquid minus solid). Formally, it is always possible to decompose the actual values of g, h, and s into the values for the bulk material, g_0, h_0, and s_0, and the respective Gibbs excess quantity per area, A, of interface, $\{G\}$, $\{H\}$, and $\{S\}$. For instance,

$$V g = V g_0 + A \{G\} \tag{1}$$

When melting is treated as a first order phase transition with $G = H - TS$, Eq. (1) leads immediately to:

$$T_M = (\Delta h_{M,0} + \alpha \, \Delta\{H\}_M) / (\Delta s_{M,0} + \alpha \, \Delta\{S\}_M), \tag{2}$$

where α denotes the specific interface area (area per volume), $\alpha = A/V$. Models which ignore the excess entropy, for instance by assuming temperature-independent excess free energies $\{G\}$, and which approximate H and S as temperature-independent and the excess enthalpy as size-independent, will therefore predict a linear dependence of T_M on α. Since α is inversely proportional to the particle size, D, this is equivalent to a dependency of the form

$$T_M = T_{M,0} + c / D \tag{3}$$

with c a constant. Experimental data for T_M as a function of D have repeatedly been analyzed by this law and good agreement was generally found [5, 6]. Since $\Delta H_M = T_M \, \Delta S_M$, the above assumptions also suggest that the enthalpy of melting has the same size-dependence as the melting temperature, in other words:

$$\frac{\Delta H_M}{\Delta H_{M,0}} = \frac{T_{M,0} + c/D}{T_{M,0}}, \tag{4}$$

$$\frac{\Delta H_M}{\Delta H_{M,0}} = \frac{T_M}{T_{M,0}}. \tag{5}$$

Apparently, this prediction has not been checked against experimental data.

Although some uncertainty is introduced by the fact that the melting of nanoparticles generally takes place over a finite temperature interval, experimental data for ΔH_M and T_M allow the entropy of melting to be estimated according to $\Delta S_M = \Delta H_M / T_M$. This allows at least for a qualitative check of the assumption of a temperature-independent interface excess free energy.

A second class of models considers premelting of the interfacial region. It has been proposed that the enthalpy change during premelting cannot be resolved experimentally due to thermal smearing. Thus, since only the melting of the core is observed, the experimental enthalpy of melting should be reduced by a factor that corresponds to the volume fraction of the premolten layer of thickness, t [2]:

$$\Delta H_M = \Delta H_{M,0} (1 - 2 \, t / D)^3 \tag{6}$$

It is seen that, independent of the details of the premelting process, Eq. (3) follows simply by assuming an interfacial 'inert layer', which does not contribute to the latent heat and entropy of melting. Equation (6) has been found to agree well with data for Sn nanoparticles [2]. However, since the same argument should also hold for the entropy of melting, it would seem that in this case also following equation holds:

$$\frac{\Delta H_M}{\Delta H_{M,0}} = \frac{\Delta S_M}{\Delta S_{M,0}}, \tag{7}$$

which is obviously problematic since it suggests that:

$$T_M = T_{M,0}, \tag{8}$$

in other words T_M is predicted to be independent of the particle size, which is contrary to what is generally observed by experiment.

The third type of model that we chose to compare to our data derives a size-dependence of the T_M and H_M based on considerations of the increased mean square atomic displacement at small particle size. This leads to a size-dependent interfacial Gibbs excess free energy, $\{G\}$, and to the postulate of the following size-dependencies of T_M and of ΔH_M [12]:

$$\frac{T_M}{T_{M,0}} = \exp\left(-\frac{2\,\Delta S_{M,0}^{mol}}{3\,R}\,\frac{D_0}{D-D_0}\right), \tag{9}$$

$$\frac{\Delta H_M}{\Delta H_{M,0}} = \frac{T_M}{T_{M,0}}\,\frac{D-2\,D_0}{D-D_0}, \tag{10}$$

where $\Delta S_{M,0}^{mol}$ denotes the molar entropy of melting, R is the gas constant, and $D_0 = 6\,(6\Omega/\pi)^{1/3}$ with Ω the atomic volume.

Conclusions on the size-dependence of the melting temperature have also been derived by considerations based on the effects of a capillary pressure [2, 6, 13]. These models generally apply concepts which are valid for fluid droplets in a fluid matrix, but which are invalid if at least one of the systems (particle or matrix) is solid [14]. We shall therefore disregard these approaches.

Experimental

Solid mixtures of Al (purity 99.999%) and Pb (purity 99.9999%) were alloyed in a SPEX 8000 shaker mill. Charges of 2.5 g in weight were milled for 12 h in a steel vial with two large (8,3 g each) and four small (1 g each) hardened steel balls. The milling time was sufficient to achieve a steady-state average particle size as observed by x-ray diffraction (XRD). Contamination from the milling media was monitored by energy-dispersive x-ray spectroscopy (EDX); the major impurity component was found to be Fe with a maximum solute fraction of 0.1 at.%.

Structural characterization of the milled samples was performed by XRD using Mo-$K\alpha$ radiation. The lattice parameters were determined from the peak positions using Cohen's method and the extrapolation function $\cos^2\theta/\sin\theta$ [15]. The (volume-weighted) average particle size and the inhomogeneous strain were estimated from the integral widths of the first eight fcc reflections assuming Lorentzian grain-size broadening and Gaussian strain broadening [16]. The calorimetric characterization was carried out in a differential scanning calorimeter (DSC, Perkin-Elmer Pyris I), under Ar gas and with a heating rate of 10 K/min. The accuracy of the

temperature measurements amounted to ±0.2 K, the relative accuracy of the melting enthalpy measurements was ±1.5%.

Results and Discussion

Fig.1 shows the particle size for the ball-milled $Al_{1-x}Pb_x$ samples as a function of the atomic fraction, x, of Pb. The particle size D for as-prepared samples increases rapidly with increasing Pb content (solid symbols); after five melting/solidification cycles (each cycle from room temperature to 615 K and back) the particles have undergone limited coarsening (open symbols). Since no further increase of the particle size was observed between the fourth and the fifth cycle the open circles in Fig. 1 are assumed to represent the steady state. The measured lattice parameters, a, of Al and Pb are found to be independent of the lead concentration within the error of the measurements (standard deviation) of 5×10^{-4} and 2×10^{-4} for $\Delta a/a$ of Pb and Al,

Fig. 1: Average particle size D of the as-prepared and the annealed samples vs. Pb atom fraction x.

respectively. Because of the large size mismatch of Al and Pb atoms, even small amounts of Al in Pb or of Pb in Al would measurably influence the respective lattice constant. Therefore, the result suggests that Al and Pb remain mutually immiscible even after mechanical milling.

Fig. 2: DSC heat flow, normalized to mass of Pb, of several $Al_{1-x}Pb_x$ samples vs. temperature T. Curves have been displaced vertically for better readability.

Fig. 2 shows the DSC heat flow, normalized to the Pb mass fraction. With decreasing Pb concentration, the position of the endothermic peak moves to lower temperatures and the peak width increases. Additionally, the heat flow of a pure lead sample with comparable mass than the Pb fractions in the nanocomposite samples is indicated. The melting temperature T_M is seen to decrease with decreasing particle size, and the reduced total area of the peaks indicates a reduction of the respective melting enthalpies ΔH_M. The observation of a size dependent melting temperature reduction is typical for the melting of small isolated particles in general and in particular for matrix-embedded Pb nanoparticles prepared by ball milling [7].

In Fig. 3, the reduced melting enthalpy, $\eta = \Delta H_M / \Delta H_{M,0}$ is shown as a function of the reduced melting temperature, $\tau = T_M / T_{M,0}$. Also shown are the theoretical predictions by Eqs. (4, 7, and 10). It is seen that the data disprove the identity of η and τ, Eq. (5), which suggests that the interfacial excess entropy is not negligible. The agreement with Eq. (10) is somewhat better, but
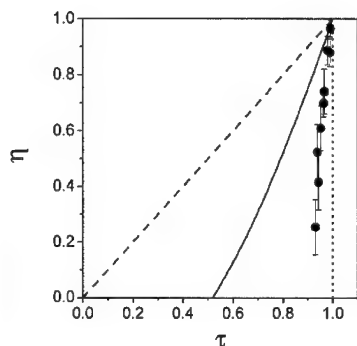
Fig. 3: Reduced melting enthalpy η vs. reduced melting temperature τ. The lines represent Eq. (5) (dashed), Eq. (8) (dotted), and Eq. (9) (solid).

nonetheless the pronounced differences between data and theory appear to rule out the underlying model. Moreover, analyses of the quantitative x-ray measurements taken at room temperature [17] indicate, that the mean square displacement values are independent of the particle size, contrary to the predictions of the model. Although Eq. (8) is unrealistic in predicting no variation of τ at all, it is seen that the experimental variation in τ is indeed much smaller than predicted by the other models, and that Eq. (6) provides the closest values for η.

Fig. 4 displays the variation of η and of the reduced entropy, $\sigma = \Delta S_M / \Delta S_{M,0}$, with D. Also shown are the predictions by Eqs. (4), (6), and (10) for the variation of η as a function of D. The constant c in Eq. (4) was determined by the fit to the variation of τ with D, see Fig. 5, and the layer thickness t determined by fitting the data in Fig. 4 by Eq. (6) was $t = (0.9\pm0.3)$ nm. Again, it is found that Eq. (6) provides the best fit to the data, suggesting that the inert layer model is the most adequate model. We have pointed out that

the inert layer model also suggests that the entropy of melting varies with the particle size in a similar manner as the enthalpy of melting. Such behavior is indeed indicated by the data in Fig. 4, which show that σ and η vary nearly identically with D. This is not in contradiction to the grain-size dependence of τ, since one can readily verify that small differences between σ and η give rise to noticeable variations of the melting temperature. In other words, while the inert layer model does explain the size-dependence of the enthalpy and entropy of melting, it is poorly adopted to the task of predicting the size-dependence of T_M. Obviously, the model fails to appropriately account for the detailed energetics of the particle matrix interface, which manifest themselves in the dependency of the melting point (increase or decrease) of Pb in Al on the preparation technique (melt spinning or ball milling) and, potentially, on the degree of coherency of the interfaces. In the absence of more detailed investigations of the atomic structure and its variation with T near T_M the layer model must be considered merely as an operational concept for parameterizing the size-dependence of the enthalpy and entropy of melting.

Fig. 4: Experimental data for the reduced melting enthalpy η ($\bullet$) and for the reduced melting entropy σ ($\circ$)vs. average particle size D. The lines represent model predictions for η, namely Eq. (9) (solid) and bests fits by Eq. (4) (dashed) and (6) (dotted).

In the above context we also emphasize that while our results confirm the functional variation of the enthalpy and entropy of melting as a function of the particle size predicted by the inert layer model, they neither support nor contradict the previously suggested model of surface
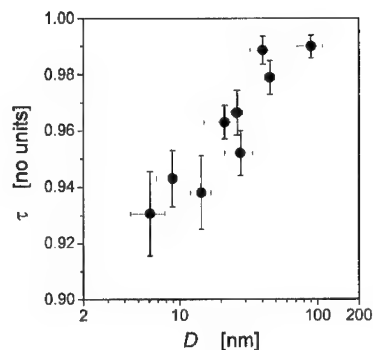
Fig. 5: Reduced melting temperature $\tau = T_M/T_{M,0}$ versus particle size D.

premelting [2]. In fact, an equally consistent explanation of the data would be obtained if it was assumed that, instead of a liquid-like disordered layer *below* T_M, the particle would actually exhibit a solid-like ordered surface layer *above* T_M. Such layering at solid-liquid-interfaces is in fact well supported by experiments and computer simulations for planar interfaces, where it can extend over many atomic monolayers into the liquid [18].

Acknowledgements

References

[1] M. Takagi, *J. Phys. Soc. Jpn.* **9** (1954), 359.
[2] S. L. Lai, J. Y. Guo, V. Petrova, G. Ramanath, L. H. Allen, *Phys. Rev. Lett.* **77** (1996), 99.
[3] P. R. Couchman, W. A. Jesser, *Nature* **269** (1977), 481.
[4] M. Mitome, *Surf. Sci. Lett.* **442** (1999), L953.
[5] H. W. Sheng, K. Lu, E. Ma, *Acta Mater.* **49** (1998), 5195.
[6] K. M. Unruh, J. F. Sheedan, T. E. Huber, C. A. Huber, *NanoStruct. Mater.* **3** (1993), 425.
[7] H. W. Sheng, Z. Q. Hu, K. Lu, *NanoStruct. Mater.* **9** (1997), 661.
[8] K. Chattopadhyay and R. Goswami, *Prog. Mat. Sci.* **42** (1997), 287.
[9] D.L. Zhang and B. Cantor, *Acta Met. Mater.* **39** (1991), 1595.
[10] H.W. Sheng, K. Lu and E. Ma, *Nanostruct. Mater.* **5** (1998), 865.
[11] L. Zhang, Z.H. Jin, L.H. Zhang, M.L. Sui and K. Lu, *Phys. Rev. Lett.* **85** (2000), 1484.
[12] Z. Zhang, X. X. Lü, Q. Jiang, *Physica B* **270** (2000), 249.
[13] K.-J. Hanszen, *Z. Physik* **157** (1960), 523.
[14] J. Weissmüller and J.W. Cahn, *Acta Mater.* **45** (1997), 1899.
[15] B. D. Cullity, *Elements of x-ray diffraction*, 2nd edition (London: Addison-Wesley, 1974), 363.
[16] H. P. Klug and L. E. Alexander, *X-ray diffraction procedures for polycrystalline and amorphous materials*, 2nd ed. (Wiley, New York, 1974), 618.
[17] H. Ehrhardt, J. Weissmüller and G. Wilde, to be published.
[18] O.M. Magnusson, M.J. Regan, E.H. Kawamoto, B.M. Ocko, P.S. Pershan, N. Maskil, M. Deutsch, S. Lee, K. Penanen and L.E. Berman, *Physica B* **221** (1996), 257.

Stacking Faults Created by Mechanical Milling in Nanostructured WC-Co Composite Powder

Yang Zhimin, Mao Changhui, Du Jun
General Research Institute for Non-ferrous Metals, Beijing 100088, P. R. China
Michel Daniel, Champion Yannick, Hagège Serge and Hÿtch Martin
Centre d'Etudes de Chimie Métallurgique / CNRS, 94407 Vitry-sur-Seine, France

ABSTRACT

Nanostructured WC-Co powders obtained by mechanical milling were investigated by combination of X-ray diffraction (XRD) and high-resolution transmission electron microscopy (HRTEM) techniques. HRTEM image analysis shows that in the as-milled nanostructured powder, many WC grains contain stacking faults lying on the plane{10.0}. Analysis of phase images showed that these defects were nearly periodically ordered along the [10.0] direction. Based on these observations, a structural model is proposed for the WC grains with ordered stacking faults, which is in fact equivalent to a superstructure of WC with space group Amm2. When this model is introduced together with the normal WC structure (space group $P\bar{6}m2$) into the Rietveld refinement, a much better agreement between the calculated and experimental XRD profiles is obtained. This study allowed obtaining the lattice parameters, grain size, microstrain and other structural information on the as-milled powders.
Keyword: structural properties, mechanical milling, WC-Co

1 INTRODUCTION

Nanocrystalline materials exhibit a crystallite size in the range of a few nanometers (typically 5-20 nm). It was reported that the mechanical properties of nanocrystalline WC- 10%Co cemented carbides are much better than conventional materials [1]. A lot of processes have been used for synthesizing nanocrystalline materials. Among them, high-energy mechanical milling was widely adopted because of its low cost, efficiency and simplicity of processing.

In previous studies [2], nanocrystalline WC-10%Co powder mixtures were prepared by high-energy ball milling and studied by XRD and HRTEM. The lattice parameters, size and strain were analyzed by line profile analysis using the Halder-Wagner plot [3]. Recently, another study by Ungar *et al* [4] allowed determining the particle size, the size distribution and dislocation density in a nanocrystalline tungsten carbide using a modified Williamson-Hall and Warren-Averbach method. In both previously mentioned studies, peaks were fitted separately and the information on the relative intensities of each peak was not considered. In this work, Rietveld (whole-profile) analysis was tried for the refinement of the experimental XRD patterns [4]. It rapidly appears that the XRD whole profiles could not be satisfactorily fitted using only the modeled whole pattern of WC including line broadening. In fact, intensity residues, either by excess or defect, were systematically found close to the Bragg positions. These discrepancies between calculated and observed intensities indicate that the WC structure introduced in the refinement can not represent correctly the crystal structure of the material and that significant structural modification has been induced by the milling process. HRTEM observations revealed that many nanocrystallites are heavily affected by stacking faults, which are not randomly

dispersed, but are organized with a nearly regular periodicity. This study reports on a model introducing a WC superstructure including stacking faults for explaining HRTEM observations and XRD patterns.

2 EXPERIMENTAL

Samples of different milling time were prepared using a Spex-8000 three-dimension vibrating high-energy ball mill. The milling vial and milling balls are made of WC-Co in order to avoid an eventual contamination. The mass ratio of milling balls to powder mixture was fixed to 8:1. The milling times were 0.5, 1, 2, 5, 10, 20, 40, 100, 150 hours respectively.

The XRD patterns were taken using a Philips X-ray diffractometer with Co-Kα radiation. Rietveld (whole-profile) analysis of the experimental XRD patterns was carried out using the Fullprof software [5] and Rietveld refinement guideline [6]. HRTEM observation was carried out using a 200 kV TOPCON-002B ultra-high resolution analytical electron microscope.

3 RESULTS

The XRD pattern of a WC-10%Co composite powder milled for 10 hours is shown in figure 1. Strong broadening and overlapping can be seen compared with the sample without milling. Actually after 2 hours milling, the peaks of Co get broad enough to submerge in the background and can not be observed in the experimental condition. So only WC was used to fit the experimental patterns of the as-milled powders in the following analysis. When the perfect structural model was used to refine the experimental pattern, we find that there are systematic differences between the calculated pattern and the experimental pattern for all the as-milled specimens. First, the relative intensities of some peaks change compared with the pattern of the starting powder, the experimental intensities of peak (20.0) and peak (00.2) are much stronger than the calculated ones, as shown by the difference curve in figure 2. This phenomenon can not be caused by preferred orientation effect, because the relative intensities of peak (10.0) and peak (20.0) have to be interrelate and that in this case, the $I_{cal}(20.0)$ (integrated intensity) is only 70% of $I_{exp}(20.0)$, while $I_{cal}(10.0)$ is nearly 98% of $I_{exp}(10.0)$. Second, not all the peak profiles can be well described. For example, it was not possible to match well the peak (20.1) in the whole profile matching process, even if anisotropic strain and domain-size effects were taken into account.

It was thus likely that these phenomena might be caused by structural defects created during mechanical milling. From the HRTEM study at atomic scale, it appeared that two types of WC nanocrystals were found. In particular, in addition to crystallites containing few defects, the smaller grains contained a large number of planar defects. Figure 2(a) shows a HREM image of such an as-milled WC grain. The defects correspond to the stacking fault {10.0} 1/6[-12.3], which is the most typical type of stacking faults found in WC crystals [7]. Besides, these stacking faults are periodically arranged within the nanograin. This periodicity can be visualized using the phase analysis method developed by M. Hÿtch [8]. In Figure 2(b), the power spectrum of the image is shown where two sets of periodicity associated to plane {00.1} and plane {10.0} can be seen. Figure 2(c) and 2(d) are phase images P10.0(r) and P00.1(r) reconstructed by inverse Fourier using the two reflections 10.0 and 00.1 in Figure 2(b). The phase image Pg(r) can be used to define the translation domain associated to a given diffraction vector **g** within a crystal grain. The phase shift is represented on a gray scale. In particular, when the fringe shifts by half a period, the phase

changes by π, resulting in the different color at both sides of the interface; on the other hand when the fringe does not shift or shifts by a period, the phase is kept constant and the color is the same across the field of view.

The phase image P10.0(r) [Figure2 (c)] shows almost the same color across the whole WC particle. From Figure 2 (d), it can be seen that the WC grain has several parts of different colors, each corresponding to a stacking fault. It is important to notice that in the diffraction pattern (figure 2b), the defects suppress the 00.1 spot which is replaced by a pair of satellite spots. The distance in reciprocal space between these two satellites is directly related to the periodicity or pseudoperiodicity of the stacking defect. Consequently, in the XRD patterns, the presence of the observed stacking defects will reduce the intensity of given lines such as 00.1 and introduce extra intensity out of Bragg positions at the angle corresponding to the satellite spots.
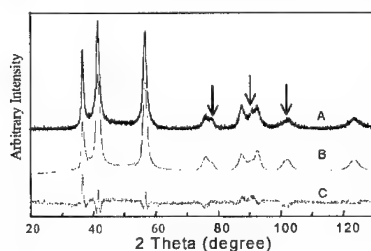
Figure 1. XRD experimental pattern and the fitting result when the WC structure was used for powder milled for 10 hours.
A: experimental pattern
B: calculated pattern
C: difference curve

4 DISCUSSION

A tentative structure model for the faulted WC grains is proposed for representing an ordered array of stacking faults. According to this model, the faulted structure of hexagonal WC can be described by a structure with space group Amm2, in which there is one stacking fault every a certain number of planes {10.0}. The number "n" can be adjusted in order to correspond to the satellite positions. Figure 3 represents a structure model with one stacking fault every 7 planes.

The as-milled powder will be now considered as a mixture of WC grains of two different structures: $P\bar{6}m2$ and Amm2. These two phases were then put into the Rietveld refinement process. In this case, the XRD experimental patterns can be fitted much better, as shown by the difference curve in figure 4 which corresponds to a sample obtained after a milling time of 10 hours. The improved agreement between the experimental and calculated profiles was also measured by the factors Rp and Rwp which decreased by about 50 percent. The previously mentioned intensity deficiencies, for instance concerning the peak (20.0), are corrected by the introduction of stacking faults. For the WC grains with stacking faults, the WC peak (20.1) is split into two peaks in the orthorhombic phase and this allows the experimental peak shape to be fitted by adding the intensities of the two parts, as shown in figure 4. So it can be concluded that the stacking faults are the main cause of the differences observed from a XRD pattern of WC solely broadened by size and strain effects. A reasonably good fit was obtained for all samples with different milling time.
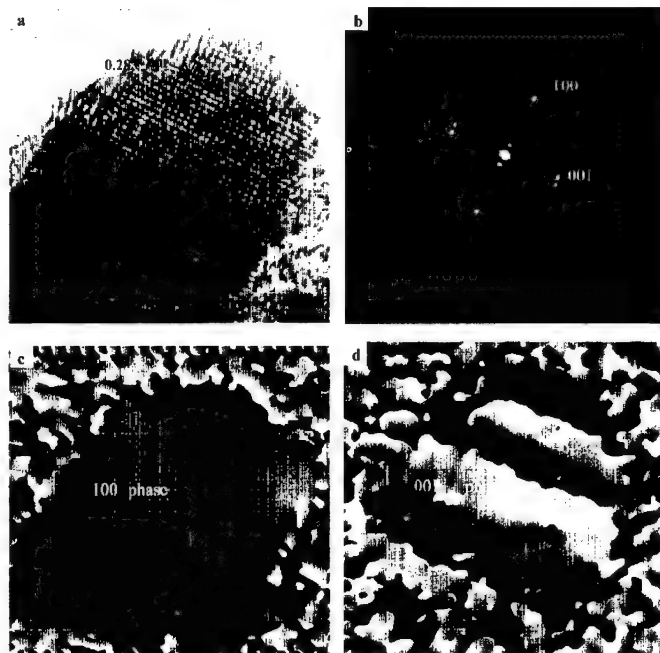
Figure 2. Analysis of the stacking faults found in ball-milled nanometric WC crystallites
(a) HRTEM image   (b) diffraction of image
(c) phase image P10.0(r) (d) phase image P00.1(r)
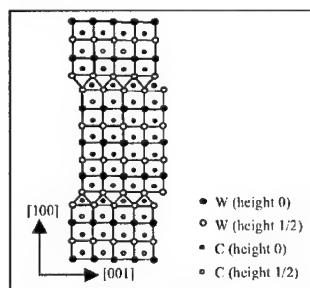
Figure 3. Structure model for faulted hexagonal WC (Space group Amm2)
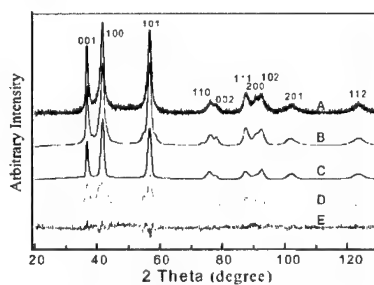
Figure 4. Fitting results when stacking faults are taken into account. A: experimental pattern; B: calculated pattern (C+D); C: calculated pattern with stacking faults; D: calculated pattern without stacking faults; E: difference curve.

The superstructure used assumes a perfectly regular spacing of the stacking faults, it is likely that an even better adjustment of the calculated patterns to the experimental ones could be achieved if some fluctuation of stacking fault distances was permitted in association with the distribution in particle size observed by TEM.

From the refinements made on all the samples, we get strain, grain size, lattice parameters and information on the stacking fault periodicity. Results reported in table 1 show that the volume fraction of the faulted WC grains is nearly 50% for many samples. The plane number between stacking faults decreases rapidly from 17 to 9 in the first five hours. As the milling time increases, the amount of stacking faults does not change noticeably. It appears that in our milling conditions, the preferred mode of deformation is the formation of a large number of stacking faults which tend to be ordered in smaller grains. This ordering seems to be destabilized by prolonged milling during 150 hours. We do not know if cobalt, which was mainly found by EDX analysis in TEM along WC grain boundary regions, may affect these phenomena.

Table 1 Volume fraction of the two phases (hexagonal WC and orthorhombic WC defective superstructure); n= number of (10.0) planes between defects, D= spacing between defects

Milling time	Volume fraction		Rp	n	D (nm)
	hexagonal	orthorhombic			
150	0.72	0.28	4.97	7	1.8
100	0.52	0.48	6.67	9	2.3
40	0.41	0.59	6.05	9	2.3
20	0.38	0.62	5.59	9	2.3
10	0.46	0.54	7.49	9	2.3
5	0.47	0.53	6.46	9	2.3
2	0.43	0.57	7.47	11	2.8
0.5	0.47	0.53	6.73	17	4.3

Figure 5 shows the variation of the unit cell volume for the phase corresponding to hexagonal WC grains in function of the milling time. It can be seen that the unit cell volume decreases slightly with the milling time. This effect can be induced either by mechanical effects and the presence of defects or by chemical modification if some cobalt can be dissolved in the crystallites.

The hexagonal WC grain size decreases rapidly in the first stages of milling, while after 10 hours of milling it decreases much more slowly (figure 6). In agreement with TEM observations, the crystallite dimensions are relatively isotropic. On the other hand, the lattice strain found for hexagonal WC crystallites shows a strong anisotropy. The lattice strain along [10.0] in the powder milled for 10 hours is much higher than along [00.1] (figure 7). This result is also probably due to the planar defects which, despite they are less numerous than in the so-called orthorhombic crystallites, are also found in hexagonal WC grains.
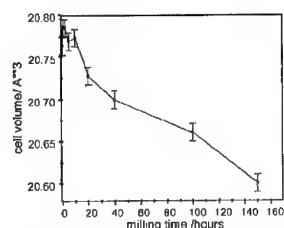
Figure 5. Cell volume of WC grains versus milling time
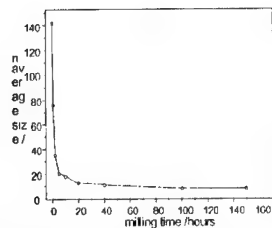
Figure 6. Grain size of WC versus milling time
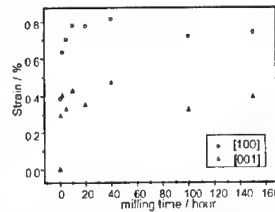
Figure 7. Strain along [001] and [100] versus milling time for WC-10%Co powder

5 CONCLUSION

(1) HRTEM images show that stacking faults in the planes {10.0} of WC grains were created by millling. Based on the HRTEM observations revealing the regular array of these defects in many crystallites, a structure model was proposed for the WC grains with stacking faults. When this new "phase" is put into the Rietveld procedure, the quality of the refinement is much improved. The refinement results show that during mechanical milling the density of stacking faults increases quickly during the first five hours, and as the milling time increases it stays almost unchanged.

(2) During mechanical milling, the lattice parameters of the WC decrease slowly. The average grain size decreases rapidly at the first 5 hours and then decreases slowly to about 8 nm. Microstrain along [10.0] is much larger than along [00.1] for the milled samples.

ACKNOWLEDGEMENT

REFERENCES

1   Suryanarayana C, International Materials Reviews, **40**, 41(1995).

2   Mao C H, Du J, Champion Y, Hagège S, Michel D, 6th Conf and Exhib of the Eur. Ceram. Soc,
     British Ceramic Proceedings n°60, **vol. 1**, 399(1999).

3   Langford J I, Accuracy in Powder Diffraction II, NIST Special Publication N° 846, ed. E. Prince & K.A. Stalick, Gaithersburg, MA (1992), 110.

4   Ungar T., Borbély A., Goren-Muginstein G R., Berger S. and Rosen A.R., Nanostructured Materials, **11**, 103(1999).

5   Langford J.I; Louër D and Scardi P, J. Appl. Cryst. **33**, 964(2000).

6   Rodriguez-Carvajal J., Reference Guide for the Computer Program Fullprof, Laboratoire Léon Brillouin, CEA-CNRS, Saclay (France)

7   Hagège S, PhD Thesis, University of Caen, 1980.

8   Hÿtch M J, Potez L, Phil. Mag. **A76**, 1119(1997).

Vibrational Properties of Silver Nanoparticles and Nanocrystalline Materials

Ralf Meyer
Département de Physique, Université de Montréal and
Groupe de Recherche en Physique et Technologie des Couches Minces (GCM)
C.P. 6128 succursale centre-ville, Montréal (Québec) H3C 3J7, Canada

ABSTRACT

The vibrational density of states of silver in the form of a free cluster, a single crystal and a nanocrystalline material has been calculated with the help of molecular-dynamics simulations. The model for the nanocrystalline material was derived by the simulation of pressureless sintering of nanometer sized silver particles. The results show a broadening of the vibrational density of states in the case of the cluster and the nanocrystalline material.

INTRODUCTION

In recent years materials scientists have paid much attention to the study of nanomaterials (see e.g. [1]). One interesting problem within this context is the vibrational density of states (VDOS) of nanocrystalline metals since the small grain sizes in these materials lead to significant changes in this quantity. Several inelastic neutron neutron scattering studies of pure metals and alloys have been published [2–7]. In two of these studies a linear onset of the VDOS at low energies has been observed [6, 7].

In this work, results of the calculation of the VDOS of silver as a free cluster, a single crystal, and a nanocrystalline material from molecular-dynamics simulations are presented. The model for the nanocrystalline material was obtained from a simulation of the pressureless sintering of nanoclusters. By this method a model material with 92.5 % of the density of the perfect solid was obtained which contains a number of nanometer sized voids. The results for the VDOS show a significant broadening in the case of the cluster and the nanocrystalline material. However, no linear onset of the VDOS is observed in the low energy regime.

COMPUTATIONAL METHODS

Molecular-dynamics simulations employing an embedded-atom method (EAM) potential [8] for silver have been performed. Details of the potential will be published elsewhere [9]. From these simulations the VDOS of the systems under investigation were calculated from the velocity autocorrelation function $\langle \mathbf{v}(t)\,\mathbf{v}(0) \rangle$ whose Fourier-transform is proportional to the VDOS [10].

Three different configurations were used in the calculations. An Ag_{1205} cluster with a diameter of 3.3 nm was constructed by cutting a spherical region out of a regular fcc lattice. Simulations of single crystalline silver were based on a supercell of $20 \times 20 \times 20$ cubic fcc elementary cells (32 000 atoms). Much more efforts were required to obtain a model for the nanocrystalline material. For this purpose, 32 randomly rotated copies of the Ag_{1205} cluster (after equilibration) were arranged
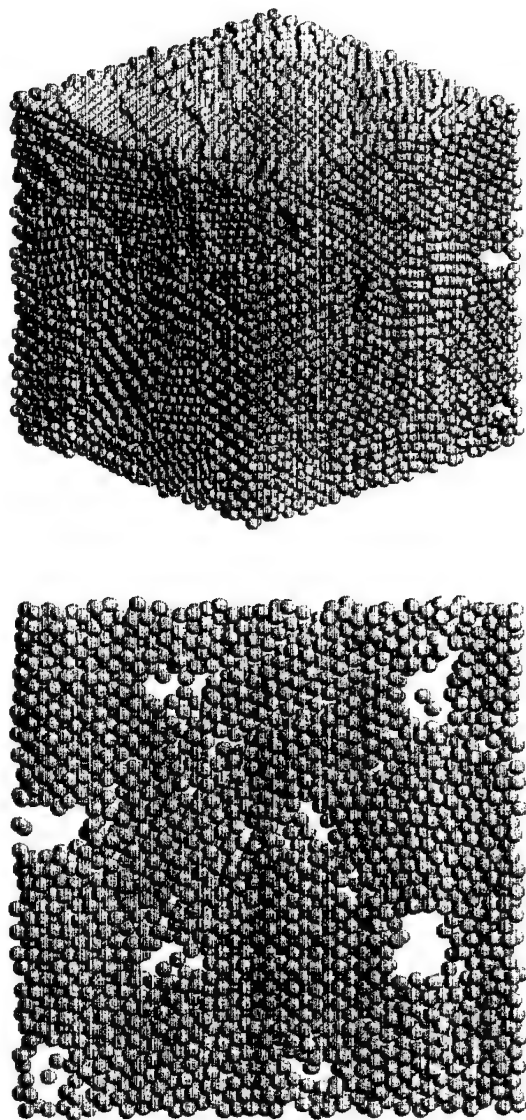
Figure 1. Upper panel: Configuration of nanocrystalline silver after pressureless sintering over 1.5 ns. The edges of the nearly cubic cell have a length of about 9 nm. Lower panel: 0.4 nm thick cross-section of the same configuration.

on a fcc lattice. The lattice constant of this super lattice was chosen in such a way that the clusters interacted only weakly with one another. Starting from this configuration the consolidation of the clusters to a dense materials was simulated at zero pressure and constant temperature over a period of 1.5 ns (1 000 000 simulation steps).

In the simulations of the single and nanocrystalline systems periodic boundary conditions were applied. Moreover these calculations were carried out in the NPT ensemble by employing a Nosé-Hoover thermostat [11] and the Parrinello-Rahman method [12]. However, since the use of methods like the Nosé-thermostat and the Parrinello-Rahman scheme modifies the dynamics of the particles, their use had to be avoided in the calculations of the VDOS. Therefore, the velocity autocorrelation functions were calculated from additional simulation runs at constant energy and volume using the average volumes derived from the constant-pressure simulations. All simulations were performed with the Verlet-Algorithm [13] using a time step of 1.5 fs and a temperature of 300 K.

RESULTS

The configuration of the nanocrystalline system resulting from the simulation of the sintering process over 1.5 ns is shown in the upper panel of figure 1. As can be seen from this figure, a dense nanocrystalline system has been formed during this simulation. The density of the system at this time has reached 92.5 % of the density of the single crystal. The figure reveals further that in spite of the closed-packed arrangement of the clusters in the starting configuration, the system contains a number of voids. The structure of these voids can be better seen from the cross-sectional view of the system given in the lower panel of figure 1. From this figure the size of the voids can be estimated to be of the order of 1 nm. However, one should be careful to draw conclusions about the general structure of the system from this figure. The closed-packed structure of the initial configuration leads to a somewhat artifical arrangement of the interfaces and voids in the system. The cross-section shown in the lower panel of figure 1, which has been specially chosen to show the voids, is therefore not representative for the core parts of the grains.

In figure 2 the VDOS of the free Ag_{1205} cluster and single crystalline silver are presented. The curves have been broadened by a finite line-width of 0.5 meV in order to reduce the noise. It can be seen that the global VDOS of the cluster is significantly broadened in comparison to the single crystal. This broadening is mainly due to the contribution of surface atoms. However, in contrast to the recently published results of a Green's function calculation [14] no linear behavior of the VDOS at low energy can be seen in figure 2. Instead of this a gap is found at energies below 1.5 meV (see also inset in figure 3; the small VDOS remaining below 1.5 meV results from the line broadening and finite simulation time). The VDOS in the core of the particle is governed by the presence of a capillary pressure of 1.5 GPa inside the cluster as discussed in [15]. The effect of the capillary pressure can be seen from figure 2, which shows that the VDOS inside the cluster is shifted with respect to the single crystal and is identical to the VDOS of the single crystal under a pressure of 1.5 GPa.

Finally, the VDOS of the nanocrystalline material, the single crystal and the cluster are compared in Figure 3. While the behavior of the nanocrystalline system at high energies is very similar to the result for the free cluster, a further increase of the VDOS at low energies can be seen in the nanocrystalline material. Although the gap in the spectrum vanishes during the consolidation
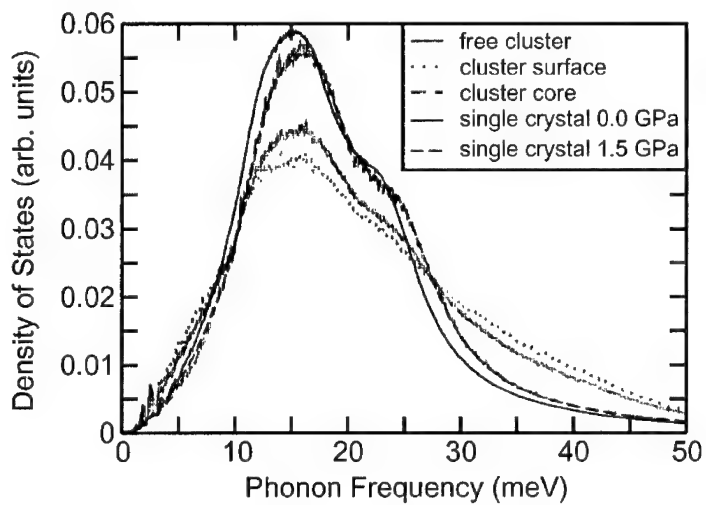
Figure 2. Vibrational density of states of a Ag$_{1205}$ cluster (thick light solid line). The thick light dotted (dashed) line denote the contributions of surface (core) atoms of the cluster. Results for single crystalline Ag at pressures of 0.0 and 1.5 GPa are given by the thin dark solid and dashed lines, respectively.
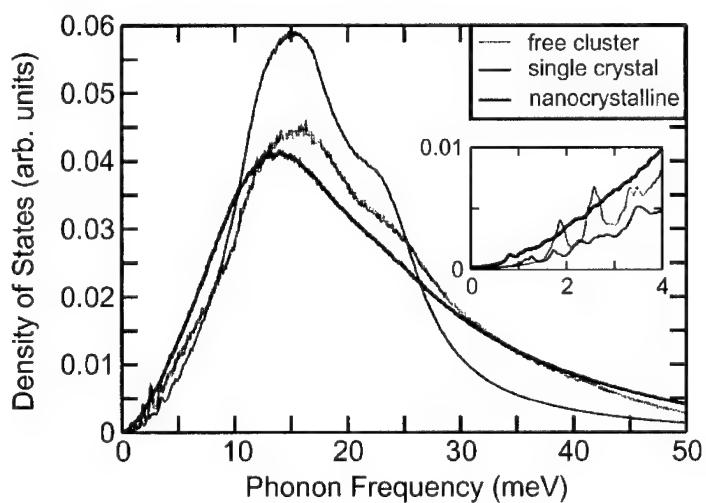
Figure 3. Vibrational density of states of nanocrystalline Ag (thick dark line), single crystalline Ag (thin dark line) at zero pressure and a Ag$_{1205}$ cluster (thick light line).

of the clusters, there is still no sign of a linear onset of the VDOS. The increase of the VDOS in the nanocrystalline material is accompanied by a decrease and loss of structure of the VDOS at medium energies.

SUMMARY AND CONCLUSIONS

The VDOS of a free silver cluster as well as single and nanocrystalline silver have been calculated from molecular-dynamics simulations. In order to construct a model for the nanocrystalline material the process of pressureless sintering has been simulated for 32 nanoparticles. From this simulation a model system of dense nanocrystalline silver with nanometer sized voids was obtained.

The calculation of the VDOS of the three systems showed a pronounced broadening of the VDOS in the cluster and the nanocrystalline material. However, the linear onset of the VDOS at low energies which has been observed in some experimental studies [6, 7] is not found in the calculations. In the case of the cluster a gap is observed at low energies which seems to be plausible since the finite size of the cluster should suppress any modes with long wavelength. Similarly the missing linear behavior in the case of the nanocrystalline material might be related to the limited size of the voids in the model system. This would mean that the presence of a linear increase of the VDOS at low energies requires the presence of extended surface structures in the material. This scenario can possibly be checked by computer simulations of much bigger nanocrystalline systems consolidated from an irregular arrangement of clusters.

ACKNOWLEDGMENTS

REFERENCES

1. A. S. Edelstein and R. C. Cammarata, editors, *Nanomaterials: Synthesis, Properties and Applications*, Institute of Physics Publishing, Bristol, 1996.

2. J. Trampenau, K. Bauszus, W. Petry, and U. Herr, Nanostruct. Mater. **6**, 551 (1995).

3. B. Fultz, J. L. Robertson, T. A. S. , L. J. Nagel, and S. Spooner, J. Appl. Phys. **79**, 8318 (1996).

4. B. Fultz, C. C. Ahn, E. E. Alp, W. Sturhahn, and T. S. Toellner, Phys. Rev. Lett. **79**, 937 (1997).

5. H. N. Frase, L. J. Nagel, J. L. Robertson, and B. Fultz, Phil. Mag. B **75**, 335 (1997).

6. U. Stuhr, H. Wipf, K. H. Andersen, and H. Hahn, Phys. Rev. Lett. **81**, 1449 (1998).

7. E. Bonnetti, L. Pasquini, E. Sampaolesi, A. Deriu, and G. Cicognani, J. Appl. Phys. **88**, 4571 (2000).

8. M. S. Daw and M. I. Baskes, Phys. Rev. B **29**, 6443 (1984).

9. R. Meyer, S. Prakash, P. Entel, and L. J. Lewis, to be published.

10. S. W. Lovesey, *Condensed matter physics: dynamic correlations*, volume 61 of *Frontiers in Physics*, Benjamin/Cummings, Menlo Park, Calif., 2 edition, 1986.

11. W. G. Hoover, Phys. Rev. A **31**, 1695 (1985).

12. M. Parrinello and A. Rahman, Phys. Rev. Lett. **45** (1980).

13. L. Verlet, Phys. Rev. **159** (1967).

14. A. Kara and T. S. Rahman, Phys. Rev. Lett. **81**, 1453 (1998).

15. R. Meyer, S. Prakash, and P. Entel, Capillary pressure and phonon density of states in Ag, Au, Cu, and Ni nanoparticles, in *Proceedings of the Symposium on Structure and Dynamics of Heterogeneous Systems II*, Duisburg, 2000, to appear in Phase Transitions.

AUTHOR INDEX

SUBJECT INDEX